UCLA
UCLA Electronic Theses and Dissertations

Title
Early Tumor Detection and Therapeutics Using an Advanced Magnetic Resonance Nano-Theranostic System

Permalink
https://escholarship.org/uc/item/04w6400t

Author
Wang, Chencai

Publication Date
2018

Peer reviewed|Thesis/dissertation

eScholarship.org Powered by the California Digital Library
University of California

UNIVERSITY OF CALIFORNIA

Los Angeles

Early Tumor Detection and Therapeutics Using an Advanced Magnetic Resonance Nano-Theranostic System

A dissertation submitted in partial satisfaction of the

requirements for the degree Doctor of Philosophy

in Chemistry

by

Chencai Wang

2018

© Copyright by

Chencai Wang

2018

ABSTRACT OF THE DISSERTATION

Early Tumor Detection and Therapeutics

Using an Advanced Magnetic Resonance Nano-Theranostic System

by

Chencai Wang

Doctor of Philosophy in Chemistry

University of California, Los Angeles, 2018

Professor Yung-Ya Lin, Chair

In this dissertation, I proposed an approach to conducting an *in vivo* nano-theranostic system of combined hyperthermia/MRI to simultaneously diagnose and treat cancer. The procedure involves injecting biocompatible magnetic nanoparticles that not only act as molecular beacons to enhance MRI contrast for early tumor detection but also destroy tumor cells when the particles are heated by exposing them to an applied magnetic field. However, the promising possibilities of this pre-clinical or clinical application can only be realized if:

(i) A more sensitive MRI method is applied to enhance the imaging contrast between the difficult-to-detect early-stage tumor and the healthy tissue while significantly reduces the lengthy acquisition time required for high quality image reconstruction.

(ii) The physical and magnetic properties of the nanoparticles are precisely controlled to optimize their heating efficiency, which is critical to focusing the energy onto tumor cells and avoiding damaging healthy tissue.

For the theranostic purpose of developing molecular diagnostics and targeted therapeutics, I performed theoretical calculations and conducted *in vivo* experiments to validate the applicability and efficacy of my proposed technique. The major research projects and the preliminary achievements during my five-year Ph.D. career under the supervision of Prof. Yung-Ya Lin include the following:

(i) I established a novel model to evaluate the heating efficiency of magnetic nanoparticles for *in vivo* nano-theranostic hyperthermia in the presence of MRI, based on three major findings about the magnetic field's effect on the relaxation process, the aggregate formation of magnetic nanoparticles, and the nonlinear response of the magnetic susceptibility.

(ii) To improve the heating efficiency of *in vivo* nano-theranostic hyperthermia in the clinical MRI environment, I proposed either using a high frequency-driven rotating magnetic field to heat small magnetic nanoparticles encapsulated along with therapeutic drugs inside thermosensitive liposomes, or else using a low frequency-driven linearly ramped alternating magnetic field combined with a built-in MRI gradient to trigger the Brownian relaxation mechanism.

(iii) By taking advantage of an active feedback electronic device that was homebuilt to implement active-feedback pulse sequences to generate avalanching spin amplification, we showed both theoretically and experimentally that our new technique enhanced the imaging contrast at the tumor site fivefold, allowing the tumor to be successfully identified without intervention.

(iv) I employed compressive sensing to extract all of the clinically important features of MR images by collecting only a small sample of the data. In comparison to the

conventional T2-weighted imaging and compressive sensing reconstruction by Gaussian sampling, my newly proposed sensing matrix was able to reconstruct feedback-based images that had less sparsity, a higher correlation coefficient, and an improved contrast-to-noise ratio.

In the interest of the clinical application of this *in vivo* nano-theranostic system of combined hyperthermia/MRI, the results of my research offer a a novel methodology to perform fast and sensitive imaging for early tumor detection and a paradigm for designing magnetic nanoparticles to treat cancer efficiently through the hyperthermia in the MR environment.

The dissertation of Chencai Wang is approved.

William M. Gelbart

Michael Albert Thomas

Yung-Ya Lin, Committee Chair

University of California, Los Angeles

2018

TABLE OF CONTENTS

1. Introduction and Highlights

1.0 Introduction....1

1.1 Research Highlights....2

1.1.1 Optimizing the Heating Efficiency of Magnetic Nanoparticles for *In Vivo* Nano-Theranostic Hyperthermia in the Presence of High-Field MRI

1.1.2 Implementing Compressive Sensing Algorithm to Reduce the Lengthy Imaging Acquisition Time for Sensitive MRI

1.1.3 Developing New MRI Pulse Sequences Using a Novel Homemade Medical Device to Enhance the Imaging Contrast for Early Tumor Detection

Part I. In Vivo MR Nano-Theranostic Hyperthermia

2. Optimizing Magnetic Nanoparticle Hyperthermia Effect in Magnetic Resonance Nanomedicine

2.0 Abstract....8

2.1 Introduction....9

2.2 Theory....11

2.2.1 Formation of Aggregates Among Magnetic Nanoparticles

2.2.2 Critical Frequency and Critical Temperature under an Alternating Magnetic Field

2.3 Methods....14

2.3.1 Setup of Model and Parameters

2.3.2 Cluster-Moving-Based Metropolis Monte Carlo Simulation

2.4 Results and Discussions....17

2.4.1 Simulation Results of the Aggregate Formation

2.4.2 Analysis of the Critical Frequency for Aggregates Disruption

2.5 Conclusion....24

2.6 References....25

3. Effective Heating of Magnetic Nanoparticle Aggregates for *In Vivo* Nano-theranostic Hyperthermia

3.0 Abstract 28

3.1 Introduction 29

3.2 Materials and Methods 32

3.2.1 Fraction of Monomers and Clusters

3.2.2 Relaxation Mechanisms

3.2.3 Equilibrium Magnetization

3.2.4 Magnetic Susceptibility

3.2.5 Power Dissipation

3.2.6 Specific Loss Power

3.2.7 Comparison with Experimental Results

3.2.8 *In Vivo* Demonstration of Magnetic Nanoparticle Aggregation in Cancer Tissues

3.3 Results and Discussion 41

3.3.1 *In Vivo* Demonstration of Magnetic Nanoparticles Aggregation in Pancreatic Cancer

3.3.2 Comparison with the Rosensweig Model

3.3.3 Comparison with the Experimental Results of Magnetite Fe_3O_4 Magnetic Nanoparticles

3.3.4 Comparison with the Experimental Results of Cobalt Ferrite $CoFe_2O_4$ Magnetic Nanoparticles

3.4 Conclusion 53

3.5 References 55

3.6 Supplementary Materials 61

4. Utilizing the Nonlinear Response of Magnetic Nanoparticle Aggregates for Effective *In Vivo* Nano-Theranostic Hyperthermia

4.0 Abstract 65

4.1 Introduction 66

4.2 Materials and Methods 69

4.2.1 Fraction of Monomers and Clusters

4.2.2 Relaxation Mechanisms

4.2.3 Magnetic Susceptibility
4.2.4 Power Dissipation and Specific Loss Power
4.2.5 Computational Parameters
4.3 Results and Discussion 79
4.3.1 Theoretical Comparisons
4.3.2 Experimental Comparisons
4.4 Conclusion 90
4.5 References 91
5. Optimizing the Heating Efficiency of Magnetic Nanoparticles for *In Vivo* MR Nano-Theranostic Hyperthermia
5.0 Abstract 96
5.1 Introduction 97
5.2 Materials and Methods 100
5.2.1 Power Dissipation
5.2.2 Relaxation Processes
5.2.3 Aggregation
5.2.4 Nonlinear Response
5.2.5 Computational Parameter
5.3 Results and Discussion 107
5.3.1 Relaxation Time Constants Comparisons
5.3.2 SLP Predictions
5.4 Conclusion 117
5.5 References 118
6. Efficient Heating of *In Vivo* Nano-Theranostic Hyperthermia in the Presence of MRI
6.0 Abstract 124
6.1 Introduction 125
6.2 Materials and Methods 128
6.2.1 Magnetic Field-Dependent Relaxation Process
6.2.2 Aggregation
6.2.3 Nonlinear Response of Magnetic Susceptibility

6.2.4 Power Dissipation and Specific Loss Power
6.2.5 Computational Parameters
6.3 Results and Discussion 135
6.3.1 Relaxation Mechanism
6.3.2 Heating Efficiency Predictions
6.4 Conclusion 146
6.5 References 147

Part II. Compressive Sensing in Efficient Imaging Acquisition

7. Designing a Sparse Sensing Matrix for Compressive Sensing to Reconstruct High Contrast MR Images in Early Tumor Detection
7.0 Abstract 153
7.1 Introduction 154
7.2 Theory 156
7.2.1 Recovery Algorithm
7.2.2 Sparse Sensing Matrix
7.3 Results and Discussion 158
7.3.1 Structure of the Sensing Matrix
7.3.2 Reconstruction Quality of the Sensing Matrix
7.3.3 Experimental Image and Simulation Results
7.4 Conclusion 166
7.5 References 167
8. Non-Linear Iteration Technique to Enhance Early Tumor Contrast in Compressive Sensing MRI
8.0 Abstract 171
8.1 Introduction 172
8.2 Theory 174
8.2.1 Feedback-Based Contrast Enhancement
8.2.2 Compressive Sensing Theory
8.2.3 Reconstruction Quality Indicator

8.3 Results and Discussion 177
8.3.1 Feedback-Based High Contrast Image
8.3.2 Sparsity of High Contrast Image
8.3.3 Reconstructed Image Results
8.4 Conclusion 187
8.5 References 187

Part III. Active Feedback MRI

9. MRI Contrast Enhancement in Early Tumor Detection by Using Nonlinear Spin Dynamics in a Radiation Damping Field: Insight from Simulation
9.0 Abstract 190
9.1 Introduction 190
9.2 Methods 192
9.2.1 Nonlinear Evolution of Spin Dynamics
9.2.2 Healthy Tissue and Early Tumor Physiological Models
9.3 Results and Discussion 196
9.3.1 Physiological Model
9.3.2 Linear Spin Dynamics
9.3.3 Nonlinear Spin Dynamics
9.3.4 *In Vivo* Experiments
9.4 Conclusion 203
9.5 References 204

10. **Conclusion and Outlook** 208

ACKNOWLEDGEMENTS

Over the past five years, I have been the recipient of much support and encouragement from a number of individuals.

First, I would like to thank my advisor, Prof. Yung-Ya Lin, for his fundamental role in my doctoral work. His guidance has made my Ph.D. career a thoughtful and rewarding journey. Without his constant mentorship and patience, graduate school would have been far more tiresome and discouraging, and I am thus deeply indebted to all the kindness he has shown me. His focus on academic independence and self-motivation has allowed me to exercise my own creativity and develop my own sense of research direction that I will take with me in my future academic endeavors. I cannot imagine having a better advisor and mentor for my Ph.D. studies.

My sincere thanks also go to the rest of my dissertation committee, Prof. William M. Gelbart, Prof. Charles M. Knobler, and Prof. Albert M. Thomas, for their support over the past four years as I moved from an idea to a completed study, for their insightful comments and encouragement, and also for asking me the hard questions that spurred me to widen my perspectives and the scope of my research.

In addition, I am very grateful to my fellow labmates Zhao Li, Chao-Hsiung Hsu, Sayoni Ray, Huimin Yang, and Fang-Chu Lin for our stimulating discussions, for the sleepless nights we worked together to meet deadlines, and for all the fun we have had in the last four years.

Last but not least, living with Chris Norlin and our pets, Ying Ying and Storm, has made this journey easier and more lovely. Above all, my parents have been there for me every step of the way. I cannot begin to imagine where I would be without their continued love, guidance, and spiritual support.

VITA

Education

- M. Sc. In Chemistry, University of California Los Angeles, Los Angeles, California, June, 2014
- B. Eng. In Electronic Science and Technology, Nankai University, Tianjin, China, June 2013
- B. Econ. In Finance, Nankai University, Tianjin, China, June 2013

Selected Awards & Distinctions

- 2016 ISMRM Educational Stipends, Singapore, Singapore, 2016
- 2016 ICHO New Investigator Travel Award, New Orleans, Louisiana, 2016
- Hanson-Dow Teaching Assistant Award, Department of Chemistry and Biochemistry, UCLA, 2015
- ACS Travel Award, Department of Chemistry and Biochemistry, UCLA, 2015
- First Prize of Micro-Mouse Searching Maze Contest host by IEEE, China, 2012
- Second Prize of the North American Mathematical Contest in Modeling, 2012
- China National Scholarship, China, 2010

Selected Publications & Presentations

- Chencai Wang, Chao-Hsiung Hsu, Yung-Ya Lin, *Effect heating of Magnetic Nanoparticle Aggregation for in vivo Nano-Theranostic Hyperthermia*. Int. J. Nanomedicine. 12, 1-15 (2017).

- Chencai Wang, Zhao Li, Yung-Ya Lin, *Optimizing Magnetic Nanoparticle Hyperthermia Effect in Magnetic Resonance Nanomedicine.* Chinese Journal of Magnetic Resonance 32(2), 248-260 (2016).
- Chencai Wang, Chao-Hsiung Hsu, Zhao Li, Yung-Ya Lin, *Nonlinear Iteration Technique to Enhance Early Cancer Contrast in Compressed Sensing MRI*, World Molecular Imaging (WMIC), Philadelphia, PA (2017).
- Chencai Wang, Chao-Hsiung Hsu, Yung-Ya Lin, *Optimizing the Heating Efficiency of Nano-theranostic Hyperthermia in MRI*, World Molecular Imaging (WMIC), Philadelphia, PA (2017).
- Chencai Wang, Susie Y. Huang, Chao-Hsiung Hsu, Stephanie Wolahan, Yung-Ya Lin, *Indirectly-detected and Spin-amplified Heteronuclear MRS and MRI*, International Society for Magnetic Resonance in Medicine (ISMRM), Singapore (2016).
- Chencai Wang, Chao-Hsiung Hsu, Yung-Ya Lin, *Heating Efficiency of Colloidal Magnetic Fluids with Nonlinear Loss Properties and Aggregate Formation*, International Congress for Hyperthermic Oncology (ICHO), New Orleans, LA (2016).
- Chencai Wang, Chao-Hsiung Hsu, Zhao Li, Yung-Ya Lin, *Early Brain Tumor Detection by Chemical Imaging of Deoxyhemoglobin*, American Chemical Society National Meeting & Exposition (ACS), San Diego, CA (2016).
- Chencai Wang, Susie Y. Huang, Zhao Li, Stephanie Wolahan, Yung-Ya Lin, *Indirect Detection of Early Tumor via the joint effect of Distant Dipolar Field and Active Feedback Field under High Magnetic Field*, World Molecular Imaging (WMIC), Honolulu, HI (2015).

Chapter 1

Introduction and Highlights

1.0 Introduction

Cancer is among the leading causes of death not only in the United States but also across the world. According to National Cancer Institute, in 2018, an estimated 1.7 million individuals have been diagnosed with cancer and 609.640 people will die from the disease. If early tumor detection and therapeutics in stage I or II can be made feasible and routine, the death tolls could be reduced approximately 30%. To achieve this goal, I proposed the *in vivo* nano-theranostic system of combined hyperthermia/MRI to simultaneously diagnose and treat cancers in this dissertation, as shown in Figure 1. The procedure involves injecting biocompatible magnetic nanoparticles that not only act as molecular beacons to enhance MRI contrast for early tumor detection, but also destroy tumor cells when the particles are heated when exposed to an applied magnetic field. Two biggest challenges, which have to overcome for realizing this clinical application, were addressed during my Ph. D. and summarized in this dissertation:

(i). A sensitive MRI method is applied to enhance the imaging contrast between the early-stage tumor and the healthy tissue while significantly reduces the lengthy acquisition time with high quality image reconstruction.

(ii). The physical and magnetic properties of the nanoparticles are precisely controlled to optimize their heating efficiency, which is critical to focusing the energy onto tumor cells and avoiding damaging healthy tissue.

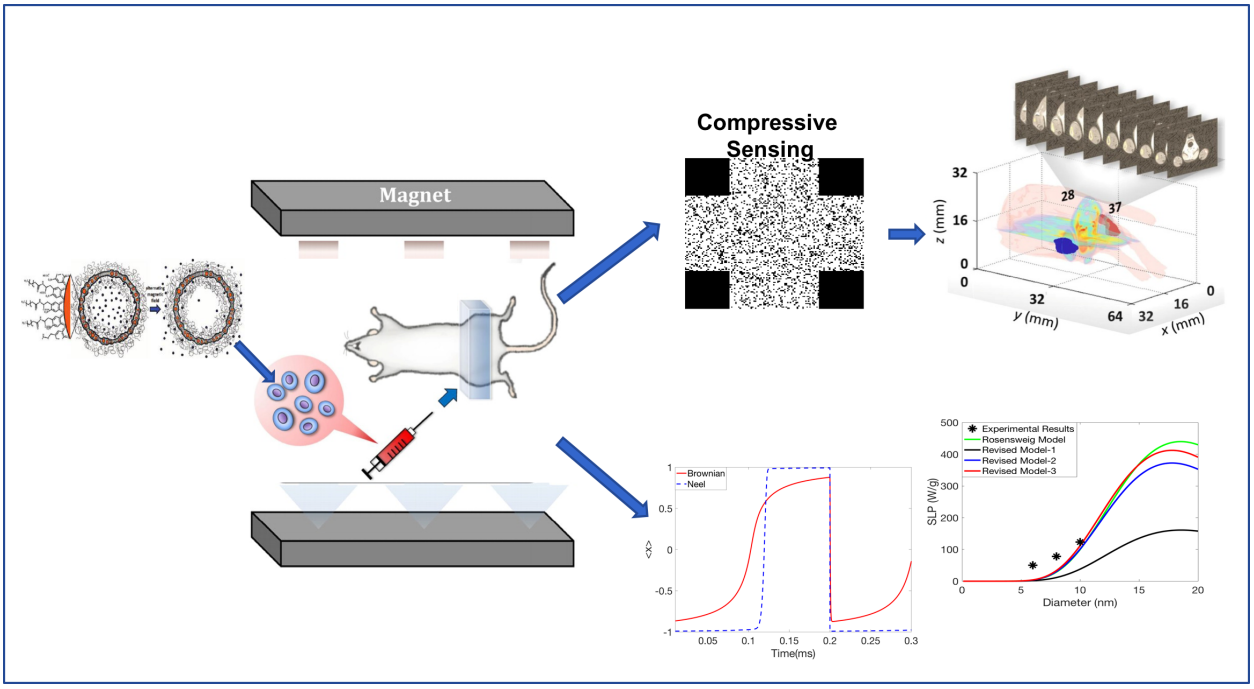


Figure 1. A schematic illustration of an *in vivo* nano-theranostic system of combined MRI and Hyperthermia

1.1 Research Highlights

Under the supervision of Professor Yung-Ya Lin, my research focuses on early tumor detection and therapeutics using advanced Magnetic Resonance nano-theranostic technique. Within this broad topic, I am undertaking three on-going projects: 1) Optimizing the heating efficiency of magnetic nanoparticles for in vivo nano-theranostic hyperthermia in the presence of high-field MRI. 2) Implementing compressive sensing algorithm to reduce the lengthy imaging acquisition time for sensitive MRI. 3) Developing new MRI pulse sequences using a novel homemade medical device to enhance the imaging contrast for early tumor detection.

The highlights of each project and associated achievements are listed below:

1.1.1 Optimizing the Heating Efficiency of Magnetic Nanoparticles for *In Vivo* Nano-Theranostic Hyperthermia in the Presence of High-Field MRI

As shown in Figure 2, I established a novel model to evaluate and optimize the heating efficiency of magnetic nanoparticles for in vivo nano-theranostic hyperthermia in the presence of MRI based on three major findings: (i) magnetic nanoparticles are interacting in the colloidal suspension, (ii) magnetic susceptibility and magnetic field amplitude are nonlinearly related, and (iii) relaxation times due to the Brownian or Néel relaxation mechanisms depend on the amplitude of the applied magnetic field. In order to assess the accuracy of our *in vivo* theoretical model's consideration of nanoparticle aggregation, the nonlinear response of the magnetic susceptibility, and the magnetic field effects on relaxation processes, predictions made by our models for previously published experimental data were compared to predictions made by the currently prevailing models. The consistency between the experimental data and our model's predications validated the importance of the three findings in understanding the heating mechanism and accurately evaluating the heating efficiency as a function of mean magnetic nanoparticle size, even when large magnetic nanoparticles are in the presence of relatively strong magnetic fields.

To improve the heating efficiency of *in vivo* nano-theranostic hyperthermia in the clinical MRI environment, we proposed either using a high frequency-driven rotating magnetic field to heat small magnetic nanoparticles encapsulated along with therapeutic drugs inside thermosensitive liposomes, or else using a low frequency-driven linearly ramped alternating magnetic field combined with a built-in MRI gradient to trigger the Brownian relaxation mechanism.

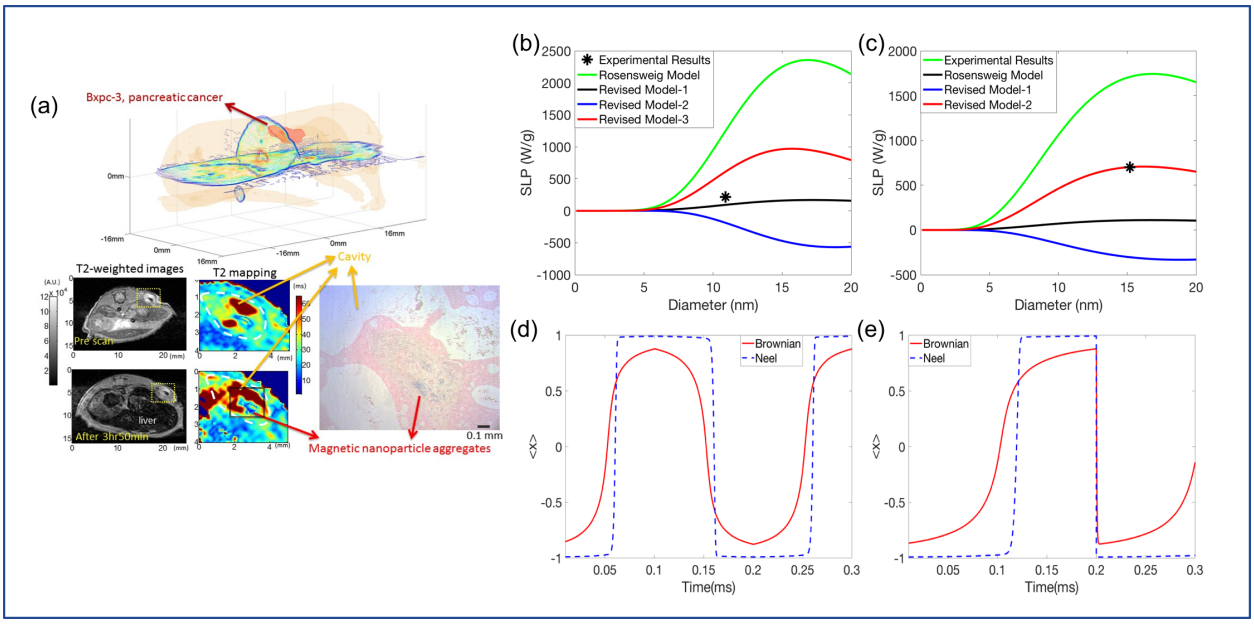


Figure 2. (a) Formation of magnetic nanoparticle aggregates in targeted pancreatic cancer tissues. In order to demonstrate the aggregation of magnetic nanoparticles in biomedical applications, we inspected MR T_2-weighted imaging and the pathological iron stain of pancreatic cancers in *in vivo* xenograft mouse models, which are targeted and labelled by magnetic nanoparticles. To enhance targeting specificity and efficiency, anti-CA 19-9 antibodies were conjugated to NH_2-PEG-coated magnetic nanoparticles. (b) & (c) Theoretical SLP comparisons between the Rosensweig model (solid green line), the revised model-1 with changes in the relaxation time constants (solid black line), the revised model-2 with changes in the relaxation time constants and nonlinear regime (solid blue line), and the further revised model-3 that takes into consideration aggregation formation, nonlinear regime and the magnetic field-based relaxation time constants (solid red line) for magnetite. The magnetic field amplitude and frequency were set to 30 *kA/m* and 210 *kHz*, respectively, both Brownian relaxation and Néel relaxation processes were deemed to take place "in parallel". (d) & (e) The time series of the normalized magnetization, $M(t)/nm_0 = \langle x(t) \rangle$, for Brownian relaxation (solid red line) and for

Néel relaxation (dashed blue line) in the presence of a 150mT, 5kHz alternating magnetic field with different shapes.

1.1.2 Implementing Compressive Sensing Algorithm to Reduce the Lengthy Imaging Acquisition Time for Sensitive MRI

As shown in Figure 3, I proposed a computational thinking method for contrast enhancement at early-stage tumor site as well as reduce the lengthy acquisition time in MRI based on two major findings:

(i) The spatial variations in magnetic susceptibility directly reflect the physiological changes that take place as tumors grow, and active feedback-based nonlinear imaging technique is sensitive to such small difference. (ii) Compressive Sensing can be used to extract all important features in MR images by collecting only a small sample of data. Stage-1 orthotopic GBM mouse models infected with human U87MG cell line were imaged. Representative results showed that in comparison to the conventional T2-weighted imaging and compressive sensing reconstruction by Gaussian sampling, newly proposed sensing matrix was able to reconstruct feedback-based image with less sparsity, but leads to a high correlation coefficient and improved contrast-to-noise ratio. With advances in clinical biomedical diagnostics, this technique becomes increasingly important because we want to optimize the contrast by trial and error while accounting for the cost and considerations of patient comfort and compliance.

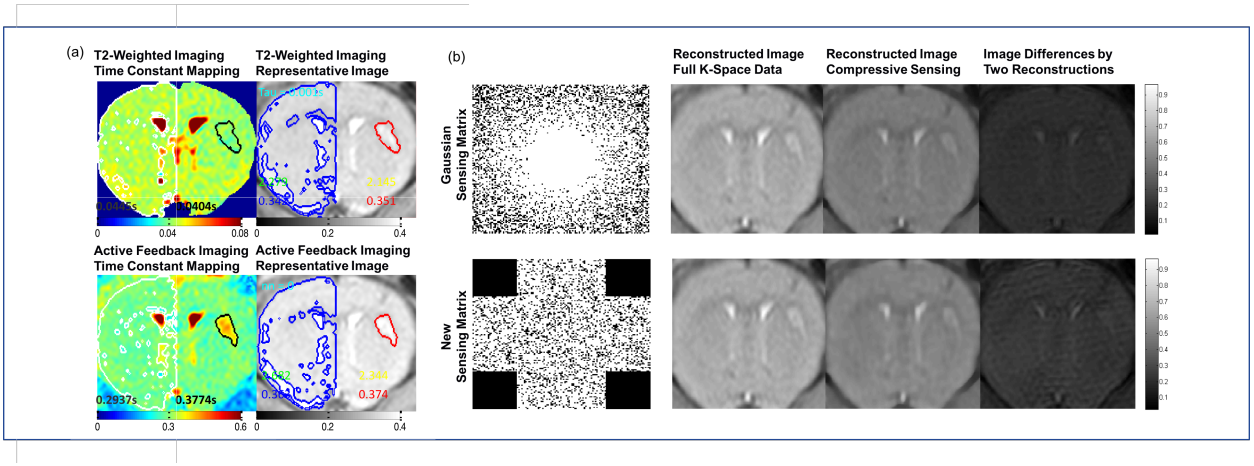


Figure 3. (a) Representative results from mouse with tumor injected for 13 days, the active-feedback image and time constant mapping successfully highlight the brain tumor in comparison to the T2-weighted image and time constant mapping. (b) Representative feedback-based images reconstructed using different sensing matrix. The 79% sparsity Gaussian sensing matrix gave a correlation coefficient of 0.99 and CNR of 12.79 at tumor site, while the 60% sparsity newly proposed sensing matrix gave a correlation coefficient of 0.98 and CNR of 21.26 at tumor site.

1.1.3 Developing New MRI Pulse Sequences Using a Novel Homemade Medical Device to Enhance the Imaging Contrast for Early Tumor Detection

As shown in Figure 4, we proposed a new Magnetic Resonance imaging method to detect early bruin tumor based on two major discoveries: (i) Deoxyhemoglobin can serve as a chemical biomarker for early brain tumor. (ii)Signal enhancement using chaotic hemodynamics. By taking advantage of an active feedback electronic device, which was homebuilt to implement active-feedback pulse sequences to generate avalanching spin amplification, we showed both theoretically and experimentally that such new technique enhanced the imaging contrast at the tumor site fivefold, and the tumor was successfully identified without intervention, which is more stable and robust in comparison to conventional methods.

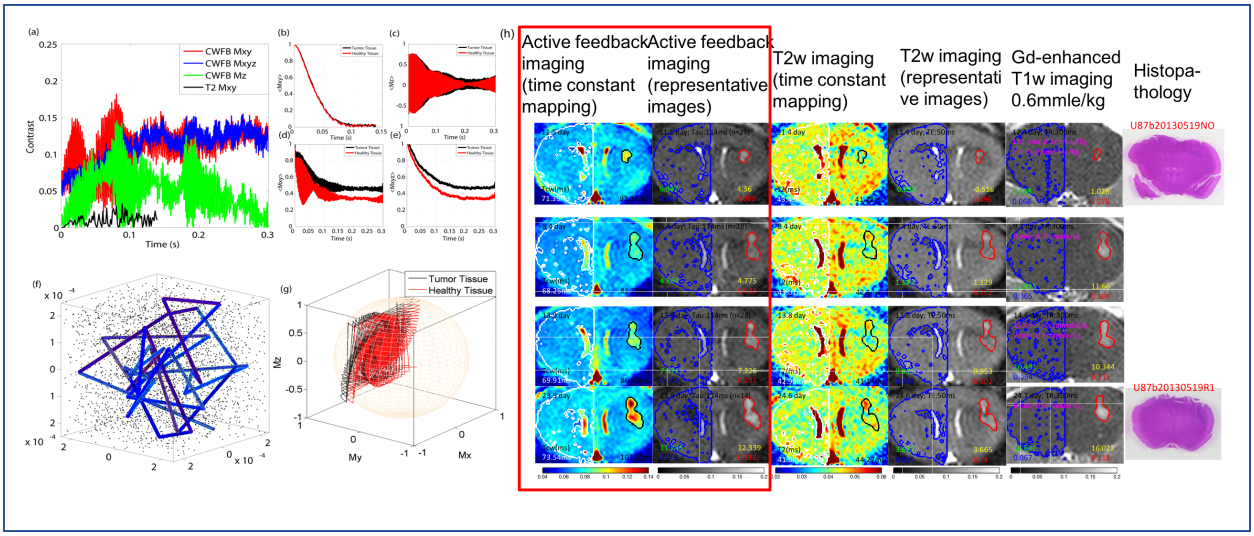


Figure 4. (a) Contrast comparison at early-stage tumor between CWFB and T_2-Weighted Imaging. (b) Spin evolution upon T_2-Relaxation mechanism. (c)-(e) Spin evolution upon CWFB mechanism. (f) Physiological model used for simulating spin dynamics upon different relaxation mechanisms. (g) 3D spin dynamics under CWFB mechanism. (h) Representative results from 4 mice were shown below. Statistical results (N=22) show that this new approach provides 5-6 times of improvements in GBM tumor contrast.

Chapter 2

Optimizing Magnetic Nanoparticle Hyperthermia Effect in Magnetic Resonance Nanomedicine

2.0 Abstract

Magnetic resonance hyperthermia is a new nano-medical therapy that emerges in recent years. In the presence of external alternating magnetic fields produced by MR instruments, magnetic nanoparticles accumulated at the tumor site can generate heat through Neel relaxation and/or Brownian relaxation. Through magnetic resonance hyperthermia, magnetic nanoparticles can serve as "molecular bullets" to kill cancer cells, leaving surrounding healthy tissues unaffected. Such hyperthermic effects can also be used for thermal activation and control releasing of cancer drugs. One major challenge of magnetic resonance hyperthermia is to optimize the heating efficiency of magnetic nanoparticle suspension. Heating efficiency depends on the size, physical properties, and aggregation state of magnetic nanoparticles. In this study, the thermodynamic behavior of magnetic nanoparticles and the aggregation/disruption of monomers/clusters under different temperatures were studied by 3D Metropolis Monte Carlo method. The relationship between the critical temperature for aggregation/disruption and the frequency of external magnetic field has been established through revised Langevin function. Simulation results show that the relative content of aggregates in colloidal magnetic nanoparticle suspension decreased with the increase of temperature, and the aggregates disrupted completely into monomers at or above the critical temperature. In addition, increasing the frequency of external alternating magnetic field significantly lowered down the critical temperature, and there

existed a critical frequency where the critical temperature stabilized and became unaffected by the frequency. Preheating the suspension under critical frequency will disrupt the aggregates into monomers and thus optimize the heating efficiency of magnetic nanoparticles.

2.1 Introduction

Magnetic nanoparticles have found popular applications in magnetic resonance molecular imaging and nanomedicine for medical diagnosis and therapy. Because these nanoparticles are biocompatible, injectable, nontoxic, and are able to target specific tissues through specific (e.g., antibody-antigen) and non-specific (e.g., enhanced permeability and retention effect) targeting mechanisms, they can serve as "molecular beacons" to enhance the MR image contrast for early tumor detection. Moreover, through interacting with external alternating magnetic fields, these magnetic nanoparticles accumulated at the tumor site can generate heat through Neel relaxation and/or Brownian relaxation.[1-4] Through magnetic resonance hyperthermia, magnetic nanoparticles can serve as "molecular bullets" to kill cancer cells, leaving surrounding healthy tissues unaffected. Such hyperthermic effects can also be used for thermal activation and control releasing of cancer drugs.

However, pre-clinical and clinical applications of magnetic resonance hyperthermia with magnetic nanoparticles is limited by a few major theoretical difficulties and experimental challenges. For example, conventional theoretical models for magnetic resonance hyperthermia assume that the magnetic nanoparticles act independently as single units and are dispersed uniformly in the colloidal suspension, thus making the interaction among the nanoparticles negligible. However, in real biomedical applications, when magnetic nanoparticles have been injected into blood vessels or been bound to cancer cells through the antibody-antigen

interaction, individual nanoparticles are highly likely to aggregate and form clusters. The resulting aggregation state changes the physical properties of the magnetic nanoparticle suspension, such as magnetic susceptibility. Furthermore, aggregate formation and disruption were found to be affected by external magnetic field conditions.[5] Consequently, a higher magnetic field strength is required to disrupt these aggregates, lowering the overall heating efficiency of the magnetic nanoparticle suspension. To optimize the heating efficiency for magnetic resonance hyperthermia, further understanding and formulation of aggregate formation and disruption is needed.

Previous magnetic resonance experiments have demonstrated that the thermal disruption of magnetic nanoparticle dimers is a second-order phase transition,[6] where the critical temperature for this second-order phase transition was then further characterized.[7] The inverse susceptibility-temperature curve of magnetic nanoparticle aggregates was also shown to respond differently to the frequency of the external magnetic field.[8] Because the critical temperature is a function of the external alternating magnetic field frequency and the heat-generation mechanism is closely related to the relaxation effects under such magnetic field, the frequency at which the aggregates of magnetic nanoparticles completely disrupt into monomers can be described by the critical temperature. In this paper, we aim to illustrate the relationship between the critical temperature and its corresponding critical frequency by a revised Langevin function. 3D cluster-moving based Metropolis Monte Carlo method is used to simulate the thermodynamic behavior and the aggregation/disruption of the magnetic nanoparticles under different temperatures. This critical frequency can then serve as an important reference for optimizing the heating efficiency of the magnetic nanoparticles. We hypothesize that preheating the magnetic nanoparticles at the

critical frequency to disrupt all clusters present in the colloidal suspension can minimize the loss of energy and therefore optimize the heating efficiency for magnetic resonance hyperthermia.

2.2 Theory

2.2.1 Formation of Aggregates Among Magnetic Nanoparticles

At room temperature, magnetic nanoparticles are stabilized in the colloidal suspension by various interactions[9] between nanoparticles, including inter-particle repulsions (e.g., electrostatic repulsion and steric repulsion) and inter-particle attractions (e.g., magnetic dipole-dipole interaction and van der Waals force). For example, for any two magnetic nanoparticles i and j with center-to-center distance r, if we assume the surface distance between these two particles is x, radii R_i and R_j, magnetic moments m_i and m_j, thickness of surface coating δ, and the distance vector pointed from nanoparticle i to j is R_{ij}, then the interaction energies among magnetic nanoparticles can be described as:

$$U_d = \frac{\mu_0}{4\pi}\left[\frac{m_i \cdot m_j}{{R_{ij}}^3} - 3\frac{(m_i \cdot R_{ij})(m_j \cdot R_{ij})}{{R_{ij}}^5}\right] \quad (1)$$

$$U_v = -\frac{A}{6}\left[\frac{2}{s^2-4} + \frac{2}{s^2} + \ln\left(\frac{s^2-4}{s^2}\right)\right] \quad (2)$$

$$U_e = \frac{\epsilon R \sigma^2}{2}\exp\left(-\frac{x}{\lambda}\right) \quad (3)$$

$$U_s = 2\pi R^2 N'\left[2 - \frac{l+2}{t}\ln\left(\frac{2(1+t)}{2+l}\right) - \frac{l}{t}\right](k_B T) \quad (4)$$

and the total interaction energy as:

$$U = U_d + U_v + U_e + U_s \quad (5)$$

where μ_0 is the permeability of free space, A the Hamaker constant for van der Waals interaction (associated with the magnetic nanoparticle surface coating layer and the dielectric properties of carrier liquid), ϵ the dielectric constant of the solvent, σ the surface potential of the particle, λ

the Debye length, k_B the Boltzmann constant, T the absolute temperature of colloidal magnetic nanoparticle suspension, and N' the number of molecules adsorbed on the surface of nanoparticles. $s = \frac{x}{R} + 1$, $l = \frac{R_{ij}-2R}{R}$, $t = \frac{\delta}{R}$. U_d, U_v, U_e, and U_s denote the magnetic dipole-dipole interaction, van der Waals' interaction, electrostatic repulsion, and steric repulsion, respectively. For the diluted nanoparticle concentrations used in MR nanomedical, theranostic applications, only the dominating dipole-dipole interaction term is considered. With higher nanoparticle concentrations and thus closer nanoparticle spacing, multipolar interactions need to be included as well.[2] Consequently, the interactions between magnetic nanoparticles depend on a number of factors such as temperature, magnetic field strength, particle size, and particle concentration (since the concentration determines the distance between the nanoparticles). The kinetic energy of the nanoparticles is not sensitive to the parameters such as temperature, magnetic field strength, particle size, and particle concentration, and therefore can be conveniently neglected (i.e., treated as a constant).

The colloidal magnetic nanoparticle suspension must sustain a balance between attraction and repulsion to maintain the stability, as any change in the external environment, such as temperature, concentration, or applied magnetic field, can influence the interaction among nanoparticles. For example, when the mutual repulsion among particles is smaller than the mutual attraction, magnetic nanoparticles tend to aggregate; in contrast, when the repulsion is larger than the attraction, magnetic nanoparticle aggregates will be disrupted into individual particles. For a certain colloidal magnetic nanoparticle suspension, adjusting experimental parameters and therefore controlling the aggregation/disruption of magnetic nanoparticles is essential for optimizing the heating efficiency of magnetic resonance hyperthermia.

2.2.2 Critical Frequency and Critical Temperature under an Alternating Magnetic Field

The relative amounts of monomers and clusters in the colloidal magnetic nanoparticle suspension can be expressed as P_m and P_c,[10] respectively:

$$P_m = \frac{T}{T^*} \tag{6}$$

$$P_c = (1 - \frac{T}{T^*})^{\frac{1}{2}} \tag{7}$$

where T is the absolute temperature of suspension and T^* the critical temperature for second-order phase transition. Based on the Langevin function, the equilibrium magnetic susceptibility for the mixed system can thus be described as[10]

$$\chi(T) = \frac{\phi}{H_0}\left[M_{dm}\left(\frac{T}{T^*}\right)\left(\coth\left(\frac{\mu_0 m H_0}{k_B T}\right) - \frac{k_B T}{\mu_0 m H_0}\right) + M_{dc}(1 - \frac{T}{T^*})^{\frac{1}{2}} \coth\left(\frac{\mu_0 \overline{m_c} H_0}{k_B T}\right) - \frac{k_B T}{\mu_0 \overline{m_c} H_0}\right] \tag{8}$$

where k_B represents the Boltzmann constant, ϕ the volume fraction of magnetic nanoparticles, H_0 the strength of external alternating magnetic field, μ_0 the permeability of free space, M_{dm} and M_{dc} the saturation magnetization for monomers and clusters, respectively, and m and $\overline{m_c}$ the average magnetic moment for monomers and clusters, respectively. When excited by an external magnetic field, magnetic nanoparticles generate heat through relaxation mechanisms, such as Brownian relaxation and Neel relaxation.[11-14] The power dissipation can be expressed as[12]

$$P = \mu_0 \pi f {H_0}^2 \chi'' = \frac{2\mu_0 {H_0}^2 (f\pi)^2 \tau \chi(T)}{1 + (2\pi f \tau)^2} \tag{9}$$

A portion of the dissipated energy contributes to the raise in temperature of magnetic nanoparticles, where another portion to the acceleration of aggregate disruption. This distribution results in a lower critical temperature for the second order phase transition. If the unmodified critical temperature is given by ${T_0}^*$, the frequency of the magnetic field as f, and the heating duration as Δt, the critical temperature can be revised to a function of frequency[8]

$$T^*(f) = T_0{}^* - P \cdot \Delta t = T_0{}^* - \frac{2\mu_0 {H_0}^2 \Delta t (f\pi)^2 \tau \chi(T)}{1+(2\pi f\tau)^2} \quad (10)$$

If the heating duration is fixed, then the relationship between the critical frequency f^* and critical temperature f$^*T^*(f^*)$ can be represented as

$$T^*(f^*) = T_0{}^* - P \cdot \Delta t = T_0{}^* - \frac{2\mu_0 {H_0}^2 \Delta t (f^*\pi)^2 \tau \chi(T)}{1+(2\pi f^*\tau)^2} \quad (11)$$

2.3 Methods

3D cluster-moving based Metropolis Monte Carlo method was used to simulate the thermodynamic behavior and to study the aggregation/disruption of magnetic nanoparticles at various temperatures. The Metropolis Monte Carlo method provides a universally applicable model and faster convergence. For this simulation, the magnetic nanoparticles were assumed to be distributed in a 3D cube, and their size as a log-normal distribution to ensure the model similar to the experimental scenario.[15]

2.3.1 Setup of Model and Parameters

The magnetic nanoparticles were set to have sizes following a log-normal distribution ($\overline{D}$, σ) and distributed randomly in a cube with edge L. The diffusion is modeled by a random walk. The thickness of surface coating of each nanoparticle is set as δ, the total number of magnetic nanoparticles as N, the volume fraction of magnetic nanoparticles as ϕ, and the saturation magnetization as M. The magnetic moment can thus be represented as $m = \frac{\pi M D^3}{6}$, pointing to an arbitrary angle that ranges from 0 to 2π. For any magnetic nanoparticle i, its current state can be determined by four variables (x_i, y_i, z_i, θ_i), where (x_i, y_i, z_i) denotes the spatial coordinates and θ_i the angle between the magnetic moment m_i and external magnetic field H. The distance vector points from nanoparticle i to j was set as R_{ij}, and the unit vector r_{ij} was set in the same

direction as R_{ij}, where n_i and n_j are unit vectors along the direction of magnetic moment m_i and m_j, respectively. The total energy U_i of any magnetic nanoparticle i under the external magnetic field can then be written as

$$U_i = U_{di} + U_{vi} + U_{ei} + U_{si} + U_{hi} \tag{12}$$

where U_{di} signifies the magnetic dipole-dipole interaction, U_{vi} the van der Waals' interaction, U_{ei} the electrostatic repulsion, U_{si} the steric repulsion, and U_{hi} the interaction between individual nanoparticle and the external magnetic field. However, in our simulation considering about the general case, electrostatic repulsion was neglected since neutralized free magnetic particles dispersed in suspension, so the common interactions among magnetic nanoparticles were magnetic dipole-dipole interaction, van der Waals' interaction and steric repulsion.

The specific values of parameters used in the computer simulation include the average diameter of the magnetic nanoparticles $\overline{D} = 11.5\ nm$, standard deviation of the particle size distribution $\sigma = 0.20\ nm$, volume fraction $\varphi = 0.01$, total number of magnetic nanoparticles $N = 300$, edge of the cube $L = 167.25\overline{D}$, thickness of the surface coating $\delta = 0.15\overline{D}$, saturated magnetization $M = 414\ kA/m$, magnetic field strength $H = 400\ A/m$, permeability of free space $\mu_0 = 4\pi\times10^{-7}\ H/m$, Boltzmann constant $k_B = 1.38\times10^{-23}\ J/K$, Hamaker constant $A = 10^{-19}J$ (corresponding to common organic layers surface coating such as glycerol in water solution), and total number of molecules absorbed on the surface per surface area $N' = 10^{18}\ /m^2$.

2.3.2 Cluster-Moving-Based Metropolis Monte Carlo Simulation

The interactions within the aggregating magnetic nanoparticle clusters are stronger than the interactions between clusters and the surrounding monomers in an actual colloidal magnetic nanoparticle suspension. The nanoparticle dynamics can be described by deterministic equations

(e.g., Newton's second law) or stochastic equations (e.g., Fokker–Planck equation). In our molecular dynamics simulations, without loss of generality and accuracy, the nanoparticle dynamics is approximated by 3D random walk with fixed step length and variable walking direction (uniform sampling in the spherical coordinates) that satisfy the experimental translational and rotational diffusion coefficients. The choices of step length, 0.5D, and maximum rotation angle per step, pi/18, is to speed up the expensive calculation without compromising the accuracy.

To better simulate the effect resulting from changes in position and energy, a cluster-moving algorithm was employed to describe particles' random walk. The procedures for the cluster-moving-based Metropolis Monte Carlo simulation are described as follows:

(1) Initialize the system and all parameters.

(2) Change the state of the i^{th} ($i = 1, 2, 3 \ldots N$) magnetic nanoparticle (x_i, y_i, z_i, θ_i).

(3) Calculate the energy change for the system, $\Delta U = U_{current} - U_{previous}$, and verify whether the new state is acceptable by the Metropolis algorithm, as the system always prefers lower energy during evolution. If $\Delta U < 0$, then accept the new state of the i^{th} magnetic nanoparticle. If $\Delta U > 0$, then calculate $h = exp\,(-\frac{\Delta U}{k_B T})$ and compare to $temp$, a random number ranges from 0 to 1. tempIf $h > temp$, accept the new state. If $h < temp$, reject the new state and maintain the previous state of the i^{th} magnetic nanoparticle.

(4) Repeat step (2) and (3) until the states of all *N* magnetic nanoparticles have been changed. Record current Monte Carlo steps $N_m = 1$.

(5) Calculate the surface distance among all magnetic nanoparticles in the suspension. If the distance is smaller than $0.25\overline{D}$, assume an aggregate is formed.

(6) Repeat steps (2) through (5) until $N_m = 2000000$ to ensure the system has reached equilibrium.

To avoid complicated calculations for the center of mass of aggregates, the movement, orientation, and magnetic moment of an aggregate were represented by those of an arbitrary particle within that aggregates. The steps for each random walk were set as $S = 0.5\overline{D}$, and the rotation angle for the magnetic moment as $\Delta\theta = \frac{\pi}{18}$.

2.4 Results and Discussions

2.4.1 Simulation Results of the Aggregate Formation

By employing the 3D cluster-moving-based Metropolis Monte Carlo method, we studied the thermodynamic behavior of 300 magnetic nanoparticles with a temperature range from 300 K to 450 K (27 ℃ to 177 ℃). The formation and disruption of magnetic nanoparticle aggregates at different temperatures were analyzed by calculating the interactions between the magnetic nanoparticles. To highlight this point, we randomly chose one magnetic nanoparticle and calculated its interaction energies evolving with Monte Carlo steps at T=300 K according to equation 12, as shown in Table 1. What's more, by assuming clusters would form when the surface distance between particles is smaller than $0.25\overline{D}$, we obtained the distribution of monomers and aggregates when the system is at equilibrium, as illustrated in Figure. 1. At room temperature T=300 K and T=310 K, aggregates with various size/structure were formed among magnetic nanoparticles. However, when the temperature was increased to T=350 K and T=360 K, aggregates first disrupted into smaller portions, then into monomers. When the temperature was further increased to T=400 K and T=450 K, the majority of the nanoparticles in the system

was in the monomeric form. It suggests that the attractive and repulsive interactions become balanced at higher temperatures.

Table 1. Interaction energies (in Joule) of randomly chosen magnetic nanoparticle evolving with Monte Carlo Steps at T=300 K

Monte Carlo Steps	U	U_d	U_v	U_s	U_h
0	1.7770×10^{-21}	3.8729×10^{-24}	-5.2130×10^{-27}	1.8267×10^{-21}	-5.3522×10^{-23}
10	3.1940×10^{-21}	4.5583×10^{-23}	-2.3155×10^{-27}	3.3207×10^{-21}	-1.3127×10^{-22}
100	3.6034×10^{-21}	9.5663×10^{-24}	-4.6260×10^{-27}	3.7501×10^{-21}	-1.5693×10^{-22}
1000	2.5901×10^{-21}	2.6149×10^{-24}	-2.0991×10^{-27}	2.6828×10^{-21}	-9.5298×10^{-23}
10000	3.7607×10^{-21}	1.0562×10^{-23}	-2.8352×10^{-27}	3.9184×10^{-21}	-1.6821×10^{-22}
50000	1.8502×10^{-21}	-6.3504×10^{-26}	-1.6851×10^{-26}	1.9074×10^{-21}	-5.7140×10^{-23}

Based on the simulation results, the relative contents of aggregates and monomers in the magnetic nanoparticle suspension were assessed at different temperatures, as shown numerically in Table 2 and diagrammatically in Figure 2. With the elevation of temperature, the relative content of monomers was found to increase, while that of aggregates to decrease. Fluctuations observed in Figure 2 are mainly due to the disruption of larger aggregates into smaller portions, resulting in a relative increase in the number of aggregates.

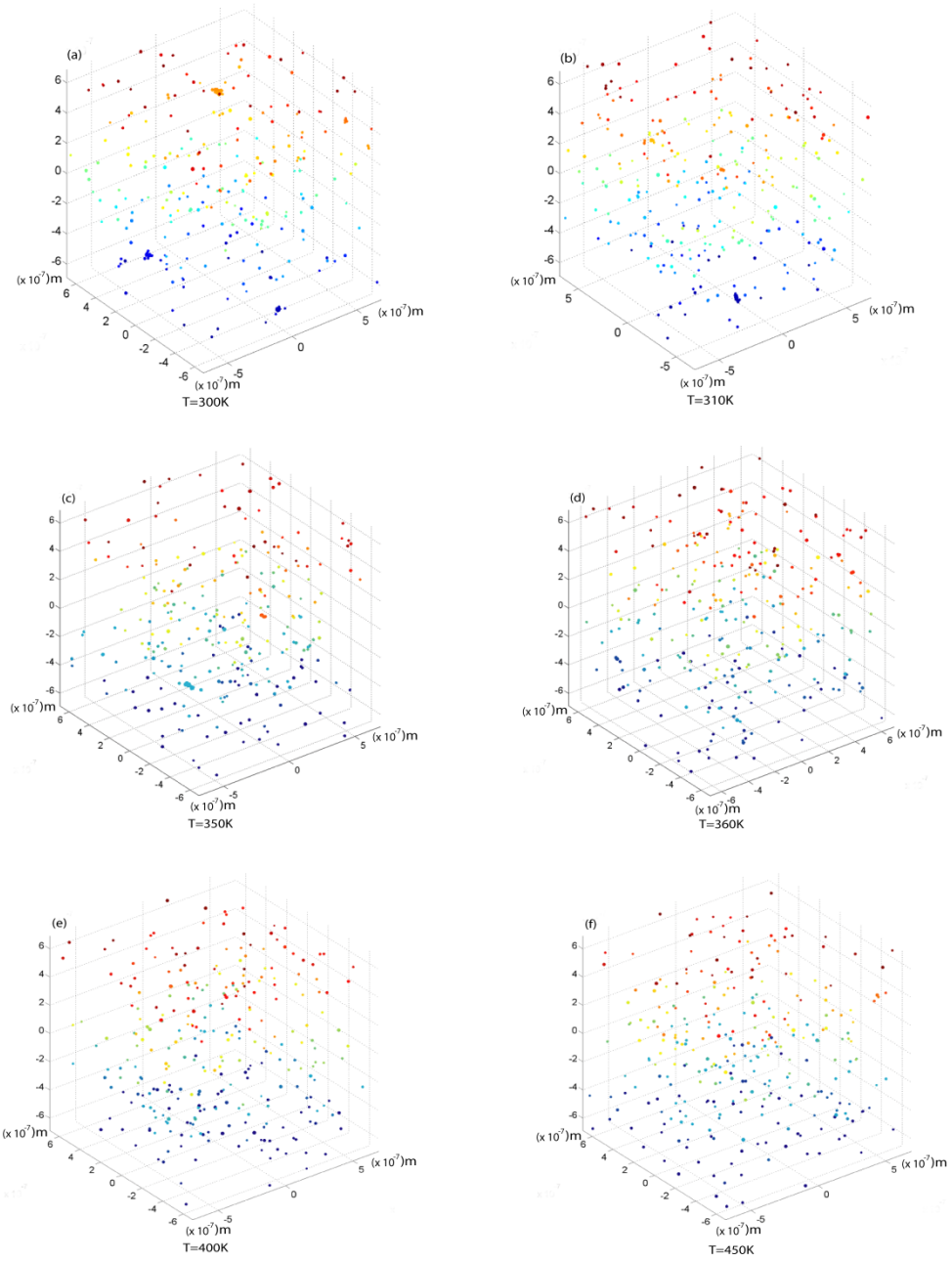


Figure 1. Distribution of monomers and clusters in magnetic nanoparticle suspension at equilibrium at different temperatures. (a) T=300 K (b) T=310 K (c) T=350 K (d) T=360 K (e) T=400 K (f) T=450 K. To aid the 3D visual effect, z-coordinates of the magnetic nanoparticles are color-coded.

Table 2. The number and relative content of both monomers and aggregates in suspension at different temperature

Temperature	Aggregates	Monomers	Relative Content
300 K	16	249	0.064
310 K	18	252	0.071
320 K	17	253	0.067
330 K	15	258	0.058
340 K	14	260	0.053
350 K	14	266	0.053
360 K	16	266	0.060
370 K	15	270	0.056
380 K	10	276	0.036
390 K	11	276	0.040
400 K	11	277	0.040
450 K	6	288	0.021

2.4.2 Analysis of the Critical Frequency for Aggregates Disruption

According to equations 10 and 11, the critical temperature can be reduced if an external alternating magnetic field with higher frequency is applied. To further explore the relationship between the critical temperature and magnetic field frequency, the critical temperature was

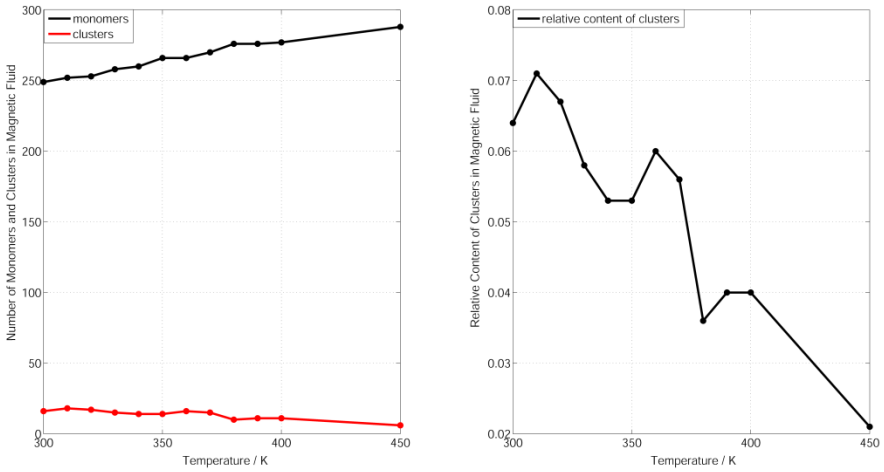


Figure 2. Relative content of clusters in suspension at different temperatures.

Table 3. Physical properties of magnetic materials

Magnetic Solid	Chemical Formula	M_d $(kA \cdot m^{-1})$	K $(kJ \cdot m^{-3})$	c $(J \cdot kg^{-1} \cdot K^{-1})$	ρ $(kg \cdot m^{-3})$
Maghemite	$\gamma - Fe_2O_3$	414	15	746	4600
Magnetite	$FeO \cdot Fe_2O_3$	446	23	670	5180
Cobalt Ferrite	$CoO \cdot Fe_2O_3$	425	180	700	4907
Barium Ferrite	$BaO \cdot 6Fe_2O_3$	380	300	650	5280

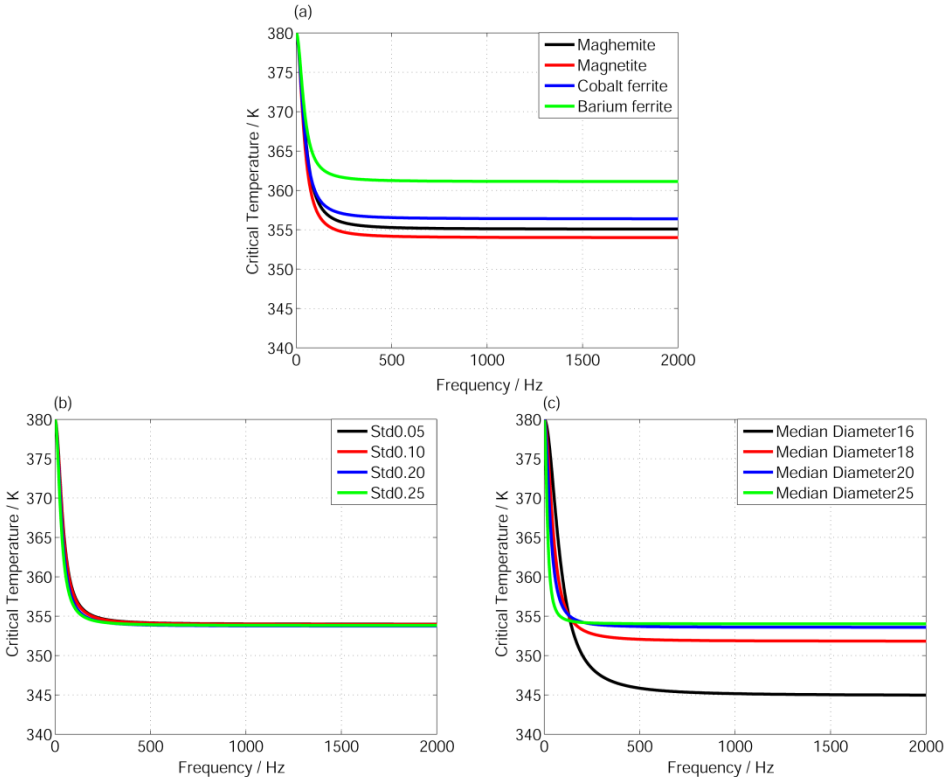


Figure. 3 The critical temperature for cluster disruption of magnetic nanoparticle suspension as a function of external magnetic field frequency. (a) The critical temperature for cluster disruption of different magnetic nanoparticle suspension versus external magnetic field frequency. (b) The critical temperature for cluster disruption of magnetite versus external magnetic field frequency under different size distribution (same median diameter $\overline{D} = 20.00\ nm$ $\overline{\mathrm{D}} = 20.00\mathrm{nm}$, the standard deviations shown in the figure are all in the unit of nm). (c) The critical temperature for cluster disruption of magnetite versus external magnetic field frequency under different median diameter (same size distribution $\sigma = 0.25\ nm$)

plotted as a function of magnetic field frequency under various scenarios shown in Figure 3. All results revealed similar trends where the critical temperature decreased dramatically as the frequency increased from 0 Hz, but remained unaffected once the frequency reached a certain critical value. Such critical value of the frequency is then defined as the “critical frequency” of

the corresponding colloidal magnetic nanoparticle suspension. Heating at or above the critical frequency can optimize the heating efficiency, resulting in the complete disruption of aggregates into monomers.

Figure 3a shows curves of the critical temperature vs. magnetic field frequency for suspensions containing four commonly used magnetic materials (listed in Table 3). When the magnetic field frequency is lower than 300 Hz, the critical temperature dramatically decreases with the increase in frequency. Continual increase in frequency does not result in a further obvious decrease in critical temperature, while at frequency values higher than 500 Hz, the critical temperature no longer decreases, but rather becomes stable. This indicates a critical frequency of around 500 Hz for all of the four magnetic materials studied, despite of their different final critical temperatures, range from 354 K to 362 K.

In a real suspension, the sizes of magnetic nanoparticles usually obey the log-normal distribution with a certain standard deviation. Therefore, we take magnetite, which is the most strongly magnetic mineral in nature, as an example and further discuss how the size distribution of magnetic nanoparticles affects the relationship between the critical temperature and the magnetic field frequency. When the mean diameter of the magnetic nanoparticles in the suspension is fixed, different size distributions does not cause notable changes in the critical temperature vs. magnetic field frequency curve, as shown in Figure 3b. When the size distribution is fixed, however, changing the mean diameter of the magnetic nanoparticles significantly changes the critical temperature vs. magnetic field frequency curve, as shown in Figure 3c. A decrease in mean diameter from 25 nm to 16 nm displays a much higher critical frequency requirement to disrupt the aggregates.

2.5 Conclusion

Magnetic nanoparticles have found popular applications as "molecular beacons" for medical diagnosis and as "molecular bullets" for targeted therapy. Consequently, the sensitive detection[16-18] and effective heating of magnetic nanoparticles are fundamental to the development of magnetic resonance molecular imaging and nanomedicine. For nanomedical, theranostic applications of magnetic resonance hyperthermia in cellular environments, the interactions between the nanoparticles with the other nanoparticles and with surrounding biomolecules such as proteins, lipids and sugars (all of which could be electrically charged) and small ions (cations and anions) could be significant and generally discount the heating efficiency[19]. As a first step in optimizing the hyperthermia effect, the thermodynamic behavior of magnetic nanoparticles and aggregation dynamics were studied in this work. 3D cluster-moving-based Monte Carlo method was used to simulate the thermodynamic behavior of the magnetic nanoparticles and to further analyze the monomer/ aggregate distribution at various temperatures. Simulation results show that the relative content of aggregates decreases with the increase of temperature, until all the particles exist as monomers at or above the critical temperature. The critical temperature is further found to be related to the frequency of the external alternating magnetic field, where the critical temperature continually decreases with the increase of frequency until the critical frequency is reached. Any increase of frequency beyond this point no longer affects the critical temperature. Our simulation suggests that the heating efficiency of magnetic nanoparticle suspension may be optimized for its potential applications in magnetic resonance hyperthermia by preheating the colloidal suspension at the critical frequency to disrupt aggregates into monomers.

2.6 References

[1] Jordan, A.; Wust, P.; Fähling, H.; John, W.; Hinz, A.; Felix, R. Inductive Heating of Ferrimagnetic Particles and Magnetic Fluids: Physical Evaluation of Their Potential for Hyperthermia. *Int. J. Hyperthermia*. **1993**, *9*, 51-68.

[2] Krishnan, K. M. Biomedical Nanomagnetics: A Spin Through Possibilities in Imaging, Diagnostics, and Therapy. *IEEE Trans. Magn*. **2010**, *46*, 2523-2558.

[3] Gordon, R. T.; Hines, J. R.; Gordon, D. A. Biophysical Approach to Cancer Treatment via Intracellular Temperature and Biophysical Alterations. *Medical Hypotheses*. **1979**, *5*, 83-102.

[4] Jordan, A.; Wust, P.; Scholz, R.; Tesche, B.; Fähling, H.; Mitrovics, T.; Vogl, T.; Cervos-Navarro, J.; Felix, R. Cellular Uptake of Magnetic Fluid Particles and Their Effects on Human Adenocarcinoma Cells Exposed to AC Magnetic Fields In Vitro. *Int. J. Hyperthermia*. **1996**, *12*, 705-722.

[5] Alexey, O. I.; Sofia, S. K.; Valentin, S. M.; Elena, S. P. Ferrofluid Aggregation in Chains under the Influence of a Magnetic Field. *J. Magn. Magn. Mater*. **2006**, *300*, e206-e209.

[6] Morais, P. C.; Gonçalves, G. R. R.; Bakuzis, A. F.; Neto, K. S.; Pelegrini, F. Experimental Evidence of Dimer Disruption in Ionic Ferrofluid: A Ferromagnetic Resonance Investigation. *J. Magn. Magn. Mater*. **2001**, *225*, 84-88.

[7] Zhong, J.; Xiang, Q.; Massa, L. O.; Qu, F.; Morais, P. C.; Liu, W. Second-Order-Like Cluster-Monomer Transition Within Magnetic Fluids and Its Impact Upon the Magnetic Susceptibility. *Nanoscale Res. Lett*. **2012**, *7*, 167.

[8] Du, Z.; Liu, W.; Zhong, J.; Zhou, M.; Zhang, P.; Morais, P. C. Signature of Cluster Disruption within Magnetic Fluid Samples: The Key Information Provided by Low

Frequency Alternating Current Susceptibility Measurements. *J. Appl. Phys*. **2014**, *115*, 194310.

[9] Ganguly, R.; Zellmer, B.; Puri, I. K. Field-Induced Self-Assembled Ferrofluid Aggregation in Pulsatile Flow. *Phys. Fluids*. **2005**, *17*, 097104.

[10] Xiang, Q.; Zhong, J.; Zhou, M.; Cesar, P.; Liu, W. AC field Dependence of Cluster Disruption in Magnetic Fluids. *J. Appl. Phys*. **2011**, *109*, 07B317.

[11] Wang, X.; Gu, H.; Yang, Z. The Heating Effect of Magnetic Fluids in an Alternating Magnetic Field. *J. Magn. Magn. Mater*. **2005**, *293*, 334.

[12] Rosensweig, R. E. Heating Magnetic Fluid with Alternating Magnetic Field. *J. Magn. Magn. Mater*. **2002**, *252*, 370.

[13] Ondeck, C. L.; Habib, A. H.; Ohodnicki, P.; Miller, K.; Sawyer, C. A.; Chaudhary, P. Theory of Magnetic Fluid Heating with an Alternating Magnetic Field with Temperature Dependent Materials Properties for Self-Regulated Heating. *J. Appl. Phys.* **2009**, *105*, 07B324.

[14] Skumiel, A.; Łabowski, M. The Heating Effect of the Biocompatible Ferrofluid in an Alternating Magnetic Field. *Molecular and Quantum Acoustics*. **2006**, *27*, 233-238.

[15] Chantrell, R. W.; Popplewell, J.; Charles, S. W. Measurements of Particle-Size Distribution Parameters in Ferrofluids. *IEEE Trans. Magn.* **1978**, *14*, 975-977.

[16] Hwang, D. W.; Lin Y.-Y.; Hwang, L.-P. Studies of Magnetic Resonance Imaging with Active Feedback RF Field. *Chinese J. Magn. Reson.* **2010**, *27*, 409-416.

[17] Huang, S. Y.; Walls, J. D.; Lin Y.-Y. Periodic Control of Spin Turbulence in Solution Magnetic Resonance. *Chinese J. Magn. Reson.* **2010**, *27*, 425-435.

[18] Li, Z.; Hsu, C.-H.; Dimitrov, N.; Hwang, D. W.; Chang, H.-W.; Hwang, L.-P.; Lin Y.-Y.

Sensitive Imaging of Magnetic Nanoparticles for Cancer Detection by Active Feedback MR. *Magn. Reson. Med*. **2015**, *74*, 33-41.

[19] Hilger, I.; Kaiser, W. A. Iron Oxide-Based Nanostructures for MRI and Magnetic hyperthermia. *Nanomedicine*. **2012**, *7*, 1443–1459.

Chapter 3

Effective Heating of Magnetic Nanoparticle Aggregates for *In Vivo* Nano-Theranostic Hyperthermia

3.0 Abstract

Magnetic resonance (MR) nano-theranostic hyperthermia uses magnetic nanoparticles to target and accumulate at the lesions and to generate heat to kill lesion cells directly through hyperthermia or indirectly through thermal activation and control releasing of drugs. Pre-clinical and translational applications of MR nano-theranostic hyperthermia are currently limited by a few major theoretical difficulties and experimental challenges in *in vivo* conditions. For example, conventional models for estimating the heat generated and the optimal magnetic nanoparticle sizes for hyperthermia do not accurately reproduce reported *in vivo* experimental results. In this work, a revised cluster-based model was proposed to predict the specific loss power (SLP) by explicitly considering magnetic nanoparticle aggregation in *in vivo* conditions. By comparing with the reported experimental results of magnetite Fe_3O_4 and cobalt ferrite $CoFe_2O_4$ magnetic nanoparticles, it is shown that the revised cluster-based model provides a more accurate prediction of the experimental values than the conventional models that assume magnetic nanoparticles act as single units. It also provides a clear physical picture: the aggregation of magnetic nanoparticles increases the cluster magnetic anisotropy while reducing both the cluster domain magnetization and the average magnetic moment, which in turn shift the predicted SLP toward smaller magnetic nanoparticle diameter with lower peak values. As a result, the heating efficiency and the SLP values are decreased. The improvement in the prediction accuracy in *in*

vivo conditions is particularly pronounced when the magnetic nanoparticle diameter is in the range of approximately 10 nm-20 nm. This happens to be an important size range for MR cancer nano-theranostics, as it exhibits the highest efficacy against both primary and metastatic tumors *in vivo*. Our studies show that a relatively 20-25% smaller magnetic nanoparticle diameter should be chosen to reach the maximal heating efficiency in comparison to the optimal size predicted by previous models.

3.1 Introduction

Theranostics refers to the development of molecular diagnostics and targeted therapeutics in an interdependent, collaborative manner. Nano-theranostics takes advantage of the high capacity of nano-platforms to ferry cargo and loads onto them both imaging and therapeutic functions. The resulting nanosystems, capable of diagnosis, drug delivery and monitoring of therapeutic response, are expected to play a significant role in the dawning era of personalized medicine, and much research effort has been devoted toward that goal. For example, magnetic resonance (MR) nano-theranostics uses magnetic nanoparticles for cancer detection by MR molecular imaging and for cancer therapy by MR nano-medicine.[1] Through active (e.g., antibody-antigen) and passive (e.g., enhanced permeability and retention effect) targeting mechanisms, the magnetic nanoparticles can serve as "molecular beacons" to enhance the MR image contrast for early lesion detection. Moreover, through interacting with external alternating magnetic fields produced by the MR hardware, these magnetic nanoparticles accumulated at the lesions can generate heat to serve as "molecular bullets" to kill cancer cells directly through hyperthermia or indirectly through thermal activation and control releasing of drugs.

MR nano-theranostic hyperthermia with magnetic nanoparticles has been an emerging field for the last decade, mainly for its promising applications to cancer treatment.[2] In particular, a number of studies have shown that these magnetic fluids, or magnetic nanoparticle suspensions, are able to release heat through various relaxation mechanisms when exposed to a weak alternating magnetic field.[3,4] The selective heating can be used to target cancer tissues, as abnormal growth is more susceptible to cell death under elevated temperatures. However, pre-clinical and translational applications of MR nano-theranostic hyperthermia with magnetic nanoparticles are limited by a few major theoretical difficulties and experimental challenges. For example, conventional theoretical models for MR nano-theranostic hyperthermia assume that the magnetic nanoparticles act independently as single units and are dispersed uniformly in the colloidal suspension, making the interaction among the nanoparticles negligible.[5] However, in real biomedical *in vivo* applications, when magnetic nanoparticles have been injected into blood vessels or been bound to cancer cells through the antibody-antigen interaction, individual nanoparticles are highly likely to aggregate and form clusters.[6,7]

Aggregation changes the physical and magnetic properties of the magnetic nanoparticles in tissues, such as magnetic susceptibility and specific loss power (SLP). Furthermore, aggregate formation and disruption were found to be affected by external magnetic field conditions.[8,9] Consequently, a higher magnetic field strength is required to disrupt these aggregates, lowering the heating efficiency of the magnetic nanoparticles in tissues. Therefore, further understanding and formulation of the effect of magnetic nanoparticle aggregation on MR nano-theranostic hyperthermia becomes critical.

To understand and optimize MR nano-theranostic hyperthermia using magnetic nanoparticles, the specific loss power (SLP) lays a constructive platform for calculating the heat

generation per mass unit of dissipating material. SLP is shown to depend on magnetic nanoparticle properties and external alternating magnetic fields, specifically the mean particle size and size distribution, as well as the amplitude and frequency of the alternating magnetic fluids.[10-12] Therefore, reaching a therapeutic temperature for cancer treatment while administering minimal amounts of magnetic nanoparticles, due to limited targeting efficiency, would thus depend greatly on manipulating magnetic-nanoparticle properties and external alternating magnetic fields to control the desired SLP and heat generated. Problematically, conventional models for estimating SLP do not accurately reproduce reported experimental results.[13] This limitation may be alleviated by analyzing the magnetic nanoparticle composition and structure under experimental conditions.

The original model proposed by Rosensweig assumes magnetic nanoparticles act independently of one another in suspension.[5] Morais *et al.* and Castro *et al.* found magnetic nanoparticles form clusters when in solution.[14,15] Ganguly *et al.* reported experimental observation on the micro- and meso-scale field-assisted self-assembly of magnetic nanoparticles due to inter-particle electrostatic attraction, electrostatic repulsion, steric repulsion, and magnetic dipolar interactions.[16] Interestingly, several groups have determined that magnetic nanoparticle aggregate formation is not sensitive to the solution composition, as magnetic nanoparticles were found to form aggregates in similar magnitudes when suspended in either water or glycerol. [17,18] Furthermore, magnetic fluid characteristics and structures differ under varying alternating magnetic field strengths, such that the fraction of agglomerates changes the magnetization and susceptibility of the ferrofluid.[19,20]

In this work, we proposed a revised cluster-based model to more accurately estimate the SLP by considering magnetic nanoparticle aggregation. Under an alternating magnetic field,

magnetic susceptibility is temperature-dependent and can be conveniently described by the Langevin function. The fraction of monomeric and clustered magnetic nanoparticles in the ferrofluid can be characterized by a critical temperature, which is defined as the temperature at which magnetic nanoparticle aggregates completely dissociate into individual units.[21] To account for a dependence on this critical temperature, we proposed a modified Langevin function to re-define the magnetic susceptibility of the ferrofluid and developed an alternative SLP model based on the revised Langevin function. The proposed model, called "revised cluster-based model", can account for the aggregate formation and the size distribution of the magnetic nanoparticles. Finally, the proposed model was compared to experimental results of magnetite Fe_3O_4 and cobalt ferrite $CoFe_2O_4$ magnetic nanoparticles.[22-25] It is shown that the revised cluster-based model provides more accurate estimates to SLP and heating efficiency for MR nano-theranostic hyperthermia in cancer therapy.

3.2 Materials and Methods

3.2.1 Fraction of Monomers and Clusters

The disruption of magnetic nanoparticle clusters follows a second-order phase transition at critical temperature.[14] Magnetic nanoparticle monomers and clusters coexist within the colloidal solution when the temperature of the ferrofluid is below the critical temperature. Correspondingly, clusters disrupt completely into monomeric units when the ferrofluid temperature is at or above the critical temperature. Therefore, the fraction of clusters (P_c) in the ferrofluid was chosen as an order parameter to describe this thermal-assisted cluster disruption, according to the Landau second-order phase transition theory, where P_c was expressed in terms of the suspension temperature, T, and the critical temperature, T^*,[21]

$$P_c = (1 - \frac{T}{T^*})^{\frac{1}{2}} \quad (1a)$$

From the expression of P_c, it can be concluded that when the temperature is much lower than the critical temperature, $T \ll T^*$, monomers and clusters coexist in the ferrofluid system, and there are no clusters when the temperature is at or above the critical temperature. Consequently, the fraction of monomers (P_m) in the ferrofluid can be simply treated to be proportional to the temperature:

$$P_m = \frac{T}{T^*} \quad (1b)$$

Notice that $P_m + P_c = 1$ when it is at two limiting conditions: $T \ll T^*$ and $T \cong T^*$.

3.2.2 Relaxation Mechanisms

To calculate the SLP of colloidal magnetic nanoparticles as an interacting system in ferrofluid, we first need to describe two major relaxation mechanisms for magnetic nanoparticles dispersed in a fluid. The first relaxation mechanism is referred to as the Brownian relaxation and was first derived by Deby.[26] It assumes the whole nanoparticle rotates towards the external field mechanically against the viscous drag in the suspending medium. Consequently, the change in the magnetization of a ferrofluid is due to the rotation of the magnetic nanoparticles with the internal magnetization remaining fixed with respect to the crystalline lattice. For this reason, it is also known as the "rigid dipole model". Assuming that the viscosity of the ferrofluid solution, η, is temperature-independent and that the effect of the magnetic nanoparticle aggregation does not depend on the suspending solution, one can derive the characteristic zero-field Brownian relaxation time constant, τ_B, to be:

$$\tau_B = \frac{3\eta V_h}{k_B T} \quad (2)$$

where the magnetic nanoparticle's hydrodynamic volume $V_h = (1 + \delta/R)^3 V$, k_B is the Boltzmann constant, T is the temperature of the ferrofluid solution (the product $k_B T$ is the thermal energy), η is the viscosity of the carrier fluid, V is the volume of the magnetic nanoparticle, R is the radius of the magnetic nanoparticle, and δ is the surfactant thickness (a property of the ferrofluid).

The second relaxation mechanism, known as the Néel relaxation, describes a process where the magnetic nanoparticles do not mechanically rotate, but the magnetization rotates internally with respect to the crystalline lattice.[27] Because of the nanoparticle's magnetic anisotropy, the magnetization has usually two stable orientations antiparallel to each other, separated by an energy barrier. The stable orientations define the magnetic easy axis of the nanoparticle. Because the magnetization rotates away from the easy axis towards the external field in the Néel relaxation process, the mechanism is also known as the "soft dipole model". The characteristic zero-field Néel relaxation time constant, τ_N, can be expressed as:

$$\tau_N = \begin{cases} \tau_0 \, \Gamma^{-\frac{1}{2}} \exp(\Gamma) & \Gamma \geq 1 \\ \tau_0 \, \Gamma & \Gamma \ll 1 \end{cases} \tag{3}$$

where $\Gamma = \frac{K_a V}{k_B T}$, $K_a V$ is the energy barrier (a product of the magnetic anisotropy constant, K_a, and the volume of the magnetic nanoparticle, V), and τ_0 is the attempt time (its reciprocal is called the attempt frequency). Typical values for τ_0 are between 10^{-9} and 10^{-10} seconds.

Because both relaxation mechanisms occur simultaneously in the ferrofluid, the effective total relaxation time constant, τ, is given by:

$$\frac{1}{\tau} = \frac{1}{\tau_B} + \frac{1}{\tau_N} \tag{4a}$$

or, alternatively, by:

$$\tau = \frac{\tau_B \cdot \tau_N}{\tau_B + \tau_N} \tag{4b}$$

When $\tau_B \ll \tau_N$, then $\tau \approx \tau_B$. Similarly, when $\tau_B \gg \tau_N$, then $\tau \approx \tau_N$. Hence, the total relaxation effect is dominated by the stronger relaxation mechanism with shorter relaxation time constant.

Since aggregation increases the magnetic anisotropy of clusters,[28-30] in our proposed model, the magnetic anisotropy constant, K_a, has different values for monomers and clusters. Denote the magnet anisotropy constants for monomers and clusters as K_{am} and K_{ac} respectively, then:

$$K_{am} = K_a \tag{5a}$$

$$K_{ac} = K_{am} + \frac{(1-P_m)K_a}{P_c} \tag{5b}$$

where the term, $\frac{(1-P_m)K_a}{P_c}$, represents the increase in the average of the magnetic anisotropy constant due to the formation of clusters, and $(1 - P_m)$ represents the fraction of monomers that comes from the disruption of clusters. Notice that when T is close to T^*, the values of K_{ac} is slightly bigger than that of K_{am}, when $T \ll T^*$, complicated structure of clusters makes K_{ac} significantly higher than K_{am}.

3.2.3 Equilibrium Magnetization

In this work, we investigated the effect of magnetic nanoparticle aggregation on the magnetization and the magnetic susceptibility of ferrofluid. Considering about the linear response of the magnetic susceptibility, one can re-write the equilibrium magnetization of ferrofluid as a function of the temperature, $M_0(T)$, as:[21]

$$M_0(T) = \phi \left[M_{dm} \left(\frac{T}{T^*}\right) L\left(\frac{\mu_0 \overline{m_m} H_0}{k_B T}\right) + M_{dc}(1 - \frac{T}{T^*})^{\frac{1}{2}} L(\frac{\mu_0 \overline{m_c} H_0}{k_B T}) \right] \tag{6}$$

where $\frac{T}{T^*} = P_m$ and $(1 - \frac{T}{T^*})^{\frac{1}{2}} = P_c$ are the fractions of monomers and clusters, respectively, as shown in equation 1, ϕ is the volume fraction of the magnetic nanoparticles, H_0 is the strength of the external alternating magnetic field, μ_0 is the magnetic permeability in free space, M_{dm} and

M_{dc} are the domain magnetization of monomers and clusters, respectively, $\overline{m_m}$ and $\overline{m_c}$ are the average magnetic moment of monomers and clusters, respectively, and L is the Langevin function with formula $L(x) = coth(x) - \frac{1}{x}$. The Langevin function describes the dependency of the magnetization on the applied magnetic field in the classical limit, with the expression:

$$L\left(\frac{\mu_0 \overline{m_m} H_0}{k_B T}\right) = \coth\left(\frac{\mu_0 \overline{m_m} H_0}{k_B T}\right) - \frac{k_B T}{\mu_0 \overline{m_m} H_0} \tag{7a}$$

$$L\left(\frac{\mu_0 \overline{m_c} H_0}{k_B T}\right) = \coth\left(\frac{\mu_0 \overline{m_c} H_0}{k_B T}\right) - \frac{k_B T}{\mu_0 \overline{m_c} H_0} \tag{7b}$$

In equation 6, the first term in the bracket indicates the contribution from monomers, while the second term in the bracket indicates the contribution from clusters. Similar to the effect of magnetic nanoparticle aggregation on the magnetic anisotropy constant, the domain magnetization (M_{dc}) and the average magnetic moment ($\overline{m_c}$) of clusters are also different from those of monomers:

$$M_{dc} = \frac{(1-P_m) M_{dm}}{P_c} \tag{8a}$$

$$\overline{m_c} = \frac{(1-P_m) \overline{m_m}}{P_c} \tag{8b}$$

where M_{dm} and $\overline{m_m}$ are the domain magnetization and the average magnetic moment of monomers, respectively. While aggregation increases the magnetic anisotropy constant for clusters, K_{ac} (equation 5b), it decreases both the domain magnetization (M_{dc}) and the average magnetic moment ($\overline{m_c}$) for clusters (equations 8a and 8b), due to the minimization of internal energy.[31] Consequently, in this work, the effect of the magnetic nanoparticle aggregation is modeled through a corrected expression for the actual magnetization using a revised Langevin function.

3.2.4 Magnetic Susceptibility

In the presence of an alternating magnetic field of the form

$$H(t) = H_0 \cos(\omega t) = Re[H_0 e^{i\omega t}] \tag{9a}$$

the magnetization, $M(t)$, lags the magnetic field, $H(t)$. Therefore, it is convenient to express the magnetization in terms of the complex magnetic susceptibility, $\chi = \chi' - i\chi''$, resulting in:

$$M(t) = Re\left[\chi H_0 e^{i\omega t}\right] = H_0(\chi' \cos\omega t + \chi'' \sin\omega t) \tag{9b}$$

As can be derived from the Shilomis relaxation equations, when an alternating magnetic field is applied to the ferrofluid, the dynamics of the magnetization, *M*(*t*), is governed by:

$$\frac{\partial M(t)}{\partial t} = \frac{1}{\tau}(M_0(t) - M(t)) \tag{10a}$$

where the equilibrium magnetization, $M_0(t)$, under the alternating magnetic field can be expressed as:

$$M_0(t) = \chi_0(T)\, H_0 \cos(\omega t) = Re[\chi_0(T)\, H_0 e^{i\omega t}] \tag{10b}$$

where $\chi_0(T)$ is the equilibrium magnetic susceptibility. Substituting equation 9b and equation 10b into equation 10a yields:

$$-\omega\tau\chi' \sin(\omega t) + \omega\tau\chi'' \cos(\omega t) = (\chi_0(T) - \chi')\cos(\omega t) - \chi'' \sin(\omega t) \tag{10c}$$

Comparing the corresponding coefficients, we can obtain the expression for both the real part and the imaginary part of the complex magnetic susceptibility, χ:

$$\chi' = \frac{\chi_0(T)}{1+(\omega\tau)^2} \tag{11a}$$

$$\chi'' = \frac{\omega\tau\chi_0(T)}{1+(\omega\tau)^2} \tag{11b}$$

where the equilibrium magnetic susceptibility, $\chi_0(T)$, can be derived from the expression for the equilibrium magnetization of ferrofluid (equation 6):

$$\chi_0(T) = \frac{M_0(T)}{H_0} = \frac{\phi}{H_0}\left[M_{dm}\left(\frac{T}{T^*}\right) L\left(\frac{\mu_0 \overline{m_m} H_0}{k_B T}\right) + M_{dc}\left(1 - \frac{T}{T^*}\right)^{\frac{1}{2}} L\left(\frac{\mu_0 \overline{m_c} H_0}{k_B T}\right)\right] \tag{12}$$

3.2.5 Power Dissipation

Using the equilibrium magnetization, $M_0(T)$, from equation 6 and the equilibrium magnetic susceptibility, $\chi_0(T)$, from equation 12, we are ready to calculate the adjusted power dissipation. For magnetic nanoparticles suspended in an alternating magnetic field, the energy dissipation is equal to the change in the internal energy, ΔU, or equivalently, the loss of the magnetic work:[5]

$$\Delta U = -\mu_0 \oint M(t) dH \tag{13a}$$

$$\Delta U = -\mu_0 \oint_0^{\frac{2\pi}{\omega}} \mathrm{Re}\left[\chi H_0 e^{-i\omega t}\right] dH \tag{13b}$$

$$\Delta U = \mu_0 \pi {H_0}^2 \chi'' \tag{13c}$$

Substituting equation 11b and $\omega = 2\pi f$ into equation 13c, we obtain the final expression for the change in the internal energy, ΔU:

$$\Delta U = \frac{2\mu_0 {H_0}^2 f \pi^2 \tau \chi_0(T)}{1+(2\pi f\tau)^2} \tag{13d}$$

Using the change in the internal energy, ΔU, the volumetric power dissipation, P, can be expressed as:

$$P = f\Delta U = f\mu_0 \pi {H_0}^2 \chi'' \tag{14a}$$

which is derived from the integration and multiplication of cyclic frequency, f, and internal energy change, ΔU. Substituting equation 13d into equation 14a, we can express the volumetric power dissipation, P, as:

$$P = \frac{2\mu_0 {H_0}^2 (f\pi)^2 \tau \chi_0(T)}{1+(2\pi f\tau)^2} \tag{14b}$$

Finally, to obtain the modified power dissipation for magnetic nanoparticle aggregates, substitute equation 12 for $\chi_0(T)$ into equation 14b:

$$P = \frac{2\mu_0 H_0 (f\pi)^2 \tau \phi}{1+(2\pi f\tau)^2} \left[M_{dm} \left(\frac{T}{T^*}\right) L\left(\frac{\mu_0 \overline{m_m} H_0}{k_B T}\right) + M_{dc}(1 - \frac{T}{T^*})^{\frac{1}{2}} L(\frac{\mu_0 \overline{m_c} H_0}{k_B T}) \right] \tag{14c}$$

3.2.6 Specific Loss Power

The specific loss power (SLP) can be calculated as:

$$SLP = \frac{P}{\rho\phi} \tag{15a}$$

where ρ denotes the mass density of the ferrofluid. The corresponding adjusted SLP accounting for cluster formation in the ferrofluid can then be expressed as:

$$\text{SLP} = \frac{2\mu_0\tau H_0(\pi f)^2}{\rho[1+(2\pi f\tau)^2]}\left[M_{dm}\left(\frac{T}{T^*}\right)L\left(\frac{\mu_0\overline{m_m}H_0}{k_BT}\right) + M_{dc}(1-\frac{T}{T^*})^{\frac{1}{2}}\,L(\frac{\mu_0\overline{m_c}H_0}{k_BT})\right] \tag{15b}$$

3.2.7 Comparison with Experimental Results

To determine the validity and accuracy of our revised cluster-based model, predicted SLP values based on the revised cluster-based model and the Rosensweig model were compared with available experimental results using magnetite Fe_3O_4 magnetic nanoparticle[22,23] and cobalt ferrite $CoFe_2O_4$ magnetic nanoparticles reported in the previous literature.[24,25] In comparison with the reported experimental results, we have taken into account different physical properties of magnetic nanoparticles such as magnetic anisotropy, surface chemistry, size distribution, and magnetic environment (e.g., applied magnetic field amplitude, applied magnetic field frequency). All the numerical calculations and nonlinear fitting were done using our custom-written program on MATLAB 2013b (The MathWorks, Natick, MA). The experimental results and the parameters used in the theoretical calculation are summarized, respectively, in Table 1 for magnetite Fe_3O_4 magnetic nanoparticles and in Table 2 for cobalt ferrite $CoFe_2O_4$ magnetic nanoparticles.

3.2.8 *In Vivo* Demonstration of Magnetic Nanoparticle Aggregation in Cancer Tissues

In order to demonstrate the aggregation of magnetic nanoparticles in biomedical applications, we inspected MR T_2-weighted imaging and the pathological iron stain of pancreatic cancers in *in vivo* xenograft mouse models, which are targeted and labelled by magnetic

nanoparticles. To enhance targeting specificity and efficiency, anti-cancer-antigen 19-9 (anti-CA 19-9) antibodies (400 μg) were conjugated to NH_2-PEG-coated magnetic nanoparticles (5 mg) utilizing reductive amination chemistry into 900 μL solution. Conjugation was verified using dynamic light scattering for particle size determination, and the Bradford protein assay. More details on the preparation, bio-conjugation, and characterization of the anti-CA 19-9 antibodies--magnetic nanoparticles can be found in the "Supplementary Materials".

The human pancreatic cancer cell line, BxPC-3, which reveals positive expression of CA19-9 antigen,[32] was purchased from Bioresource Collection and Research Center (BCRC, Taiwan), derived from American Type Culture Collection (ATCC) and cultured in RPMI-1640 medium (Sigma-Aldrich) supplemented with 10% fetal bovine serum (FBS) (Gibco) and 100 U/mL penicillin-streptomycin antibiotics (Sigma-Aldrich) and maintained in a 5% CO_2 humidified incubator at 37 ^oC. The antigen binding capacity to CA 19-9 over-expressing cell lines (BxPC3) was confirmed with *in vitro* MR cellular images. A 1-cm NMR tube containing twelve 1-mm capillaries with BxPC3 cells labelled by various concentrations of magnetic nanoparticles was imaged. The relaxation rate, R_2, parameter mapping of the twelve capillaries obtained from the axial T_2-weighted spin echo images shows quantitative agreement with the concentration of the magnetic nanoparticles.

Furthermore, two control experiments using mouse models bearing both CA19-9(+) and CA19-9(-) pancreatic cancers and mouse models bearing CA19-9(+) pancreatic cancers and no pancreatic cancers were used to additionally confirm specific, reliable targeting and binding. The subcutaneous xenograft pancreatic cancer was created with 3×10^6 CA19-9(+) BxPC-3 cells on the right flank of the mouse and 3×10^6 CA19-9(-) Mia PaCa-2 cells on the left flank. In both control experiments, magnetic nanoparticles can only be found in the CA19-9(+) pancreatic cancer tissues.

The MRI experiments were performed on Varian INOVA 7-T micro-imaging spectrometer (Varian Inc., CA, USA) at day 35 after tumor implantation. The multiple slice spin echo T_2-weighted images were acquired on the axial plane with TR = 7.5 s, TE = 10 ms, 30 ms, 50 ms, FOV = 32×32 mm,

thickness = 0.5 mm, pixel size = 128×128, number of slice = 64, number of scan = 1. Prior to injecting 200 μL CA19-9-magneic nanoparticle (corresponding to 2.0 mg Fe/Kg mouse) from tail vein of the mouse, we injected 100 μg IgG (Immunoglobulin G) from tail vein of the mouse to suppress the immune response of the mouse. Administration of IgG to mice in combination with particulate antigen suppressed the immunity response that is mediated by macromolecules found in extracellular fluids such as secreted antibodies, complement proteins, and certain antimicrobial peptides by masking B-cell epitopes.[33]

3.3 Results and Discussion

3.3.1 *In Vivo* Demonstration of Magnetic Nanoparticle Aggregation in Pancreatic Cancers

Pancreatic cancer, called the silent killer, is the fourth leading cause of cancer-related death in both men and women in US. Due to difficulties in diagnosis and therapy, pancreatic cancer patients' five-year survival rate is only about 1% in US. Nonetheless, hope for mitigating pancreatic cancers arises from the early detection and targeted thermo-chemo therapy through MR nano-theranostics. Figure 1 demonstrates the formation of magnetic nanoparticle aggregates in targeted pancreatic cancers, which motivated the authors to propose a revised cluster-based model to more accurately predict SLP and to optimize heating efficiency for future *in vivo* applications of MR nano-theranostic hyperthermia in cancer therapy.

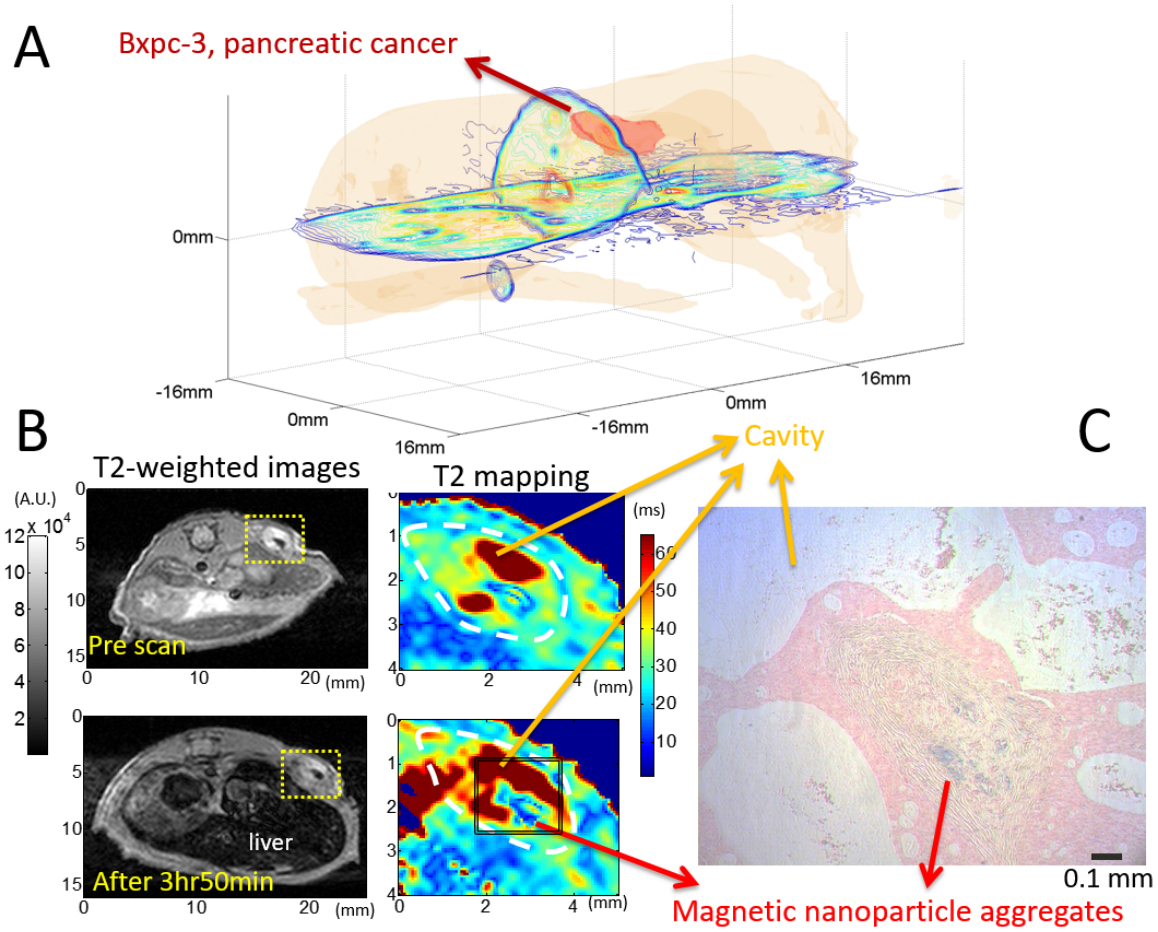


Figure 1. Formation of magnetic nanoparticle aggregates in targeted pancreatic cancer tissues. In order to demonstrate the aggregation of magnetic nanoparticles in biomedical applications, we inspected MR T_2-weighted imaging and the pathological iron stain of pancreatic cancers in *in vivo* xenograft mouse models, which are targeted and labelled by magnetic nanoparticles. To enhance targeting specificity and efficiency, anti-CA 19-9 antibodies were conjugated to NH_2-PEG-coated magnetic nanoparticles. (A) 3D reconstruction of the pancreatic cancer mouse model from 2D axial T_2-weighted images. (B) T_2-weighted images (left) and the T_2 parameter mapping corresponding to the yellow dashed line box area (right) acquired before (top) and after (bottom) the pancreatic cancer tissues (circled by white dashed line) were targeted and labelled by anti-CA 19-9 antibodies--magnetic nanoparticles. (C) To confirm and visualize the magnetic

nanoparticle aggregates in (B), Prussian blue staining was performed where magnetic nanoparticle aggregates will form an insoluble deep blue hydrated ferric ferrocyanide complex (i.e., Prussian blue dye).

3.3.2 Comparison with the Rosensweig Model

To investigate how the aggregation behavior of interacting magnetic nanoparticles affects the hyperthermia properties, the specific loss power (SLP) was computed from the revised cluster-based model and then was compared with that from the original Rosensweig model.[5] Because SLP is proportional to the volumetric power dissipation, which is in part determined by the imaginary part of the magnetic susceptibility as described in equation 14a and equation 15a, changes in the imaginary part of the magnetic susceptibility due to magnetic nanoparticle aggregation would be reflected on the resulting SLP. Experimental results reported by Hergt *et al.*[13] regarding the relationship between the frequency, f, and the imaginary part of the magnetic susceptibility of the ferrofluid, χ'', were shown to be significantly different from the predicted Rosensweig theoretical values. Specifically, experimental results for the colloidal-based ferrofluid suspension were shown to have a lower magnetic susceptibility peak value than predicted, implying the model suggested by Rosensweig alone cannot fully characterize the ferrofluid system. Our revised cluster-based model aims to explain the inconsistency between the original Rosensweig prediction and experimental results by considering cluster formation in the ferrofluid solution.

Using the experimental parameters previously reported by Hergt *et al*,[13] we compared the differences between the Rosensweig model and the revised cluster-based model, as shown in Figure 2. The imaginary part of the magnetic susceptibility, χ'', was calculated as a function of

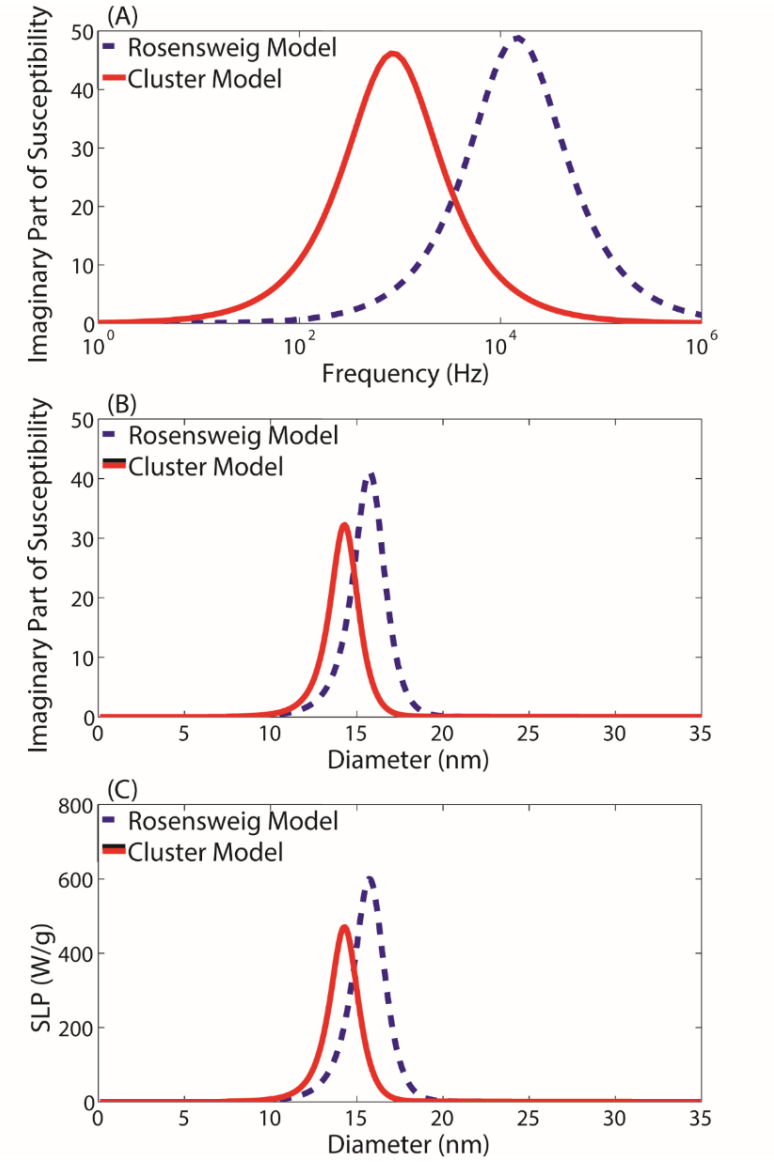


Figure 2. Comparison with the Rosensweig model. The imaginary part of the magnetic susceptibility, χ'', and the specific loss power, SLP, were computed by our revised cluster-based model (red solid line) and the Rosensweig model (blue dashed line). (A) χ'' as a function of the alternating magnetic field frequency, f, for magnetic nanoparticle diameter = 18 nm, alternating magnetic field amplitude H_0 = 11 kA/m, and magnetic anisotropy constant K_a = 15 kJ/m^3. (B) χ'' as a function of the magnetic nanoparticle diameter for alternating magnetic field frequency f = 410 kHz, alternating magnetic field amplitude H_0 = 11 kA/m, and magnetic anisotropy constant

K_a = 15 kJ/m^3. (C) The specific loss power, SLP, as a function of the magnetic nanoparticle diameter, using the same parameters as those in (B).

the alternating magnetic field frequency, f (Figure 2A), where the magnetic nanoparticle diameter was set to 18 nm and the magnetic field amplitude was set to 11 *kA/m*. The imaginary part of the magnetic susceptibility, χ'', was also calculated as a function of the magnetic nanoparticle diameter (Figure 2B) to further illustrate the effect of magnetic nanoparticle aggregation, where the magnetic field amplitude was set to 11 *kA/m* and frequency to 410 *kHz*. As a result, the revised cluster-based model shifts the curve of χ'' to lower frequency and smaller magnetic nanoparticle diameter, and decreases the maximum peak value. This is because magnetic nanoparticle aggregation increases the overall cluster magnetic anisotropy (K_{ac}), as described in equation 5b, and decreases both the domain magnetization (M_{dc}) and the average magnetic moment ($\overline{m_c}$) of clusters due to the minimization of internal energy,[31] as shown in equation 8. Particularly, the increase in cluster magnetic anisotropy is reflected in effective relaxation time constant, τ, by affecting the Neel relaxation time constant, τ_N, as denoted in equation 3 and equation 4, while the decrease in both the domain magnetization and average magnetic moment of the clusters is reflected in the equilibrium magnetic susceptibility, as shown in equation 12. These factors altogether contribute to the shift of the curve of χ'', resulting in the shifted theoretical SLP value, as shown in equation 15b. Therefore, the theoretical SLP based on equation 15b was plotted in Figure 2C as a function of the magnetic nanoparticle diameter using the same parameters as those in Figure 2B. The predicted SLP values reflect the variation in the imaginary part of the magnetic susceptibility, as these two parameters are linearly related to each other (equation 14a).

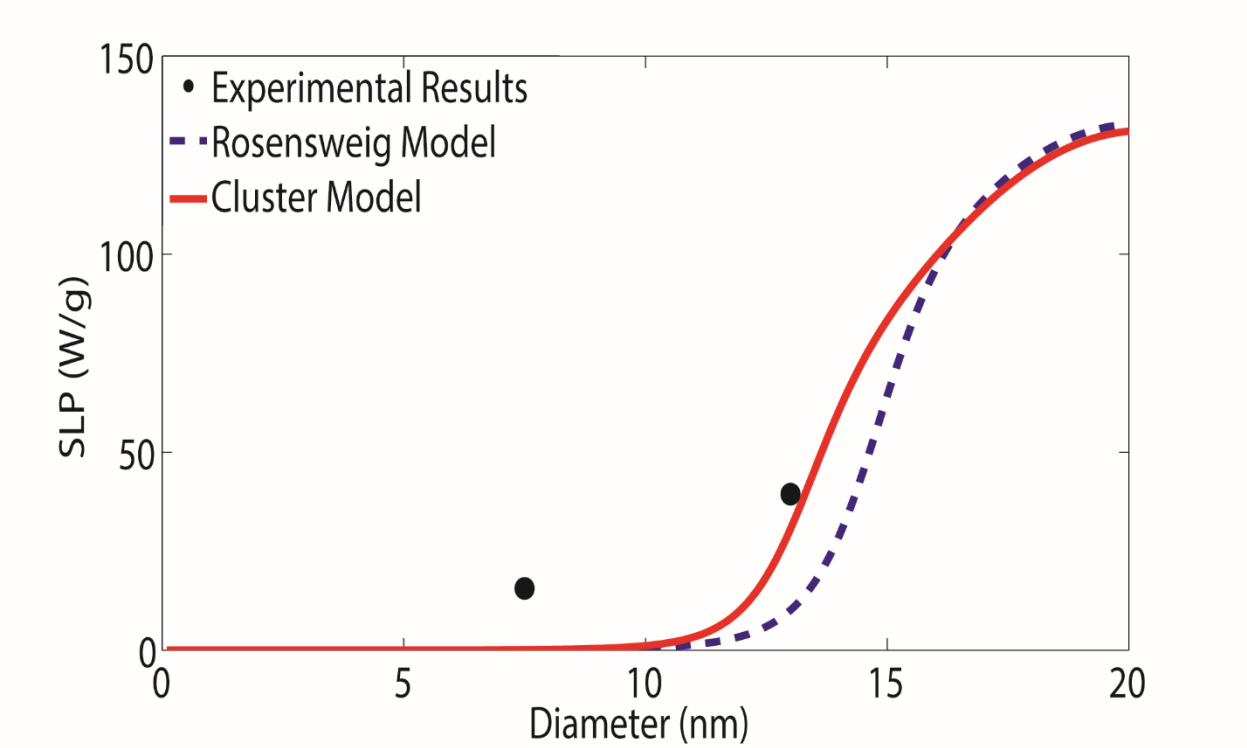


Figure 3. Comparison with the experimental results of magnetite Fe_3O_4 magnetic nanoparticles. The specific loss power (SLP) values were computed as a function of the magnetic nanoparticle diameter, based on our revised cluster-based model (red solid line) and the Rosensweig model (blue dashed line), using the experimental results and parameters reported by Ma *et al.*[22] (black filled circle). The experimental results and parameters used in the theoretical calculations are summarized in Table 1: magnetite Fe_3O_4, magnetic anisotropy constant K_a = 21 kJ/m^3, domain magnetization of monomers M_{dm} = 446 kA/m, alternating magnetic field frequency f = 80 kHz, alternating magnetic field amplitude H_0 = 32.5 kA/m, viscosity of the carrier fluid (water) η = 0.0007 kg m^{-1} s^{-1}, temperature T = 300 K, and critical temperature T^*= 358 K.

Table 1. Experimental results and parameters used in the theoretical calculations of the specific loss power (SLP) for magnetite Fe_3O_4 magnetic nanoparticles,[22,23] to determine the validity and accuracy of the revised cluster-based model, as shown in Figures 3 and 4.

Magnetic nanoparticle		Magnetite Fe_3O_4						
Magnetic anisotropy constant, K_a (kJ/m^3)		21						
Domain magnetization of monomers, M_{dm} (kA/m)		446						
Viscosity of the carrier fluid, η (kg m^{-1} s^{-1})		0.0007 (Water)						
Temperature, T (K)		300						
Critical temperature, T^* (K)		358						
Alternating magnetic field	Frequency, f (kHz)	80		168				
	Amplitude, H_0(kA/m)	32.5		21				
Magnetic nanoparticle mean diameter (nm)		7.5	13	4.5	6.7	10.9	16.0	35.4
Specific loss power, SLP (W/g)	Experiment[22,23]	15.6	39.4	~ 0	3	32	61	76
	Cluster-based model	0.13	30.6	~ 0	0.14	6.87	76.1	9.38
	Rosensweig model	0.11	10.1	~ 0	0.04	2.86	101	9.42
Reference		Ma *et al.*[22]		Lartigue *et al.*[23]				
Figure number		Figure 3		Figure 4				

The main difference between the revised cluster-based model and the Rosensweig model is the consideration of magnetic nanoparticle interactions within the real ferrofluid. Because the Rosensweig model assumes magnetic nanoparticles act as individual units independent of each other, the SLP value, as well as the optimal magnetic nanoparticle size, is over-estimated. In biomedical applications, however, magnetic nanoparticles are not found simply in single units, but rather as aggregated clusters (Figure 1). Accurate theoretical models should therefore reflect the fraction of clusters in the real ferrofluid. By taking cluster formation into consideration, the revised cluster-based model predicts SLP values and the corresponding optimal magnetic

nanoparticle diameter at the maximum SLP to be about 20-25% smaller than those made by the Rosensweig model, as shown in Figure 2C.

3.3.3 Comparison with the Experimental Results of Magnetite Fe_3O_4 Magnetic Nanoparticles

SLP were computed based on the revised cluster-based model and the Rosensweig model and then were compared with the experimental results of magnetite Fe_3O_4 magnetic nanoparticles reported by Ma *et al.,*[22] and Lartigue *et al.,*[23] as summarized in Table 1 and shown in Figure 3 and Figure 4. Magnetite Fe_3O_4 is the most popular form of magnetic nanoparticles, as it is well tolerated by the human body. Although there are still some differences between our cluster-based prediction and the experimental results, our model offers relatively more accurate estimates of SLP in comparison with the Rosensweig model. Within the superparamagnetic size range (*i.e.*, magnetic nanoparticle diameter 5--50 nm), the SLP values increase significantly with the increase of the nanoparticle size, mainly due to the onset of other heat generation mechanisms.[10,13] However, aggregation of magnetic nanoparticle shifts the overall curve to the left (i.e., smaller magnetic nanoparticle diameter), predicting lower SLP values when compared with the predictions made by the Rosenswig model, in agreement with Figure 2. Notably, the revised cluster-based model works especially well within the magnetic nanoparticle diameter range 10 nm--20 nm, which is commonly chosen for MR nano-theranostics. On the other hand, neither theoretical model accurately predicts the SLP for magnetic nanoparticles with diameter larger than 20 nm (Figure 4). This divergence can be attributed to the availability of other heat generation mechanisms and nonlinear effect, such as hysteresis,[10,13] associated with larger magnetic nanoparticle diameters.

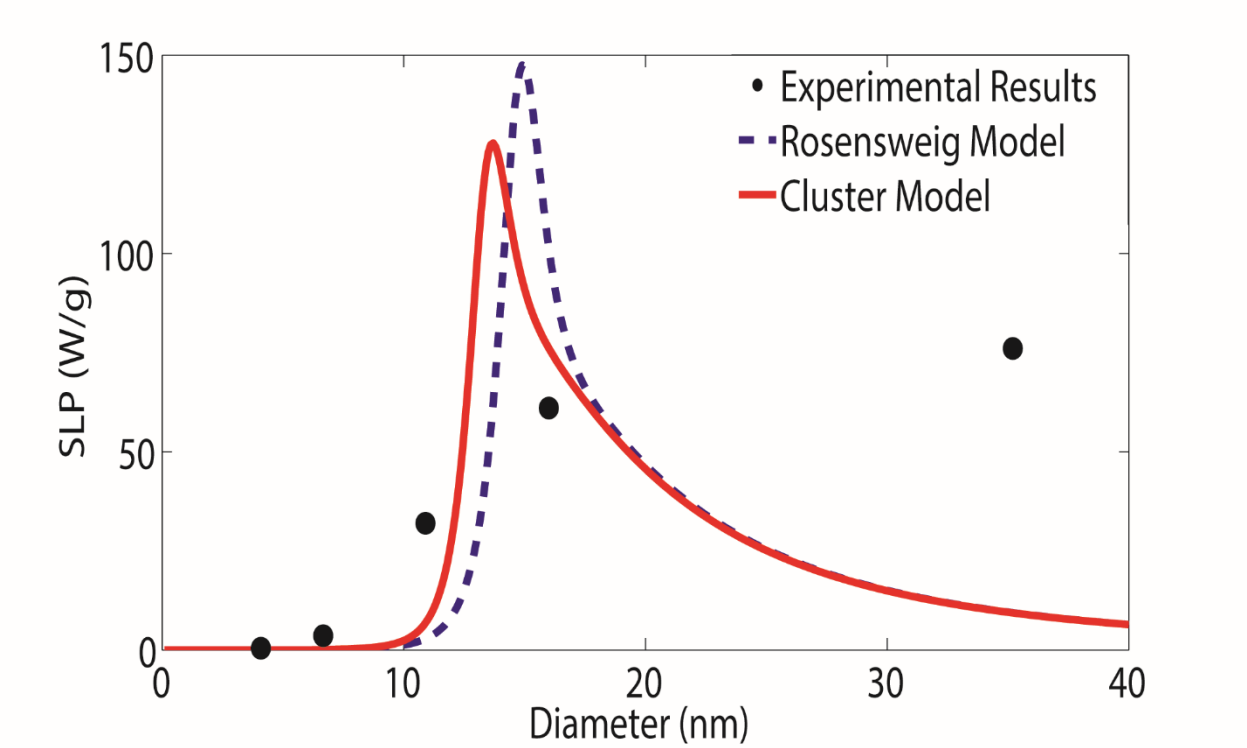


Figure 4. Comparison with the experimental results of magnetite Fe_3O_4 magnetic nanoparticles. The specific loss power (SLP) values were computed as a function of the magnetic nanoparticle diameter, based on our revised cluster-based model (red solid line) and the Rosensweig model (blue dashed line), using the experimental results and parameters reported by Lartigue *et al.*[23] (black filled circle). The experimental results and parameters used in the theoretical calculations are summarized in Table 1: magnetite Fe_3O_4, magnetic anisotropy constant K_a = 21 kJ/m^3, domain magnetization of monomers M_{dm} = 446 kA/m, alternating magnetic field frequency f = 168 kHz, alternating magnetic field amplitude H_0 = 21 kA/m, viscosity of the carrier fluid (water) η = 0.0007 kg m^{-1} s^{-1}, temperature T = 300 K, and critical temperature T^* = 358 K.

Table 2. Experimental results and parameters used in the theoretical calculations of the specific loss power (SLP) for cobalt ferrite $CoFe_2O_4$ magnetic nanoparticles,[24,25] to determine the validity and accuracy of the revised cluster-based model, as shown in Figure 5 and Figure 6.

Magnetic nanoparticle		Cobalt ferrite $CoFe_2O_4$						
Magnetic anisotropy constant, K_a (kJ/m^3)		1200						
Domain magnetization of monomers, M_{dm} (kA/m)		425						
Viscosity of the carrier fluid, η (kg m^{-1} s^{-1})		0.0007 (Water)						
Temperature, T (K)		300						
Critical temperature, T^* (K)		358						
Alternating magnetic field	Frequency, f (kHz)	167					700	
	Amplitude, H_0(kA/m)	21					24.8	
Magnetic nanoparticle size	Mean Diameter (nm)	5.5	5.9	6.0	6.2	6.7	3.9	9.1
	Standard Deviation, σ	0.19	0.18	0.19	0.23	0.21	0.40	0.22
Specific loss power, SLP (W/g)	Experiment[24,25]	76.7	105	153	188	250	40	360
	Cluster-based model	140	183	199	235	294	33.1	361
	Rosensweig model	151	198	215	255	318	35.8	387
Reference		Baldi *et al.*[24]					Fortin *et al.*[25]	
Figure Number		Figure 5					Figure 6	

3.3.4 Comparison with the Experimental Results of Cobalt Ferrite $CoFe_2O_4$ Magnetic Nanoparticles

Additional comparisons were made using experimental results of cobalt ferrite $CoFe_2O_4$ reported by Baldi *et al.,*[24] and Fortin *et al.,*[25] as summarized in Table 2 and shown in Figure 5 and Figure 6, respectively. Similar to the previous comparison with the experimental results of magnetite Fe_3O_4 magnetic nanoparticles, the revised cluster-based model approaches the experimental results better than the Rosensweig model, as the maximum and overall SLP is

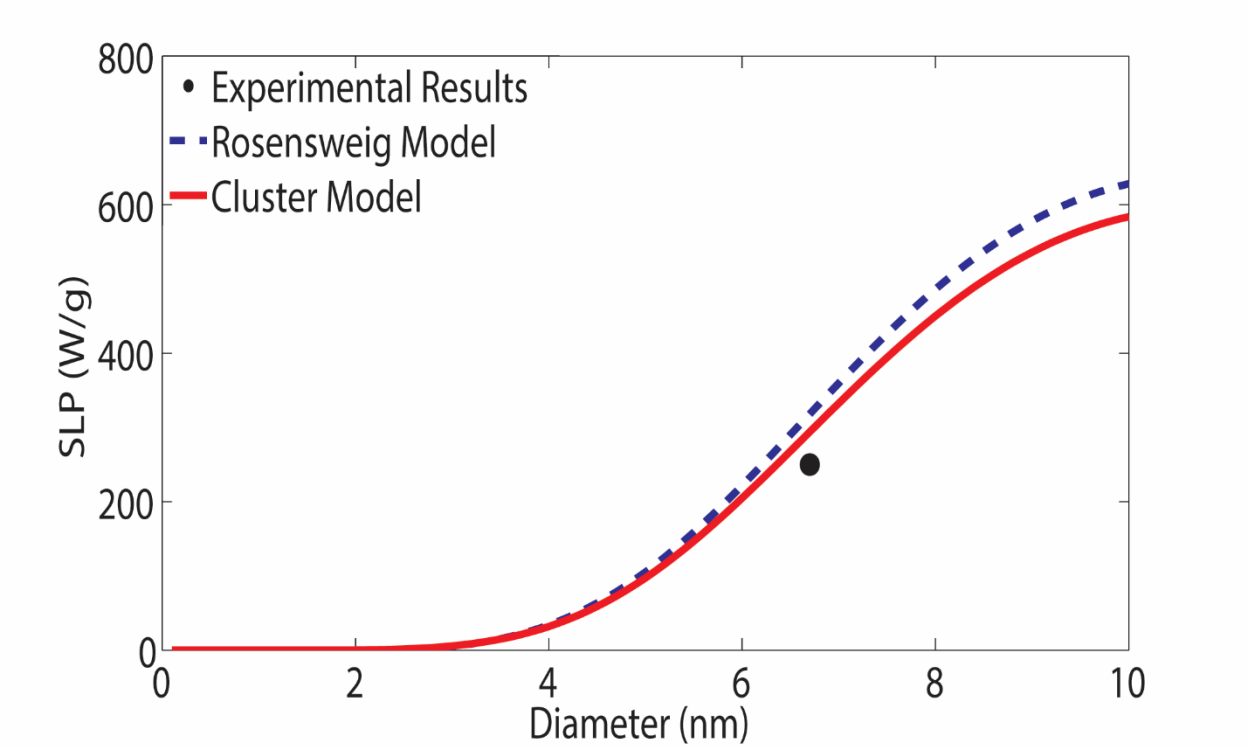


Figure 5. Comparison with the experimental results of cobalt ferrite $CoFe_2O_4$ magnetic nanoparticles. The specific loss power (SLP) values were computed as a function of the magnetic nanoparticle diameter, based on our revised cluster-based model (red solid line) and the Rosensweig model (blue dashed line), using the experimental results and parameters reported by Baldi *et al.*[24] (black filled circle). The experimental results and the parameters used in the theoretical calculations are summarized in Table 2: cobalt ferrite $CoFe_2O_4$, magnetic anisotropy constant K_a = 1200 kJ/m^3, domain magnetization of monomers M_{dm} = 425 kA/m, alternating magnetic field frequency f = 167 kHz, alternating magnetic field amplitude H_0 = 21 kA/m, viscosity of the carrier fluid (water) η = 0.0007 kg m^{-1} s^{-1}, temperature T = 300 K, critical temperature T^*= 358 K, and the mean (standard deviation σ) of the magnetic nanoparticle diameter = 6.7 nm (σ = 0.23 nm).

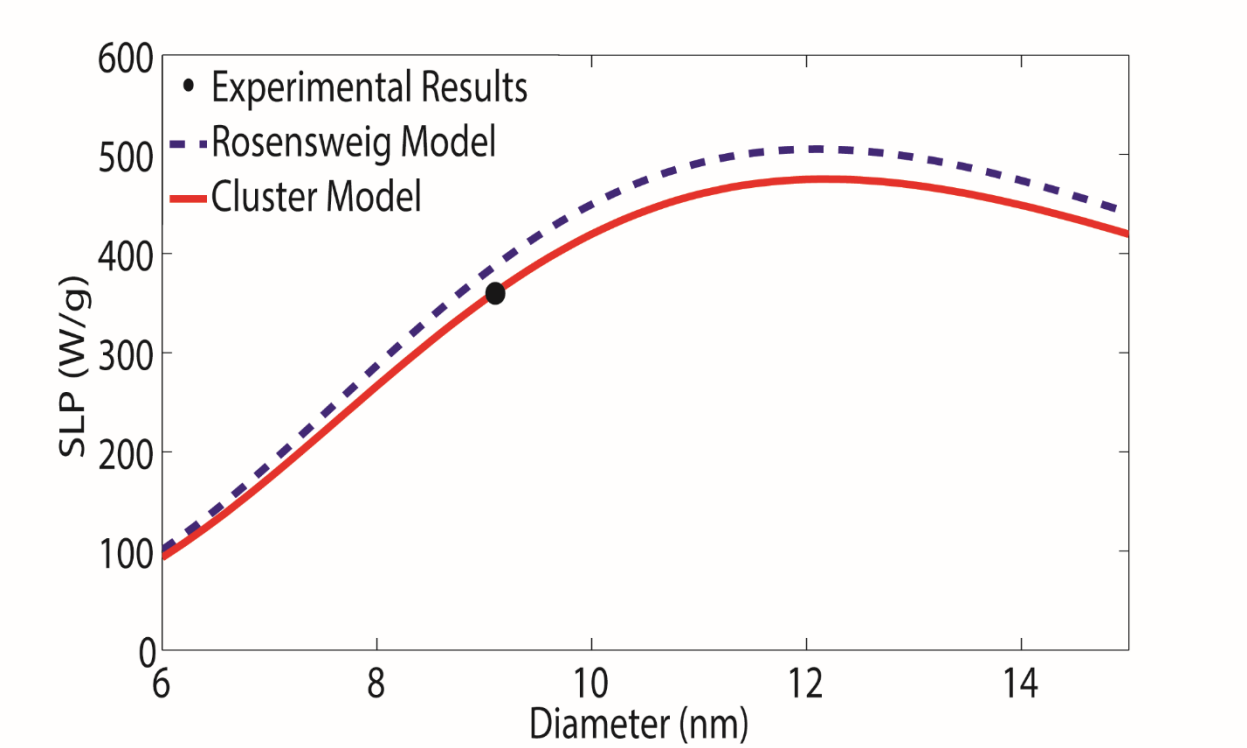


Figure 6. Comparison with the experimental results on cobalt ferrite $CoFe_2O_4$ magnetic nanoparticles. The specific loss power (SLP) values were computed as a function of the magnetic nanoparticle diameter, based on our revised cluster-based model (red solid line) and the Rosensweig model (blue dashed line), using the experimental results and parameters reported by Fortin *et al.*[25] (black filled circle). The experimental results and parameters used in the theoretical calculations are summarized in Table 2: cobalt ferrite $CoFe_2O_4$, magnetic anisotropy constant K_a = 1200 kJ/m^3, domain magnetization of monomers M_{dm} = 425 kA/m, alternating magnetic field frequency f = 700 kHz, alternating magnetic field amplitude H_0 = 24.8 kA/m, viscosity of the carrier fluid (water) η = 0.0007 kg m^{-1} s^{-1}, temperature T = 300 K, critical temperature T^* = 358 K, and the mean (standard deviation σ) of the magnetic nanoparticle diameter = 9.1 nm (σ = 0.22 nm).

reduced by the aggregation of magnetic nanoparticles. Again, SLP of magnetic nanoparticles with diameters between 10 nm--20 nm was more accurately predicted by the revised cluster-based model. However, since cobalt ferrite $CoFe_2O_4$ possesses a relatively larger magnetic anisotropy constant than magnetite Fe_3O_4, the effect of aggregation on magnetic anisotropy becomes less significant, resulting in smaller shift to the left (i.e., smaller magnetic nanoparticle diameter) by the revised cluster-based model, as portrayed in both Figure 5 and Figure 6.

3.4 Conclusion

Magnetic resonance (MR) nano-theranostic hyperthermia uses nontoxic, biocompatible magnetic nanoparticles to target and accumulate at the lesions to generate enhanced contrast for early lesion detection and to generate heat to kill lesion cells directly through hyperthermia or indirectly through thermal activation and control releasing of drugs.[34-38] By considering the effects of magnetic nanoparticle aggregation on MR nano-theranostic hyperthermia, our revised cluster-based model provides a more accurate prediction of experimental values, as shown in Figures 3-6 for magnetite Fe_3O_4 and cobalt ferrite $CoFe_2O_4$ magnetic nanoparticles. The aggregation of magnetic nanoparticles increases the cluster magnetic anisotropy while reducing both the cluster domain magnetization and the average magnetic moment, which in turn decreases the imaginary part of the magnetic susceptibility to shift the predicted SLP toward smaller magnetic nanoparticle diameter with lower peak values. The effect of magnetic nanoparticle aggregation can also be understood in terms of energy transfer. A portion of the energy provided by the magnetic field is absorbed by the magnetic nanoparticle aggregates to overcome inter-nanoparticle interactions, such as electrostatic attraction, electrostatic repulsion, steric repulsion, and magnetic dipolar interactions to disrupt the aggregates into monomers. As a

result, the heating efficiency is decreased and the SLP values are less than the prediction made by the Rosensweig theory.

The improvement in the prediction accuracy provided by the revised cluster-based model is particularly pronounced when the magnetic nanoparticle diameter is in the range of approximately 10 nm--20 nm or, equivalently, the resulting drug-nanoparticle-ligand conjugates in the range of approximately 30 nm--50 nm. This happens to be an important size range for MR nano-theranostics, as recent studies showed that anti-cancer nanomedicine with 50 nm nanoparticle size provides the optimal combination of deep tumor tissue penetration, efficient cancer cell internalization, and slow tumor clearance, and therefore exhibits the highest efficacy against both primary and metastatic tumors *in vivo*.[39] When the magnetic nanoparticle becomes larger, as seen for the case of magnetite Fe_3O_4 in Figure 4, the prediction becomes inaccurate even with the revised cluster-based model, mainly due to alternative heat generation mechanisms and nonlinear response of magnetic susceptibility,[40-42] which motivates more sophisticated and accurate theoretical models in the future.

Finally, nanoparticle size plays a pivotal role in nano-theranostics, as it determines their biodistribution, tumor penetration, cellular internalization, clearance from blood plasma and tissues, as well as excretion from the body — all of which impact the overall therapeutic efficacy against cancers.[39,43] Our studies show that, as far as MR nano-theranostic hyperthermia is concerned, a relatively 20-25% smaller magnetic nanoparticle diameter should be chosen to reach the maximal heating efficiency in comparison to the optimal size predicted by previous models.

3.5 References

[1] Cantillon-Murphy, P.; Wald, L. L.; Zahn, M.; Adalsteinsson, E. Proposing Magnetic Nanoparticle Hyperthermia in Low-Field MRI. *Concepts in Magn Reson A.* **2010**, *36*, 36–47.

[2] Gordon, R. T.; Hines, J. R.; Gordon, D. Intracellular Hyperthermia: A Biophysical Approach to Cancer Treatment via Intracellular Temperature and Biophysical Alterations. *Med Hypotheses*. **1979**, *5*, 83-102.

[3] Jordan, A.; Wust, P.; Fähling, H.; John, W.; Hinz, A.; Felix, R. Inductive Heating of Ferrimagnetic Particles and Magnetic Fluids: Physical Evaluation of Their Potential for Hyperthermia. *Int. J. Hyperthermia*. **1993**, *9*, 51-68.

[4] Jordan, A.; Wust, P.; Scholz, R.; Tesche, B.; Fähling, H.; Mitrovics, T.; Vogl, T.; Cervos-Navarro, J.; Felix, R. Cellular Uptake of Magnetic Fluid Particles and Their Effects on Human Adenocarcinoma Cells Exposed to AC Magnetic Fields *In Vitro*. *Int J Hyperthermia*. **1996**, *12*, 705-722.

[5] Rosensweig, R. E. Heating Magnetic Fluid with Alternating Magnetic Field. *J. Magn. Magn. Mater*. **2002**, *252*, 370-374.

[6] Banobre, M.; Teijeiro, A.; Rivas, J. Magnetic Nanoparticle-Based Hyperthermia for Cancer Treatment. *Rep. Prac. Oncol. Radiother*. **2013**, *18*, 397-400.

[7] Guibert, C.; Dupuis, V.; Peyre, V.; Fresnais, J. Hyperthermia of Magnetic Nanoparticles: Experimental Study of the Role of Aggregation. *J. Phys. Chem. C.* **2015**, *199*, 28148-28154.

[8] Xiang, Q.; Zhong, J.; Zhou, M.; Morais, P. C.; Liu, W. AC Field Dependence of Cluster Disruption in Magnetic Fluids. *J. Appl. Phys*. **2011**, *109*, 07B317.

[9] Bordelon, D. E.; Cornejo, C.; Grüttner, C.; Westphal, F.; DeWeese, T. L.; Ivkov, R. Magnetic Nanoparticle Heating Efficiency Reveals Magneto-Structural Differences When Characterized with Wide Ranging and High Amplitude Alternating Magnetic Fields. *J. Appl. Phys*. **2011**, *109*, 124904.

[10] Hergt, R.; Dutz, S.; Röder, M. Effects of Size Distribution on Hysteresis Losses of Magnetic Nanoparticles for Hyperthermia. *J. Phys. Condens. Matter*. **2008**, *20*, 385214.

[11] Li, Z.; Kawashita, M.; Araki, N.; Mistumori, M.; Hiraoka, M. Effects of Particle Size of Magnetite Nanoparticles on Heat Generating Ability under Alternating Magnetic Field. *Bioceram. Dev. Appl.* **2011**, *1*, D110128.

[12] Khandhar, A. P.; Ferguson, R. M.; Simon, J. A.; Krishnan, K. M. Enhancing Cancer Therapeutics using Size-Optimized Magnetic Fluid Hyperthermia. *J. Appl. Phys.* **2012**, *111*, 07B306.

[13] Hergt, R.; Dutz, S.; Müller, R.; Zeizberger, M. Magnetic Particle Hyperthermia: Nanoparticle Magnetism and Materials Development for Cancer Therapy. *J. Phys. Condens. Matter*. **2006**, *18*, S2919-S2934.

[14] Morais, P. C.; Gonçalves, G. R. R.; Bakuzis, A. F.; Neto, K. S.; Pelegrini, F. Experimental Evidence of Dimer Disruption in Ionic Ferrofluid: A Ferromagnetic Resonance Investigation. *J. Magn. Magn. Mater*. **2001**, *225*, 84-88.

[15] Castro, L. L.; da Silva, M. F.; Bakuzis, A. F.; Miotto, R. Aggregate Formation on Polydisperse Ferrofluids: A Monte Carlo Analysis. *J. Magn. Magn. Mater*. **2005**, *293*, 553-558.

[16] Ganguly, R.; Zellmer, B.; Puri, I. K. Field-Induced Self-Assembled Ferrofluid Aggregation in Pulsatile Flow. *Phys. Fluids*. **2005**, *17*, 097104.

[17] Minkowycz, W. J.; Sparrow, E. M.; Abraham, J. P. *Nanoparticle Heat Transfer and Fluid Flow*. CRC Press; **2012**.

[18] Dennis, C. L.; Jackson, A. J.; Borchers, J. A.; Hoopes, P. J.; Strawbridge, R.; Foreman, A. R.; van Lierop, J.; Gruttner, C.; Ivkov, R. Nearly Complete Regression of Tumors via Collective Behavior of Magnetic Nanoparticles in Hyperthermia. *Nanotechnology*. **2009**, *20*, 395103.

[19] Liu, W.; Zhong, J.; Xiang, Q.; Yang, G.; Zhou, M. Discretization of Magnetization Curves and Their Application in Size Estimation of Nanosized Ferrofluid. *IEEE Trans. Nanotechnol*. **2011**, *10*, 1231-1237.

[20] Sherman, S. G.; Wereley, N. M. Effect of Particle Size Distribution on Chain Structures in Magnetoheological Fluids. *IEEE Trans. Magn*. **2013**, *49*, 3430-3433.

[21] Zhong, J.; Xiang, Q.; Massa, L. O.; Qu, F.; Morais, P. C.; Liu, W. Second-order-like Cluster-monomer Transition within Magnetic Fluids and Its Impact upon the Magnetic Susceptibility. *Nanoscale Res. Lett*. **2012**, *7*, 167.

[22] Ma, M.; Wu, Y.; Zhou, J.; Sun, Y.; Zhang, Y.; Gu, N. Size Dependence of Specific Power Absorption of Fe_3O_4 Particles in AC Magnetic Field. *J. Magn. Magn. Mater*. **2004**, *268*, 33-39.

[23] Lartigue, L.; Innocenti, C.; Kalaivani, T., et al. Water-Dispersible Sugar-Coated Iron Oxide Nanoparticles: An Evaluation of Their Relaxometric and Magnetic Hyperthermia Properties. *J. Am. Chem. Soc.* **2011**, *133*, 10459–10472.

[24] Baldi, G.; Lorenzi, G.; Ravagli, C. Hyperthermic Effect of Magnetic Nanoparticles under Electromagnetic Field. *PAC*. **2009**, *3*, 103-109.

[25] Fortin, J. P.; Wilhelm, C.; Servais, J.; Menager, C.; Bacri, J. C.; Gazeau, F. Size-Sorted Anionic Iron Oxide Nanomagnets as Colloidal Mediators for Magnetic Hyperthermia. *J. Am. Chem. Soc*. **2007**, *129*, 2628-2635.

[26] Debye, P. *Polar Molecules*. New York: The Chemical Catalog Co. Inc.; **1929**.

[27] Néel, L. Theorie du Trainage Magnetique des Ferromagnetiques en Grains Fins Avec Applications Aux Terres Cuites. *Geophysics*. **1949**, *5*, 99-136. France.

[28] Kumar, C. *Magnetic Nanomaterials*. John Wiley & Sons; **2009**.

[29] Saville, S. L.; Qi, B.; Baker, J., et al. The Formation of Linear Aggregate in Magnetic Hyperthermia: Implication on Specific Absorption Rate and Magnetic Anisotropy. *J. Colloid Interface Sci*. **2014**, *424*, 141-151.

[30] Mehdaoui, B.; Tan, R. P.; Meffre, A., et al. Increase of Magnetic Hyperthermia Efficiency due to Dipolar Interactions in Low-Anisotropy Magnetic Nanoparticles: Theoretical and Experimental Results. *Phys. Rev. B*. **2013**, *87*, 174419.

[31] Feynman, R. P.; Leighton, R. B.; Sands. M. *The Feynman Lectures on Physics*. The Definitive and Extended ed. Addison Wesley; **2005**.

[32] McElroy, M.; Kaushal, S.; Luiken, G. A., et al. Imaging of Primary and Metastatic Pancreatic Cancer using a Fluorophore-Conjugated Anti-CA19-9 Antibody for Surgical Navigation. *World J. Surg.* **2008**, *32*, 1057–1066.

[33] Cerottini, J. C.; McConahey, P. J.; Dixon, F. J. The Immunosuppressive Effect of Passively Administered Antibody IgG Fragments. *J. Immunol.* **1969**, *102*, 1008-1015.

[34] Chen, K. J.; Wolahan, S. M.; Wang, H., et al. A Small MRI Contrast Agent Library of Gadolinium(III)-Encapsulated Supramolecular Nanoparticles for Improved Relaxivity and Sensitivity. *Biomaterials.* **2011**, *32*, 2160-2165.

[35] Ho, L. C.; Hsu, C. H.; Ou, C. M.; Wang, C. W.; Liu, T. P.; Hwang, L. P. Lin, Y. Y.; Chang, H. T. Unibody Core-Shell Smart Polymer as a Theranostic Nanoparticle for Drug Delivery and MR Imaging. *Biomaterials*. **2015**, *37*, 436-446,

[36] Li, Z.; Hsu, C. H.; Dimitrov, N.; Hwang, D. W.; Chang, H. W.; Hwang, L. P.; Lin, Y. Y. Sensitive Imaging of Magnetic Nanoparticles for Cancer Detection by Active Feedback Magnetic Resonance. *Magn. Reson. Med.* **2015**, *74*, 33–41.

[37] Yao, J.; Hsu, C. H.; Li, Z.; Kim, T. S.; Hwang, L. P.; Lin, Y. C.; Lin, Y. Y. Magnetic Resonance Nano-Theranostics for Glioblastoma Multiforme. *Curr. Pharm. Des.* **2015**, *21*, 5256-5266.

[38] Wang, C.; Li, Z.; Lin Y. Y. Optimizing Magnetic Nanoparticle Hyperthermia Effect in MR Nanomedicine. *Chinese Journal of Magnetic Resonance.* **2015**, *32*, 248-260.

[39] Li, T.; Yang, X.; Yin, Q., et al. Investigating the Optimal Size of Anticancer Nanomedicine. *PNAS.* **2014**, *111*, 15344–15349.

[40] Fannin, P. C.; Charles, S. W.; Oireachtaigh, C. M.; Odenbach, S. Investigation of Possible Hysteresis Effects Arising from Frequency- and Field-Dependent Complex Susceptibility Measurements of Magnetic Fluids. *J. Magn. Magn. Mater*. **2006**, *302*, 1-6.

[41] Oireachtaigh, C. M.; Fannin, P. C. Investigation of the Non-Linear Loss Properties of Magnetic Fluids Subject to Large Alternating Fields. *J. Magn. Magn. Mater*. **2008**, *320*, 871-880.

[42] Fannin, P. C.; Oireachtaigh, C. M. Investigating the Isotropic Properties of a Magnetic Fluid Following the Removal of a Polarising Field. *J. Magn. Magn. Mater*. **2007**, *316*, e802-e804.

[43] Arami, H.; Khandhar, A.; Liggitt, D.; Krishnan, K. M. *In Vivo* Delivery, Pharmacokinetics, Biodistribution, and Toxicity of Iron Oxide Nanoparticles. *Chem. Soc. Rev.* **2015**, *44*, 8576-8607.

3.6 Supplementary Materials

Orthotopic Pancreatic Cancer Mouse Models

The 4-week-old male BALB/c Nude mice (N = 4) were obtained from BioLASCO, Taiwan. BALB/c is an albino, laboratory-bred strain of the house mouse from which a number of common substrains are derived. BALB/c mice are distributed globally, and are among the most widely used inbred strains used in animal experimentation.

Orthotopic pancreatic cancer mouse models are preferred in this work, because they offer tissue site-specific pathology, allow studies of metastasis, and are generally deemed more clinically relevant. Orthotopic implantation of pancreatic cancer cells includes the following steps: (i) Make incision with sterile microscissors beside the splenic silhouette. (ii) Expose the entire pancreas and spleen by using a pair of blunt-nose forceps. (iii) Insert the needle with the human pancreatic cancer cells into the tail of the pancreas and pass into the pancreatic head area. Suture the abdominal muscle layer first as putting back the pancreas and spleen into the abdominal cavity and close the skin.

We waited until the volume of the subcutaneous xenograft pancreatic cancer reached 5 mm^3. We first injected 100 μg IgG (Immunoglobulin G) from the tail vein of the mouse to suppress the immune response of the mouse. Then we injected 200 μL CA19-9-magneic nanoparticle (corresponding to 2.0 mg Fe/Kg mouse) from the tail vein of the mouse. All injections were performed under anesthesia by isoflurane (Panion & BF Biotech Inc.) and all efforts were made to minimize suffering.

Duirng the MRI acquisition, mice were anesthetized by inhalation of isoflurane (Panion & BF Biotech). A vaporizer specially calibrated for isoflurane was used to accurately control the anesthetic concentration during MRI scanning. The physiological status of the mice was kept

under surveillance with a small animal monitoring system (SA Instruments). Mice were humanely sacrificed after experiments. All animal procedures were in accordance with the regulations approved by the Institution Animal Care and Utilization Committee at National Taiwan University (approval number NTU-103-EL-61).

Tissues were fixed in 10% formalin overnight, embedded in paraffin, and then sectioned. Tissues sections with a thickness of 5 μm were deparaffinized in xylene, rehydrated in a gradient ethanol series, and incubated in blocking buffer. To visualize nuclei and cytoplasm, H&E staining was performed according to the standard protocols. Images of the tissues were acquired using a wield-field scanner with a 40× objective and detected with a color microscope camera (DFC7000T, Leica).

To visualize the magnetic nanoparticle aggregates, Prussian blue staining was performed according to the standard protocols. The staining is an optical method based on the binding of cellular ferric ions to the soluble ferrocyanide salt at low pH, forming an insoluble deep blue hydrated ferric ferrocyanide complex (i.e., Prussian blue dye). Therefore, in order to detect magnetic nanoparticle aggregates in tissue sections, the specimens were deparaffinized and treated with 20% aqueous solution of concentrated HCl to dissolve the magnetic nanoparticles to release ferric iron in the cells.

Preparation, Bioconjugation, and Characterization of the Anti-CA 19-9 Antibodies--Magnetic Nanoparticles

To oxidize the glycosylated anti-CA 19-9 antibodies, 400 μg of the antibody was mixed with 40 μL of 0.10 M sodium periodate solution and reacted for 45 minutes in dark at room temperature. Then 40 μL of 0.20 M Na_2SO_3 solution was immediately added into the mixture

and let react for another 10 minutes. The sample was then run through D-Salt Dextran Desalting Columns (Thermo Scientific, Rockford, IL, USA) to isolate the oxidized antibody from the mixture.

The oxidized antibody was quickly mixed with the amine-coated magnetic nanoparticles (0.054 nmole/mL) (Ocean Nanotech, Springdale, AR) at a pH of 8.0 to reduce aggregation and maximize Schiff base formation while preventing the denaturation of the antibody. The reaction was then shaked at room temperature for 6 hours. To stabilize the Schiff bases, 53 μL of 5.0 M sodium cyanoborohydride solution was added and reacted for 45 minutes to reduce the bond to a secondary amine linkage. Additionally, 268 μL of 1.0 M ethanolamine solution was added to the mixture to quench the unreacted aldehyde groups on the antibody. This reaction mixture was then purified by washing 5 times using Amicon Ultra Centrifugal Filters (Millipore, Carrigtwohill, Ireland) to remove the quenching reagents. Unbound antibody was also purified from conjugated magnetic nanoparticles through a separation magnet (Ocean Nanotech, Springdale, AR) overnight. The final solution was suspended in PBS at a concentration of 5 mg Fe/mL.

Dynamic light scattering (DLS) measurements were taken to verify the bio-conjugation between the anti-CA 19-9 antibodies and the magnetic nanoparticles. DLS measurements were taken on a Zetasizer Nano using a disposable, low volume cuvette. The standard protein method on the detector was utilized to generate a size distribution plot. The diameter of unconjugated magnetic nanoparticles was measured to be 25 nm, while that of the conjugated magnetic nanoparticles was 38 nm, as shown in Figure S1.

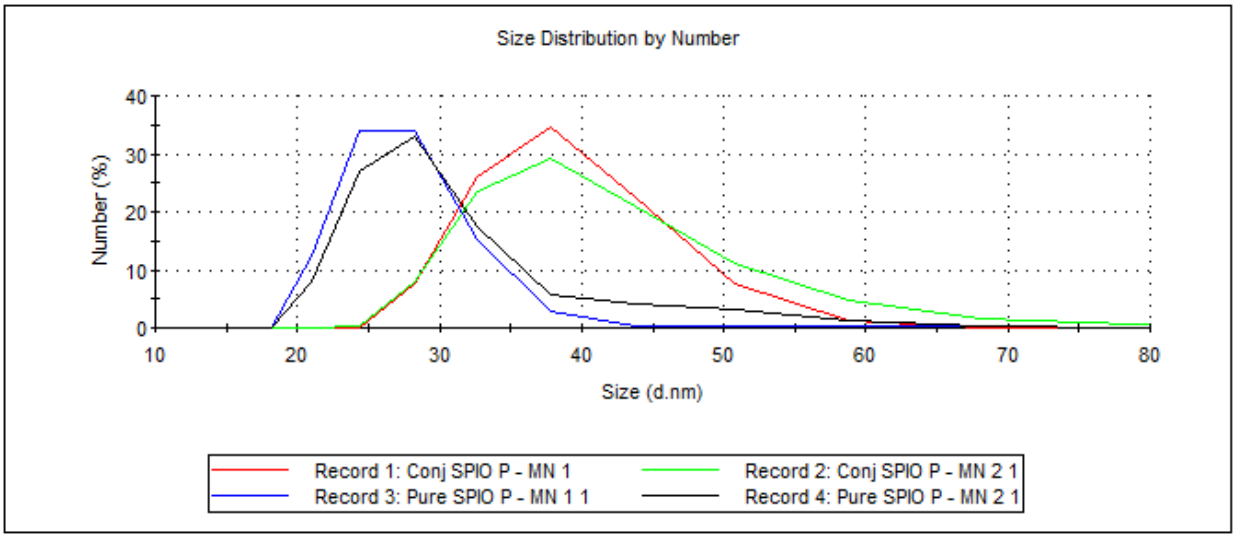


Figure S1. Dynamic light scattering (DLS) measurements were taken to verify the bio-conjugation between the anti-CA 19-9 antibodies and the magnetic nanoparticles. The standard protein method on the detector was utilized to generate a size distribution plot. The diameter of unconjugated magnetic nanoparticles was measured to be 25 nm, while that of the bio-conjugated magnetic nanoparticles was 38 nm.

Chapter 4

Utilizing the Nonlinear Response of Magnetic Nanoparticle Aggregates for Effective *In Vivo* Nano-Theranostic Hyperthermia

4.0 Abstract

Nano-theranostic hyperthermia is one of the most promising novel techniques for simultaneously diagnosing and treating cancer. The procedure involves injecting biocompatible magnetic nanoparticles that not only act as molecular beacons to enhance MRI contrast for early tumor detection, but also destroy tumor cells when the particles are heated when exposed to an applied magnetic field. In order to control and optimize the *in vivo* nano-theranostic hyperthermia's heating efficiency, measured as specific loss power (SLP), we proposed a novel theoretical model to better understand the fundamentals of heat generation, so that we can modify the design magnetic nanoparticles for the purpose of effective heating. In contrast to previous models such as those using the Rosensweig approach, our new model moves beyond viewing magnetic nanoparticles act as single units whose magnetic susceptibility responds linearly to the changes in magnetic field amplitude. To confirm the accuracy and validity of this model, we compared its calculated results and those of the currently prevailing models to experimental data. We concluded that the aggregation of magnetic nanoparticles and the nonlinear response property of the magnetic susceptibility can both strongly affect the heating efficiency. The added consideration of these two features in the theoretical model gives us a more accurate estimation framework for experimental results. Moreover, the proposed model works at its best when predicting the heating efficiency for the types of magnetic nanoparticles

and magnetic fields that are most commonly used clinically for hyperthermia cancer therapy. With recent advances in the emerging theranostics, especially in the application of a combined MRI detection and treatment system, this work provides an important physical insight: the additional heating effect induced by the nonlinear response of magnetic susceptibility can negatively influence the heating efficiency as magnetization approaches and reaches saturation. Based on our proposed model, the nano-theranostic hyperthermia system's heating efficiency can be optimized by placing magnetic nanoparticles with a diameter of 15nm in a magnetic field with a moderate amplitude of around $25 kA/m$.

4.1 Introduction

Nano-theranostic system has been gaining in popularity, due largely to its combination of diagnostic and local treatment of cancers.[1-3] By taking advantage of the unique targeting property of nontoxic magnetic nanoparticles, which occurs at the nanoscale level, the nano-theranostic system is able to detect and treat cancer in a single setting simultaneously. It holds great potential to change the current medical paradigm from "see, then treat" to "see and treat". Magnetic nanoparticles have been decorated with a wide variety of materials to improve their biocompatibility for controlling drug delivery and release, encapsulate/bind imaging agents to enhance the Magnetic Resonance (MR) image contrast for early lesion detection, carry therapeutic payloads and produce local heat in the presence of an external alternating magnetic field.[4-6]

MR nano-theranostic hyperthermia has been shown to be a promising cancer thermotherapy, as long as the injected magnetic nanoparticles are able to readily heat up tumors under alternating magnetic fields without damaging healthy tissue.[7-8] A primary challenge to

achieve this goal has been determining the optimal strength of the magnetic field. A field that is too weak does not generate sufficient heat to destroy the lesion; a field that is too strong can produce significantly harmful side effects. The ideal nano-theranostic hyperthermia system maximizes heating efficiency so that the strongest possible heating effect can be achieved using the weakest possible magnetic field.

Unfortunately, the fundamental heating generation mechanism of magnetic nanoparticles under biological conditions is still poorly understood. The previously proposed theoretical linear response model[9] does not sufficiently inform the design of an *in vivo* nano-theranostic hyperthermia system that uses magnetic nanoparticles. As a result, the inaccurate estimation of the heating efficiency for colloidal magnetic nanoparticle suspensions has severely limited the expanded use of nano-theranostic hyperthermia systems in clinical applications.

The proposed nonlinear response model is more complex and nuanced, allowing for the heating efficiency, which is usually represented by specific loss power (SLP), to be optimized by adjusting several parameters, including the magnetic field amplitude and frequency, the magnetic nanoparticle size and size distribution, the clustering of the magnetic nanoparticles, domain magnetization, and magnetic anisotropy.[10-12]

Currently, most studies rely on the Rosensweig approach,[9] which assumes 1) that magnetic nanoparticles are non-interacting units in the colloidal suspension and 2) that for the heat generation mechanism of the magnetic nanoparticles, the magnetic susceptibility and the magnetic field amplitude are linearly related, in accordance with Curie's Law. Consequently, predictions of SLP based upon those assumptions are reasonably accurate only when magnetic nanoparticles have a small diameter and are in the presence of a weak magnetic field.

Theoretical models based on the assumptions of the Rosensweig approach have been shown to be inadequate predictors of experimental results.[13] Magnetic nanoparticles have been found to exhibit several interactions, including magnetic dipole-dipole interaction, steric repulsion, and van der Waals attraction.[14-17] These interactions contribute to the formation of nanoparticle aggregate clusters in the colloidal suspension, which decrease the induced heating efficiency. Moreover, as the magnetic nanoparticle size and the magnetic field amplitude increase, the heat generation mechanism becomes more complicated, since the linear regime only holds true under high temperatures or in weak magnetic fields. In contrast, strong magnetic fields can induce loss process and heating effects, driving the nonlinear response of the magnetic susceptibility.[18-21] With the recent advances in the biotechnological applications of high amplitude magnetic fields for nano-theranostic hyperthermia, this consideration is becoming increasingly necessary. Understanding the dynamical magnetic response of nanoparticles placed in an alternating magnetic field allows us not only to precisely evaluate the *in vivo* heating efficiency in living tissues[22-23] but also to optimize the design of targeted nano-theranostic MR hyperthermia for cancer therapy.[24-26]

Studies have confirmed the need to account for complex environments where aggregation occurs and the magnetic field changes in which the magnetic nanoparticles accumulate when establishing the heating efficiency estimation model. However, much of that effort has gone into investigating the mechanism of aggregate formation and the behavior of magnetic nanoparticles in colloidal suspension under different magnetic conditions.[16-17,27-31]

A few groups have proposed untested models that evaluate the heating efficiency by giving consideration to aggregate formation or the nonlinear response of the magnetic susceptibility.[32-34] For instance, using the Fanning model, Wang *et al.*[32] revised the energy

calculation method for a real ferrofluid-based system based to account for the aggregation. However, they did not confirm that the SLP predicted by the model matched existing experimental results. Coral *et al.*[33] modeled the aggregation using an analytical form for the structure function that was derived from a fractal model of aggregation where the power law form of the scattering function was limited by a finite cluster size. But the authors reported that their linear response based model does not reproduce the experimental SLP. Accounting for the nonlinear heat generation mechanism[34] by using the equation for electric susceptibility proposed by Coffey and Paranjape[35] brings the theoretical SLP closer to the experimental results, but failing to factor in the formation of aggregate gives rise to overestimating the heating efficiency.

The present paper proposes a novel theoretical model for designing a nano-theranostic hyperthermia system that predicts and allows for the optimization of the heating efficiency of magnetic nanoparticles by looking into both the aggregate formation and the nonlinear relationship between the magnetic susceptibility and the magnetic field. Our understanding of the magnetic nanoparticles has been revised to account for the nonlinear response of the magnetic susceptibility. Cluster formation calculations used in our proposed theoretical model have been compared to experimental data and results previously published[13,36-39] to confirm the accuracy and validity of this nonlinear, cluster-based model.

4.2 Materials and Methods

4.2.1 Fraction of Monomers and Clusters

At the critical temperature, a second-order phase transition is followed by the disruption of magnetic nanoparticle clusters.[42] In order to properly characterize this heat-induced cluster

breakup at the critical temperature, T^*, and the suspension temperature, T,[43] the fraction of clusters (P_c) in the ferrofluid was chosen as an order parameter

$$P_c = (1 - \frac{T}{T^*})^{\frac{1}{2}} \quad (1a)$$

From the expression of P_c, it can be concluded that when the temperature is significantly lower than the critical temperature, $T \ll T^*$, magnetic nanoparticle monomers exist alongside clusters in the ferrofluid system and that there are no clusters when the temperature is at or above the critical temperature. Thus, the fraction of monomers (P_m) in the ferrofluid can be simply treated to be proportional to the temperature:

$$P_m = \frac{T}{T^*} \quad (1b)$$

Note that $P_m + P_c = 1$ under two limiting conditions: $T \ll T^*$ and $T \geq T^*$.

4.2.2 Relaxation Mechanisms

Calculating the specific loss power (SLP) of interacting colloidal magnetic nanoparticles in the ferrofluid requires that we first describe two major relaxation mechanisms for the gradual alignment of the particles' magnetic moments during the magnetization. The Brownian relaxation time constant, τ_B, is given by the following relationship:[44]

$$\tau_B = \frac{3\eta V_h}{k_B T} \quad (2)$$

where $V_h = (1 + \delta/R)^3$ is the magnetic nanoparticle's hydrodynamic volume, V is the volume of the magnetic nanoparticle, R is the radius of the magnetic nanoparticle, and δ is the surfactant thickness (a property of the ferrofluid). k_B is the Boltzmann constant, T is the temperature of the ferrofluid solution (the product $k_B T$ is the thermal energy), and η is the viscosity of the carrier fluid.

The Néel relaxation time constant, τ_N, can be expressed as:[45]

$$\tau_N = \begin{cases} \tau_0 \, \Gamma^{-\frac{1}{2}} \exp(\Gamma) & \Gamma \geq 1 \\ \tau_0 \, \Gamma & \Gamma \ll 1 \end{cases} \quad (3)$$

where $\Gamma = \frac{K_a V}{k_B T}$, $K_a V$ is the energy barrier (a product of the magnetic anisotropy constant, K_a, and the volume of the magnetic nanoparticle, V), and τ_0 is the attempt time (its reciprocal is called the attempt frequency). Typical values for τ_0 are between 10^{-9} and 10^{-10} seconds.

Because both relaxation mechanisms occur in parallel, the effective total relaxation time constant, τ, is given by:

$$\frac{1}{\tau} = \frac{1}{\tau_B} + \frac{1}{\tau_N} \quad (4a)$$

or, alternatively, by:

$$\tau = \frac{\tau_B \cdot \tau_N}{\tau_B + \tau_N} \quad (4b)$$

When $\tau_B \ll \tau_N$, then $\tau \approx \tau_B$. Similarly, when $\tau_B \gg \tau_N$, then $\tau \approx \tau_N$. Thus, the net relaxation effect is influenced primarily by the stronger relaxation mechanism with shorter relaxation time constant.

Since aggregation increases the magnetic directional dependence of clusters,[29,46] the magnetic anisotropy constant in our proposed model, K_a, uses different values for monomers and clusters. If the magnetic anisotropy constants for monomers and clusters are defined as K_{am} and K_{ac} respectively, then:

$$K_{am} = K_a \quad (5a)$$

$$K_{ac} = K_{am} + \frac{(1-P_m)K_a}{P_c} \quad (5b)$$

where the term, $\frac{(1-P_m)K_a}{P_c}$, represents the increase in the average of the magnetic anisotropy constant due to the formation of clusters, and $(1 - P_m)$ represents the fraction of monomers that comes from the disruption of clusters.

4.2.3 Magnetic Susceptibility

To calculated the heating efficiency of magnetic nanoparticles, the effect of aggregation and nonlinear response of the magnetic susceptibility of ferrofluid were investigated at first. Briefly, in the presence of an alternating magnetic field, the magnetization, $M(t)$, lags the magnetic field, $H(t)$. In the framework of linear response function, $M(t) = \chi H(t)$, the magnetic susceptibility is conveniently denoted as a complex number, $\chi = \chi' - i\chi''$, with the following expressions for both the real part (χ') and the imaginary part (χ''):

$$\chi' = \frac{\chi_0(T)}{1+(\omega\tau)^2} \tag{6a}$$

$$\chi'' = \frac{\omega\tau\chi_0(T)}{1+(\omega\tau)^2} \tag{6b}$$

where $\chi_0(T)$ is the equilibrium magnetic susceptibility, $\omega = 2\pi f$ is the angular frequency, and χ'' is the loss component of magnetic susceptibility, representing the portion of magnetization which is in quadrature with the magnetic field.

However, equation 6 only describes the linear contribution of the equilibrium magnetic susceptibility in the presence of weak magnetic field, as characterized by Curie's Law. When a strong bias magnetic field is superimposed on the smaller alternating magnetic field, the relationship between the magnetic susceptibility and the magnetic field is no longer linear. In addition, applying a stronger alternating magnetic field will further induce a nonlinear response from the magnetic susceptibility.[19,27,34] Based on the equation for the electric susceptibility as

proposed by Coffey and Paranjape,[35] the real part and imaginary part of the complex magnetic susceptibility can be written as

$$\chi'(\omega, H_0) = \frac{\chi_0(T)}{1+(\omega\tau)^2}\{1 - \left(\frac{mH_0}{k_BT}\right)^2 \frac{27-13(\omega\tau)^2}{60[1+(\omega\tau)^2][9+4(\omega\tau)^2]}\} \quad (7a)$$

$$\chi''(\omega, H_0) = \frac{\chi_0(T)\omega\tau}{1+(\omega\tau)^2}\{1 - \left(\frac{mH_0}{k_BT}\right)^2 \frac{21+(\omega\tau)^2}{30[1+(\omega\tau)^2][9+4(\omega\tau)^2]}\} \quad (7b)$$

As shown in equation 7, the first term in both equations represents the linear property of the magnetic susceptibility, same as the expression in equation 6, while the remaining terms in both equations represent the nonlinear response of the magnetic susceptibility.

By accounting for the formation of aggregate, the equilibrium magnetic susceptibility of ferrofluid, which is a function of the temperature, $\chi_0(T)$, can be re-written as:[43]

$$\chi_0(T) = \frac{\phi}{H_0}\left[M_{dm}\left(\frac{T}{T^*}\right)L\left(\frac{\mu_0\overline{m_m}H_0}{k_BT}\right) + M_{dc}(1-\frac{T}{T^*})^{\frac{1}{2}}L(\frac{\mu_0\overline{m_c}H_0}{k_BT})\right] \quad (8)$$

where $\frac{T}{T^*} = P_m$ and $(1-\frac{T}{T^*})^{\frac{1}{2}} = P_c$ are the fractions of monomers and clusters, respectively, as shown in equation 1, ϕ is the volume fraction of the magnetic nanoparticles, H_0 is the amplitude of the applied alternating magnetic field, μ_0 is the magnetic permeability in free space, M_{dm} and M_{dc} are the domain magnetization of monomers and clusters, respectively, $\overline{m_m}$ and $\overline{m_c}$ are the average magnetic moment of monomers and clusters, respectively, and L is the Langevin function with formula $L(x) = \coth(x) - 1/x$. The Langevin function describes the dependency of the magnetization on the applied magnetic field in the classical limit, with the expression:

$$L\left(\frac{\mu_0\overline{m_m}H_0}{k_BT}\right) = \coth\left(\frac{\mu_0\overline{m_m}H_0}{k_BT}\right) - \frac{k_BT}{\mu_0\overline{m_m}H_0} \quad (9a)$$

$$L\left(\frac{\mu_0\overline{m_c}H_0}{k_BT}\right) = \coth\left(\frac{\mu_0\overline{m_c}H_0}{k_BT}\right) - \frac{k_BT}{\mu_0\overline{m_c}H_0} \quad (9b)$$

In equation 8, the first term in the bracket indicates the contribution from monomers, while the second term in the bracket indicates the contribution from clusters. Similar to the effect of

magnetic nanoparticle aggregation on the magnetic anisotropy constant, the domain magnetization (M_{dc}) and the average magnetic moment ($\overline{m_c}$) of clusters are also different from those of monomers:

$$M_{dc} = \frac{(1-P_m)M_{dm}}{P_c} \tag{10a}$$

$$\overline{m_c} = \frac{(1-P_m)\overline{m_m}}{P_c} \tag{10b}$$

where M_{dm} and $\overline{m_m}$ are the domain magnetization and the average magnetic moment of monomers, respectively. While aggregation increases the magnetic anisotropy constant for clusters, K_{ac} (equation 5b), it decreases both the domain magnetization (M_{dc}) and the average magnetic moment ($\overline{m_c}$) for clusters (equations 10a and 10b), due to the minimization of internal energy.[38] Consequently, in this work, the effect of the magnetic nanoparticle aggregation is modeled through a corrected expression for the actual magnetization using a revised Langevin function.

4.2.4 Power Dissipation and Specific Loss Power

Analytical relationships of power dissipation in a suspension of magnetic nanoparticles have been derived by Rosensweig.[9] For a number $f = \omega/2\pi$ of field cycles per second, the mean volumetric power dissipation is given by

$$P = f\mu_0\pi {H_0}^2\chi'' \tag{11a}$$

The specific loss power (SLP) can be calculated through volumetric power dissipation as:

$$SLP = \frac{P}{\rho\phi} \tag{11b}$$

where ρ denotes the mass density of the ferrofluid. By taking the aggregation and nonlinear response of the magnetic susceptibility into consideration, the SLP for the colloidal magnetic

nanoparticles suspension can be calculated by substituting equations 7b, 8 and 11a into equation 11b:

$$SLP = \frac{\mu_0 \tau H_0 \omega^2}{2\rho[1+(\omega\tau)^2]}\left\{1 - \left(\frac{\overline{m_m} H_0}{k_B T}\right)^2 \frac{21+(\omega\tau)^2}{30[1+(\omega\tau)^2][9+4(\omega\tau)^2]}\right\} \times$$

$$\left[M_{dm}\left(\frac{T}{T^*}\right) L\left(\frac{\mu_0 \overline{m_m} H_0}{k_B T}\right) + M_{dc}\left(1 - \frac{T}{T^*}\right)^{\frac{1}{2}} L\left(\frac{\mu_0 \overline{m_c} H_0}{k_B T}\right)\right] \quad (12)$$

Using equation 12, the SLP of a colloidal magnetic nanoparticle suspension can be calculated and compared to the predictions made by other models, as well as with previously published experimental results.

4.2.5 Computational Parameters

To determine the validity and accuracy of our revised cluster-based model, predicted SLP values based on the nonlinear cluster-based model, nonlinear model and the Rosensweig model were compared with experimental results previously reported,[13,36-39] which are summarized, respectively, in Table 1 for maghemite γ-Fe_2O_3 magnetic nanoparticles,[13] in Table 2 for magnetite Fe_3O_4 magnetic nanoparticles[36-38] and in Table 3 for cobalt ferrite $CoFe_2O_4$ magnetic nanoparticles.[39]

Table 1. Experimental parameters used in the theoretical calculations of the imaginary part of the magnetic susceptibility (χ'') and the specific loss power (SLP) for maghemite γ-Fe_2O_3 magnetic nanoparticles,[13] to determine the validity and accuracy of the revised nonlinear cluster-based model, as shown in Figure 1.

Magnetic nanoparticle		Maghemite γ-Fe_2O_3	
Magnetic anisotropy constant, K_a (kJ/m^3)		15	
Domain magnetization of monomers, M_{dm} (kA/m)		410	
Viscosity of the carrier fluid, η (kg m^{-1} s^{-1})		0.0007 (Water)	
Temperature, T (K)		300	
Critical temperature, T^* (K)		358	
Alternating magnetic field	Frequency, f (kHz)	10^0-10^6	410
	Amplitude, H_0(kA/m)	11	11
Magnetic nanoparticle diameter (nm)		18	0-35
Reference		Hergt *et al.*[13]	
Figure number		Figure 1A	Figure 1B and 2C

Table 2. Experimental results and parameters used in the theoretical calculations of the specific loss power (SLP) for magnetite Fe_3O_4 magnetic nanoparticles,[36] to determine the validity and accuracy of the revised nonlinear cluster-based model, as shown in Figure 2.

Magnetic nanoparticle		Magnetite Fe_3O_4								
Magnetic anisotropy constant, K_a (kJ/m^3)		21								
Domain magnetization of monomers, M_{dm} (kA/m)		446								
Viscosity of the carrier fluid, η (kg m^{-1} s^{-1})		0.0007 (Water)								
Temperature, T (K)		300								
Critical temperature, T^* (K)		358								
Alternating magnetic field	Frequency, f (kHz)	110								
	Amplitude, H_0(kA/m)	11.14								
Magnetic nanoparticle size	Mean Diameter(nm)	4.2	5.8	7.9	9.8	11.5	14.0	16.5	20.0	22.5
	Polydispersity, σ	0.3								
Specific loss power, SLP (W/g)	Experiment	45	30	28	28	150	201	249	309	322
	Rosensweig model	0.0	0.4	5.0	20	43	86	122	147	147
	Nonlinear model	0.0	0.4	6.0	26	61	137	223	326	378
	Nonlinear cluster-based mode	0.0	0.7	8.1	30	67	140	216	308	353
Reference		Jeun *et al.*[36]								
Figure Number		Figure 2								

Table 2 (continued). Experimental results and parameters used in the theoretical calculations of the specific loss power (SLP) for magnetite Fe_3O_4 magnetic nanoparticles,[37-38] to determine the validity and accuracy of the revised nonlinear cluster-based model, as shown in Figures 3 and 4.

Magnetic nanoparticle		Magnetite Fe_3O_4					
Magnetic anisotropy constant, K_a (kJ/m^3)		21					
Domain magnetization of monomers, M_{dm} (kA/m)		446					
Viscosity of the carrier fluid, η (kg m^{-1} s^{-1})		0.0007 (Water)					
Temperature, T (K)		300					
Critical temperature, T^* (K)		358					
Alternating magnetic field	Frequency, f (kHz)	400				80	
	Amplitude, H_0 (kA/m)	24.5				32.5	
Magnetic nanoparticle size	Mean Diameter(nm)	4.6	8.5	9.6	11.2	7.5	13
	Polydispersity, σ	0.075	0.15	0.22	0.21	-	
Specific loss power, SLP (W/g)	Experiment	180	130	200	447	15.6	39.4
	Rosensweig model	0.1	15.5	92.2	207	0.11	10.1
	Nonlinear model	0.1	16.9	130	322	0.11	12.8
	Nonlinear cluster-based mode	0.1	36.6	195	408	0.13	37.7
Reference		Gonzales *et al.*[37]				Ma *et al.*[38]	
Figure Number		Figure 3				Figure 4	

Table 3. Experimental results and parameters used in the theoretical calculations of the specific loss power (SLP) for cobalt ferrite $CoFe_2O_4$ magnetic nanoparticles,[39] to determine the validity and accuracy of the revised nonlinear cluster-based model, as shown in Figure 5.

Magnetic nanoparticle		Cobalt ferrite $CoFe_2O_4$				
Magnetic anisotropy constant, K_a (kJ/m^3)		1200				
Domain magnetization of monomers, M_{dm} (kA/m)		425				
Viscosity of the carrier fluid, η (kg m^{-1} s^{-1})		0.0007 (Water)				
Temperature, T (K)		300				
Critical temperature, T^* (K)		358				
Alternating magnetic field	Frequency, f (kHz)	167				
	Amplitude, H_0 (kA/m)	21				
Magnetic nanoparticle size	Mean Diameter (nm)	5.5	5.9	6.0	6.2	6.7
	Polydispersity, σ	0.19	0.18	0.19	0.23	0.21
Specific loss power, SLP (W/g)	Experiment	76.7	105	153	188	250
	Rosensweig model	151	198	215	255	318
	Nonlinear model	150	196	213	255	320
	Nonlinear cluster-based mode	138	180	196	235	295
Reference		Baldi *et al.*[39]				
Figure Number		Figure 5				

4.3 Results and Discussion

To assess the SLP prediction accuracy of proposed nonlinear model with cluster consideration and compare it to the accuracy of the current prevailing Rosensweig model and the nonlinear model without cluster consideration, we computed SLP values from the three models and then compared them to existing experimental results.[13,36-39] To eliminate potential sources of variation, the three modeling predictions were calculated using experimental parameters of

conditions previously reported, as summarized in the Methods Section. We focused mainly on magnetite (Fe_3O_4),[36-38] as it is better tolerated by the human body than other MNPs. In addition, we used cobalt ferrite ($CoFe_2O_4$),[39] which has significant greater magnetic anisotropy than magnetite, to further verify the accuracy and universality of our model.

4.3.1 Theoretical Comparisons

Experimental results reported by Hergt *et al.*[13] for the relationship between the magnetic field frequency and the imaginary part of the magnetic susceptibility of the ferrofluid were shown to differ significantly from the theoretical values predicted through Rosensweig approach. Specifically, experimental results for the colloidal-based ferrofluid suspension were shown to have a lower and left-shift susceptibility peak, as well as broader susceptibility vs frequency curve shape compared to the conventional theoretical prediction, implying that the Rosensweig model alone cannot fully characterize the ferrofluid system. Our proposed model aimed to explain the inconsistency between this original prediction and experimental results by considering cluster formation and the nonlinear magnetic susceptibility response in the ferrofluid solution.

We first looked at how the nonlinear response of the magnetic susceptibility and the aggregation behavior of interacting MNPs affect the prediction of SLP values by comparing the calculated imaginary part of the magnetic susceptibility of three theoretical models. Because SLP is linearly related to the imaginary part of the magnetic susceptibility, as described by equation 11, changes in the imaginary part of the magnetic susceptibility due to the ferrofluid behavior and magnetic response give rise to changes in SLP. Using the parameters outlined in the Methods Section Table 1, the imaginary part of the magnetic susceptibility was calculated as a function of the magnetic field frequency to illustrate the difference caused by the nonlinear

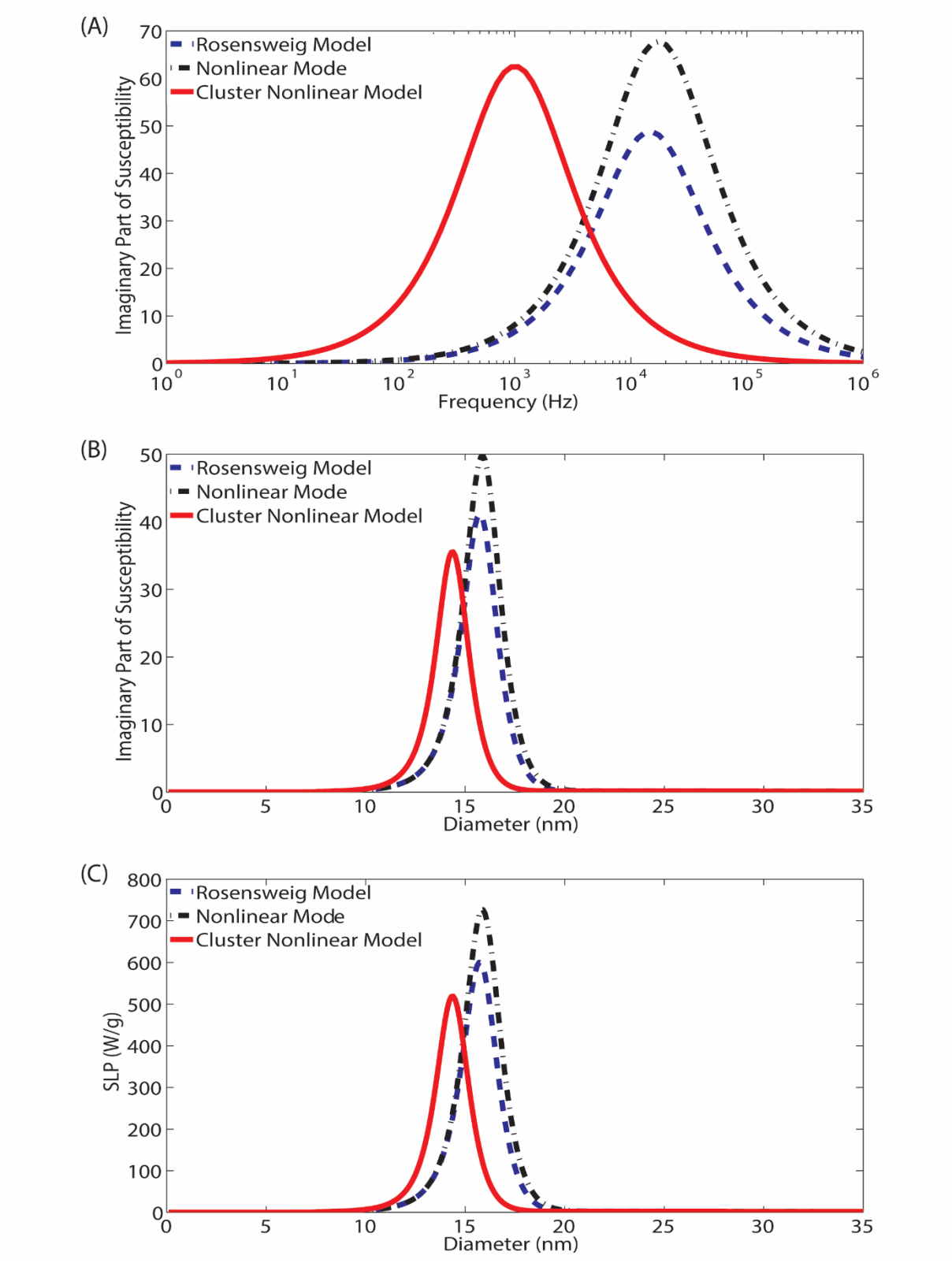

(A)
Rosensweig Model
Nonlinear Mode
Cluster Nonlinear Model
Imaginary Part of Susceptibility
Frequency (Hz)
(B)
Rosensweig Model
Nonlinear Mode
Cluster Nonlinear Model
Imaginary Part of Susceptibility
Diameter (nm)
(C)
Rosensweig Model
Nonlinear Mode
Cluster Nonlinear Model
SLP (W/g)
Diameter (nm)

Figure 1. SLP was recalculated with the parameters reported by Hergt *et al.*[13] using the Rosenweig model (dashed blue curve), nonlinear model (dotted black curve), and the proposed nonlinear cluster-based model (solid red curve). The imaginary part of the magnetic susceptibility was plotted as a function of frequency with a magnetic nanoparticle diameter of 18nm (A). The imaginary part of the magnetic susceptibility was then calculated as a function of magnetic nanoparticle diameter, with the magnetic field frequency of 410 *kHz* and the magnetic field amplitude of *11 kA/m* (B). The resulting SLP was then computed as a function of magnetic nanoparticle diameter (C) using the same conditions as part (B), which were summarized in Table 1.

response, as depicted in Figure 1A. The results show that, for magnetic nanoparticles with a diameter of 18nm and in the presence of the magnetic field with an amplitude of 11 *kA/m*, the imaginary parts of the magnetic susceptibility calculated using the nonlinear cluster-based model (solid red curve) were generally less than the values calculated using the nonlinear model without cluster consideration (dotted black curve), and larger than the values estimated using the Rosensweig model (dashed blue curve), which is based on the linear regime. Technically speaking, when the amplitude of the magnetic field is stronger than 1 *kA/m*, the nonlinear response of the magnetic susceptibility becomes observable. The induced loss process and heating effects contributed to the shift of both the solid red curve and the dotted black curve, making them higher than the dashed blue curve, which can be traced to the second term in equation 7. Also noteworthy is that the overall amplitude of solid red curve was lower than that of dotted black curve and appeared to be shifted to the left due to the contribution of aggregation,[40] which can be traced to equation 8. The formation of clusters increased the overall

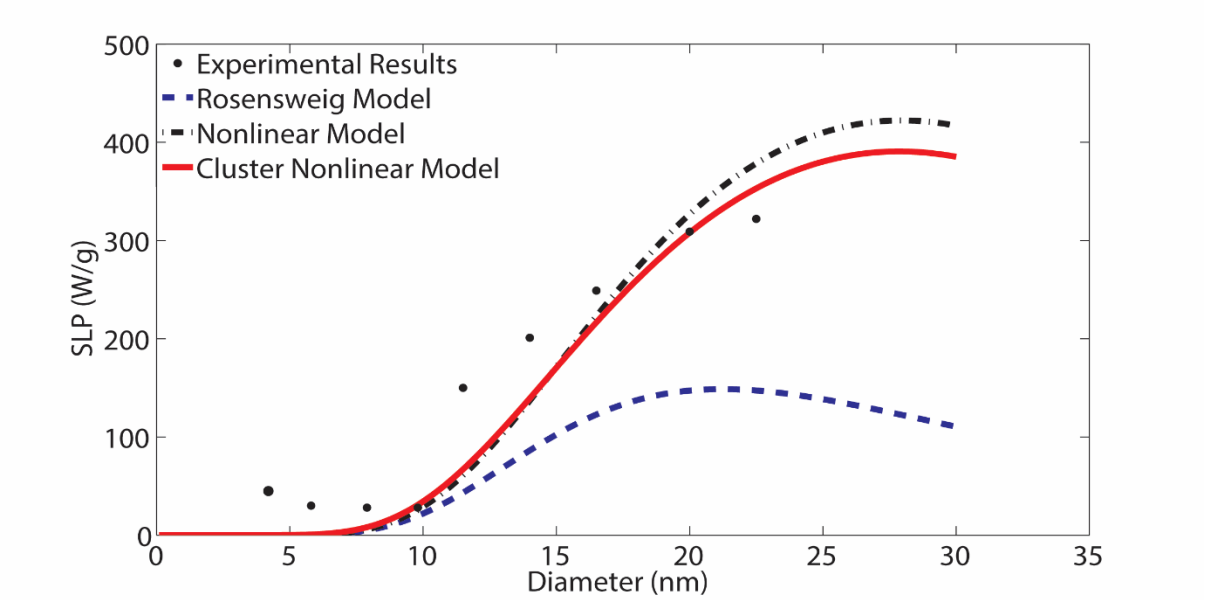


Figure 2. Theoretical SLP comparisons between the Rosenweig model (dashed blue curve), nonlinear model (dotted black curve) and the proposed nonlinear cluster-based model (solid red curve) for magnetite. The magnetic field frequency and amplitude were set to 110 *kHz* and 11.14 *kA/m*, separately, and the magnetic nanoparticle polydispersity (σ) was 0.3. Computational calculations of all models used the corresponding experimental parameters, and were then compared to experimental results, published by Jeun *et al.*[36] summarized in Table 2. Each experimental value was also used as a reference point to assess how each model approached the experimental result.

cluster magnetic anisotropy (K_{ac}), as described in equation 5b, and decreased both the domain magnetization (M_{dc}) and the average magnetic moment (m_c) of clusters due to the minimization of internal energy, as shown in equation 10. Particularly, the increase in cluster magnetic anisotropy is reflected in effective relaxation time constant by affecting the Neel relaxation time constant, as denoted by equation 4 and equation 3, while the decrease in both the cluster domain magnetization and average magnetic moment is reflected in the equilibrium magnetic

susceptibility, as shown in equation 8. The effect of the nonlinear response of the magnetic susceptibility and the aggregation was also illustrated in Figure 1B by plotting the imaginary part of the magnetic susceptibility as a function of the magnetic nanoparticle mean diameter, where the magnetic field amplitude was set to 11 kA/m and frequency to 410 kHz, as summarized in Methods Section Table 1. Similar to the result shown in Figure 1A, the nonlinear cluster-based model (solid red curve) yielded theoretical values smaller than that of the nonlinear model (dotted black curve), except that the Rosensweig model (dashed blue curve) also produced a theoretical prediction values larger than those of our proposed nonlinear cluster-based model. This difference results from the relatively weak magnetic field amplitude that was applied, making the effect of the nonlinear response of the magnetic susceptibility less significant. The nonlinear property, along with the effect of aggregation, contributed to the shift in the curve of the imaginary part of the magnetic susceptibility, resulting in the shifted theoretical SLP value, as derived by equation 12. Therefore, the theoretical SLP based on the equation 12 was plotted in Figure 1C as a function of the magnetic nanoparticle diameter using the same parameters as those in Figure 1B. The predicted SLP values reflect the variation in the imaginary part of the magnetic susceptibility, as these two parameters are linearly related, as shown in equation 11.

The analysis gets more complicated when it comes to the real experimental SLP estimation of different magnetic nanoparticles with different physical properties and under various magnetic field conditions with different nonlinear responses. By taking into account the nonlinear relationship between the magnetic susceptibility and magnetic field, and the formation of aggregate, we performed the prediction of SLP with experimental parameters,[36-39] as summarized in Methods Section Table 2 and Table 3. We saw how colloidal arrangement and magnetic field conditions induced a change to the imaginary part of the magnetic susceptibility,

which ultimately produced a different value for the heating efficiency of the colloidal suspension. The proposed theoretical model not only offers more accurate theoretical predictions of the SLP, but also provides a framework that allows us to design the nano-theranostic hyperthermia system and optimal magnetic nanoparticle setup for maximizing SLP.

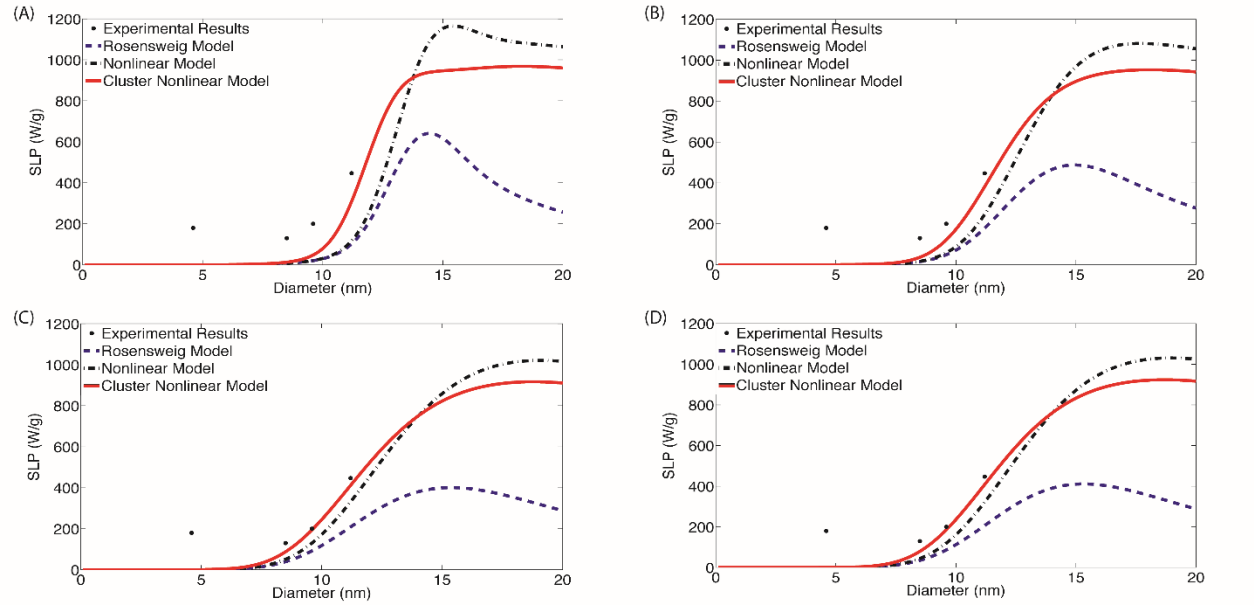


Figure 3. Theoretical SLP comparisons between the Rosenweig model (dashed blue curve), nonlinear model (dotted black curve), and the proposed nonlinear cluster-based model (solid red curve) for magnetite. Similar to the previous models, but the magnetic field frequency and amplitude were set to 400 *kHz* and 24.5 *kA/m*, respectively, and the magnetic nanoparticle polydispersity (σ) was (A) 0.075 (B) 0.15 (C) 0.22 (D)0.21. Computational calculations of all models used the corresponding experimental parameters, and were then compared to experimental results, published by Gonzales *et al.*[37] summarized in Table 2 (continued). Each experimental value was also used as a reference point to assess how each model approached the experimental result.

4.3.2 Experimental Comparisons

To gain a comprehensive understanding of the fundamental heating mechanism of magnetic nanoparticles, available experimental results[36-39] were compared to determine how well each model's prediction approached the experimental data as a function of the magnetic nanoparticle mean diameter. The first example involved magnetite exposed to an external magnetic field with an amplitude of 11.14 *kA/m* and a frequency of 110 *kHz*, as shown in Figure 2. When aggregate formation is ignored and only the linear regime of the complex magnetic susceptibility is taken into account, as in the Rosensweig model, theoretical predictions deviate significantly from the experimental SLP, described by the dashed blue curve. Alternatively, the nonlinear complex magnetic susceptibility without cluster consideration produced theoretical predictions much closer to available experimental results, as described by the dotted black curve. Adjusting this nonlinear model to account for aggregation, as depicted by the solid red curve, further improves the prediction accuracy for the SLP of the magnetite colloidal suspension.

The second example also involved also magnetite but was carried out by further increasing the magnetic field amplitude to 24.5 *kA/m* and the frequency to 400 *kHz*, as shown in Figure 3. Those four figures were different in their size distribution, as a larger polydispersity index σ induced lower maximum SLP values and a broader shape of the over curve. The results here demonstrated that, in the presence of a stronger magnetic field, larger magnetic nanoparticles possess a more complicated heat generation mechanism that is not restricted only to Neel and Brownian relaxation. Therefore, by using a nonlinear model with cluster consideration, the heating efficiency can be more accurately estimated as a nonlinear response elevates the overall values produced by larger magnetic nanoparticles.

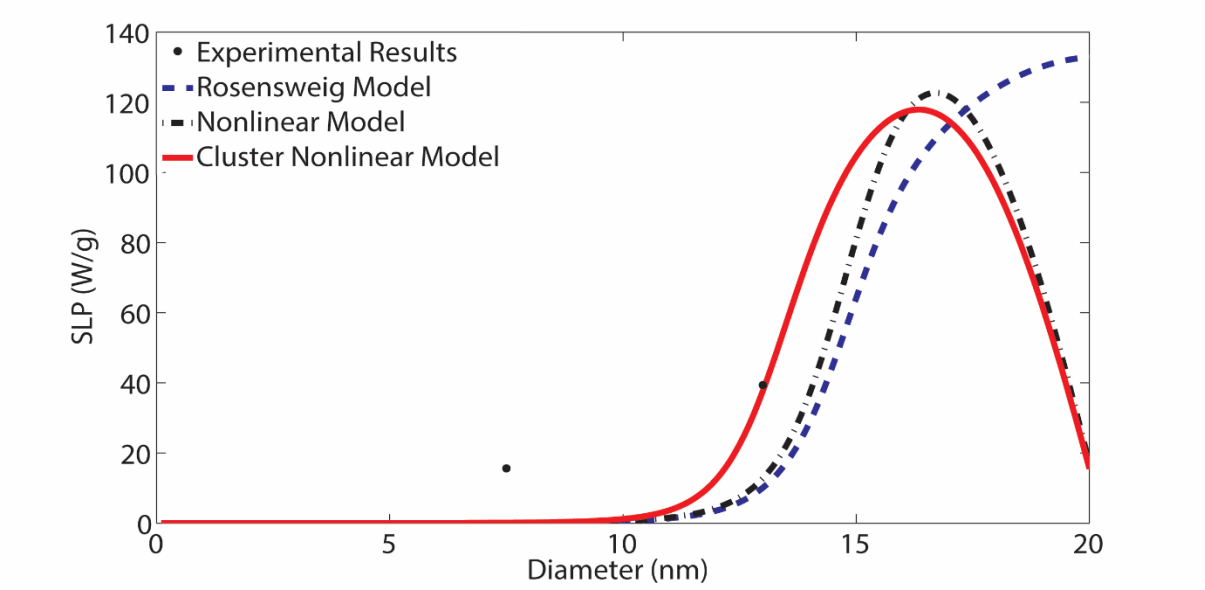


Figure 4. Additional theoretical SLP comparisons between the Rosenweig model (dashed blue curve), nonlinear model (dotted black curve), and the proposed nonlinear cluster-based model (solid red curve) for magnetite. The magnetic field frequency was set to 80 *kHz*, and amplitude 32.5 *kA/m*. Computational calculations of all models used the corresponding experimental parameters, and were then compared to experimental results, published by Ma *et al.*[38] summarized in Table 2 (continued). Each experimental value was also used as a reference point to assess how each model approached the experimental result.

A final example of magnetite was shown in Figure 4. Similar to the previous comparisons, the proposed cluster-based model comes closer to the experimental results than the original model. Accounting for aggregation in the suspension shifts the theoretical trend to the left and lowers the overall values, so that magnetic nanoparticles with a smaller diameter give an increased SLP prediction, as was demonstrated in the comparisons shown in the previous three figures. This shift in the predicted SLP relative to the nanoparticle size to SLP can be attributed to the increase in

cluster anisotropy property of the magnetic nanoparticle material and to the decrease in both average magnetic moment and domain magnetization, respectively.

While the differences in the heating efficiencies of the same magnetic nanoparticle magnetite in Figures 2, 3 and 4 are due largely to the magnetic field conditions, other factors such as the size distribution and surfactant coating thickness also influence the resulting prediction of SLP. Moreover, in the presence of the stronger magnetic field, as shown in Figure 4, the value of SLP starts to drop dramatically as a result of saturated magnetization. But with the consideration of the nonlinear property of the magnetic susceptibility and the formation of aggregate, our proposed model offers us a deeper and more comprehensive understanding of the heating mechanism and provides more accurate estimate of heating efficiency, even under various physical and magnetic field conditions.

When the single domain magnetic anisotropy constant is larger, as seen for cobalt ferrite in Figure 5, there is no significant shift to the left in the cluster-based nonlinear model depicted in this figure. As opposed to the magnetite colloidal solution, the larger magnetic anisotropy K_{ac} of the cobalt ferrite colloidal solution gives rise to a smaller SLP value for corresponding magnetic nanoparticle sizes and a lowered maximum SLP estimate.

In all four examples presented here, there remains some difference between our proposed nonlinear cluster-based prediction and experimental results, especially for the heating efficiency of magnetic nanoparticles with diameter less than 8nm. But for clinical purposes, the use of smaller magnetic nanoparticles is not recommended since they generate limited heating in the presence of a magnetic field and thus are not optimal for effective hyperthermia cancer treatment. As for magnetic nanoparticles where the mean diameter is larger than 8nm, the variance between theoretical calculation based on proposed new model and the experimental data

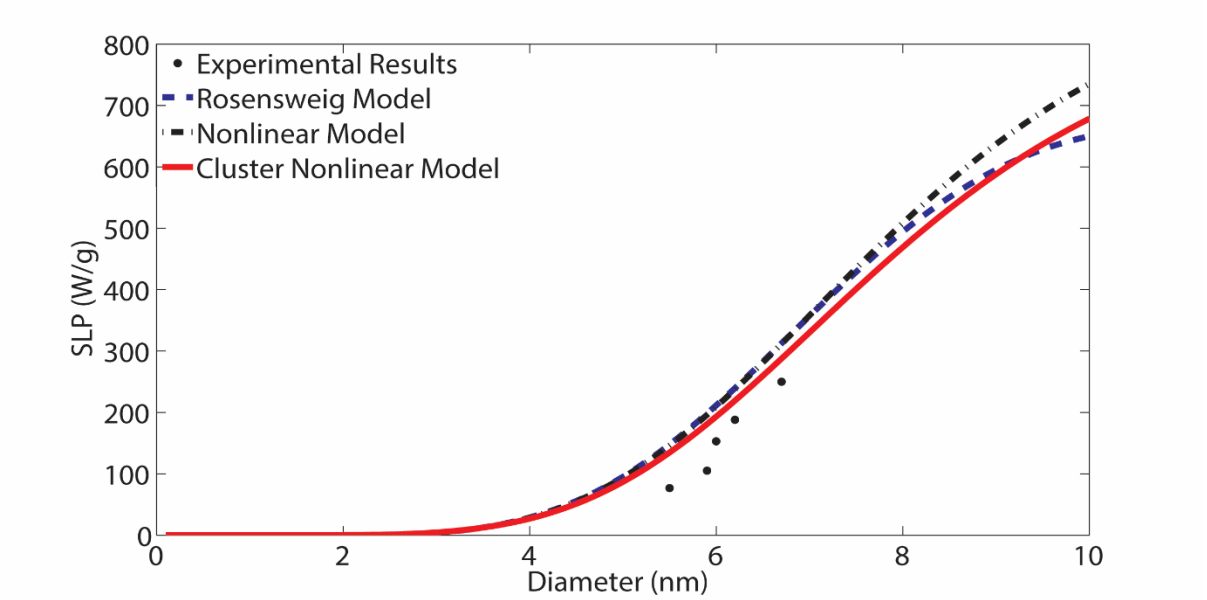


Figure 5. Theoretical SLP comparisons between the Rosenweig model (dashed blue curve), nonlinear model (dotted black curve), and the proposed nonlinear cluster-based model (solid red curve) for cobalt ferrite. The magnetic field frequency and amplitude were set to 167 kHz and 21 *kA/m*, respectively, and the magnetic nanoparticle polydispersity (σ) 0.23. Applying parameters published by Baldi *et al.,*[39] summarized in Table 3, experimental data was compared to all theoretical models. Each model was then shown to approach experimental values to analyze the prediction accuracy of SLP as a function of magnetic nanoparticles diameter.

is caused by the rough estimation of cluster magnetic anisotropy, domain magnetization, and the average magnetic moment. To further refine our model, factors such as how the orientation of the easy axis can influence the aggregation degree should be taken into consideration.[41]

The proposed theoretical model offers insights that can improve the design of nano-theranostic hyperthermia systems and the use of magnetic nanoparticles. We can conclude that, while the Rosensweig model works well for small magnetic nanoparticles, its predictions are less accurate for the larger nanoparticles that are the preferred candidate to use in a hyperthermia

system because of their optimal heating efficiency. Both the aggregate formation of magnetic nanoparticles and the nonlinear response of the magnetic susceptibility play an important role in the optimization of heating efficiency for large magnetic nanoparticles. Magnetic nanoparticles should be synthesized with a thick surface coating to avoid agglomeration, as the heating efficiency can be significantly reduced when aggregate forms. The nonlinear regime induces an additional heating effect; however, the saturated magnetization in the presence of a stronger magnetic field will have a negative impact on heating efficiency. The ideal design for the hyperthermia system would appear to involve placing magnetic nanoparticles with a size of around 15nm in a magnetic field with a moderate amplitude of around 25 kA/m.

In addition to its contribution to improving the clinical effectiveness of in vivo nano-theranostic hyperthermia, application of the proposed model can also benefit the design of time-release drugs. For most clinical uses, magnetic nanoparticles are encapsulated in a liposome and are highly accumulated at the targeted lesion. The proposed model can offer a more accurate estimate of heating efficiency, taking into consideration the use of aggregate to control the release of the drug over time. With advances in emerging theranostics, this work can provide a framework for the design and use of magnetic nanoparticles in new cancer treatments.

4.4 Conclusion

The utilization of biocompatible, nontoxic magnetic nanoparticles makes the in vivo nano-theranostic hyperthermia the best candidate for an integrated nanotherapeutic system, where the injected magnetic nanoparticles enable the diagnosis and treatment of cancer to be performed in a single setting using the combinational strategies of targeting, imaging, and thermotherapy. The proposed nonlinear cluster-based model closely tracks experimental results

of SLP as a function of mean magnetic nanoparticle size and presents us with a more comprehensive understanding of the heating mechanism. With the consideration of aggregate formation and the nonlinear response of magnetic susceptibility, this model can help us design a greatly improved in vivo nano-theranostic hyperthermia system and is able to calculate the SLP of larger magnetic nanoparticles and in the presence of stronger magnetic fields, as shown in Figures 2-5. For in vivo nano-theranostic hyperthermia, accurate predictions for magnetic nanoparticles in the presence of strong magnetic field are particularly useful, as larger magnetic field can negatively affect the heating efficiency due to the magnetization saturation. The ideal design for the nano-theranostic hyperthermia system would appears to involve placing magnetic nanoparticles with a diameter of 15nm in a magnetic field with a moderate amplitude of around 25 *kA/m*.

4.5 References

[1] Zhou, H.; Qian, W.; Uckun, F. M.; Wang, L.; Wang, Y. A.; Chen, H.; Kooby, D.; Yu, Q.; Lipowska, M.; Staley, C. A.; Mao, H.; Yang, L. IGF1 Receptor Targeted Theranostic Nanoparticles for Targeted and Image- Guided Therapy of Pancreatic Cancer. *ACS Nano*. **2015**, *9*, 7976-7991.

[2] Sanson, C.; Diou, O.; The venot, J.; Ibarboure, E.; Soum, A.; Bru^let, A.; Miraux, S.; Thiaudie re, E.; Tan, S.; Brisson, A.; Dupuis, V.; Sandre, O.; Lecommandoux, S. Doxorubicin Loaded Magnetic Polymersomes: Theranostic Nanocarriers for MR Imaging and Magneto-Chemotherapy. *ACS Nano*. **2011**, *5*, 1122-1140.

[3] Fazal, S.; Paul-Prasanth, B.; Nair, S. V.; Menon, D. Theranostic Iron Oxide/Gold Ion Nanoprobes for MR Imaging and Noninvasive RF Hyperthermia. *ACS Appl. Mater. Interfaces.* **2017**, *9*, 28260-28272.

[4] Ho, D.; Sun, X.; Sun, S. Monodisperse Magnetic Nanoparticles for Theranostic Applications. *Acc. Chem. Res*. **2011**, *44*, 875-882.

[5] Yoo, D.; Lee, J.; Shin, T.; Cheon, J. Theranostic Magnetic Nanoparticles. *Acc. Chem. Res*. **2011**, *44*, 863-874.

[6] Béalle, G.; Di Corato, R.; Kolosnjaj-Tabi, J.; Dupuis, V.; Clement, O.; Gazeau, F.; Wilhelm, C.; Ménager, C. Ultra Magnetic Liposomes for MR Imaging, Targeting, and Hyperthermia. *Langmuir.* **2012**, *28*, 11834-11842.

[7] Jordan, A.; Wust, P.; Fähling, H.; John, W.; Hinz, A.; Felix, R. Inductive Heating of Ferrimagnetic Particles and Magnetic Fluids: Physical Evaluation of Their Potential for Hyperthermia. *Int. J. Hyperthermia*. **1993**, *9*, 51–68.

[8] Jordan, A.; Wust, P.; Scholz, R.; Tesche, B.; Fähling, H.; Mitrovics, T.; Vogl, T.; Cervós-Avarro, J.; Felix, R. Cellular Uptake of Magnetic Fluid Particles and Their Effects on Human Adenocarcinoma Cells Exposed to AC Magnetic Fields In Vitro. *Int. J. Hyperthermia*. **1996**, *12*, 705–722.

[9] Rosensweig, R. E. Heating Magnetic Fluid with Alternating Magnetic Field. *J. Magn. Magn. Mater*. **2002**, *252*, 370–374.

[10] Hergt, R.; Dutz, S.; Röder, M. Effects of Size Distribution on Hysteresis Losses of Magnetic Nanoparticles for Hyperthermia. *J. Phys.: Condens. Matter*. **2008**, *20*, 385214.

[11] Li, Z.; Kawashita, M.; Araki, N.; Mistumori, M.; Hiraoka, M. Effects of Particle Size of Magnetite Nanoparticles on Heat Generating Ability Under Alternating Magnetic Field. *Bioceram. Dev. Appl.* **2011**, *1*, D110128.

[12] Khandhar, A. P.; Ferguson, R. M.; Simon, J. A.; Krishnan, K. M. Enhancing Cancer Therapeutics Using Size-Optimized Magnetic Fluid Hyperthermia. *J. Appl. Phys*. **2012**, *111*, 07B306.

[13] Hergt, R.; Dutz, S.; Müller, R.; Zeizberger, M. Magnetic Particle Hyperthermia: Nanoparticle Magnetism and Materials Development for Cancer Therapy. *J. Phys.: Condens. Matter*. **2006**, *18*, 2919–2934.

[14] Kuhn, L. T.; Bojesen, A.; Timmermann, L.; Fauth, K.; Goering, E.; Johnson, E.; Nielson, M. M.; Morup, S. Core-Shell Iron–Iron Oxide Nanoparticles: Magnetic Properties and Interactions. *J. Magn. Magn. Mater*. **2004**, *272–276*, 1485–1486.

[15] Ganguly, R.; Zellmer, B.; Puri, I. K. Field-Induced Self-Assembled Ferrofluid Aggregation in Pulsatile Flow. *Phys. Fluids*. **2005**, *17*, 097104.

[16] Castro, L. L.; da Silva, M. F.; Bakuzis, A. F.; Miotto, R. Aggregate Formation on Polydisperse Ferrofluids: A Monte Carlo Analysis. *J. Magn. Magn. Mater*. **2005**, *293*, 553–558.

[17] Wang, C.; Li, Z.; Lin, Y. Y. Optimizing Magnetic Nanoparticles Hyperthermia Effect in MR Nanomedicine. *Chinese Journal of Magnetic Resonance*. **2015**, *32*, 248-260

[18] De´jardin, J. L. Fractional Dynamics and Nonlinear Harmonic Responses in Dielectric Relaxation of Disordered Liquids. *Phys. Rev*. **2003**, *68*, 031108.

[19] Giannitsis, A. T.; Fannin, P. C.; Charles, S. W. Nonlinear Effects in Magnetic Fluids. *J. Magn. Magn. Mater*. **2005**, *289*, 165–167.

[20] Fannin, P. C.; Oireachtaigh, C. M. Investigating the Isotropic Properties of a Magnetic Fluid Following the Removal of a Polarising Field. *J. Magn. Magn. Mater*. **2007**, *316*, e802–e804.

[21] Singh, V.; Banerjee, V.; Sharma, M. Dynamics of Magnetic Nanoparticle Suspensions. *J. Phys. D.: Appl. Phys*. **2009**, *42*, 245006.

[22] Cabrera, D.; Coene, A.; Leliaert, J.; Artes-lbanez, E. J.; Dupre, L.; Telling, N. D.; Teran, F. J. Dynamical Magnetic Response of Iron Oxide Nanoparticles Inside Live Cells. *ACS Nano*. **2018**, *12*, 2741-2752.

[23] Rodrigues, H. F.; Capistrano, G.; Mello, F. M. Zufelato, N.; Silveira-Lacerda, E. Bakuzis, A. F. Precise Determination of the Heat Delivery During *In Vivo* Magnetic Nanoparticle Hyperthermia with Infrared Thermography. *Phys. Med. Biol.* **2017**, *62*, 4062-4082.

[24] Mamiya, H. Recent Advances in Understanding Magnetic Nanoparticles in AC Magnetic Fields and Optimal Design for Targeted Hyperthermia. *J. Nanomater*. **2013**, 752973.

[25] Reeves, D. B.; Weaver, J. B. Nonlinear Simulations to Optimize Magnetic Nanoparticle Hyperthermia. *Appl. Phys. Lett*. **2014**, *104*, 102403.

[26] Carriao, M. S.; Aquino, V. R. R.; Landi, G. T.; Verde, E. L.; Sousa, M. H.; Bakuzis, A. F. Giant-Spin Nonlinear Response Theory of Magnetic Nanoparticle Hyperthermia: A Field Dependence Study. *J. Appl. Phys*. **2017**, *121*, 173901.

[27] Verde, E. L.; Landi, G. T.; Carrião, M. S.; Drummond, A. L; Gomes, J. A.; Vieira, E. D.; Sousa, M. H.; Bakuzis, A. F. Field Dependent Transition to the Non-Linear Regime in Magnetic Hyperthermia Experiments: Comparison Between Maghemite, Copper, Zinc, Nickel, and Cobalt Ferrite Nanoparticles of Similar Sizes. *AIP Adv*. **2012**, *2*, 032120.

[28] Branquinho, L. C.; Carriao, M. S.; Costa, A. S.; Zufelato, N. Sousa, M. H.; Miotto, R.; Ivkov, R.; Bakuzis, A. F. Effect of Magnetic Dipolar Interactions on Nanoparticle Heating

Efficiency: Implications for Cancer Hyperthermia. *Sci. Rep*. **2013**, *3*, 2887.

[29] Saville, S. L.; Qi, B.; Baker, J.; Stone, R.; Camley, R. E.; Livesey, K. L.; Ye, L.; Crawford, T. M.; Mefford, O. T. The Formation of Linear Aggregates in Magnetic Hyperthermia: Implications on Specific Absorption Rate and Magnetic Anisotropy. *J. Colloid Interface Sci.* **2014**, *424*, 141–151.

[30] Reeves, D. B.; Weaver, J. B. Approaches for Modeling Magnetic Nanoparticle Dynamics. *Crit. Rev. Biomed. Eng.* **2014**, *42*, 85–93.

[31] Guibert, C.; Dupuis, V; Peyre, V.; Fresnais, J. Hyperthermia of Magnetic Nanoparticles: Experimental Study of the Role of Aggregation. *J. Phys. Chem. C.* **2015**, *119*, 28148–28154.

[32] Wang, X.; Gu, H.; Yang, Z. The Heating Effect of Magnetic Fluids in an Alternating Magnetic Field. *J. Magn. Magn. Mater.* **2005**, *293*, 334–340.

[33] Coral, D. F.; Zelis, P. M.; Marciello, M.; Morales, M. P.; Craievich, A.; Sanchez, F. H.; Fernandez van Raap, M. B. Effect of Nanoclustering and Dipolar Interactions in Heat Generation for Magnetic Hyperthermia. *Langmuir*. **2016**, *32*, 1201–1213.

[34] Oireachtaigh, C. M.; Fannin, P. C. Investigation of the Non-Linear Loss Properties of Magnetic Fluids Subject to Large Alternating Ffields. *J. Magn. Magn. Mater*. **2008**, *320*, 871–880.

[35] Coffey, W. T.; Paranjape. B. V. Dielectric and Kerr Effect Relaxation in Alternating Electric Fields. *Proc. Roy. Irish Acad*. **1978**, *78*, 17–25.

[36] Jeun, M.; Lee, S.; Kang, J. K.; Tomitaka. A.; Kang, K. W.; Kim, Y. I.; Takemura, Y.; Chung, K. W.; Kwak, J.; Bae, S. Physical limits of Pure Superparamagnetic Fe3O4 Nanoparticles for a Local Hyperthermia Agent in Nanomedicine. *Appl. Phys. Lett*. **2012**, *100*, 092406.

[37] Gonzales, M.; Mitsumori, L. M.; Kushleika, J. V.; Rosenfeld, M. E.; Krishnan, K. M. Cytotoxicity of Iron Oxide Nanoparticles Made from the Thermal Decomposition of Organometallics and Aqueous Phase Transfer with Pluronic F127. *Contrast Media Mol Imaging*. **2010**, *5*, 286–293.

[38] Ma, M.; Wu, Y.; Zhou, J.; Sun, Y.; Zhang, Y.; Gu, N. Size Dependence of Specific Power Absorption of Fe3O4 Particles in AC Magnetic Field. *J. Magn. Magn. Mater*. **2004**, *268*, 33–39.

[39] Baldi, G.; Lorenzi, G.; Ravagli, C. Hyperthermic Effect of Magnetic Nanoparticles under Electromagnetic Field. *PAC*. **2009**, *3*, 103–109.

[40] Wang, C.; Hsu, C. H.; Li, Z.; Hwang, L. P.; Lin, Y. C.; Chou, P. T.; Lin, Y. Y. Effective Heating of Magnetic Nanoparticle Aggregates for In Vivo Nano-theranostic Hyperthermia. *Int. J. Nanomedicine*. **2017**, *12*, 6273–6287.

[41] Deissler, R. J; Wu, Y.; Martens, M. A. Dependence of Brownian and Néel relaxation times on magnetic field strength. *Med. Phys.* **2014**, *41*, 012301.

[42] Morais, P. C.; Gonçalves, G. R. R.; Bakuzis, A. F.; Neto, K. S.; Pelegrini, F. Experimental Evidence of Dimer Disruption in ionic Ferrofluid: A Ferromagnetic Resonance Investigation. *J. Magn. Magn. Mater*. **2001**, *225*, 84–88.

[43] Zhong, J.; Xiang, Q.; Massa, L. O.; Qu, F.; Morais, P. C.; Liu, W. Second-Order-Like Cluster-Monomer Transition within Magnetic Fluids and Its Impact upon the Magnetic Susceptibility. *Nanoscale Res. Lett*. **2012**, *7*, 167.

[44] Debye, P. Polar Molecules. *The Chemical Catalog Co*. Dover: New York, **1929**.

[45] Néel, L. Theorie du Trainage Magnetique des Ferromagnetiques en Grains Fins avec Applications aux Terres Cuites. *Geophysics*. **1949**, *5*, 99–136.

[46] Mehdaoui, B.; Tan, R. P.; Meffre, A.; Carrey, J.; Lachaize, S.; Chaudret, B.; Respaud, M. Increase of Magnetic Hyperthermia Efficiency Due to Dipolar Interactions in Low-Anisotropy Magnetic Nanoparticles: Theoretical and Experimental Results. *Phys. Rev. B*. **2013**, *87*, 174419.

Chapter 5

Optimizing the Heating Efficiency of Magnetic Nanoparticles for *In Vivo* MR Nano-Theranostic Hyperthermia

5.0 Abstract

In Vivo MR nano-theranostic hyperthermia has been widely investigated for its potential to simultaneously diagnose and treat cancer. However, the promising possibilities of this pre-clinical or clinical application can only be realized if the physical and magnetic properties of the injected nanoparticles are precisely controlled to optimize their heating efficiency, which is critical to focusing the energy onto tumor cells and minimizing damage to healthy tissue. For this purpose, we have proposed a novel model to evaluate and optimize the heating efficiency, based on three major findings: (i) magnetic nanoparticles are interacting in the colloidal suspension, (ii) the magnetic susceptibility and the magnetic field amplitude are nonlinearly related, and (iii) relaxation times due to the Brownian or Néel relaxation mechanisms depend on the amplitude of the applied magnetic field. In order to assess the accuracy of our *in vivo* theoretical model's consideration of nanoparticle aggregation, the nonlinear response of the magnetic susceptibility, and the magnetic field effects on relaxation processes, predictions made by our model for previously published experimental data were compared to predictions made by the currently prevailing models. The strong correlation between the experimental data and our model's predictions validated the importance of the three findings in understanding the heating mechanism and accurately evaluating the heating efficiency as a function of mean magnetic nanoparticle size, even when large magnetic nanoparticles are in the presence of relatively strong

magnetic fields. In the clinical application of *in vivo* MR nano-theranostic hyperthermia, the proposed model offers a paradigm for designing magnetic nanoparticles and pulsing the hyperthermia in the MR environment to optimize their heating efficiency.

5.1 Introduction

In the last decade, ferro-magnetic nanoparticles have gained attention in biomedical nano-theranostic applications due to their nontoxicity, biocompatibility, injectability, and capacity for high-level accumulation in the target tissue. These unique properties allow for magnetic nanoparticles to simultaneously serve as imaging probes that locate cancerous lesions and as drug delivery vehicles that carry therapeutic agents preferentially to those lesions. The recent investigative trend of using magnetic nanoparticles in cancer treatment has also turned toward concurrent therapy, giving rise to the distinction of magnetic nanoparticle hyperthermia as a promising, minimally invasive tool for treating small and deep-seated tumors.[1-6]

Magnetic nanoparticle hyperthermia is enabled by the application of an alternating magnetic field to the magnetic colloidal suspension.[7-8] In order to develop an effective cancer detection and treatment protocol, the heating efficiency or specific loss power (SLP) of magnetic nanoparticles must be properly understood, as it is essential to determining what is the clinically appropriate amplitude and frequency for the applied magnetic field. In recent years, factors that affect SLP, including the amplitude and frequency of the applied alternating magnetic field, and the structural and magnetic properties of magnetic nanoparticles, have been extensively investigated.[9-12] These studies, which were based on the prevailing Rosensweig model,[13] provided us with a rudimentary approach to revealing the heating mechanism and calculating

SLP but were not sufficiently accurate in evaluating the experimental results, making it difficult to determine the optimal nanoparticle design and magnetic conditions.[14]

In the prevailing Rosensweig Model,[13] magnetic nanoparticles were assumed to be non-interacting single units dispersed in the suspension, and the heat generation mechanism was based on the linear response theory. But in fact, magnetic nanoparticles aggregate together because of the contribution of several interactions among particles.[15-18] Moreover, magnetic susceptibility and magnetic field amplitude are nonlinearly related. As the particle size and magnetic field amplitude increase, the heat-generation mechanism becomes more complicated as loss process and heating effects are introduced by the nonlinear response of the magnetic susceptibility.[19-22] In addition, relaxation time constants due to Brownian or Néel relaxation mechanisms depend on the amplitude of the applied magnetic field.[23] The currently accepted zero-field relaxation time calculations can underestimate the actual relaxation times and, in particular, can underestimate the Néel relaxation time by many orders of magnitude, as it is more sensitive to the magnetic field amplitude than the Brownian relaxation time.

Much work has been carried out to demonstrate the importance of examining those factors that contribute to the complexity of evaluating the heating efficiency,[17-18,24-27] including nanoparticle aggregation and magnetic field amplitude effects. Less effort has been devoted to predicting SLP by taking this complexity into account. A few groups have proposed theoretical models to evaluate SLP that either discard the linear response regime or account for the aggregation formation,[28-29] but no group has considered the effect of the magnetic field amplitude on the relaxation mechanism when evaluating the heating efficiency. For example, Branquinho *et al*[30] showed that high particle concentrations correlated with an increasing chain length produced decreasing SLP, and a theoretical model describing dipole interactions valid for

the linear response regime was proposed to explain the observed trends. Fernandez van Raap *et al*[31] revised the relaxation time constant using a representative mean activation energy derived from four independent experiments to accurately reproduce experimental heating efficiencies, but the conditions have to be within the framework of the linear response theory. Accounting for the nonlinear heat generation mechanism,[20,24] which is based on the equation for the electric susceptibility as proposed by Coffey and Paranjape,[32] will result in a theoretical SLP closer to the experimental results, while a failure to model the formation of aggregate gives rise to an overestimated heating efficiency.

In the interest of optimizing the heating efficiency of magnetic nanoparticles for *in vivo* MR nano-theranostic hyperthermia, we proposed a novel model by accounting for the formation of aggregate, the nonlinear response of the magnetic susceptibility, and the alternating magnetic field-based relaxation mechanism. For the aggregate, the concept of critical temperature,[28,33-34] defined as the temperature at which magnetic nanoparticle aggregates completely dissociate into individual units, was introduced to characterize the fraction of monomeric and clustered magnetic nanoparticles in the ferrofluid. For the nonlinear response theory, the high-field magnetic susceptibility was calculated in order to represent the complex heating mechanism.[20,24,32] As for the magnetic-field effect, instead of using the zero-field relaxation time constants, eigenvalues derived from the Fokker–Planck equation were calculated as a reference of the time-varying field relaxation time constants for a range of parameter values.[23] To assess the accuracy of this model, calculations used for our proposed theoretical model were compared to experimental data and previously published results.[35-37] Not only do we aim to lay the groundwork for evaluating the heating efficiency of magnetically induced nano-theranostic hyperthermia, we also seek to design a model for future clinical applications of nano-theranostic

hyperthermia in cancer therapy that describes the temperature-dependent function of nanoparticle size in heat generation.

5.2 Materials and Methods

5.2.1 Power Dissipation

We began with an ensemble of spherical single-domain non-interacting magnetic nanoparticles. In the presence of an alternating magnetic field, the magnetization, $M(t)$, lags the magnetic field, $H(t)$. Therefore, in the framework of linear response theory, $M(t) = \chi H(t)$, the magnetic susceptibility is conveniently denoted as a complex number, $\chi = \chi' + i\chi''$, with the following expressions for both the real part (χ') and the imaginary part (χ''):

$$\chi' = \frac{\chi_0(T)}{1+(\omega\tau_{eff})^2} \tag{1a}$$

$$\chi'' = \frac{\omega\tau_{eff}\chi_0(T)}{1+(\omega\tau_{eff})^2} \tag{1b}$$

Where $\chi_0(T)$ is the equilibrium magnetic susceptibility, $\omega = 2\pi f$ is the angular frequency, τ_{eff} is the effective relaxation time constant, and χ'' is the loss component of magnetic susceptibility.

The internal energy of a magnetic nanoparticles suspension in an adiabatic process is equal to the magnetic work done on it:[13]

$$\Delta U = -\mu_0 \oint M(t)\,\mathrm{d}\,H = -\mu_0 \int_0^{2\pi/\omega} \mathrm{Re}\left[\chi H_0 \mathrm{e}^{-\mathrm{i}\omega t}\right] \mathrm{d}H = \pi\mu_0 H_0^2 \chi'' \tag{2}$$

The power dissipation in the ferrofluid system, during a complete magnetic field cycle, is equal to the internal energy divided by the time. Thus, the power dissipation, during several cycles, is equal to the internal energy multiplied by the frequency:

$$P = f\Delta U \tag{3}$$

The heating efficiency, which is represented by the specific loss power (SLP), is given by:

$$SLP = \frac{P}{\rho\phi} = \frac{\pi\mu_0\chi'' f H_0^2}{\rho\phi} \quad (4)$$

where ρ is the mass per unit volume of particles, ϕ is the volume fraction of particles, and μ_0 is the magnetic permeability in free space. In the presence of a specific magnetic field with the frequency, f, and the strength, H_0, the optimization of the heating efficiency of the magnetic fluid system can be achieved by maximizing the imaginary part of the dynamic susceptibility, χ'', where χ'', as indicated by equation 1b, can be altered through the relaxation processes, aggregation, and nonlinear property.

5.2.2 Relaxation Processes

The conventional zero-field Brownian (τ_B) and Néel (τ_N) relaxation time constants are expressed as,[38-39]

$$\tau_B = \frac{3\eta V_H}{k_B T} \quad (5a)$$

$$\tau_N = \frac{\sqrt{\pi}\beta(1+\alpha'^2)M_s}{4\gamma\alpha'(\beta K_a)^{3/2}} e^{\beta K_a} \quad (5b)$$

where η is the viscosity of the carrier fluid, k_B is the Boltzmann constant, T is the absolute temperature (K), and $V_H = (1 + \delta/R)^3 V_M$ is the hydrodynamic volume of the particle, where δ is the thickness of a surfactant layer, $V_M = 4\pi R^3/3$, is the magnetic volume of a particle with radius R. $\beta = V_M/k_B T$, α' is the damping constant, M_s is the saturated magnetization, and K_a is the anisotropy constant which may depend on the shape and size of nanoparticles.

The use of conventional zero-field relaxation times is problematic because both the Brownian (Debye) and the Néel relaxation mechanisms depend on the magnetic field, and the Néel relaxation time is particularly sensitive to changes in the magnetic field amplitude.[23] For

this reason, the Fokker-Planck equation for Brownian and Néel Relaxation was used to derive more realistic relaxation time constants.[40] To accelerate the calculation speed, the eigenvalues of the diagonal matrix for the Brownian relaxation (tridiagonal matrix in equation 6a) and Néel relaxation (pentadiagonal matrix in equation 6b) were calculated using the standard recursion relations for Legendre polynomials,[23]

$$A_{n,n} = -\frac{n(n+1)}{2}\ n = 1, 2, 3, \dots, N,$$

$$A_{n,n+1} = -\frac{n(n+1)}{2(2n+3)}\alpha\ n = 1, 2, 3, \dots, N-1,$$

$$A_{n,n-1} = \frac{n(n+1)}{2(2n-1)}\alpha\ n = 2, 3, 4, \dots, N, \tag{6a}$$

$$A_{n,n} = \frac{n(n+1)}{2}\ n = 1, 2, 3, \dots, N,$$

$$A_{n,n+1} = -\frac{n(n+1)}{2(2n+3)}\alpha\ n = 1, 2, 3, \dots, N-1,$$

$$A_{n,n-1} = \frac{n(n+1)}{2(2n-1)}\alpha\ n = 2, 3, 4, \dots, N,$$

$$A_{n,n+2} = -\frac{n(n+1)(n+2)}{2(2n+3)(2n+5)}\alpha_K\ n = 1, 2, 3, \dots, N-2,$$

$$A_{n,n-2} = \frac{n(n+1)(n-1)}{2(2n-1)(2n-3)}\alpha_K\ n = 3, 4, 5, \dots, N, \tag{6b}$$

with $\alpha(t) \equiv \frac{m_0}{k_B T} B(t)$ and $\alpha_K \equiv \frac{2K_a V_M}{k_B T}$, where $m_0 = M_s V_M$ is the magnetic dipole moment with the saturated magnetization M_s.

Then the largest real part, λ^{max}, of the calculated eigenvalues of A were used to describe the Brownian relaxation time constant (equation 7a) and the Néel relaxation time constant (equation 7b):

$$\tau_B = -\frac{\tau_{B0}}{Re(\lambda_B^{max})} \tag{7a}$$

$$\tau_N = -\frac{\tau_{N0}}{Re(\lambda_N^{max})} \tag{7b}$$

with $\tau_{B0} \equiv \frac{3\eta V_H}{k_B T}$ and $\tau_{N0} \equiv \frac{\beta(1+\alpha'^2)M_s}{2\gamma\alpha'}$, where γ is the electron gyromagnetic ratio.

Instead of treating the two mechanisms in the traditional way, where both act simultaneously, the calculated values of equation 7a for the Brownian relaxation time constant and equation 7b for the Néel relaxation time constant were compared with the consideration of the magnetic field amplitude and magnetic nanoparticle size to determine the dominant relaxation mechanism as well as the effective relaxation time constant, τ_{eff}.

5.2.3 Aggregation

The disruption of magnetic nanoparticle clusters follows a second-order phase transition at the critical temperature.[33] Therefore, the fraction of clusters (P_c) in the ferrofluid was chosen as an order parameter to describe this thermal-assisted cluster disruption in terms of the critical temperature, T^*, and the suspension temperature, T:[28,34]

$$P_c = (1 - \frac{T}{T^*})^{\frac{1}{2}} \tag{8a}$$

From the expression of P_c, it can be concluded that when the temperature is much lower than the critical temperature, $T \ll T^*$, magnetic nanoparticle monomers and clusters coexist in the ferrofluid system, and there are no clusters when the temperature is at or above the critical temperature. Consequently, the fraction of monomers (P_m) in the ferrofluid can be simply treated as proportional to the temperature:

$$P_m = \frac{T}{T^*} \tag{8b}$$

Notice that $P_m + P_c = 1$ when it is at two limiting conditions: $T \ll T^*$ and $T \geq T^*$.

By accounting for the formation of aggregate, the equilibrium magnetic susceptibility of ferrofluid, which is a function of the temperature, $\chi_0(T)$, can be written as:[28]

$$\chi_0(T) = \frac{\phi}{H_0}\left[M_{dm}\left(\frac{T}{T^*}\right)L\left(\frac{\mu_0\overline{m_m}H_0}{k_B T}\right) + M_{dc}(1 - \frac{T}{T^*})^{\frac{1}{2}}\, L(\frac{\mu_0\overline{m_c}H_0}{k_B T})\right] \tag{9}$$

where ϕ is the volume fraction of the magnetic nanoparticles, H_0 is the amplitude of the applied alternating magnetic field, M_{dm} and M_{dc} are the domain magnetization of monomers and clusters, respectively, $\overline{m_m}$ and $\overline{m_c}$ are the average magnetic dipole moment of monomers and clusters, respectively, and L is the Langevin function with formula $L(x) = \coth(x) - 1/x$. In classical assumptions, the Langevin function describes the dependency of the magnetization on the applied magnetic field.

5.2.4 Nonlinear Response

Equation 9 describes only the linear contribution of the equilibrium magnetic susceptibility in the presence of weak alternating magnetic field, as characterized by Curie's Law. When a strong bias magnetic field is superimposed onto the weaker alternating magnetic field, the relationship between the magnetic susceptibility and the magnetic field is no longer linear. In addition, applying a stronger alternating magnetic field will further induce a nonlinear response from the magnetic susceptibility.[20-21,29] Based on the equation for the electric susceptibility as proposed by Coffey and Paranjape,[32] the real part and the imaginary part of the complex magnetic susceptibility can be written as

$$\chi'(\omega, H_0) = \frac{\chi_0(T)}{1+(\omega\tau_{eff})^2}\{1 - \left(\frac{m_0 H_0}{k_B T}\right)^2 \frac{27-13(\omega\tau_{eff})^2}{60\left[1+(\omega\tau_{eff})^2\right]\left[9+4(\omega\tau_{eff})^2\right]}\} \quad (10a)$$

$$\chi''(\omega, H_0) = \frac{\chi_0(T)\omega\tau_{eff}}{1+(\omega\tau_{eff})^2}\{1 - \left(\frac{m_0 H_0}{k_B T}\right)^2 \frac{21+(\omega\tau_{eff})^2}{30\left[1+(\omega\tau_{eff})^2\right]\left[9+4(\omega\tau_{eff})^2\right]}\} \quad (10b)$$

As shown in equation 10, the first term in both equations represents the linear property of the magnetic susceptibility, while the remaining terms in both equations represent the nonlinear response of the magnetic susceptibility.

By taking into consideration the magnetic field effect, aggregation, and nonlinear response of the magnetic susceptibility, the SLP for the colloidal magnetic nanoparticles suspension can be calculated by substituting equations 9 and 10b into equation 4:

$$SLP = \frac{\mu_0 \tau H_0 \omega^2}{2\rho[1+(\omega\tau)^2]}\left\{1 - \left(\frac{\overline{m_m} H_0}{k_B T}\right)^2 \frac{21+(\omega\tau)^2}{30[1+(\omega\tau)^2][9+4(\omega\tau)^2]}\right\} \times \left[M_{dm}\left(\frac{T}{T^*}\right) L\left(\frac{\mu_0 \overline{m_m} H_0}{k_B T}\right) + M_{dc}\left(1 - \frac{T}{T^*}\right)^{\frac{1}{2}} L\left(\frac{\mu_0 \overline{m_c} H_0}{k_B T}\right)\right] \quad (11)$$

5.2.5 Computational Parameters

To determine the feasibility and accuracy of our proposed model, predicted SLP values based on this model and the Rosensweig model[13] were compared with experimental results previously reported,[35-37] which were summarized in Table 1 for magnetite Fe_3O_4 magnetic nanoparticles.

Table 1. Computational parameters and experimental results used in the theoretical calculation of relaxation time constants and the heating efficiency (SLP) for magnetite Fe_3O_4 magnetic nanoparticles to determine the accuracy of the proposed mode, as shown in all figures.

Magnetic nanoparticle		Magnetite Fe_3O_4									
Magnetic anisotropy constant, K_a (kJ/m^3)		20	10			21				16	
Domain magnetization of monomers, M_{dm} (kA/m)		474	446								
Viscosity of the carrier fluid, η (kg m^{-1} s^{-1})		0.001 (water)	0.000545			0.0007					
Electron Gyromagnetic Ratio, γ (rad/s T)		1.75×10^{11}									
Damping Constant, α'		0.1									
Temperature, T (K)		300									
Critical temperature, T^* (K)		358									
Alternating magnetic field	Amplitude, H_0(kA/m)	0-150	7			21				30	
	Frequency, f (kHz)	167	63			168				210	
Magnetic nanoparticle size	Mean Diameter (nm)	0-20	6	8	10	4.1	6.7	10.9	16.0	10.9	15.2
	Polydispersity, σ	-	0.35			-				0.37	0.51
Specific loss power, SLP (W/g)	Experiment	-	50	78	123	0	3	32	61	216	702
	Rosensweig model	-	3.66	28.1	97.6	0.02	0.08	1.87	113	1248	1710
	Proposed model	-	4.10	35.7	123	0	0	1.83	59.0	689	863
Reference			Wang *et al*[35]			Lartigue *et al*[36]				Muller *et al*[37]	
Figure number		Figure 1-2	Figure 3			Figure 4				Figure 5	

5.3 Results and Discussion

To evaluate the prediction accuracy of the proposed model alongside the prevailing Rosensweig model, we computed the relaxation time constants and SLP values for both models and compared them to existing experimental data. To eliminate potential variables for the purpose of comparison, each computed setup used the corresponding experimental parameters,[35-37] including the physical properties of the magnetic nanoparticles and the conditions of the applied alternating magnetic field, as summarized in Table 1. We focused exclusively on nanoparticles made of magnetic iron oxide Fe_3O_4 (magnetite), as it is well-tolerated by the human body unlike other magnetic nanoparticles.

5.3.1 Relaxation Time Constants Comparisons

To accurately approach the evaluation for heating efficiency (SLP) of magnetic nanoparticles, one must take the magnetic field effect into account. We began by investigating the relaxation time constants, since they measure the response of magnetization to the applied alternating magnetic field. Both the Brownian relaxation time constant (τ_B, dashed line) and the Néel relaxation time constant (τ_N, solid line) were plotted in Figure 1 as function of the nanoparticle diameter in the presence of alternating magnetic fields with different amplitudes. We considered two cases: a 20mT alternating magnetic field as shown in Figure 1a and a 60mT alternating magnetic field shown in Figure 1b. The conventional zero-field relaxation time constants (red and blue lines) were calculated using equation 5, while the revised relaxation time constants (green and black lines) were calculated using equation 7 through the eigenvalue approach.

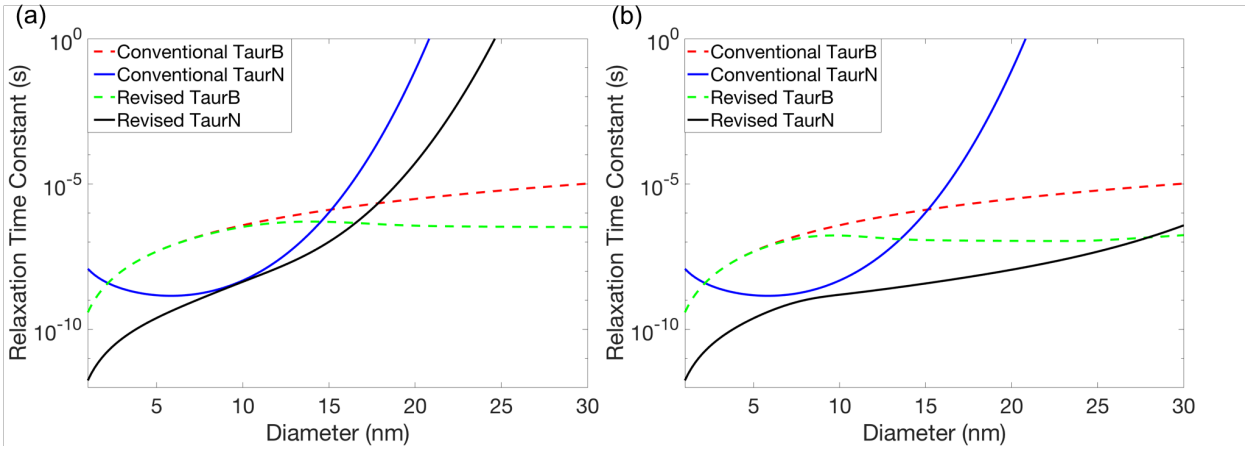


Figure 1. Relaxation time constants for Brownian (τ_B, dashed line) and Néel (τ_N, solid line) processes as a function of nanoparticle diameter in the presence of alternating magnetic field with amplitude of (a)20mT and (b)60mT. Conventional relaxation time constants were calculated from equation 5 (red for τ_B and blue for τ_N), while revised relaxation time constants were calculated from equation 7 (green for τ_B and black for τ_N). Major parameters used for the calculation were summarized in Table 1.

Increasing the amplitude of the applied alternating magnetic field did not change either the zero-field Brownian relaxation time constant (dashed red line) or the zero-field Néel relaxation time constant (solid blue line). As seen in equation 5, the conventional calculation of zero-field relaxation time constants did not include parameters that take into account the contribution of the magnetic field. Moreover, when the diameter of the magnetic nanoparticles was smaller than 14nm, as shown in both Figure 1a and 1b, the solid blue line was lower than the dashed red line, indicating that $\tau_N \ll \tau_B$ and showing that the Néel relaxation mechanism dominated, whereas when the diameter of magnetic nanoparticles was larger than 16nm, the Brownian relaxation mechanism dominated since $\tau_B \ll \tau_N$.

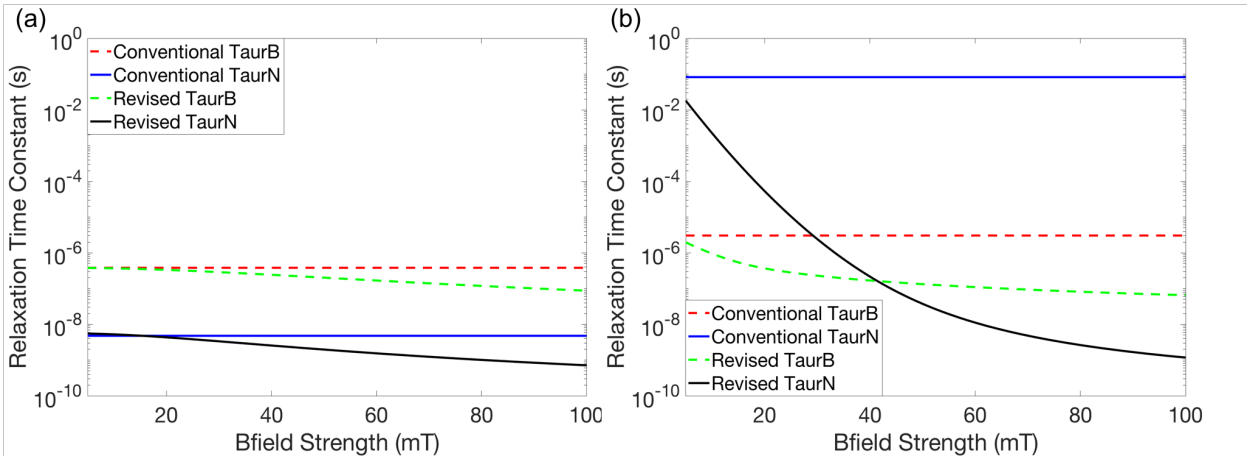


Figure 2. Relaxation time constants for Brownian (τ_B, dashed line) and Néel (τ_N, solid line) processes as a function of the magnetic field strength with nanoparticle diameters of (a)6nm and (b)18nm. Conventional relaxation time constants were calculated from equation 5 (red for τ_B and blue for τ_N), while revised relaxation time constants were calculated from equation 7 (green for τ_B and black for τ_N). Major parameters used for the calculation were summarized in Table 1.

However, the eigenvalue-based approach used to calculate the Brownian relaxation time constant (dashed green line) and the Néel relaxation time constant (solid black line) offered a different picture. The shift of both lines indicated the influence of changes in the magnetic field, where the values of τ_B and τ_N calculated from equation 7 were much smaller than the values calculated from equation 5. Furthermore, in comparison to the Brownian relaxation constant, the Néel relaxation time constant showed a greater response to changes in the magnetic field. As illustrated in Figure 1a and 1b, not only the overall value of τ_N decreased with the increase in the amplitude of the magnetic field, but also the size range of magnetic nanoparticles being affected was wider. When the diameter of magnetic nanoparticles was relatively small, particularly smaller than 8 nm, the varying magnetic field did not introduce a significant change to the relaxation process. In contrast, when the diameter of magnetic nanoparticles was relatively

large, particularly larger than 10nm, the values of both τ_B and τ_N decreased with the increase in the amplitude of the applied alternating magnetic field, and the change in the Néel relaxation time constant was more pronounced.

The relaxation time constants were also plotted as a function of the magnetic field amplitude, where the diameters of the magnetic nanoparticles used in the calculation were separately set up as 6nm, as shown in Figure 2a, and 18nm, as shown in Figure 2b. It was clear that the values of zero-field τ_B and τ_N using the conventional calculation method (equation 5) did not change with increases in the amplitude of the magnetic field. As for the eigenvalue-based τ_B and τ_N, when the diameter of magnetic nanoparticles was 6nm, the values of the relaxation time constants slightly decreased with the increase in amplitude of the magnetic field. When the diameter of the magnetic nanoparticle was 18nm, both values decreased dramatically as the amplitude of the magnetic field increased, and the Néel relaxation time was significantly more sensitive than the Brownian relaxation time, by many orders of magnitude, to the change in the magnetic field amplitude. This phenomenon can be attributed to the dependence of the magnetic energy density on the amplitude of the applied magnetic field. The axis-symmetry of the magnetic energy density of the magnetic field direction is broken in the presence of the alternating magnetic field. Thus, the size of the energy barrier for the magnetic dipole moment to transition from one minima to the other is reduced, resulting in the reduced average time to transition from the higher energy minimum to the lower energy minimum, when compared to the transition time given by the zero-field relaxation time calculated from equation 1. This barrier is made greater by increasing the magnetic field amplitude. However, when the diameter of magnetic nanoparticles is smaller, the energy barrier is minimized, and thus, variations in the magnetic field will not introduce a significant change in the relaxation time constant.

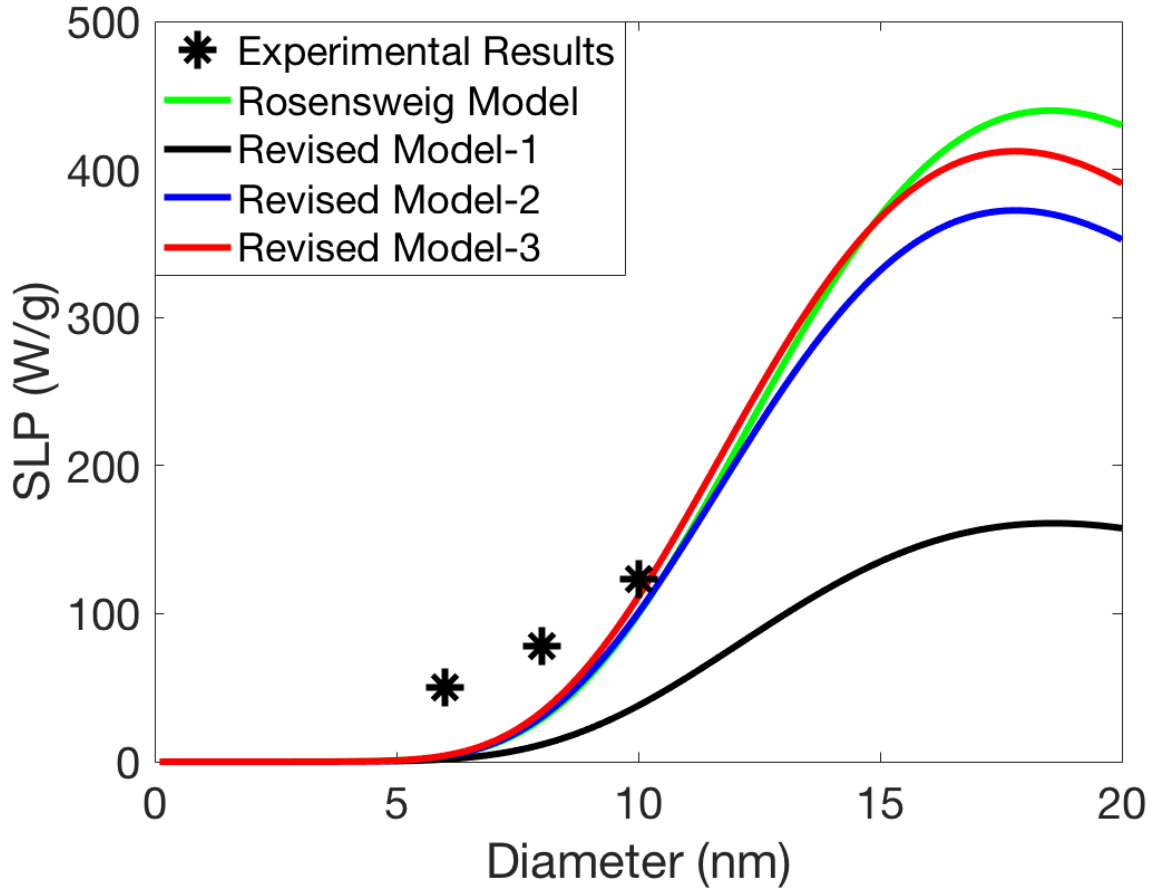


Figure 3. Theoretical SLP comparisons between the Rosensweig model (solid green line), the revised model-1 with change in relaxation time constants (solid black line), the revised model-2 with change in relaxation time constants and nonlinear regime (solid blue line), and the further revised model-3 with the consideration of aggregation formation, nonlinear regime and the magnetic field-based relaxation time constants (solid red line) for magnetite. With the magnetic field amplitude and frequency set to 7 *kA/m* and 63 *kHz*, respectively, the dominant relaxation process was Néel relaxation, and the polydispersity of magnetite was 0.35. The computational calculations for all models used the corresponding experimental parameters and were then compared to experimental results, published by Wang et al, as summarized in Table 1. Each

experimental value was also used as a reference point to assess how each model approached the experimental result.

It can be concluded that, in the presence of a weak magnetic field, the Brownian relaxation process can be ignored for small magnetic nanoparticles, while its effect grows in significance as the nanoparticle diameter increases and becomes dominant for large magnetic nanoparticles. As the amplitude of the magnetic field increases, one might expect the Néel relaxation process to exert greater influence, regardless of the size of magnetic nanoparticles, since it is more sensitive to the varying magnetic field and decreased by many orders of magnitude. However, evaluating the heating efficiency becomes more complicated when taking into consideration the formation of aggregate and the nonlinear response of the magnetic susceptibility, as will be illustrated in detail by comparing the predicted results to the experimental results.

5.3.2 SLP Predictions

The predicted SLP values were calculated using equation 11 and compared to available experimental data[35-37] to determine how well these theoretical predictions approach the reported results, as shown in Figure 3, Figure 4, and Figure 5. The first comparison was magnetite exposed to an external magnetic field with an amplitude of 7 *kA/m* and a frequency of 63 *kHz*, as shown in Figure 3. When magnetic nanoparticles were assumed to be single units and the magnetic field effect was ignored, as in the Rosensweig model, theoretical predictions did not deviate much from the experimental SLP, plotted with the solid blue line. Taking into consideration the magnetic field effect on the relaxation time constant, it can be seen that, for smaller magnetic nanoparticles in the presence of a relatively weak magnetic field, the dominant

relaxation process is the Néel relaxation mechanism, as illustrated and discussed in previous section. Reduced relaxation time constants result in less efficient SLP, as is the case in the revised model-1 drawn in the solid black line in Figure 3. Further revising the model by accounting for the magnetic effect on the nonlinear response of the magnetic susceptibility will elevate SLP values, as depicted by the revised model-2 in the solid blue line. The prediction of SLP for the magnetic colloidal suspension is more accurate when taking the aggregate formation into account, as shown in the revised model-3 in solid red line. This is because the formation of aggregate can prolong the Néel relaxation time in the presence of the weak magnetic field, leading to an increased SLP.

The second example of magnetite was carried out by increasing the magnetic field amplitude to 21 *kA/m* and increasing the frequency to 168 *kHz*, as shown in Figure 4. The prediction of heating efficiency for small size magnetic nanoparticles, which is the case in Figure 4a, is consistent with the result summarized in Figure 3, where the dominant relaxation process is the Néel relaxation mechanism. The difference here is that the enhanced magnetic field amplifies the nonlinear response of the magnetic susceptibility. As the size of the magnetic nanoparticles increases, the Brownian relaxation process starts to play a role in the presence of weak magnetic fields. Therefore, instead of selecting a dominant relaxation process, we treated both Brownian and Néel relaxation mechanisms as taking place "in parallel". As shown in Figure 4b, the contribution from Brownian relaxation process elevated the heating efficiency, which can improve the accuracy of SLP predictions for larger magnetic nanoparticles.

An additional example of magnetite was shown in Figure 5, where the magnetic field amplitude was increased to 30 *kA/m* and the frequency was increased to 210 *kHz*. Figure 5a and

Figure 5b were different in their size distribution, as the bigger polydispersity index induced lower maximum SLP values and broadened the shape of the overall curve. Similar to the

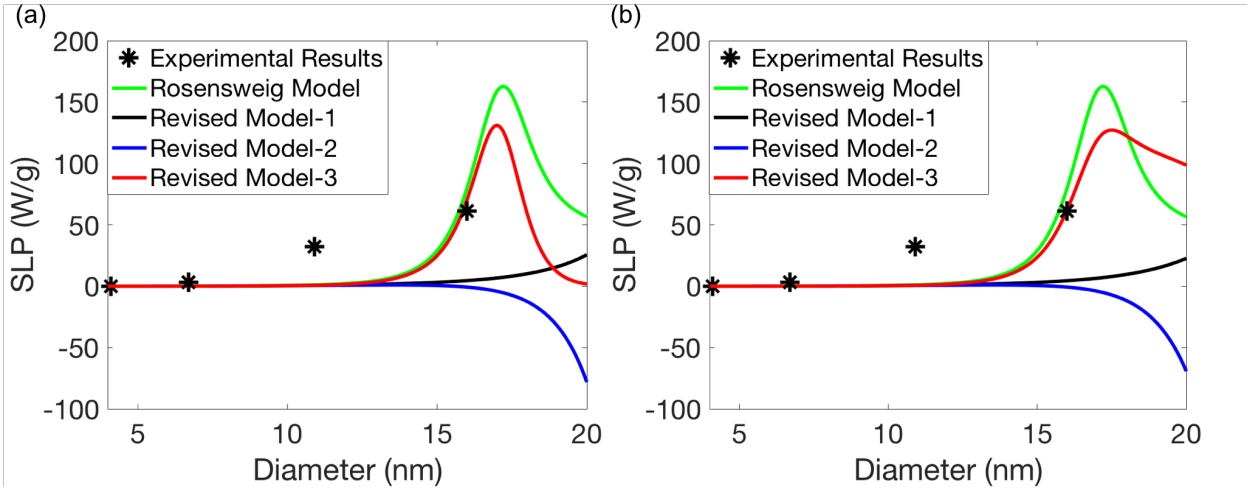


Figure 4. Theoretical SLP comparisons between the Rosensweig model (solid green line), the revised model-1 with change in relaxation time constants (solid black line), the revised model-2 with change in relaxation time constants and nonlinear regime (solid blue line), and the further revised model-3 with the consideration of aggregation formation, nonlinear regime and the magnetic field-based relaxation time constants (solid red line) for magnetite. The magnetic field amplitude and frequency were set to 21 *kA/m* and 168 *kHz*, respectively, and the dominant relaxation time was (a) the Néel relaxation mechanism alone and (b) both the Brownian relaxation and the Néel relaxation mechanism. Computational calculations of all models used the corresponding experimental parameters and were then compared to experimental results, published by Lartigue et al, as summarized in Table 1. Each experimental value was also used as a reference point to assess how each model approached the experimental result.

previous comparison shown in Figure 4b, in the presence of a relatively weak magnetic field with an intermediate frequency such as 200 *kHz*, both Brownian and Néel relaxation mechanisms play an important role in the heat generation, especially for magnetic nanoparticles from 11nm to 16nm in diameter. By treating both processes as taking place in parallel and accounting for the aggregate formation and the magnetic field effect, the SLP values can be more accurately predicted, as illustrated by the revised model-3 in solid red line.

A comparison of the results presented in Figure 3 and Figure 4 shows that, regardless of the dominant relaxation process, the linear response theory is valid only for small magnetic nanoparticles in the presence of weak magnetic fields. As the amplitude of the magnetic field increases, we begin to see the nonlinear response of the magnetic susceptibility. This response is more pronounced for magnetic nanoparticles with a larger diameter, as shown in Figure 5. The experimental data shows that the linear regime only holds in the presence of high temperatures or weak magnetic fields, in accordance with Curie's Law. As the magnetic nanoparticle size and the magnetic field amplitude increases, the heat generation mechanism becomes more complicated due to the induced loss process and heating effects, driving the nonlinear response of the magnetic susceptibility. The evaluation of SLP becomes more interesting and complex by further revising the SLP calculation model to account for the formation of aggregate and the magnetic field effect on the relaxation process. On the one hand, increasing the magnetic field amplitude will reduce the energy barrier by breaking the symmetry of the magnetic energy density and shortening the relaxation time constant. As illustrated in figures 1 through 5, the SLP calculated by considering the changes in the relaxation time constants rendered significantly lower values (solid black line). On the other hand, the formation of aggregate can prolong the relaxation time, leading to an increased SLP compared to the model accounting only for the magnetic field effect

on relaxation process, while at the same time the decreased cluster magnetic anisotropy caused by aggregation can result in an overall reduced SLP compared to the evaluation made by Rosensweig model, especially for larger magnetic nanoparticles. If the Néel relaxation is the dominant process, as shown in Figure 3 and Figure 4a, a stronger magnetic field will result in

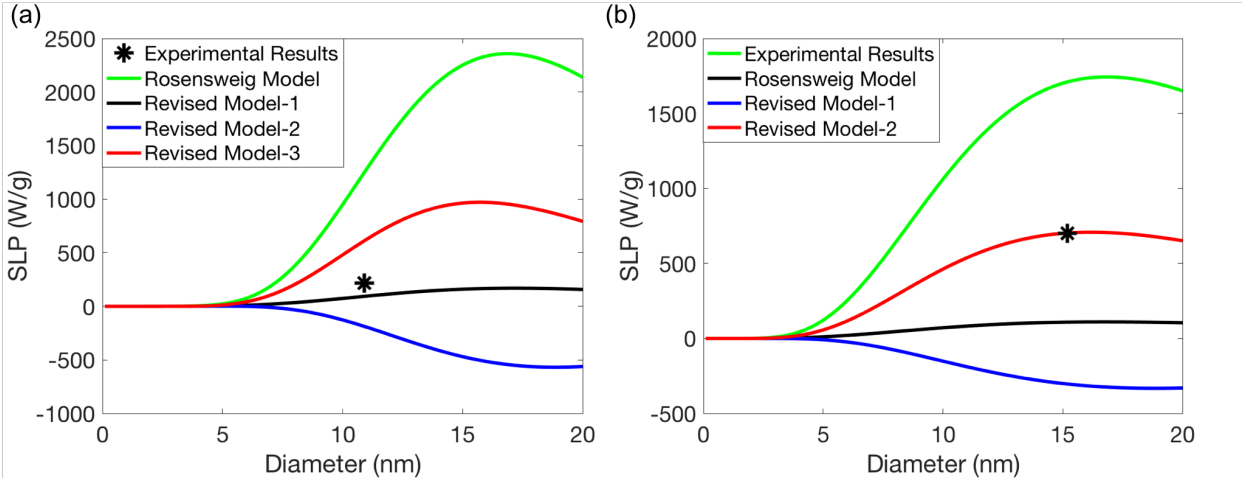


Figure 5. Theoretical SLP comparisons between the Rosensweig model (solid green line), the revised model-1 with changes in the relaxation time constants (solid black line), the revised model-2 with changes in the relaxation time constants and nonlinear regime (solid blue line), and the further revised model-3 that takes into consideration aggregation formation, nonlinear regime, and the magnetic field-based relaxation time constants (solid red line) for magnetite. The magnetic field amplitude and frequency were set to 30 *kA/m* and 210 *kHz*, respectively, both Brownian relaxation and Néel relaxation processes were deemed to take place "in parallel", and the polydispersity of magnetite was (a) 0.37, (b) 0.51. Computational calculations of all models used the corresponding experimental parameters and were then compared to experimental results, published by Muller et al, as summarized in Table 1. Each experimental value was also used as a reference point to assess how each model approached the experimental result.

less efficient SLP, an effect that is more pronounced for larger magnetic nanoparticles. If we consider both relaxation processes taking place “in parallel”, as illustrated in Figure 4b and Figure 5, the SLP will show the major features of whichever the process is dominant.

The importance and advantage of the proposed model is most pronounced when evaluating the heating efficiency in a strong magnetic field, especially in the presence of MRI with the clinically common amplitude of 1.5T where magnetic nanoparticles are encapsulated in a liposome and are highly accumulated at the targeted lesion. The conventional method does not reflect the magnetic influence on either the heating mechanism or the nonlinear response of the magnetic susceptibility. Instead, our model was established by incorporating the effect of the aggregate formation of magnetic nanoparticles, the nonlinear response of the magnetic susceptibility, and the magnetic field-dependent relaxation process, offering a deeper insight on how to control the physical properties of magnetic nanoparticles and the magnetic field parameters to achieve the most efficient heating in *in vivo* nano-theranostic hyperthermia.

5.4 Conclusion

Utilizing magnetic nanoparticles enables the *in vivo* MR nano-theranostic hyperthermia system to serve as a multifunctional nanoplatform for the purpose of simultaneous diagnosis and therapy. The proposed novel model is able to reflect magnetic influence and the reveal heating mechanism based on three major findings: (i) magnetic nanoparticles are interacting in the colloidal suspension, (ii) the magnetic susceptibility and the magnetic field amplitude are nonlinearly related, and (iii) relaxation times due to the Brownian or Néel relaxation mechanisms depend on the amplitude of the applied magnetic field. In comparison to the prevailing Rosensweig Model, our model approaches the experimental results in a more accurate way

irrespective of the size of magnetic nanoparticles and the setup of magnetic field, as shown in Figures 3-5. In the interest of efficient heating of magnetic nanoparticles used in cancer treatment, the precise evaluation of heating efficiency will inform the design of magnetic nanoparticles and improve heat control in nano-theranostic hyperthermia. Based on the published data we reviewed, we suggest placing magnetic nanoparticles with a diameter of 15nm in a magnetic field with a moderate amplitude of around 25kA/m.

5.5 References

[1] Zhou, H.; Qian, W.; Uckun, F. M.; Wang, L.; Wang, Y. A.; Chen, H.; Kooby, D.; Yu, Q.; Lipowska, M.; Staley, C. A.; Mao, H.; Yang, L. IGF1 Receptor Targeted Theranostic Nanoparticles for Targeted and Image- Guided Therapy of Pancreatic Cancer. *ACS Nano*. **2015**, *9*, 7976-7991.

[2] Sanson, C.; Diou, O.; The venot, J.; Ibarboure, E.; Soum, A.; Bru^let, A.; Miraux, S.; Thiaudie re, E.; Tan, S.; Brisson, A.; Dupuis, V.; Sandre, O.; Lecommandoux, S. Doxorubicin Loaded Magnetic Polymersomes: Theranostic Nanocarriers for MR Imaging and Magneto-Chemotherapy. *ACS Nano*. **2011**, *5*, 1122-1140.

[3] Fazal, S.; Paul-Prasanth, B.; Nair, S. V.; Menon, D. Theranostic Iron Oxide/Gold Ion Nanoprobes for MR Imaging and Noninvasive RF Hyperthermia. *ACS Appl. Mater. Interfaces.* **2017**, *9*, 28260-28272.

[4] Ho, D.; Sun, X.; Sun, S. Monodisperse Magnetic Nanoparticles for Theranostic Applications. *Acc. Chem. Res*. **2011**, *44*, 875-882.

[5] Yoo, D.; Lee, J.; Shin, T.; Cheon, J. Theranostic Magnetic Nanoparticles. *Acc. Chem. Res*. **2011**, *44*, 863-874.

[6] Béalle, G.; Di Corato, R.; Kolosnjaj-Tabi, J.; Dupuis, V.; Clement, O.; Gazeau, F.; Wilhelm, C.; Ménager, C. Ultra Magnetic Liposomes for MR Imaging, Targeting, and Hyperthermia. *Langmuir.* **2012**, *28*, 11834-11842.

[7] Jordan, A.; Wust, P.; Fähling, H.; John, W.; Hinz, A.; Felix, R. Inductive Heating of Ferrimagnetic Particles and Magnetic Fluids: Physical Evaluation of Their Potential for Hyperthermia. *Int. J. Hyperthermia*. **1993**, *9*, 51–68.

[8] Jordan, A.; Wust, P.; Scholz, R.; Tesche, B.; Fähling, H.; Mitrovics, T.; Vogl, T.; Cervós-Avarro, J.; Felix, R. Cellular Uptake of Magnetic Fluid Particles and Their Effects on Human Adenocarcinoma Cells Exposed to AC Magnetic Fields In Vitro. *Int. J. Hyperthermia*. **1996**, *12*, 705–722.

[9] Hergt, R.; Dutz, S.; Röder, M. Effects of Size Distribution on Hysteresis Losses of Magnetic Nanoparticles for Hyperthermia. *J. Phys.: Condens. Matter*. **2008**, *20*, 385214.

[10] Li, Z.; Kawashita, M.; Araki, N.; Mistumori, M.; Hiraoka, M. Effects of Particle Size of Magnetite Nanoparticles on Heat Generating Ability Under Alternating Magnetic Field. *Bioceram. Dev. Appl.* **2011**, *1*, D110128.

[11] Bordelon, D. E.; Cornejo, C.; Grüttner, C.; Westphal, F.; DeWeese, T. L.; Ivkov, R. Magnetic Nanoparticle Heating Efficiency Reveals Magneto-Structural Differences When Characterized with Wide Ranging and High Amplitude Alternating Magnetic Fields. *J. Appl. Phys*. **2011**, *109*, 124904.

[12] Khandhar, A. P.; Ferguson, R. M.; Simon, J. A.; Krishnan, K. M. Enhancing Cancer Therapeutics Using Size-Optimized Magnetic Fluid Hyperthermia. *J. Appl. Phys*. **2012**, *111*, 07B306.

[13] Rosensweig, R. E. Heating Magnetic Fluid with Alternating Magnetic Field. *J. Magn. Magn. Mater*. **2002**, *252*, 370–374.

[14] Hergt, R.; Dutz, S.; Müller, R.; Zeizberger, M. Magnetic Particle Hyperthermia: Nanoparticle Magnetism and Materials Development for Cancer Therapy. *J. Phys.: Condens. Matter*. **2006**, *18*, 2919–2934.

[15] Kuhn, L. T.; Bojesen, A.; Timmermann, L.; Fauth, K.; Goering, E.; Johnson, E.; Nielson, M. M.; Morup, S. Core-Shell Iron–Iron Oxide Nanoparticles: Magnetic Properties and Interactions. *J. Magn. Magn. Mater*. **2004**, *272–276*, 1485–1486.

[16] Ganguly, R.; Zellmer, B.; Puri, I. K. Field-Induced Self-Assembled Ferrofluid Aggregation in Pulsatile Flow. *Phys. Fluids*. **2005**, *17*, 097104.

[17] Castro, L. L.; da Silva, M. F.; Bakuzis, A. F.; Miotto, R. Aggregate Formation on Polydisperse Ferrofluids: A Monte Carlo Analysis. *J. Magn. Magn. Mater*. **2005**, *293*, 553–558.

[18] Wang, C.; Li, Z.; Lin, Y. Y. Optimizing Magnetic Nanoparticles Hyperthermia Effect in MR Nanomedicine. *Chinese Journal of Magnetic Resonance*. **2015**, *32*, 248-260

[19] De´jardin, J. L. Fractional Dynamics and Nonlinear Harmonic Responses in Dielectric Relaxation of Disordered Liquids. *Phys. Rev*. **2003**, *68*, 031108.

[20] Giannitsis, A. T.; Fannin, P. C.; Charles, S. W. Nonlinear Effects in Magnetic Fluids. *J. Magn. Magn. Mater*. **2005**, *289*, 165–167.

[21] Fannin, P. C.; Oireachtaigh, C. M. Investigating the Isotropic Properties of a Magnetic Fluid Following the Removal of a Polarising Field. *J. Magn. Magn. Mater*. **2007**, *316*, e802–e804.

[22] Singh, V.; Banerjee, V.; Sharma, M. Dynamics of Magnetic Nanoparticle Suspensions. *J. Phys. D.: Appl. Phys*. **2009**, *42*, 245006.

[23] Deissler, R. J.; Wu, Y.; Martens, M. A. Dependence of Brownian and Néel Relaxation Times on Magnetic Field Strength. *Med. Phys.* **2014**, *41*, 012301.

[24] Verde, E. L.; Landi, G. T.; Carrião, M. S.; Drummond, A. L; Gomes, J. A.; Vieira, E. D.; Sousa, M. H.; Bakuzis, A. F. Field Dependent Transition to the Non-Linear Regime in Magnetic Hyperthermia Experiments: Comparison Between Maghemite, Copper, Zinc, Nickel, and Cobalt Ferrite Nanoparticles of Similar Sizes. *AIP Adv*. **2012**, *2*, 032120.

[25] Saville, S. L.; Qi, B.; Baker, J.; Stone, R.; Camley, R. E.; Livesey, K. L.; Ye, L.; Crawford, T. M.; Mefford, O. T. The Formation of Linear Aggregates in Magnetic Hyperthermia: Implications on Specific Absorption Rate and Magnetic Anisotropy. *J. Colloid Interface Sci.* **2014**, *424*, 141–151.

[26] Reeves, D. B.; Weaver, J. B. Approaches for Modeling Magnetic Nanoparticle Dynamics. *Crit. Rev. Biomed. Eng.* **2014**, *42*, 85–93.

[27] Guibert, C.; Dupuis, V; Peyre, V.; Fresnais, J. Hyperthermia of Magnetic Nanoparticles: Experimental Study of the Role of Aggregation. *J. Phys. Chem. C.* **2015**, *119*, 28148–28154.

[28] Wang, C.; Hsu, C. H.; Li, Z.; Hwang, L. P.; Lin, Y. C.; Chou, P. T.; Lin, Y. Y. Effective Heating of Magnetic Nanoparticle Aggregates for In Vivo Nano-theranostic Hyperthermia. *Int. J. Nanomedicine*. **2017**, *12*, 6273–6287.

[29] Oireachtaigh, C. M.; Fannin, P. C. Investigation of the Non-Linear Loss Properties of Magnetic Fluids Subject to Large Alternating Ffields. *J. Magn. Magn. Mater*. **2008**, *320*, 871–880.

[30] Branquinho, L. C.; Carriao, M. S.; Costa, A. S.; Zufelato, N. Sousa, M. H.; Miotto, R.; Ivkov, R.; Bakuzis, A. F. Effect of Magnetic Dipolar Interactions on Nanoparticle Heating Efficiency: Implications for Cancer Hyperthermia. *Sci. Rep*. **2013**, *3*, 2887.

[31] Fernandez van Raap, M. B.; Coral, D. F.; Yu, S.; Munoz, G. A.; Sanchez, F. H.; Roig, A. Anticipating Hyperthermic Efficiency of Magnetic Colloids using a Semi-expirical Model: a Tool to Help Medical Decisions. *Phys. Chem. Chem. Phys.* **2017**, *19*, 7176.

[32] Coffey, W. T.; Paranjape. B. V. Dielectric and Kerr Effect Relaxation in Alternating Electric Fields. *Proc. Roy. Irish Acad*. **1978**, *78*, 17–25.

[33] Morais, P. C.; Gonçalves, G. R. R.; Bakuzis, A. F.; Neto, K. S.; Pelegrini, F. Experimental Evidence of Dimer Disruption in ionic Ferrofluid: A Ferromagnetic Resonance Investigation. *J. Magn. Magn. Mater*. **2001**, *225*, 84–88.

[34] Zhong, J.; Xiang, Q.; Massa, L. O.; Qu, F.; Morais, P. C.; Liu, W. Second-Order-Like Cluster-Monomer Transition within Magnetic Fluids and Its Impact upon the Magnetic Susceptibility. *Nanoscale Res. Lett*. **2012**, *7*, 167.

[35] Wang, X.; Gu, H.; Yang, Z. The Heating Effect of Magnetic Fluids in an Alternating Magnetic Field. *J. Magn. Magn. Mater*. **2005**, *293*, 334-340.

[36] Lartigue, L.; Innocenti, C.; Kalaivani, T.; Awwad, A.; Mar Sanchez Duque, M.; Guari, Y.; Larionova, J.; Guerin, C.; Georges Montero, J.; Barragan-Montero, V.; Arosio, P.; Lascialfari, A.; Gatteschi, D.; Sangregorio, C.; Water-Dispersible Sugar-Coated Iron Oxide Nanoparticles. An Evaluation of Their Relaxometric and Magnetic Hyperthermia Properties. *J. Am. Chem. Soc.* **2011**, *133*, 10459-10472.

[37] Muller, R.; Dutz, S.; Neeb, A.; Cato, A. C. B.; Zeisberger, M. Magnetic Heating Effect of Nanoparticles with Different Sizes and Size Distributions. *J. Magn. Magn. Mater*. **2013**, *328*, 80-85.

[38] Debye, P. Polar Molecules. *The Chemical Catalog Co*. Dover: New York, **1929**.

[39] Néel, L. Theorie du Trainage Magnetique des Ferromagnetiques en Grains Fins avec Applications aux Terres Cuites. *Geophysics*. **1949**, *5*, 99–136.

[40] Coffey, W. T.; Kalmykov, Y. P.; Waldron, J. T. The Langevin Equation. *World Scientific*: Singapore, **2004**.

Chapter 6

Efficient Heating of *In Vivo* Nano-theranostic Hyperthermia in the Presence of MRI

6.0 Abstract

The *in vivo* nano-theranostic system of combined MRI and hyperthermia has recently been proposed and constructed to simultaneously diagnose and treat many different types of cancer. The success of this promising *in vivo* application depends upon optimizing both the magnetic settings and the design of the magnetic nanoparticles. For the purpose of the efficient heating of this combined MRI/hyperthermia system, it is essential to understand the properties and the mechanisms responsible for magnetic heating. In this paper, we used a novel model to evaluate the heating efficiency in the presence of an MRI DC field, which in clinical applications typically has an amplitude of $B_0 = 1.5\ T$. The model is based on three major findings about the magnetic field's effect on the relaxation process, the aggregate formation of magnetic nanoparticles, and the nonlinear response of the magnetic susceptibility. Our evaluation of the model showed that the relaxation time constants due to Brownian or Néel relaxation mechanisms decrease in the presence of the MRI DC field as a result of the magnetization saturation, which limits the heat being generated. The heating efficiency for large magnetic nanoparticles that one would expect to be elevated by the superposition of strong alternating magnetic field actually dropped dramatically. To improve the heating efficiency of *in vivo* nano-theranostic hyperthermia in the clinical MRI environment, we proposed either using a high frequency-driven rotating magnetic field to heat small magnetic nanoparticles encapsulated along with therapeutic

drugs inside thermosensitive liposomes, or else using a low frequency-driven linearly ramped alternating magnetic field combined with a built-in MRI gradient to trigger the Brownian relaxation mechanism.

6.1 Introduction

During the last decade, significant scientific research efforts have been devoted toward understanding cancer at the genetic, cellular, and molecular levels and finding new ways to diagnose and treat cancer. The introduction of magnetic nanoparticles has boosted the hopes for early cancer detection and treatment, due to their unique properties, including nontoxicity, biocompatibility, injectability, and capacity for high-level accumulation in the target tissue.[1-6] Among all the biomedical nano-theranostic applications of magnetic nanoparticles, their reaction to the magnetic field makes them an ideal choice as a drug delivery and magnetic resonance imaging (MRI) contrast enhancement agent.

Intriguing about magnetic nanoparticles is their potential for nano-theranostic hyperthermia, where the injected particles generate localized heat through superparamagnetic relaxation mechanisms when exposed to an external alternating magnetic field.[7-9] Early investigation has shown that, in addition to the reduced side effects compared to traditional chemotherapy and radiotherapy, magnetic nanoparticles are more therapeutically effective than microscale particles in terms of specific loss power (SLP) due to the heating mechanisms.[10] This relaxation-based heating effect is heavily dependent upon the applied field's strength and frequency, as well as the size and makeup of the magnetic nanoparticles,[7-9] highlighting the importance of properly designing the nanoparticles and optimizing the magnetic settings so that

the combined system of hyperthermia/MRI can achieve the goal of simultaneous diagnosis and treatment of cancer.

The appeal of this nano-theranostic MR hyperthermia system is that the same RF resource that is used to excite hydrogen protons during imaging can also be employed to generate heat therapeutically. While the combined system of MRI and conventional therapy (i.e., radiotherapy and thermotherapy) in the absence of magnetic nanoparticles has previously been investigated,[11-12] its imprecise targeting, heat attenuation below the body's surface, and generation of undesirable hot spots in healthy tissues results in ineffective treatment of deep-seated tumors. Much research has also been conducted into utilizing the magnetic nanoparticles in imaging and hyperthermia, separately,[13-17] such as functionalizing magnetic nanoparticles as a contrast agent that binds to tumors for MRI, and optimizing the heating efficiency in hyperthermia. But few groups have studied the efficient heating of magnetic nanoparticles in the MR nano-theranostic hyperthermia system.

Cantillon-Murphy *et al*[18] examined the practical advantages and disadvantages of utilizing magnetic nanoparticles in a combined MRI/magnetic particle hyperthermia system to treat cancerous tumors. Their study used the Rosensweig approach,[19] to make a rough prediction of the temperature response to a low-field MRI. Unfortunately, their model's limitations prevented us from knowing how to appropriately design the nanoparticles and optimize their magnetic field-induced heating efficiency.

The Rosensweig approach does not take into account that magnetic nanoparticles are interacting and can aggregate in the colloidal suspension.[20-21] In the presence of MRI, magnetic nanoparticles that serve as an MRI contrast agent will accumulate at tumor site, leading to additional aggregate formation that further influences the amount of heat generated. Moreover,

relaxation times due to the Brownian or Néel relaxation mechanisms depend on the applied magnetic field.[22] The well-known zero-field relaxation times underestimate the actual relaxation times in clinical settings. The stronger a magnetic field is, the more it will complicate the heat generation mechanism and trigger the nonlinear response of the magnetic susceptibility.[23-27] In the presence of a high-field MRI, which has the commonly used amplitude of $B_0 = 1.5\ T$, the heating effect will be further reduced as a result of the magnetic saturation associated with the external Zeeman DC magnetic field.

For the *in vivo* nano-theranostic system of combined MRI/Hyperthermia to be clinically effective, maximizing the heating efficiency is critical to avoiding damage to adjacent healthy tissues when targeting the tumor cells. We used a novel model to evaluate and optimize the heating efficiency of magnetic fluid hyperthermia that accounts for the aggregate formation of magnetic nanoparticles, the magnetic field effect on the relaxation mechanism and the nonlinear heat generation mechanism. We showed that both the Brownian and Néel relaxation processes become shorter in the presence of MRI DC field with an amplitude of $B_0 = 1.5\ T$, leading to the dramatic drop in the heating efficiency due to the saturation of magnetization. While consideration of aggregation and the nonlinear response of the magnetic susceptibility complicates the analysis of the heating efficiency, especially for large magnetic nanoparticles highly accumulated near the target tumor site, we found ways to optimize the heating efficiency of magnetic nanoparticles for *in vivo* hyperthermia in the clinical MRI environment. We proposed to heat small magnetic nanoparticles encapsulated along with therapeutic drugs inside thermosensitive liposomes by using a high frequency-driven rotating magnetic field, where the Néel relaxation is the dominant relaxation mechanism. Taking advantage of the MRI machine's built-in gradient also allows us to boost the heating efficiency by subjecting medium-sized

magnetic nanoparticles to a low frequency-driven linearly ramped alternating magnetic field that triggers the Brownian relaxation mechanism.

6.2 Materials and Methods

6.2.1 Magnetic Field-Dependent Relaxation Process

Magnetic relaxation is the basic principle governing the heat generation mechanism for magnetic nanoparticles dispersed in fluid. The conventional models use zero-field relaxation time constants[28-29] when calculating SLP and assume that the Brownian (Debye) and the Néel relaxation mechanisms take place in parallel. However, both relaxation processes depend on the magnetic field, and the phase lag caused by the frequency of the applied alternating magnetic field can affect the role of the dominant relaxation mechanism. Therefore, solving the Fokker-Planck equation for Brownian (equation 1a) and Néel relaxation (equation 1b) allowed us to calculate more realistic relaxation time constants and determine the dominant relaxation mechanism.[30]

$$2\tau_{B0}\frac{\partial W}{\partial t} = \frac{\partial}{\partial x}\left[(1-x^2)\left(\frac{\partial W}{\partial x} - \alpha(t)W\right)\right] \quad (1a)$$

$$2\tau_{N0}\frac{\partial W}{\partial t} = \frac{\partial}{\partial x}\left[(1-x^2)\left(\frac{\partial W}{\partial x} - \alpha(t)W - \alpha_K xW\right)\right] \quad (1b)$$

Where $\tau_{B0} \equiv \frac{3\eta V_H}{k_B T}$, $\tau_{N0} \equiv \frac{\beta(1+\alpha'^2)M_s}{2\gamma\alpha'}$, $\alpha(t) \equiv \frac{m_0}{k_B T}B(t)$ and $\alpha_K \equiv \frac{2K_a V_M}{k_B T}$. k_B is the Boltzmann constant, T is the absolute temperature (K), $B(t)$ is the external magnetic flux density, and $V_M = 4\pi R^3/3$, is the magnetic volume of a particle with radius R. Moreover, $m_0 = M_s V_M$ is the magnetic dipole moment, where $M_s = \phi M_d$ is the saturated magnetization, M_d is the domain magnetization, ϕ is the volume fraction of nanoparticles, and K_a is the anisotropy constant which may depend on the shape and size of nanoparticles. $\beta = V_M/k_B T$, η is the viscosity of the carrier

fluid, γ is the electron gyromagnetic ratio, α' is the damping constant, and $V_H = (1 + \delta/R)^3 V_M$ is the hydrodynamic volume of the particle, where δ is the thickness of a surfactant layer.

The solution $W(x,t)$ solved from equation 1 can be used to calculated the magnetization of the ensemble of nanoparticles through equation 2,

$$\vec{M}(t) = nm_0 < x(t) > \hat{z} \tag{2}$$

where n is the nanoparticle number density, $< x(t) >= \int_{-1}^{1} xW(x,t)dx$, and the distribution function is normalized such that $\int_{-1}^{1} W(x,t)dx = 1$.

Regarding the relaxation time constants, an eigenvalue approach[22] was used for the purpose of accelerating the calculation speed. As a result, the eigenvalue of the Brownian relaxation was calculated from tridiagonal matrix in equation 3a,

$$A_{n,n} = -\frac{n(n+1)}{2} \; n = 1, 2, 3, \dots, N,$$

$$A_{n,n+1} = -\frac{n(n+1)}{2(2n+3)}\alpha \; n = 1, 2, 3, \dots, N-1,$$

$$A_{n,n-1} = \frac{n(n+1)}{2(2n-1)}\alpha \; n = 2, 3, 4, \dots, N, \tag{3a}$$

And the eigenvalue of the Néel relaxation was calculated from pentadiagonal matrix in equation 3b,

$$A_{n,n} = \frac{n(n+1)}{2} \; n = 1, 2, 3, \dots, N,$$

$$A_{n,n+1} = -\frac{n(n+1)}{2(2n+3)}\alpha \; n = 1, 2, 3, \dots, N-1,$$

$$A_{n,n-1} = \frac{n(n+1)}{2(2n-1)}\alpha \; n = 2, 3, 4, \dots, N,$$

$$A_{n,n+2} = -\frac{n(n+1)(n+2)}{2(2n+3)(2n+5)}\alpha_K \; n = 1, 2, 3, \dots, N-2,$$

$$A_{n,n-2} = \frac{n(n+1)(n-1)}{2(2n-1)(2n-3)}\alpha_K \; n = 3, 4, 5, \dots, N, \tag{3b}$$

Then the largest real part, λ^{max}, of the calculated eigenvalues of A were used to describe the Brownian relaxation time constant (equation 4a) and the Néel relaxation time constant (equation 4b),

$$\tau_B = -\frac{\tau_{B0}}{Re(\lambda_B^{max})} \tag{4a}$$

$$\tau_N = -\frac{\tau_{N0}}{Re(\lambda_N^{max})} \tag{4b}$$

6.2.2 Aggregation

The disruption of magnetic nanoparticle clusters follows a second-order phase transition at the critical temperature.[31] Therefore, the fraction of clusters (P_c) in the ferrofluid was chosen as an order parameter to describe this thermal-assisted cluster disruption in terms of the critical temperature, T^*, and the suspension temperature, T,[32-33]

$$P_c = (1 - \frac{T}{T^*})^{\frac{1}{2}} \tag{5a}$$

and the fraction of monomers (P_m) in the ferrofluid can be simply treated to be proportional to the temperature,

$$P_m = \frac{T}{T^*} \tag{5b}$$

Notice that $P_m + P_c = 1$ when it is at two limiting conditions: $T \ll T^*$ and $T \geq T^*$.

6.2.3 Nonlinear response of magnetic susceptibility

When a strong bias magnetic field, such as an MRI DC field, is superimposed on a weaker alternating magnetic field, the relationship between the magnetic susceptibility and the magnetic field is no longer linear. Applying an even stronger alternating magnetic field will further induce a nonlinear response from the magnetic susceptibility.[23-27] Based on the equation for the electric susceptibility as proposed by Coffey and Paranjape,[34-35] the analytical expression of the nonlinear increment in magnetic susceptibility is,

$$\Delta\chi_{non} = -\chi_i \left(\frac{m_0 H_0}{k_B T}\right)^2 \frac{27-13\omega^2{\tau_{eff}}^2+\mathrm{i}\omega\tau_{eff}\left(42+2\omega^2{\tau_{eff}}^2\right)}{60\left(1+\omega^2{\tau_{eff}}^2\right)\left(9+4\omega^2{\tau_{eff}}^2\right)} \quad (6)$$

where H_0 is the amplitude of the alternating magnetic field, and $\chi_i = \phi\mu_0 M_d^2 V_M/3k_{\mathrm{B}}T$ is the initial magnetic susceptibility with the constant μ_0 as the magnetic permeability in free space.

6.2.4 Power Dissipation

Analytical relationships of power dissipation in a colloidal suspension of magnetic particles have been derived by Rosensweig.[19] In order to incorporate the impact of different alternating magnetic fields on the optimization of the heating efficiency of hyperthermia in the presence of MRI, we extended Rosensweig's approach and started from the perspective of magnetization response to the magnetic field.[36]

We considered the placement of spherical single-domain non-interacting magnetic nanoparticles in the *in vivo* MR nano-theranostic hyperthermia system. The superimposed magnetic fields, which consist of the external uniform DC field (MRI) and the alternating magnetic field (hyperthermia), require the decomposition of the magnetic flux density **B** and magnetic field **H**.

$$\mathbf{B} = \Re e\left[\left(\widehat{b_x}\boldsymbol{i}_x + \widehat{b_y}\boldsymbol{i}_y\right)e^{i\omega t}\right] + B_0\boldsymbol{i}_z \quad (7a)$$

$$\mathbf{H} = \Re e\left[\left(\widehat{h_x}\boldsymbol{i}_x + \widehat{h_y}\boldsymbol{i}_y\right)e^{i\omega t}\right] + H_0\boldsymbol{i}_z \quad (7b)$$

The internal energy of the magnetic nanoparticles suspension in an adiabatic process is equal to the magnetic work done on it:

$$\Delta U = -\mu_0 \oint \mathbf{M} d\mathbf{H} \quad (8)$$

Where the magnetization, **M**, is the vector whose components are the complex amplitudes, $\widehat{m_x}$ and $\widehat{m_y}$ given by equation 9a and 9b, separately,

$$\widehat{m_x} = \chi_0 \frac{\left(i\omega\tau_{eff}+1+\chi_0\right)\widehat{h_x}-\left(\omega_z\tau_{eff}\right)\widehat{b_y}/\mu_0}{\left(i\omega\tau_{eff}+1\right)\left(i\omega\tau_{eff}+1+\chi_0\right)+\left(\omega_z\tau_{eff}\right)^2} \quad (9a)$$

$$\widehat{m_y} = \chi_0 \frac{(\omega_z \tau_{eff})\widehat{h_x} + (i\omega\tau_{eff}+1)\widehat{b_y}/\mu_0}{(i\omega\tau_{eff}+1)(i\omega\tau_{eff}+1+\chi_0)+(\omega_z\tau_{eff})^2} \tag{9b}$$

$$\mathbf{M} = \mathfrak{Re}\left[\left(\widehat{m_x}\boldsymbol{i}_x + \widehat{m_y}\boldsymbol{i}_y\right)e^{i\omega t}\right] + M_0\boldsymbol{i}_z \tag{9c}$$

The spin-velocity, ω_z, which is z-directed, was given in equation 10 with the assumption of no imposed flow.

$$\omega_z = \frac{1}{8\zeta}\mathfrak{Re}[\widehat{m_x}\widehat{b_y^*} - \mu_0\left(\widehat{h_x} + \widehat{m_x}\right)\widehat{m_y^*}] \tag{10}$$

where ζ is the ferrofluid vortex viscosity, given by $\frac{3\eta\phi}{2}$. $\chi_0 = \frac{M_0}{H_0}$ is the equilibrium susceptibility. Accounting for the aggregation discussed in equation 5, we can re-denote the equilibrium susceptibility of ferrofluid in terms of the temperature as,

$$\chi_0(T) = \frac{M_0}{H_0} = \frac{\phi}{H_0}\left[M_{dm}\left(\frac{T}{T^*}\right)L\left(\frac{\mu_0\overline{m_m}H_0}{k_BT}\right) + M_{dc}(1-\frac{T}{T^*})^{\frac{1}{2}}L(\frac{\mu_0\overline{m_c}H_0}{k_BT})\right] \tag{11}$$

Where M_{dm} and M_{dc} are the domain magnetization of monomers and clusters, respectively, $\overline{m_m}$ and $\overline{m_c}$ are the average magnetic moment of monomers and clusters, respectively, and L is the Langevin function with formula $L(x) = coth(x) - \frac{1}{x}$.

For a complete magnetic field cycle, $T = \frac{2\pi}{\omega}$, the time-averaged internal energy is

$$< \Delta U >= -\mu_0 \int_0^T \mathbf{M}\frac{\partial \mathbf{H}}{\partial t}\,dt \tag{12}$$

Using the relationship between **B**, **H**, and **M** given in equation 12,

$$\mathbf{B} = \mu_0(\mathbf{H} + \mathbf{M}) \tag{13}$$

and substituting equation 7 and equation 9 into equation 12, we can get

$$< \Delta U >= \mu_0\mathfrak{Re}[i\pi(\widehat{m_x}\widehat{h_x^*} + \widehat{m_y}(\widehat{b_y^*}/\mu_0))] \tag{14}$$

For a purely alternating-sinusoidal field, $\widehat{b_y}$ can be zero so that the field can oscillate along x direction. If we superimpose a rotating magnetic field onto the transverse plane in the presence of

DC MRI field, $\widehat{h_x}$ and $\widehat{b_y}$ are the imposed x and y field components with, $\widehat{h_x} = H_0$ and $\widehat{b_y} = iB_e$, where H_0 is the amplitude of the applied rotating magnetic field and $B_e = \mu_0 H_0$.

The heating efficiency, which is represented by the specific loss power (SLP), is given by:

$$SLP = \frac{f<\Delta U>}{\rho\phi} \tag{15}$$

where ρ is the mass per unit volume of iron oxide. By taking the nonlinear response of the magnetic susceptibility (equation 6) into consideration, the SLP for the colloidal magnetic nanoparticles suspension can be further revised following Rosensweig approach as

$$SLP = \frac{f}{\rho\phi}[< \Delta U > + \mu_0 \pi {H_0}^2 \Im m(\Delta \chi_{non})] \tag{16}$$

6.2.5 Computational Parameters

The primary computational parameters used to calculate the theoretical relaxation time constants and heating efficiency (SLP), including the physical properties of magnetic nanoparticles and magnetic conditions of the magnetic field, were summarized in Table 1.

Table 1. Computational parameters used in the calculation of theoretical relaxation time constants and evaluation of the heating efficiency (SLP) for magnetite Fe_3O_4 magnetic nanoparticles, as shown in all figures.

Magnetic nanoparticle		Magnetite Fe_3O_4					
Magnetic anisotropy constant, K_a (kJ/m^3)		20					
Saturated Magnetization, M_s (kA/m)		474					
Viscosity of the carrier fluid, η (kg m^{-1} s^{-1})		0.0010049 (Water)					
Electron Gyromagnetic Ratio, γ (rad/s T)		1.75×10^{11}					
Damping Constant, α'		0.1					
Temperature, T (K)		300					
Critical temperature, T^* (K)		358					
Mass Density of Magnetic Nanoparticles, ρ (kg/m^{-3})		5180					
Alternating/ Rotating Magnetic Field	Frequency, f (kHz)	200	200	200	200,400, 700,1000	400	5,20, 100,1000
	Amplitude, H_0(mT)	20	15,25,35	15,25,35	15,25,35	15	150
MRI DC Field, B_0(T)		1.5	NA	1.5	1.5	1.5	1.5
Magnetic nanoparticle size (nm)		0-30	0-20	0-20	0-20	0-20	20
Figure Number		Figure 1	Figure 2	Figure 3	Figure 4	Figure 5	Figure 6-7

6.3 Results and Discussion

6.3.1 Relaxation Mechanism

To optimize the heating efficiency of *in vivo* nano-theranostic hyperthermia in the presence of MRI, we began by analyzing the change that took place in the relaxation processes, since they measure the response of magnetization to the applied magnetic field. Both the Brownian relaxation time constant (τ_B, dashed line) and the Néel relaxation time constant (τ_N, solid line) were derived from equation 4 using the eigenvalue approach to show the magnetic field's effect on the relaxation processes and plotted as a function of nanoparticle diameter with the consideration of aggregation, as illustrated in Figure 1. Two cases were presented here: in the absence of an MRI DC field (green for τ_B and black for τ_N), and in the presence of a 1.5T DC field (red for τ_B and blue for τ_N), which is the most common amplitude used in clinical MRI. The amplitude and the frequency of the alternating magnetic field were set up as 25mT and 400kHz, respectively.

The overall values of τ_B and τ_N calculated by assuming a 1.5T MRI field were much smaller than the values of τ_B and τ_N calculated in the absence of MRI. Particularly, the Néel relaxation process was more sensitive to the magnetic field change than the Brownian relaxation process, by several orders of magnitude. By comparing dashed lines with solid lines, one sees that the size range of the magnetic nanoparticles affected by the Néel relaxation process was

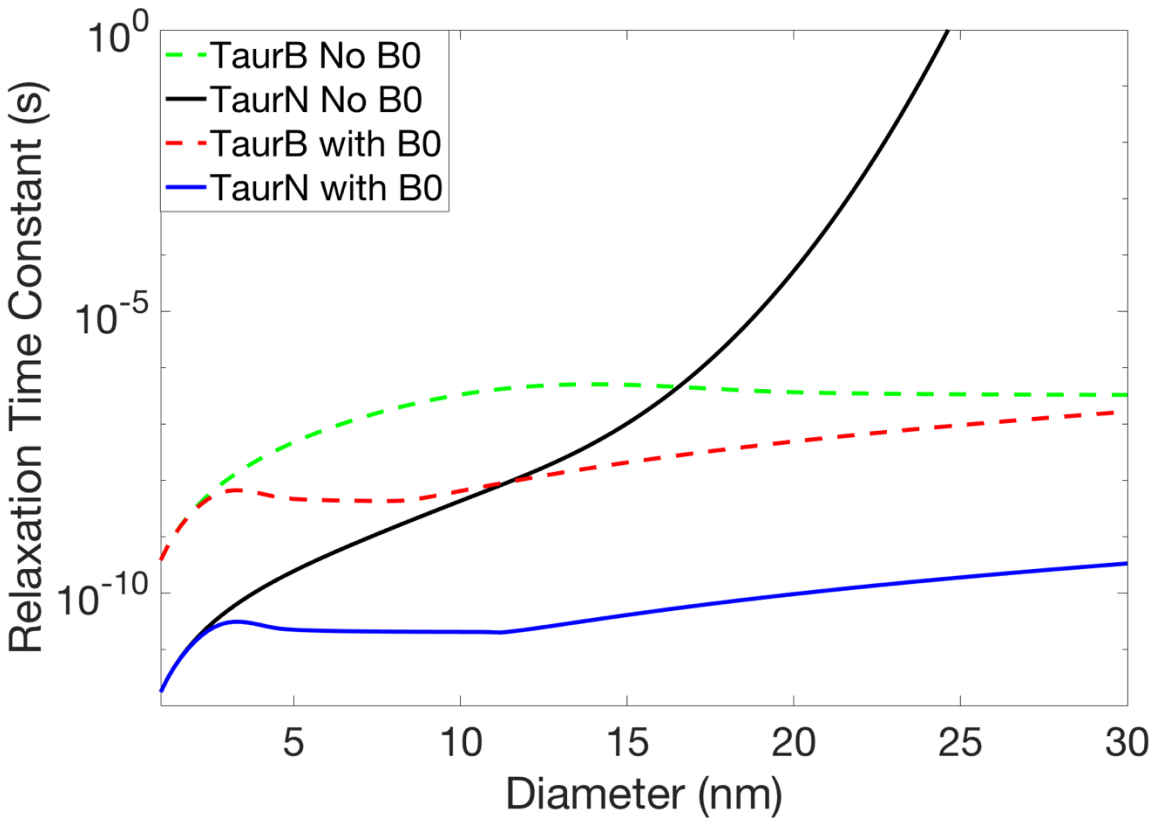


Figure 1. Relaxation time constants for pure Brownian (τ_B, dashed line) and pure Néel (τ_N, solid line) processes as a function of the nanoparticle diameter in the absence of an MRI DC field (green for τ_B and black for τ_N) and in the presence of an MRI DC field with an amplitude of $B_0 = 1.5T$ (red for τ_B and blue for τ_N). Both relaxation time constants were from derived from equation 4 using the eigenvalue approach. The major parameters used for the calculation are summarized in Table 1.

wider than the range of those affected in Brownian relaxation process. Recall that the effect of the magnetic field on the relaxation mechanism, on the one hand, prevents particles from freely rotating in the fluid, thus reducing the Brownian relaxation effect, while on the other hand, the symmetry of the magnetic energy density is broken, thus reducing the energy barrier and

accelerating the Néel relaxation process. Particularly in the presence of an MRI DC field, the strong bias magnetic field not only freezes the rotation of magnetic nanoparticles but also saturates the magnetization of colloidal nanoparticles, causing the Néel relaxation process to dominate, regardless of the particle size.

The analysis becomes more complicated when evaluating the heating efficiency, as the various physical properties of the magnetic nanoparticles and alternating magnetic field settings can trigger the nonlinear response of the magnetic susceptibility. Moreover, the phase delay induced by the frequency change of the alternating magnetic field influences the dominant relaxation process, which affects the optimization of the heating efficiency in *in vivo* MR nano-theranostic hyperthermia.

6.3.2 Heating Efficiency Predictions

The heating efficiency, which is usually represented by the specific loss power (SLP), was evaluated using equation 16, taking into consideration the aggregation, the nonlinear response of the magnetic susceptibility, and the magnetic field's effect on relaxation processes. In order to optimize the heating efficiency of colloidal magnetic nanoparticles in MR hyperthermia for the purpose of clinical theranostics, the Fokker-Planck equation for the Brownian relaxation (equation 1a) and the Néel relaxation (equation 1b) was solved numerically to determine the range of possible settings for the applied alternating magnetic field, including its shape, orientation, and frequency.

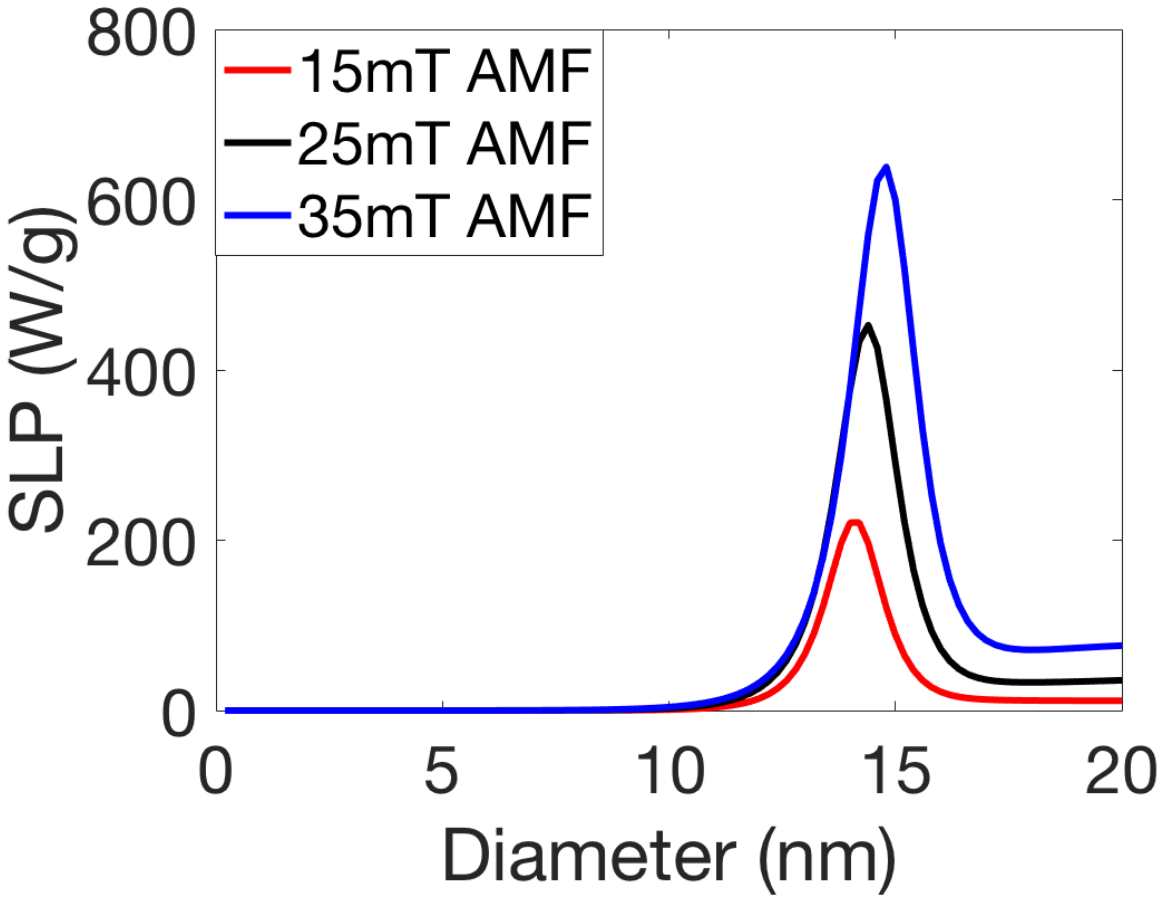


Figure 2. Theoretical SLP plotted as a function of nanoparticle diameter, accounting for the effect of magnetic field-dependent relaxation time, the nonlinear response of the magnetic susceptibility, and the formation of aggregate. An alternating magnetic field (AMF) with the same frequency of 200kHz but different magnitudes was applied in the absence of an MRI DC field: 15mT (solid red line), 25mT (solid black line), and 35mT (solid blue line). Both Brownian and Néel relaxation processes take place "in parallel". SLP values were calculated using equation 16, and major parameters the regarding physical properties of the magnetic nanoparticles are summarized in Table 1.

We began with the simplest case of no MRI DC field being applied, where both Brownian relaxation process and Néel relaxation process take place "in parallel". As shown in Figure 2, the heating efficiency can be improved by imposing a stronger alternating magnetic field. However, the nonlinear response of the magnetic susceptibility also becomes significant with the increase in amplitude of the applied alternating magnetic field, particularly for larger magnetic nanoparticles. The optimal SLP value can be achieved using magnetic nanoparticles with a diameter of 14nm-16nm.

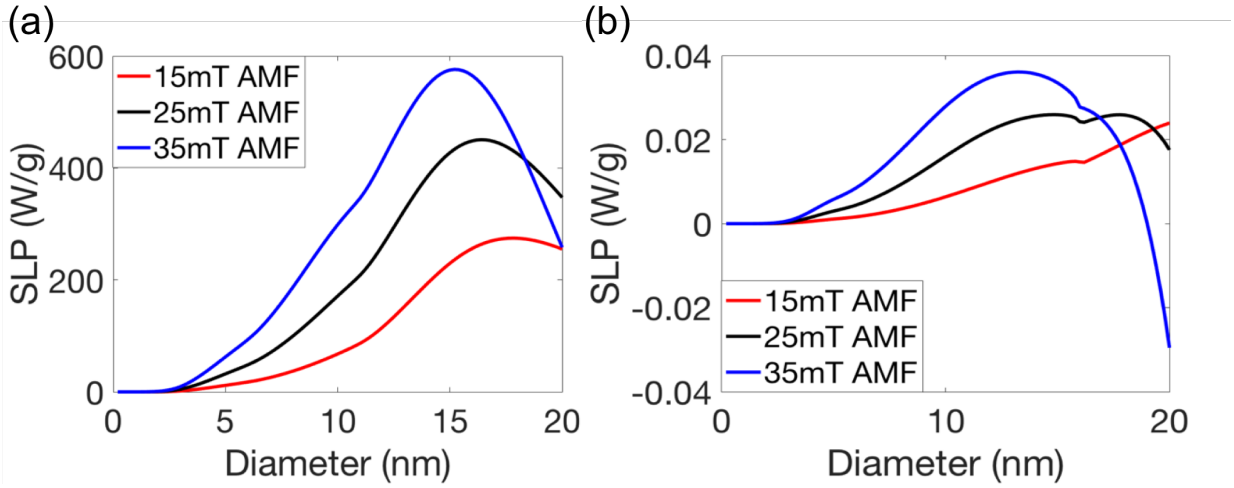


Figure 3. Theoretical SLP plotted as a function of nanoparticle diameter in the presence of an MRI DC field with an amplitude of 1.5T. The dominant relaxation mechanism for (a) is pure Brownian relaxation process, and (b) is pure Néel relaxation process. The frequency of the applied alternating magnetic field is 200kHz, while the amplitudes of the applied alternating magnetic field were 15mT (solid red line), 25mT (solid green line), and 135mT (solid black line), respectively. SLP values were calculated using equation 16, and major parameters regarding the physical properties of the magnetic nanoparticles are summarized in Table 1.

In the presence of a high-field MRI, which in clinical applications typically has an amplitude of 1.5T, the SLP value was also plotted as a function of the nanoparticle diameter with respect to an alternating magnetic field with the same frequency of 200kHz but different amplitudes, as shown in Figure 3. We considered two relaxation mechanisms: the pure Brownian relaxation process (Figure 3a) and the pure Néel relaxation process (Figure 3b). The comparison shows that, for identical magnetic settings, the SLP value is much greater if the dominant relaxation process is Brownian relaxation. This is because, in the presence of an MRI field, the magnetization of the nanoparticles is approaching saturation. Their magnetic moments remain "locked" in parallel with the applied DC field, resulting in the Brownian relaxation time constants being greater than the Néel relaxation time constants. This difference becomes significantly more pronounced with a stronger DC magnetic field, since Néel relaxation is more sensitive to the magnetic field change. It should also be noted that SLP increased with the elevation of the alternating magnetic field amplitude, regardless of the dominant relaxation process. This response can be understood in the way that the sinusoidal field excitation partially "unfreezes" some of the nanoparticles as the amplitude increases. The SLP decreased when larger magnetic nanoparticles were employed and, as a result of nonlinear response of the magnetic susceptibility, the decrease became more pronounced when a stronger alternating magnetic field was applied.

The relaxation time constants illustrated in Figure 1 indicated to us that, under the influence of a strong bias magnetic field, the Néel relaxation process should dominate even though the SLP based on the Brownian relaxation mechanism is several orders of magnitude greater than the SLP based on the Néel relaxation mechanism, because the Néel relaxation time constant is so much smaller than the Brownian relaxation time constant. Therefore, boosting the

SLP values based on the Néel relaxation process and triggering the Brownian relaxation process become two important keys to improving the heating efficiency of *in vivo* nano-theranostic hyperthermia in the presence of MRI.

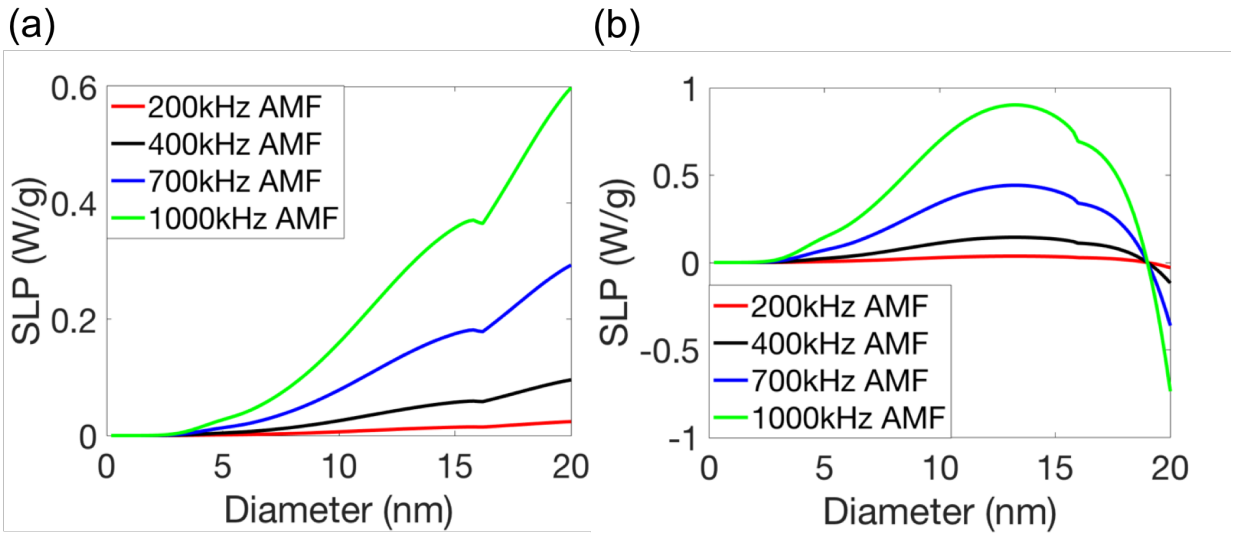


Figure 4. Theoretical SLP plotted as a function of nanoparticle diameter in the presence of an MRI DC field with an amplitude of 1.5T and an alternating magnetic field with an amplitude of (a)15mT and (b)35mT. The dominant relaxation mechanism is the pure Néel relaxation process. The frequencies of the applied alternating magnetic field were 200kHz (solid red line), 400kHz (solid black line), 700kHz (solid black line), and 1000kHz (solid green line). SLP values were calculated using equation 16, and the major parameters of the physical properties of the magnetic nanoparticles are summarized in Table 1.

When Néel relaxation is the dominant process, one way to improve the heating efficiency is to apply a high frequency-driven alternating magnetic field instead of continuing to strengthen the amplitude of the alternating magnetic field. As the results show in Figure 4, where theoretical SLP values were plotted as a function of the nanoparticle diameter with different frequency

settings, heating efficiency increased in conjunction with increases in the frequency of the alternating magnetic field. Comparing the SLP based on a 15mT alternating magnetic field to the SLP based on a 35mT alternating magnetic field shows how a stronger alternating magnetic field can amplify the nonlinear response of the magnetic susceptibility for large magnetic nanoparticles and thus improve the heating efficiency.

Another option, shown in Figure 5, is using a rotating magnetic field (solid blue line) instead of an alternating magnetic field (solid red line). Both fields have the same amplitude of 15mT and the same frequency of 400kHz. The rotating field is generated by means of an imposed, *y*-directed flux density of amplitude $B_e = \mu_0 H_0$, which is temporally displaced by a quarter time period from the x component.

For most clinical applications of *in vivo* MR nano-theranostic hyperthermia, magnetic nanoparticles will be co-encapsulated with a therapeutic drug and an MR imaging contrast agent inside a thermosensitive liposome. The nanoparticles' adherence or binding at the tumor site freezes their rotation, causing the Néel relaxation process to become dominant. However, even the significant improvement in SLP that is achieved by following the proposed strategy based on the Néel relaxation mechanism is negligible when compared to the SLP improvement without MRI. As shown in both Figure 4 and Figure 5, the maximum achievable heating efficiency is under 5W/g. Therefore, rather than heating tumor cells directly, the limited heat generated by magnetic nanoparticles can be used to increase the permeability of the thermosensitive liposome, thus triggering the extravasation and bioavailability of the encapsulated therapeutic drug at the tumor site. In addition, the slightly higher temperature achieved through mild hyperthermia was shown improve the efficacy of the drug. To conduct such a drug delivery and therapeutic procedure in conjunction with an MRI diagnostic and monitoring system, it is recommended to

place small magnetic nanoparticles in a high-frequency driven rotating magnetic field (such as 1000kHz) with moderate amplitude of around 50mT.

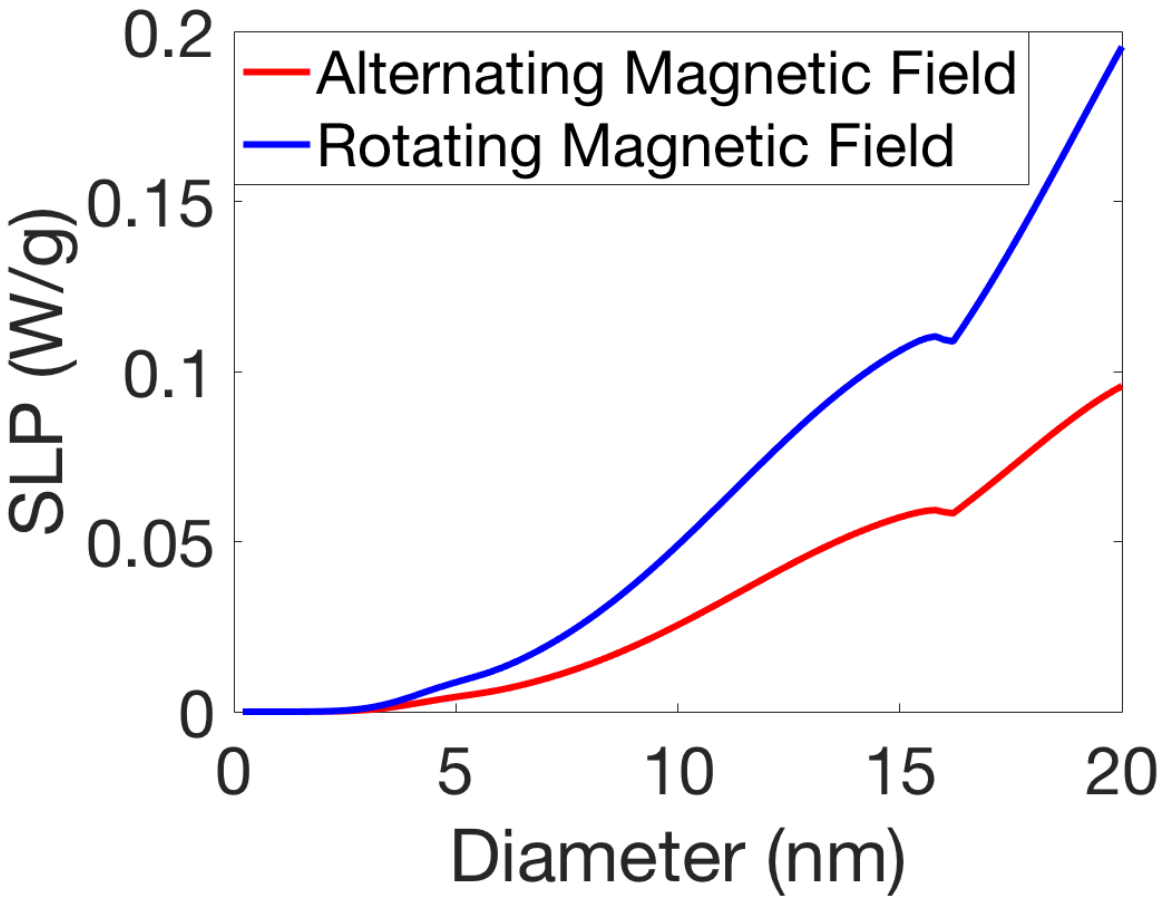


Figure 5. Theoretical SLP plotted separately as a function of nanoparticle diameter in the presence of an MRI DC field with an amplitude of 1.5T imposed on a 15mT alternating magnetic field with a frequency of 400kHz (solid red line), and a 15mT rotating magnetic field with a frequency of 400kHz (solid black line). The dominant relaxation mechanism is the Néel relaxation process. SLP values were calculated using equation 16, and the major parameters of the physical properties of the magnetic nanoparticles are summarized in Table 1.

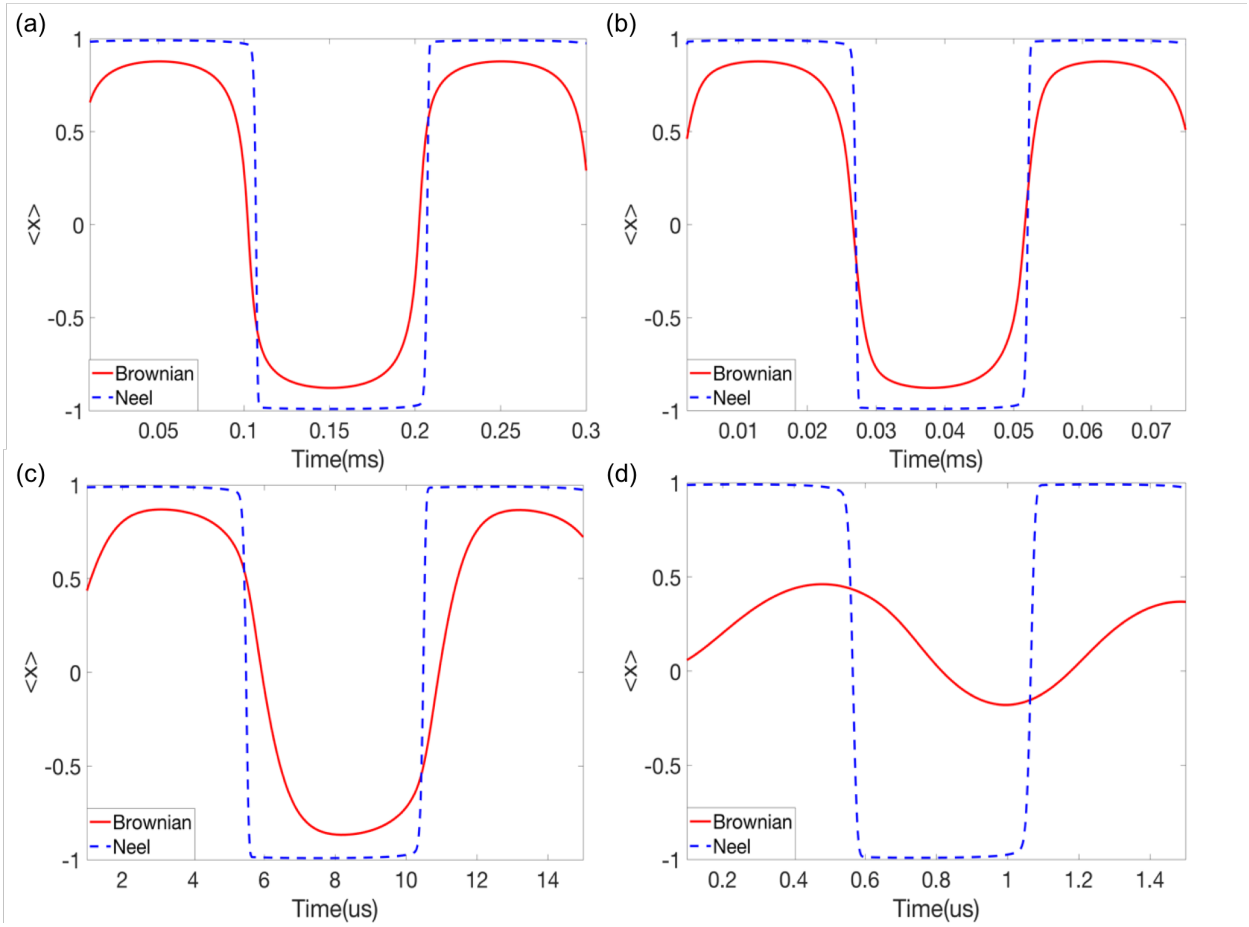


Figure 6. The time series of the normalized magnetization, $M(t)/nm_0 = \langle x(t) \rangle$, for Brownian relaxation (solid red line) and for Néel relaxation (dashed blue line) in the presence of a 150mT sinusoidal alternating magnetic field with various values for the driving frequency, (a)5kHz, (b)20kHz, (c)100kHz, and (d) 1000kHz. The diameter of the magnetic nanoparticles is 20nm. The response of the magnetization was solved using equation 1, and other major parameters regarding physical properties of magnetic nanoparticles are summarized in Table 1.

To trigger the Brownian relaxation process, it is important to take advantage of the phase lag in the presence of a low frequency-driven alternating magnetic field. When the frequency is as low as 5 kHz, as shown in Figure 6a, the phase of the magnetization for the Néel time series

lags that of the Brownian time series. Thus, the particles in the ferrofluid are able to rotate nearly 180° before the Néel mechanism can contribute to the relaxation, which creates the opportunity for the Brownian relaxation process to take place. Increasing the frequency to 20kHZ, as shown in Figure 6b, allows the nanoparticle as a whole to begin to rotate before the Néel relaxation comes into play. For this reason, it is necessary to treat both processes as occurring in parallel. However, when the frequency is set to around 100kHz (Figure 6c), or even as high as 1000kHz (Figure 6d), it is clear that Néel relaxation becomes the dominant mechanism responsible for heating. The occurrence of the Brownian relaxation mechanism requires that, in addition to the specific magnetic settings, the magnetic nanoparticles are of medium size and properly coated to ensure their sufficient dispersion in the fluid.

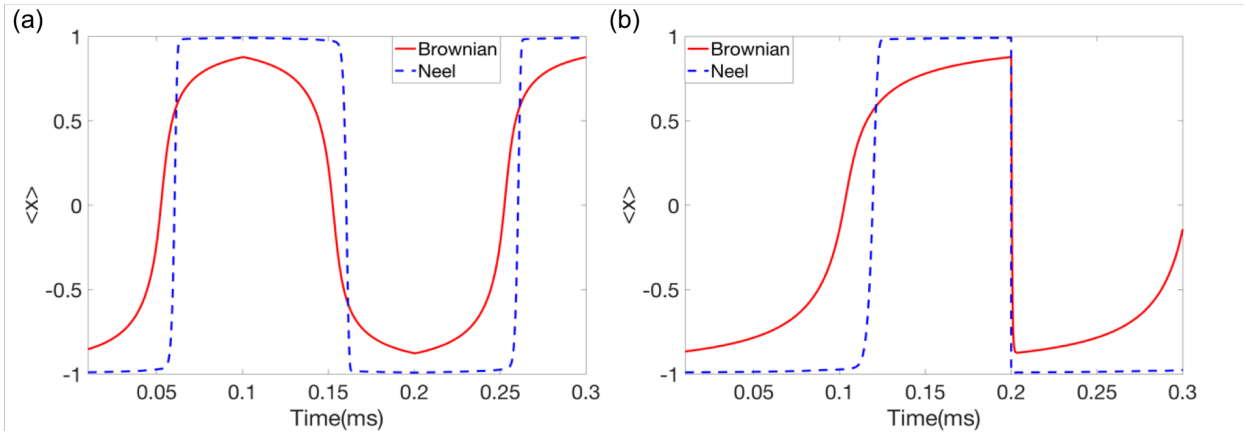


Figure 7. The time series of the normalized magnetization, $M(t)/nm_0 = \langle x(t) \rangle$, for Brownian relaxation (solid red line) and for Néel relaxation (dashed blue line) in the presence of a 150mT, 5kHz alternating magnetic field with (a) triangular magnetic field, and (b) linearly ramped magnetic field. The diameter of the magnetic nanoparticles is 20nm. The response of the magnetization was solved using equation 1, and other major parameters regarding the physical properties of the magnetic nanoparticles are summarized in Table 1.

An alternating magnetic field with different shapes but the same amplitude of 150mT and a frequency of 5kHz was also applied to magnetic nanoparticles. In comparison to the time series of the normalized magnetization illustrated in Figure 7a, the triangular magnetic field is able to further trigger the Brownian relaxation to come into play before the Néel Relaxation process. And if we shape the magnetic field linearly ramped, as shown in Figure 7b, the nanoparticle as a whole can rotate 180°, allowing for Brownian relaxation to be the dominant heating generation mechanism.

The results shown in Figure 6 and Figure 7 gave us an important insight into the efficient heating of magnetic nanoparticles in *in vivo* MR nano-theranostic hyperthermia. Track back to the heat generation mechanism through the Brownian relaxation process, where the entire magnetic nanoparticle rotates mechanically towards the external field and against the viscous drag in the suspending medium. In the presence of a high-field MRI, magnetic moments remain "locked" in parallel with the applied DC field, but increasing the amplitude of the alternating magnetic field can partially unfreeze the "locked" magnetic nanoparticles and free them to rotate. Combined with the built-in MRI gradients, we were able to localize a weaker field area and apply a low-frequency driven (around 5kHz) alternating magnetic field with a linearly ramped shape to ensure the Brownian relaxation took place before the magnetization became saturated.

6.4 Conclusion

The *in vivo* MR hyperthermia system has been demonstrated to be a novel theranostic approach for cancer treatment that simultaneously diagnoses early stage tumors and monitors drug release. We proposed to evaluate the heating efficiency of magnetic nanoparticles for

hyperthermia in the presence of an MRI DC field by accounting for the aggregation of magnetic nanoparticles, the nonlinear response of the magnetic susceptibility, and the effect of the magnetic field on the relaxation process. We showed that the presence of a high-field MRI significantly shortens both the Brownian and Néel relaxation processes, and saturates the magnetization. As a result, the heating efficiency of the magnetic nanoparticles is reduced by many orders of magnitude. When superimposed on the alternating magnetic field, the nonlinear response of the magnetic susceptibility further complicates the SLP analysis. For the purpose of optimizing the heating efficiency of *in vivo* theranostic hyperthermia in the clinical MRI environment, we recommended heating small magnetic nanoparticles co-encapsulated inside thermosensitive liposomes with a therapeutic drug using a high frequency-driven rotating magnetic field, where the Néel relaxation is the dominant process, or else placing medium-size magnetic nanoparticles in a low frequency-driven, linearly ramped alternating magnetic field combined with a built-in MRI gradient to trigger the Brownian relaxation mechanism and thus improve the heating efficiency. We believe the use of this novel model can lead to improved clinical outcomes by helping researchers determine the optimal magnetic and structural properties of the magnetic nanoparticles, tailor synthesis methods for specific alternating magnetic field frequency and amplitude conditions, and make reliable predictions about the performance of thermal dosimetry.

6.5 References

[1] Zhou, H.; Qian, W.; Uckun, F. M.; Wang, L.; Wang, Y. A.; Chen, H.; Kooby, D.; Yu, Q.; Lipowska, M.; Staley, C. A.; Mao, H.; Yang, L. IGF1 Receptor Targeted Theranostic

Nanoparticles for Targeted and Image- Guided Therapy of Pancreatic Cancer. *ACS Nano*. **2015**, *9*, 7976-7991.

[2] Sanson, C.; Diou, O.; The venot, J.; Ibarboure, E.; Soum, A.; Bru^let, A.; Miraux, S.; Thiaudie re, E.; Tan, S.; Brisson, A.; Dupuis, V.; Sandre, O.; Lecommandoux, S. Doxorubicin Loaded Magnetic Polymersomes: Theranostic Nanocarriers for MR Imaging and Magneto-Chemotherapy. *ACS Nano*. **2011**, *5*, 1122-1140.

[3] Fazal, S.; Paul-Prasanth, B.; Nair, S. V.; Menon, D. Theranostic Iron Oxide/Gold Ion Nanoprobes for MR Imaging and Noninvasive RF Hyperthermia. *ACS Appl. Mater. Interfaces.* **2017**, *9*, 28260-28272.

[4] Ho, D.; Sun, X.; Sun, S. Monodisperse Magnetic Nanoparticles for Theranostic Applications. *Acc. Chem. Res*. **2011**, *44*, 875-882.

[5] Yoo, D.; Lee, J.; Shin, T.; Cheon, J. Theranostic Magnetic Nanoparticles. *Acc. Chem. Res*. **2011**, *44*, 863-874.

[6] Béalle, G.; Di Corato, R.; Kolosnjaj-Tabi, J.; Dupuis, V.; Clement, O.; Gazeau, F.; Wilhelm, C.; Ménager, C. Ultra Magnetic Liposomes for MR Imaging, Targeting, and Hyperthermia. *Langmuir.* **2012**, *28*, 11834-11842.

[7] Jordan, A.; Wust, P.; Fähling, H.; John, W.; Hinz, A.; Felix, R. Inductive Heating of Ferrimagnetic Particles and Magnetic Fluids: Physical Evaluation of Their Potential for Hyperthermia. *Int. J. Hyperthermia*. **1993**, *9*, 51–68.

[8] Jordan, A.; Wust, P.; Scholz, R.; Tesche, B.; Fähling, H.; Mitrovics, T.; Vogl, T.; Cervós-Avarro, J.; Felix, R. Cellular Uptake of Magnetic Fluid Particles and Their Effects on Human Adenocarcinoma Cells Exposed to AC Magnetic Fields In Vitro. *Int. J. Hyperthermia*. **1996**, *12*, 705–722.

[9] Hergt, R.; Dutz, S.; Röder, M. Effects of Size Distribution on Hysteresis Losses of Magnetic Nanoparticles for Hyperthermia. *J. Phys.: Condens. Matter*. **2008**, *20*, 385214.

[10] Dutz, S.; Hergt, R. Magnetic Nanoparticle Heating and Heat transfer on a Microscale: Basic Principles, Realities and Physical Limitations of Hyperthermia for Tumour Therapy. *Int. J. Hyperthermia*. **2013**, 2*9*, 790–800.

[11] Delannoy, J.; LeBihan, D.; Levin, R.; Hoult, D. Hyperthermia System Combined with MRI Unit. *Proc. Annu. Int. Conf. IEEE. Eng. Med. Biol. Soc.* **1988**, *1*, 344-345.

[12] Gellermann, J.; Wlodarczyk, W.; Hildebrandt, B.; Ganter, H.; Nicolau, A.; Rau, B.; Tilly, W.; Fahling, H.; Nadobny, J.; Felix, R.; Wust, P. Noninvasive Magnetic Resonance Thermography of Recurrent Rectal Carcinoma in a 1.5 Tesla Hybrid System. *Cancer. Res*. **2005**, *65*, 5872–5880.

[13] Pittet, M. J.; Swirski, F. K.; Reynolds, F.; Josephson, L.; Weissleder, R. Labeling of Immune Cells for in Vivo Imaging Using Magnetofluorescent Nanoparticles. *Nat. Protoc.* **2006**, *1*, 73−79.

[14] Jun, Y. W.; Jang, J. T.; Cheon, J. Magnetic Nanoparticle Assisted Molecular MR Imaging. *Adv. Exp. Med. Biol*. **2007**, *620*, 85−106.

[15] Gazeau, F.; Levy, M.; Wilhelm, C. Optimizing Magnetic Nanoparticle Design for Nanothermotherapy. *Nanomedicine*. **2008**, *3*, 831−844.

[16] Johannsen, M.; Thiesen, B.; Wust, P.; Jordan, A. Magnetic Nanoparticle Hyperthermia for Prostate Cancer. *Int. J. Hyperthermia*. **2010**, *26*, 790−795.

[17] Cervadoro, A.; Giverso, C.; Pande, R.; Sarangi, S.; Preziosi, L.; Wosik, J.; Brazdeikis, A.; Decuzzi, P. Design Maps for the Hyperthermic Treatment of Tumors with Superparamagnetic Nanoparticles. *PLoS One.* **2013**, *8*, e57332.

[18] Cantillon-Murphy, P.; Wald, L. L.; Zahn, M.; Adalsteinsson, E. Proposing Magnetic Nanoparticle Hyperthermia in Low-field MRI. *Concepts. in Magn. Reson. A*. **2010**, *36*, 36–47.

[19] Rosensweig, R. E. Heating Magnetic Fluid with Alternating Magnetic Field. *J. Magn. Magn. Mater*. **2002**, *252*, 370–374.

[20] Castro, L. L.; da Silva, M. F.; Bakuzis, A. F.; Miotto, R. Aggregate Formation on Polydisperse Ferrofluids: A Monte Carlo Analysis. *J. Magn. Magn. Mater*. **2005**, *293*, 553–558.

[21] Wang, C.; Li, Z.; Lin, Y. Y. Optimizing Magnetic Nanoparticles Hyperthermia Effect in MR Nanomedicine. *Chinese Journal of Magnetic Resonance*. **2015**, *32*, 248-260

[22] Deissler, R. J.; Wu, Y.; Martens, M. A. Dependence of Brownian and Néel Relaxation Times on Magnetic Field Strength. *Med. Phys.* **2014**, *41*, 012301.

[23] De´jardin, J. L. Fractional Dynamics and Nonlinear Harmonic Responses in Dielectric Relaxation of Disordered Liquids. *Phys. Rev*. **2003**, *68*, 031108.

[24] Giannitsis, A. T.; Fannin, P. C.; Charles, S. W. Nonlinear Effects in Magnetic Fluids. *J. Magn. Magn. Mater*. **2005**, *289*, 165–167.

[25] Fannin, P. C.; Oireachtaigh, C. M. Investigating the Isotropic Properties of a Magnetic Fluid Following the Removal of a Polarising Field. *J. Magn. Magn. Mater*. **2007**, *316*, e802–e804.

[26] Singh, V.; Banerjee, V.; Sharma, M. Dynamics of Magnetic Nanoparticle Suspensions. *J. Phys. D.: Appl. Phys*. **2009**, *42*, 245006.

[27] Verde, E. L.; Landi, G. T.; Carrião, M. S.; Drummond, A. L; Gomes, J. A.; Vieira, E. D.; Sousa, M. H.; Bakuzis, A. F. Field Dependent Transition to the Non-Linear Regime in

Magnetic Hyperthermia Experiments: Comparison Between Maghemite, Copper, Zinc, Nickel, and Cobalt Ferrite Nanoparticles of Similar Sizes. *AIP Adv*. **2012**, *2*, 032120.

[28] Debye, P. Polar Molecules. *The Chemical Catalog Co*. Dover: New York, **1929**.

[29] Néel, L. Theorie du Trainage Magnetique des Ferromagnetiques en Grains Fins avec Applications aux Terres Cuites. *Geophysics*. **1949**, *5*, 99–136.

[30] Coffey, W. T.; Kalmykov, Y. P.; Waldron, J. T. The Langevin Equation. *World Scientific*: Singapore, **2004**.

[31] Morais, P. C.; Gonçalves, G. R. R.; Bakuzis, A. F.; Neto, K. S.; Pelegrini, F. Experimental Evidence of Dimer Disruption in ionic Ferrofluid: A Ferromagnetic Resonance Investigation. *J. Magn. Magn. Mater*. **2001**, *225*, 84–88.

[32] Zhong, J.; Xiang, Q.; Massa, L. O.; Qu, F.; Morais, P. C.; Liu, W. Second-Order-Like Cluster-Monomer Transition within Magnetic Fluids and Its Impact upon the Magnetic Susceptibility. *Nanoscale Res. Lett*. **2012**, *7*, 167.

[33] Wang, C.; Hsu, C. H.; Li, Z.; Hwang, L. P.; Lin, Y. C.; Chou, P. T.; Lin, Y. Y. Effective Heating of Magnetic Nanoparticle Aggregates for In Vivo Nano-theranostic Hyperthermia. *Int. J. Nanomedicine*. **2017**, *12*, 6273–6287.

[34] Coffey, W. T.; Paranjape. B. V. Dielectric and Kerr Effect Relaxation in Alternating Electric Fields. *Proc. Roy. Irish Acad*. **1978**, *78*, 17–25.

[35] Oireachtaigh, C. M.; Fannin, P. C. Investigation of the Non-Linear Loss Properties of Magnetic Fluids Subject to Large Alternating Ffields. *J. Magn. Magn. Mater*. **2008**, *320*, 871–880.

[36] Cantillon-Murphy, P.; Wald, L. L.; Adalsteinsson, E; Zahn, M. Heating in the MRI Environment due to Superparamagnetic Fluid Suspensions in a Rotating Magnetic Field. *J. Magn. Magn. Mater.* **2010**, *322*, 727–733.

[37] Tay, Z. W.; Chandrasekharan, P.; Chiu-Lam, A.; Hensley, D. W.; Dhavalikar, R.; Zhou, X. Y.; Yu, E. Y.; Goodwill, P. W.; Zheng, B.; Rinaldi, C.; Conolly, S. M. Magnetic Particle Imaging-Guided Heating *in Vivo* Gradient Fields for Arbitrary Localization of Magnetic Hyperthermia Therapy. *ACS Nano*. **2018**, *12*, 3699-3713.

Chapter 7

Designing a Sparse Sensing Matrix for Compressive Sensing to Reconstruct High Contrast MR Images in Early Tumor Detection

7.0 Abstract

Despite the numerous advantages of using Magnetic Resonance Imaging (MRI) in the clinical biomedical diagnosis of early stage tumors, its application is severely limited by the time and expense of image acquisition. Compressive sensing (CS) has been used in a diverse set of MRI methods to reduce the image acquisition time. The critical task in this mathematical framework is to carefully design a sensing matrix that can extract all the important MR features from highly under-sampled measurements. Most existing methods in the literature attempted to select data normally from Gaussian or other random distributions; however, these approaches required a sophisticated sensing matrix structure that requires a large amount of memory and is very challenging to implement. In this current paper, we proposed a patch structure for the sensing matrix based on centrally concentrated sampling. The experimental and simulation results clearly confirmed that the proposed approach, in spite of its simplicity, can yield higher reconstruction correlation coefficients and contrast-to-noise ratios with less sparsity than the existing methods. The proposed method also outperformed the existing methods in computation time by speeding up recovery algorithms. With advanced image acquisition techniques, the proposed sensing matrix becomes increasingly important for reducing scanning time for patients, avoiding physiological effects, and speeding up the image processing of dynamic structures.

7.1 Introduction

In the last decade, Magnetic Resonance Imaging (MRI) has shown great potential in the clinical biomedical diagnosis of early stage tumors due to its use of noninvasive radiation and, particularly, the fact that the sensitivity of its images to tissue properties can be extensively enhanced by alternating the timing with which MR signals are collected and by using magnetization preparation or a contrast agent. However, the lengthy image acquisition time has always been a barrier to its further application in routine clinical practice.

Images are typically formed by taking the Fourier Transform of the individually-collected gradient-encoded k-space data,[1] which must be acquired to meet the Nyquist sampling theorem.[2-3] Researchers have long been working on designing different pulse sequences, such as FLASH and RARE, to reduce the acquisition time.[4-6] By shortening either the repetition time or the number of echoes, they were able to improve the efficiency of imaging by a few orders of magnitude. Recently, alternative methods, known as compressive sensing (CS),[7-8] have been proposed to significantly reduce the image acquisition time by not having to collect the entire k-space data demanded by the Nyquist criterion. Nevertheless, how to best design a practical sensing matrix and computationally efficient recovery algorithms for compressed sensing is still under investigation.

The role played by the sensing matrix is vital in the faithful reconstruction of images. A dense sensing matrix requires significant storage space, which results in high computational costs. The CS experts originally showed that random sensing matrices, such as the Gaussian matrix, were suitable for solving the compressive sensing problem and leading to precise image recovery.[7,9] However, the drawbacks of such sensing matrices are that the high number of

required measurements is not optimal and the memory required when using random sampling techniques is not minimized.

Different measuring algorithms have been proposed to improve the performance of sensing matrices in signal sampling within the CS framework. Some groups attempted to design a specific, randomized structure for the sensing matrix. Others proposed to optimize the existing randomized sensing matrix. For example, Lustig *et al* proposed a Monte Carlo scheme for random incoherent sampling, believing that better performance can be achieved with more undersampling in the periphery of k-space and less undersampling near the k-space origin.[8] Poisson disk in Cartesian sampling, radical sampling, and spiral sampling were also proposed for collecting more data at the center of k-space with decreased density towards the periphery.[10-15] Wang *et al* proposed a variable density sampling strategy by exploiting the prior information about the statistical distributions of natural images in the wavelet domain.[16] Abolghasemi *et al* proposed an intermediate structure for the sensing matrix that was simple and yet performed comparably to conventional techniques.[17] And Tiwari *et al* designed an approach based on a sparse block circulant matrix with a few modifications that reduced the computation cost while maintaining the quality of the reconstructed image.[18]

In this current paper, we combined two categories of algorithms and proposed a patch structure for the sensing matrix based on a centrally concentrated sampling mechanism. The main advantages to this proposed technique are its simplicity and its improved performance compared to conventional techniques. The simulation and experimental results clearly confirmed that in spite of its simplicity, the reconstruction quality of proposed approach is comparable to the existing methods, with higher reconstruction correlation coefficients and an increased contrast-to-noise ratio with less sparsity. It also outperformed existing methods in computation

time by speeding up recovery algorithms. All presented figures have been processed with the MATLAB software package (The Mathworks, Natick, Massachusetts) using obtained MRI data. With advances in fast image acquisition techniques, the proposed sensing matrix becomes increasingly important for reducing scanning time on patients, avoiding physiological effects, and speeding up the image processing of dynamic structures.

7.2 Theory

The fundamental advantage of applying compressive sensing to MRI is that images acquired from MRI conveniently satisfy the sparsity requirement within the Fourier domain, where the data is collected. If we denote the recovered image as u, the measured sparse image as f, and the sensing matrix as A, we are able to reconstruct the image by solving the basis pursuit problem:[7-9]

$$\min_u \{\|u\|_1 : Au = f\} \quad (1)$$

It can be seen from equation 1 that the performance of image reconstruction depends on two factors: the recovery algorithm and the sensing matrix A.

7.2.1 Recovery Algorithm

Many algorithms have been proposed to reconstruct the sparse image sets. [19-22] In this paper, we made use of the Split-Bregman method to solve the $l1$ constrained minimization problem.[23] The Split Bregman method is a general technique for minimizing a large class of $l1$ regularized energies, and it is particularly well-suited to solving problems that arise in compressed sensing MRI. For this application, we wish to solve

$$\min_u \|\nabla u\|_1 + \frac{\lambda}{2}\|Au - f\|_2^2 \quad (2)$$

The left-most term in equation 2 enforces that the Fourier transform of the recovered image be compatible with the known portion of the k-space data. The right-most term in equation 2 enforces that the recovered image has a sparse gradient (i.e. that the recovered image be the "smoothest" image compatible with the observed k-space data).

The split Bregman method works by "decoupling" the $l1$ and $l2$ terms in equation 2 by introducing the auxiliary variable $d \leftarrow \nabla u$. The problem in equation 2 then becomes

$$\min_{u,d} \ \|d\|_1 + \frac{\lambda}{2}\|Au - f\|_2^2 \text{ such that } d = \nabla u \tag{3}$$

The resulting constrained problem is then solved using a Bregman iteration technique. While the formulation in equation 3 may seem more complicated than the original problem in equation 2, it is shown that the problem can be broken down into a sequence of simple sub-problems. Each of these sub-problems can be solved directly using only shrinkage operators and fast Fourier transforms. Moreover, the method is extremely effective at denoising.

7.2.2 Sparse Sensing Matrix

Most of the existing sensing matrices are normally selected from Gaussian or other random distributions. However, working with those matrices in practical applications is challenging. In addition to the challenge of incorporating the matrices into the hardware, they also require a large amount of memory. Sensing matrices with a specific structure can give rise to fast algorithms for matrix-vector multiplication, which will significantly speed up recovery algorithms. Thus, the typical sensing matrix in practice is not Gaussian or Bernouli, but one with a very specific structure. Therefore, we proposed a more practical sensing matrix which reduces the memory required for sampling data without degrading the reconstructed image quality.

Sparse representations of MR images exhibit a variety of significant nonrandom structures. For example, a high amplitude signal is concentrated close to the k-space origin is

essential for the delineation of contrast in the image, rendering early stage tumors distinguishable from normal tissue, while a low amplitude signal in the periphery of k-space affect the spatial resolution of images. For the purpose of improving the contrast-to-noise efficiency, the sensing matrix and sampling pattern should also reflect the underlying signal density of k-space. For this reason, we designed a cross-shaped patch structure for the sensing matrix, which naturally led to dense sampling at the center of k-space and decreasing density towards the periphery. Because the k-space being conjugated is symmetrical, the proposed sensing matrix can be divided into several patches in order to reduce storage requirements. Instead of regular undersampling patterns, which would have resulted in structured artifacts under inverse the Fourier transform, data points were collected randomly by constructing a probability density function (PDF). The percentage of data points required for reconstruction diminishes with the distance from the k-space origin, leading to a centrally concentrated random sampling pattern.

7.3 Results and Discussion

In compressive sensing MRI, the role played by the sensing matrix is vital to faithful image reconstruction. To assess the performance of our proposed patch sensing matrix, we first compared its structure and sampling mechanism to the prevailing Gaussian sensing matrix by illustrating data points collected from k-space using those two matrices. Then the average correlation coefficients and the average contrast-to-noise ratios, which represent the reconstruction quality, were calculated from the two matrices. By calculating and comparing the average reconstruction times via the same reconstruction algorithm, we showed that the patch sensing matrix is faster than the Gaussian sensing matrix in recovering images. In the end, representative results of images recovered by using the Gaussian sensing matrix and the patch

sensing matrix were compared; the comparison between the original images and the recovered images showed that the patch sensing matrix performed better in reconstructing MR images with a higher contrast, which improves early tumor detection.

7.3.1 Structure of the Sensing Matrix

Data points for the image reconstruction were collected using Gaussian and patch sensing matrices, as shown in Figure 1. Both matrices have the same dimensions as the original image, but the sparsity was only 50% with respect to the full k-space data. It can be seen from Figure 1that the Gaussian sensing matrix created a random sampling pattern, while the patch sensing matrix reflected the underlying signal density of k-space, which is not uniform but for the low-frequency components is most dense at the center of k-space and becomes sparser towards the periphery.

7.3.2 Reconstruction Quality of the Sensing Matrix

To compare the reconstruction performance of the Gaussian sensing matrix and the proposed patch sensing matrix, the image reconstruction quality indicator, including the correlation coefficient with the original image and the correlation coefficient at the tumor site, was computed for both the Gaussian sensing matrix and the patch sensing matrix. The overall random nature of sampling data points requires that the reconstruction be run for many different sets of missing data in order to obtain an accurate measurement for the quality indicator. Therefore, the average correlation coefficients calculated from 30 different sets were plotted as a function of sparsity in Figure 2. A comparison of the solid blue line and solid red line shows that the patch sensing matrix performed better than the Gaussian sensing matrix in image reconstruction, as the average correlation coefficients represented by the solid red line are greater than those represented by the solid blue line. More specifically, it can be seen that the average

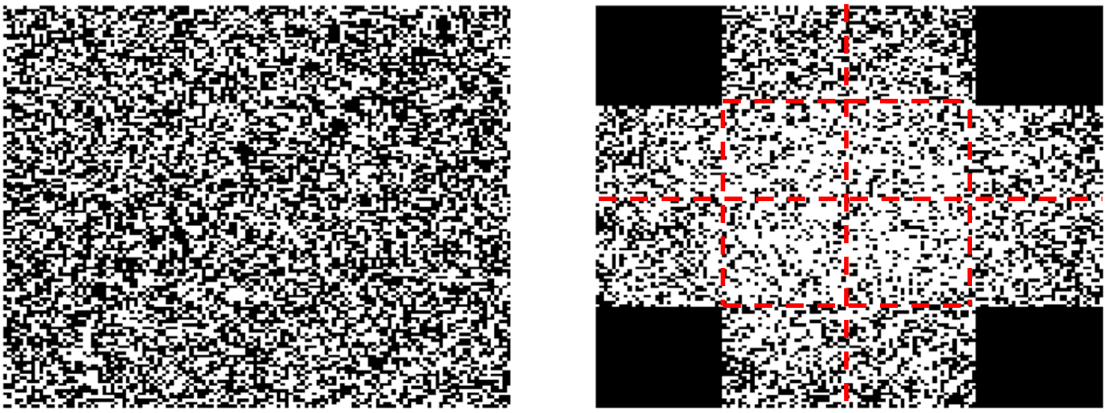


Figure 1. The structure and sampling mechanism of (left) the Gaussian sensing matrix and (right) the Patch sensing matrix. Both sensing matrices have the same dimensions as the original image, but the sparsity is only 50% with respect to the full k-space data.

correlation coefficient of the image calculated using the patch sensing matrix is almost 1.0 for as little as 50% of the original collected data, whereas the average correlation coefficient of the image is around 0.8 if using a 50% sparse Gaussian sensing matrix to recover the image. In addition, the Gaussian sensing matrix yielded poor reconstruction quality when less data was selected, as shown where the solid blue line drops dramatically with the increasing sparsity, while even at 70% sparsity the patch sensing matrix is still able to give a high-quality reconstruction with the average correlation coefficient of the image close to 0.8. Overall, both sensing matrices offered comparable reconstruction quality for the purpose of tumor detection when the average correlation coefficient at the tumor site was close to 1.0, but the proposed patch sensing matrix performed better than the Gaussian sensing matrix as the matrix sparsity increased.

The resulting average contrast-to-noise ratio (CNR), which was plotted as a function of sparsity in Figure 4, further confirmed the advantage of using the proposed patch sensing matrix in MRI. It can be seen that the patch sensing matrix (solid red line), in comparison to the Gaussian sensing matrix (solid blue line), was able to improve the CNR over 1.5 times with around 60% of the data collected. With the increase in the amount of unsampled data, both sensing matrices showed a decreasing trend in CNR values. However, the solid blue line drops faster and even elicited negative CNR values with the increasing sparsity, indicating that the original image was not recovered successfully, as excessive noise interfered with major MR features. This is because even though sufficient randomly selected data will result in a coherent, near-optimal reconstruction using the completely unstructured Gaussian matrix, as the sensing matrix sparsity increases, the reconstruction quality drops off dramatically. In contrast, the proposed patch sensing matrix reflects the underlying signal density of k-space, as most of the energy of the images is concentrated close to the k-space origin. Thus, the image that was recovered using the patch sensing matrix yielded better reconstruction quality in terms of the average correlation coefficients, and provided a robust and enhanced contrast-to-noise ratio to facilitate early tumor detection.

The use of the proposed patch sensing matrix not only saves time in signal acquisition, it also accelerates the reconstruction process. As shown in Figure 4, it took both sensing matrices less time to reconstruct the image when more data was collected; however, the recovery algorithm performed faster on the proposed patch sensing matrix than on the conventional Gaussian sensing matrix. This effect becomes more pronounced when the sparsity of sensing matrix is around 50%, where the patch sensing matrix was able to offer a higher quality reconstruction in terms of greater correlation coefficients and contrast-to-noise ratios. When

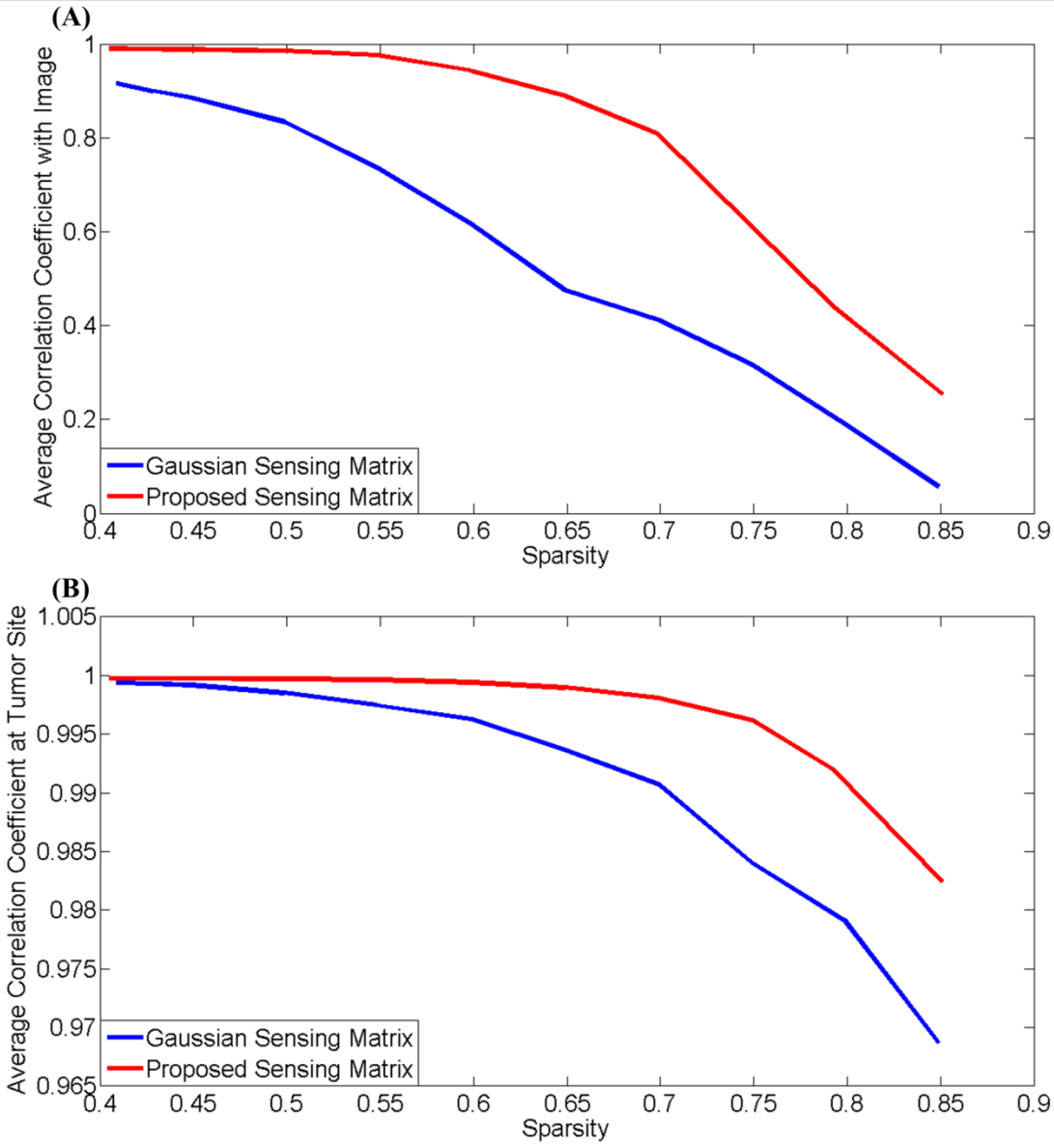


Figure 2. Plot of the average correlation coefficient with the image (A) and the average correlation coefficient at the tumor site (B) as a function of sparsity. Values of average correlation coefficients were computed from two reconstructions: recovered T2-weighted image using the Gaussian sensing matrix (solid blue line), and recovered T2-weighted image using the proposed patch sensing matrix (solid red line). 30 different sets of random sampled data were collected for an accurate measurement of the reconstruction performance.

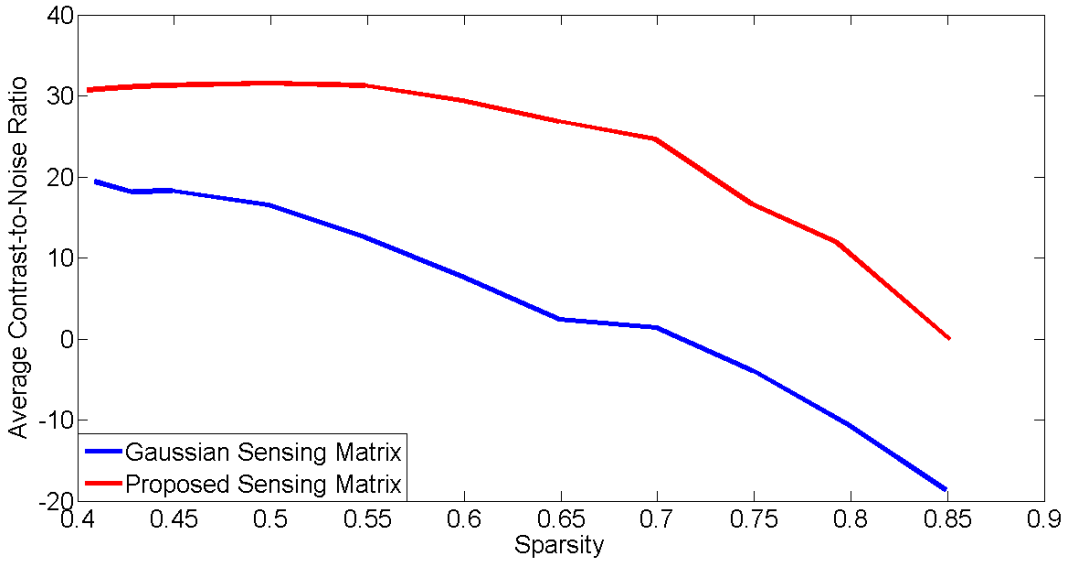


Figure 3. Plot of the average contrast-to-noise ratio as a function of sparsity. Values of CNR were computed from two reconstructions: a recovered T2-weighted image using a Gaussian sensing matrix (solid blue line), and a recovered T2-weighted image using the proposed patch sensing matrix (solid red line). 30 different sets of random sampled data were collected for an accurate measurement of the reconstruction performance.

increasingly less data was collected for image recovery, the calculation times began to fluctuate and both sensing matrices performed poorly in image reconstruction quality.

7.3.3 Experimental Image and Simulation Results

In vivo experiments and reconstruction simulations were carried out to further validate the advantages of applying the patch sensing matrix in recovering images. Stage-1 orthotopic glioblastoma (GBM) mouse models infected with the human U87MG cell line were imaged thirteen days after tumor implantation. The original T2-weighted image that was reconstructed using the full k-space data (A) was separately compared to the recovered images using the Gaussian sensing matrix (B) and the proposed patch sensing matrix (C). Both sensing matrices

are 50% sparse and have the same dimension as the original k-space. As the results show in Figure 5, recovered images revealed important features and details, such as the shape of the brain, the size of the tumor, and white and gray matters. However, since only 50% of the original data was collected, the Gaussian sensing matrix performed poorly in image recovery relative to the patch sensing matrix. In addition to the smaller average correlation coefficients and contrast-to-noise ratios as calculated and shown in Figure 2 and Figure 3, it can be seen that, in comparison to the smooth image (C) recovered by the patch sensing matrix, the Gaussian sensing matrix yielded a blurrier and noisier image (B), which became more problematic at the tumor

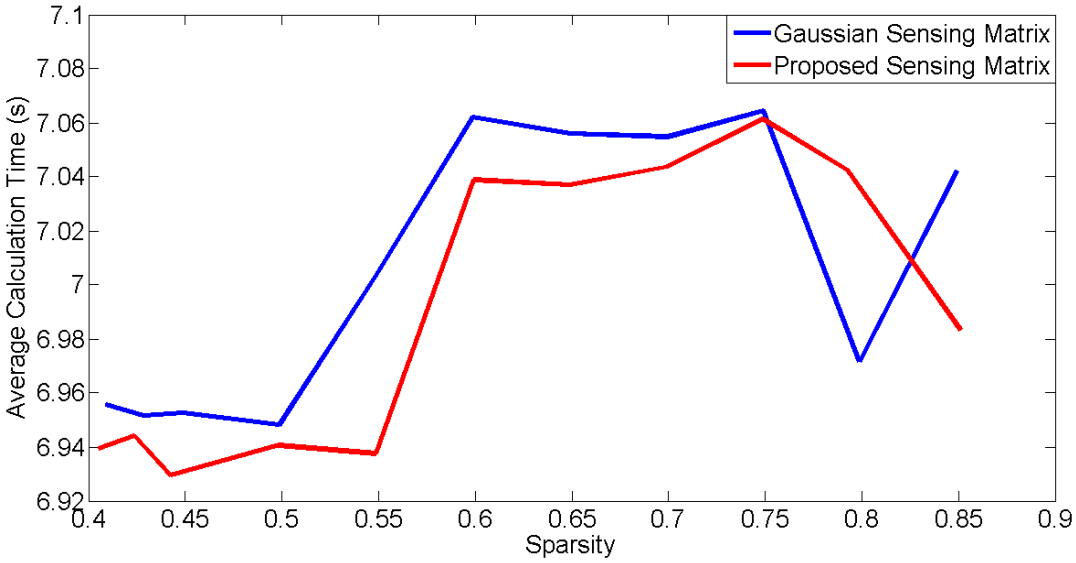


Figure 4. Plot of the average calculation time as a function of sparsity. Values of reconstruction time were computed using three algorithms: reconstructing the T2-weighted image using Gaussian sensing matrix (blue solid line), and reconstructing the T2-weighted image using the proposed patch sensing matrix (solid red line). 30 different sets of randomly sampled data were collected for an accurate measurement of the algorithm performance.

site, where sufficient high amplitude signals were required to distinguish it from surrounding tissues. Analyses of the difference between the original image and the recovered image were also carried out to further confirm that the patch sensing matrix leads to a higher quality reconstruction. It can be seen in Figure 5(D) that the use of the Gaussian sensing matrix results in a recovered image full of noise. In contrast, the use of the patch sensing matrix as shown in Figure 5(E) filters out noise along with some edge information of the original image, which is to be expected since centrally concentrated random sampling results in an enhanced contrast and less noise at the expense of missing most periphery data at the cost of special resolution.

Another important merit to the proposed approach is its applicability to real-world scenarios. For the purpose of effective image reconstruction without artifacts, the data points much be selected randomly. However, generating a fully random sensing matrix is challenging. Moreover, it can be problematic since, conventionally, the k-space data is obtained on a Cartesian grid, while the readout dimension is obtained continuously. The proposed patch sensing matrix is a practical solution to this problem. The centrally concentrated randomization is confined within a cross structure to minimize the storage requirement, and the new sensing matrix can be divided into patches as k-space is conjugated symmetrically.

More work regarding sampling optimization is needed. For example, how to create the optimal probability density function to improve the overall efficiency of the reconstruction algorithm should be investigated and overcome. There is also the possibility of using either radial or spiral sampling schemes, which can give the appearance of random sampling in Cartesian space.[24-28]

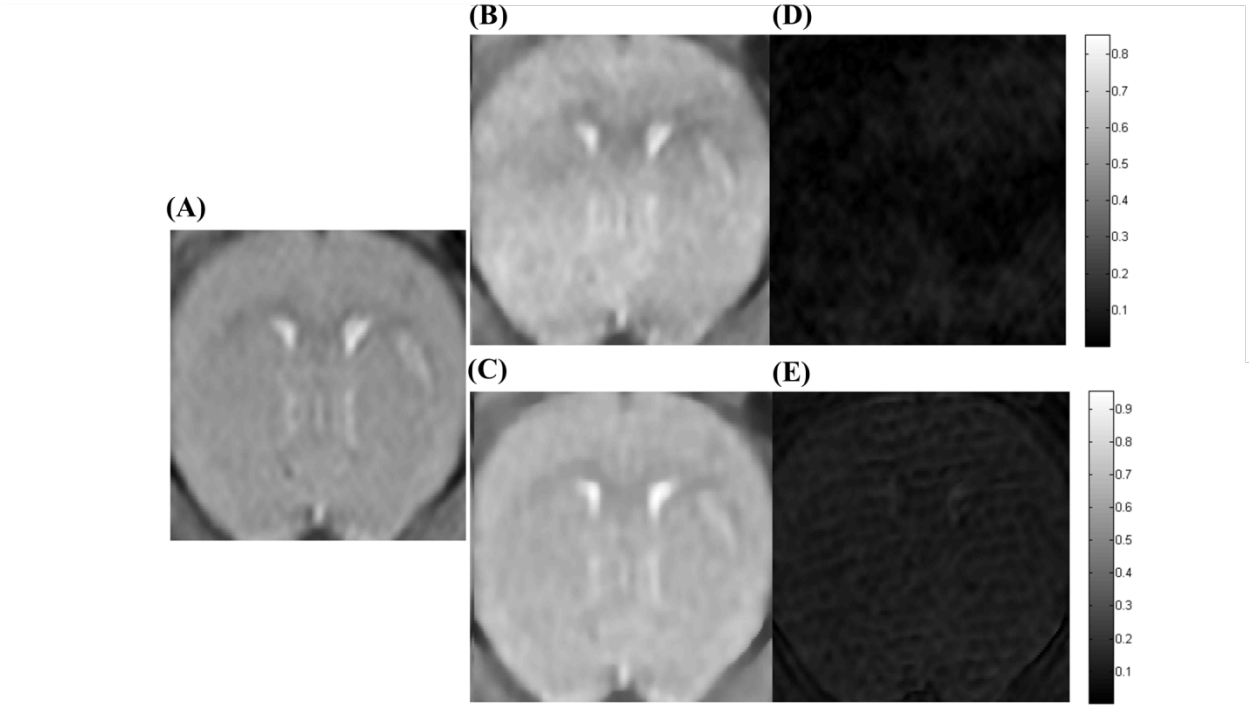


Figure 5. MRI reconstruction results: (A) original T2-weighted image reconstructed from the full k-space data, (B) reconstructed T2-weighted image using a 50% sparse Gaussian sensing matrix, (C) reconstructed T2-weighted image using 50% sparse proposed patch sensing matrix, (D) difference between the original image and Gaussian-based recovered image, and (E) difference between the original image and patch-based recovered image.

7.4 Conclusion

A new and simple method to design the sensing matrix for image recovery in compressive sensing MRI has been presented in this paper. The resulting sensing matrix has a patch structure that reflects the underlying signal density of k-space, rendering it more efficient in terms of the required memory storage. The proposed patch sensing matrix undersampled more data at the periphery of k-space and less data near the k-space origin, resulting in a higher reconstruction quality in terms of the correlation coefficient and the contrast-to-noise ratio. Our

experimental and simulation results revealed that, by using the proposed sensing matrix, we can achieve better recovery performance than what can be obtained using the Gaussian sensing matrix. In addition, the recovery time was reduced when the proposed scheme was used, due to simpler structure of the proposed sensing matrix and sampling mechanism. The success of applying a sensing matrix to compressive sensing MRI can benefit the fast acquisition of high contrast images, which is especially useful and practical in making an accurate medical diagnosis in early tumor detection. More investigation is needed in future research to improve the recovery performance as well as optimize the sampling process.

7.5 References

[1] Brown, R. W.; Cheng, Y. N.; Haacke, E. M.; Thompson, M. R.; Venkatesan, R. Magnetic Resonance Imaging: Physical Principles and Sequence Design. Wiley, **1999**.

[2] Shannon, C. E. Communication in the Presence of Noise. *Proc. IRS.* **1949**, *37*, 10-21.

[3] Nyquist, H. Certain Topics in Telegraph Transmission Theory. *Trans. Am. IEE.* **1928**, *47*, 617-644.

[4] Haase, A.; Frahm, J.; Matthaei, D.; Hnicke, W.; Merboldt, K. D. FLASH Imaging. Rapid NMR Imaging using Low Flip-Angle Pulses. *J. Magn. Reson*. **1986**, *67*, 258-266.

[5] Stehling, M. K.; Turner, R.; Mansfield, P. Echo-Planar Imaging: Magnetic Resonance Imaging in a Fraction of a Second. *Science*. **1991**, *254*, 43-50.

[6] Hennig, J.; Naureth, A.; Friedburg, H. RARE Imaging: a Fast Imaging Method for Clinical MR. *Magn. Reson. Med.* **1986**, *3*, 823-33.

[7] Candes, E. J.; Romberg, J.; Tao, T. Robust Uncertainty Principles: Exact Signal Reconstruction from Highly Incomplete Frequency Information. *IEEE Trans. Inf. Theory.* **2006**, *52*, 489-509.

[8] Lustig, M.; Donoho, D. L.; Pauly, J. M. Sparse MRI: The Application of Compressed Sensing for Rapid MR Imaging. *Magn. Reson. Med.* **2007**, *58*, 1182-95.

[9] Donoho, D. L. Compressed Sensing. *IEEE Trans. Inf. Theory*. **2006**, *52*, 1289-1306.

[10] Cook, R. L. Stochastic Sampling in Computer Graphics. *ACM Trans. Graph.* **1986**, *5*, 51-72.

[11] Gdaniec, N.; Eggers, H.; Bornert, P.; Doneva, M.; Mertins, A. Robust Abdominal Imaging with Incomplete Breath-holds. *Magn. Reson. Med.* **2014**, *71*, 1733-42.

[12] Block, K. T.; Uecker, M.; Frahm, J. Undersampled Radial MRI with Multiple Coils: Iterative Image Reconstruction using a Total Variation Constraint. *Magn. Reson. Med.* **2007**, *57*, 1086-98.

[13] Chandarana, H.; Feng, L.; Block, T. K.; Rosenkrantz, A. B.; Lim, R. P.; Babb, J. S.; Sodickson, D. K.; Otazo, R. Free-breathing Contrast-enhanced Multiphase MRI of the Liver using a Combination of Compressed Sensing, Parallel Imaging and Golden-angle Radial Sampling Invest. *Radiol*. **2013**, *48*, 10-16.

[14] Holland, D. J.; Liu, C.; Song, X.; Mazerolle, E. L.; Stevens, M. T.; Sederman, A. J.; Gladden, L. F.; D'Arcy, R. C.; Bowen, C. V.; Beyea, S. D. Compressed Sensing Reconstruction Improves Sensitivity of Variable Density Spiral fMRI. *Magn. Reson. Med.* **2013**, *70*, 1634-43.

[15] Seeger, M.; Nickisch, H.; Pohmann, R.; Scholkopf, B. Optimization of K-Space Trajectories for Compressed Sensing by Bayesian Experimental Design. *Magn. Reson. Med.* **2010**, *63*, 116-26.

[16] Wang, Z.; Arce, G. R. Variable Density Compressed Image Sampling. *IEEE Trans. Image Process*. **2010**, *19*, 264-270.

[17] Abolghasemi, V.; Ferdowsi, S.; Sanei, S. A Block-Wise Random Sampling Approach: Compressed Sensing Problem. *JAIDM*. **2015**, *3*, 93-100.

[18] Tiwari, V.; Bansod, P. P.; Kumar, A. Designing Sparse Sensing Matrix for Compressive Sensing to Reconstruction High Resolution Medical Images. *Cogent Engineering*. **2015**, *2*, 1017244.

[19] Rudin, L. I.; Osher, S.; Fatemi, E. Nonlinear Total Variation Based Noise Removal Algorithms. *Physica D.* **1992**, *60*, 259-268.

[20] Osher, S.; Burger, M.; Goldfarb, D.; Xu, J. J.; Yin, W. T. An Iterative Regularization Method for Total Variation-based Image Restoration. *Multiscale Model Simul.* **2005**, *4*, 460-489.

[21] Osher, S.; Mao, Y.; Dong, B.; Yin, W. Fast Linearized Bregman Iteration for Compressive Sensing and Sparse Denoising. *Commun. Math. Sci.* **2010**, *8*, 93-111.

[22] Wright, S. J.; Nowak, R. D.; Figueiredo, M. A. T. Sparse Reconstruction by Separable Approximation. *IEEE Trans. Signal Process.* **2009**, *57*, 2479-2493.

[23] Goldstein, T.; Oscher, S. The Split Bregman Method for L1-Regluarized Problems. *SIAM J. Imaging Sci*. **2009**, *2*, 323-343.

[24] Marseille, G. J.; de Beer, R.; Fuderer, M.; Mehlkopf, A. F.; van Ormondt, D. Nonuniform Phase-encode Distributions for MRI Scan Time Reduction. *J. Magn. Reson.* **1996**, *111*, 70-75.

[25] Scheffler, K.; Hennig, J. Reduced Circular Field-of-View Imaging. *Magn. Reson. Med.* **1998**, *40*, 474-480.

[26] Tsai, C.; Nishimura, M. D. Reduced Aliasing Artifacts using Variable Density K-Space Sampling Trajectories. *Magn. Reson. Med.* **2000**, *43*, 452-458.

[27] Peters, D. C.; Korosec, F. R.; Grist, T. M.; Block, W. F.; Holden, J. E.; Vigen, K. K.; Mistretta, C. A. Undersampled Projection Reconstruction Applied to MR Angiography. *Magn. Reson. Med.* **2000**, *43*, 91-101.

[28] Greiser, A.; von Kienlin, M. Efficient K-Space Sampling by Density Weighted Phase-Encoding. *Magn. Reson. Med*. **2003**, *50*, 1266-1275.

Chapter 8

Non-Linear Iteration Technique to Enhance Early Tumor Contrast in Compressive Sensing MRI

8.0 Abstract

Magnetic resonance imaging (MRI) has revolutionized biomedical diagnosis by providing sensitive and non-invasive measurements of tissue structures. The challenge in successfully implementing this promising clinical application for early tumor detection lies in increasing the image contrast at the early-stage tumor site while reducing the lengthy acquisition time. For this purpose, we proposed a computational thinking method for contrast enhancement and imaging acceleration based on two major findings: (1) an active feedback-based nonlinear imaging technique is sensitive to small spatial variations in the magnetic susceptibility, whereby the response of the system can be modified in real-time to amplify the contrast difference between healthy tissues and early tumors. (2) compressive sensing can be used to extract all important features in MR images by collecting only a small sample of the data, and a sensing matrix with a specific structure can give rise to a faster recovery algorithm which leads to a marked improvement in compressive sensing performance in feedback-based MRI. To confirm the feasibility and advantages of our method, stage-1 orthotopic glioblastoma mouse models infected with the human U87MG cell line were imaged. Representative results showed that, when compared to conventional fast imaging techniques, the proposed method was able to reconstruct feedback-based images that had less sparsity but higher correlation coefficients and a fivefold improvement in the contrast-to-noise ratio. With advances in clinical biomedical

diagnostics, this technique becomes increasingly important as we seek to optimize the contrast while taking into account cost considerations as well as patient comfort and compliance.

8.1 Introduction

Magnetic Resonance Imaging (MRI) is one of the most successful analytical tools for a diverse array of applications in the sciences. By using low-energy and non-ionizing radiation, MRI has become an important non-invasive and sensitive technique in the clinical biomedical diagnosis of tumors. While MRI has its advantages over using other imaging methods for early tumor detection, it is severely constrained by the limited image contrast at the early-stage tumor site and its lengthy image acquisition times.

Conventional MR imaging techniques generate contrast based on different relaxation time constants that vary from tissue to tissue.[1] This is problematic in early tumor detection because the morphological differences between early-stage tumors and healthy tissues are too subtle to change the relaxation properties, so that even when a long evolution time is used, the resulting contrast still remains invisible in MR images. Consequently, more sensitive imaging mechanisms are needed to delineate the exact extent of tumors at early stage.

Various pulse sequences have been designed to enhance the contrast in early cancer detection.[2-4] However, the addition of complicated pulse sequences extends the duration of spin preparation, which hampers the development of faster imaging techniques. Moreover, the specific set of parameters that yield optimal contrast is typically unknown and must be iteratively determined through experimentation. This iterative process is long and tedious, due to a lengthy MRI acquisition time that requires sufficient raw data to be collected to meet the Nyquist criteria.[5-6] Some common acceleration methods have been proposed to reduce the acquisition

time. For example, partial Fourier transformation has been used based on the conjugated symmetry of k-space, but the signal-to-noise ratio (SNR) is too low, where the number of TRs required is reduced twofold by acquiring half of k-space data in the phase encoding.[7] Parallel imaging also shows potential in shortening the acquisition time as an undersampled data set in the phase where encoding directions of k-space is acquired, combining the signal of several coil arrays.[8-10] However, this technique requires iterative reconstructions and has not yet been widely used in clinical systems. Other regular undersampling approaches in k-space give rise to aliasing artifacts in MR images through the Fourier reconstruction, not to mention their poor resolution and low contrast-to-noise ratio.

Therefore, in this current paper, we proposed an accelerated non-linear iteration technique to enhance the contrast in early cancer detection in MRI using compressive sensing. More specifically, we used the radiation damping feedback to create the nonlinear evolution of spins, leading to the amplification of the slight contrast difference between early-stage tumors and healthy tissues. In order to reduce the total imaging time, we used compressive sensing techniques to accelerate the data acquisition process.[11-13] Rather than select data normally from Gaussian or other random distributions, we used a more realistic sensing matrix for the purpose of achieving non-linear contrast enhancement to produce high quality images.[14] Representative experimental results showed that, in comparison to the conventional T2-weighted imaging, the feedback-based image was able to not only highlight the location of the early-stage tumor but also increase the contrast over fivefold. Extensive simulations suggested that the newly proposed patch sensing matrix led to a marked improvement in compressed sensing performance with less sparsity, including a higher reconstruction correlation coefficient and a higher contrast-to-noise ratio around the tumor site. With advances in clinical biomedical diagnostics, this combined

nonlinear iteration technique becomes increasingly important, because we want to optimize the contrast through trial and error while taking into account the cost as well as patient comfort and compliance.

8.2 Theory

8.2.1 Feedback-Based Contrast Enhancement

The fundamental physics can be described by the modified Bloch equations. [1,15] We defined the normalized magnetization in a voxel at spatial position $\vec{r}$ as $\vec{m}(\vec{r},t) = \vec{M}(\vec{r},t)/M_0$, where M_0 is the equilibrium magnetization. Therefore, the evolution of a normalized magnetization vector can be approximated as

$$\frac{\partial \vec{m}(\vec{r},t)}{\partial t} = \gamma \vec{m}(\vec{r},t) \times \left[\frac{\delta\omega(\vec{r})}{\gamma}\hat{\boldsymbol{z}} + \vec{B}(\vec{r},t)\right] - \frac{m_z(\vec{r},t)-1}{T_1(\vec{r})}\hat{\boldsymbol{z}} - \frac{m_x(\vec{r},t)\hat{\boldsymbol{x}}+m_y(\vec{r},t)\hat{\boldsymbol{y}}}{T_2(\vec{r})} \quad (1)$$

where $\vec{B}(\vec{r},t)$ is the effective local field experienced by $\vec{m}(\vec{r},t)$ in the rotating frame precessing with Lamor frequency $\omega_0 = \gamma B_0$, γ is the gyromagnetic ratio, B_0 is the strength of the externally applied Zeeman field. $T_1(\vec{r})$ and $T_2(\vec{r})$ are the longitudinal and transverse relaxation time constants respectively, and $\delta\omega = \omega - \omega_0$ is the resonance offset of a spin in the rotating frame Assume the effective local field $\vec{B}(\vec{r},t)$ consists of the feedback field, i.e. $\vec{B}(\vec{r},t) = \vec{B}_{FB}(\vec{r},t)$, which is a macroscopic reactionary field dependent on the total transverse state of the magnetization given by[16-17]

$$\gamma B_{FB,+}(t) = \frac{ie^{-i\varphi}}{V\tau_r}\int_V \vec{m}_+(\vec{r},t)\, d^3\vec{r} \quad (2)$$

where $m_+ = m_x + im_y$, φ is the radiation damping field phase, and τ_r is the radiation damping field strength

$$\tau_r = \frac{1}{2\pi\eta M_0 Q\gamma} \quad (3)$$

where Q is the quality factor of the probe and η is the filling factor of receiver coil.

The explicit dependence of the radiation damping on the instantaneous state of the magnetization renders the evolution of the system as nonlinear. The exact trajectory (and the corresponding contrast) is thus highly sensitive to the small resonance offset differences between healthy tissues and early-stage tumors, making it possible to gain positive and robust imaging contrast at tumor site.

8.2.2 Compressive Sensing Theory

Much of the groundwork for compressive sensing has already been worked out,[11-13] so only a brief summary will be provided here, focused on a specific patch structure of the sensing matrix[14] for contrast-to-noise efficiency using split-Bregman reconstruction algorithm.[18]

The idea of compressive sensing MRI stems from the notion that many MR images satisfy the sparsity requirement within the Fourier domain, since each data point collected in k-space contains the information of the entire image. A high amplitude signal, which is concentrated at the center of k-space, is essential to the delineation of contrast in the image, making tumors detectable relative to normal tissues. Therefore, the sensing matrix and sampling mechanism should naturally lead to denser data collection closer to the center of k-space, with decreased density toward the periphery. For this purpose, we used a patch structure for the sensing matrix combined with a probability density function for the random sampling. The advantage of this patch structure is that it requires less memory for storing the data. The sensing matrix can be divided into patches due to the characteristics of conjugated symmetry in k-space. And by filtering out corner areas, we can select certain low amplitude signals from the overwhelmingly large amount of periphery data to ensure the spatial resolution.

Of the many algorithms that can be used to reconstruct the undersampled data set;[19-22] in this paper, we make use of the recently proposed Split-Bregman method for $\ell 1$ regularized problems.[18] The Split Bregman method is a general technique for minimizing a large class of $l1$ regularized energies, but it is particularly well-suited to problems that arise in compressed sensing MRI. For this application, we wish to solve

$$\min_{u} \ \|\nabla u\|_1 + \frac{\lambda}{2}\|Au - f\|_2^2 \tag{4}$$

The split Bregman method works by "decoupling" the $l1$ and $l2$ terms in equation (4) by introducing the auxiliary variable $d \leftarrow \nabla u$. The problem in equation (4) then becomes

$$\min_{u,d} \ \|d\|_1 + \frac{\lambda}{2}\|Au - f\|_2^2 \text{ such that } d = \nabla u \tag{5}$$

The resulting constrained problem is then solved using a Bregman iteration technique. This method has an extremely effective denoising capability. While the formulation in equation (5) may seem more complicated than the original problem in equation (5), it is shown in reference that the problem can be broken down into a sequence of simple sub-problems. Each of these sub-problems can be solved directly using only shrinkage operators and fast Fourier transforms.

8.2.3 Reconstruction Quality Indicator

The performance of sensing matrices can be evaluated by the quality of reconstructed images, which is indicated using parameters such as the correlation coefficient (r). The formula is given below,

$$r = \frac{\sum_m \sum_n (A_{mn} - \bar{A})(B_{mn} - \bar{B})}{\sqrt{(\sum_m \sum_n (A_{mn} - \bar{A})^2)(\sum_m \sum_n (B_{mn} - \bar{B})^2)}} \tag{6}$$

where A is the original image and B is the recovered image.

8.3 Results and Discussion

8.3.1 Feedback-Based High Contrast Image

Ideally, a high-contrast image contains little information aside from the shape and location of the tumor. Therefore, to validate the efficacy of our feedback-based nonlinear imaging technique in early tumor detection, stage-1 orthotopic glioblastoma mouse (GBM) models infected with the human U87MG cell line were imaged 13 days after tumor implantation. As shown in Figure1, the tumor area was highlighted in the feedback images with strong contrast, whereas these features were barely observable in the conventional T2-weighted images. If we fit the time constant for each pixel, we can get the mapping for both methods, and it becomes clear that feedback mapping is able to highlight the tumor location. Recall that for the physical origin of the feedback field as expressed in equation (2), the dependence on the instantaneous magnetization amplifies the difference in the magnetic susceptibility between early-stage tumors and normal healthy tissues, leading to the contrast enhancement around fivefold in early tumor detection.

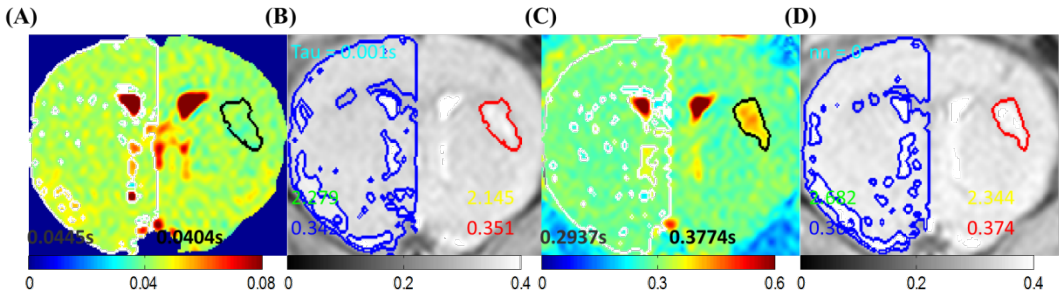


Figure 1. Representative result from mouse brain thirteen days after tumor injection. In comparison to the low contrast T2 weighted (A) time constant mapping and (B) image, a high contrast (C) time constant mapping and (D) image using the radiation damping feedback field successfully highlight and circle the location of the actual tumor.

8.3.2 Sparsity of High Contrast Image

Sampling images using an appropriate mechanism is essential to the faithful reconstruction of those images. Thus, a sensing matrix plays a significant role in the compressive sensing framework. Data points for the image reconstruction were collected using Gaussian and patch sensing matrices, both having the same dimensions as the original image, but the sparsity was only 50% of the full k-space data. As the shown in Figure 2, the Gaussian sensing matrix creates a random sampling pattern, while the patch sensing matrix reflects the underlying signal density of k-space, which is not uniform but is more concentrated for the lower-frequency components at the center of k-space and falls away towards the periphery.

In order to evaluate the performance of the patch sensing matrix-based nonlinear iteration technique in compressive sensing MRI, the image reconstruction quality indicator, including the correlation coefficient with the original image and the correlation coefficient at the tumor site, was computed from three reconstructions: a recovered T2-weighted image by Gaussian sensing matrix, a recovered feedback-based image by Gaussian sensing matrix, and a recovered feedback-based image by patch sensing matrix. The overall random nature of the sampling of data points requires that the reconstruction be run for many different sets of missing data in order to obtain an accurate measurement for the quality indicator. Thus, the average correlation coefficients calculated from 30 different sets were plotted as a function of sparsity in Figure 3. It can be seen that, regardless of the imaging technique and the sensing matrix used for recovery, values of both the average correlation coefficient with the image and the average correlation coefficient at tumor site decreased as less data was collected for the reconstruction. However, the use of the patch sensing matrix yielded a better reconstruction quality than the results achieved using the Gaussian sensing matrix. As illustrated in Figure 3, the solid red line, which

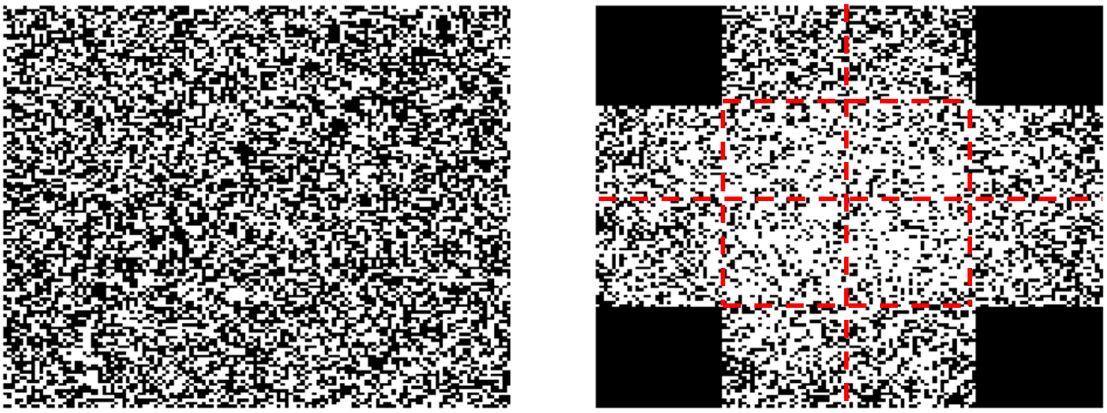


Figure 2. The structure and sampling mechanism of the Gaussian sensing matrix (left) and the Patch sensing matrix (right). Both sensing matrices have the same dimension as the original image, but the sparsity is only 50% with respect to the full k-space data.

represented the reconstruction performed by the patch sensing matrix, was higher than both the solid black line and the solid blue line, which represented the reconstruction performed by Gaussian sensing matrix. When only 40% of original data were selected, the correlation coefficient for the image calculated using the patch sensing matrix was still close to 1.0, but it was only 0.85 when using the Gaussian sensing matrix. This is because, even though both sensing matrices were based on a random sampling mechanism, the Gaussian matrix was completely unstructured, while the cross structure of the proposed sensing matrix filtered out portions of the periphery, as most of the energy of images is concentrated around the k-space origin.

The comparisons between the solid red line and the solid black line to the solid blue line revealed the advantage of using the nonlinear iteration technique. As the sensing matrices became increasingly sparse, the correlation coefficients computed from the T2 weighted imaging

technique (solid blue line) dropped dramatically, which indicated that more data is needed to ensure a satisfactory reconstruction. In contrast, the nonlinear iteration imaging technique showed a more consistent performance, since both the solid red line and the solid black line dropped slowly. If we choose the Gaussian sensing matrix as the data sampling mask, by comparing the solid black line and solid blue line in Figure 3A, we may conclude that the feedback-based imaging technique offered a relatively poor recovery performance in terms of the average correlation coefficient of the image, as the larger relative standard deviation from the T2 weighted image, as summarized in Table 1, indicated a lack of consistency in reconstruction. Moreover, for making a medical diagnosis of an early stage tumor, the correlation coefficient at the tumor site is of greater importance. As seen in Figure 3B, the average correlation coefficient calculated from the feedback-based image (solid black line) was relatively larger than the one calculated from T2 weighted image (solid blue line). And the smaller standard deviation, as summarized in Table 1, indicated that less data can be safely acquired without the significant loss of information when recovering the feedback-based image.

To further confirm that the use of the nonlinear iteration imaging technique and the patch sensing matrix can benefit early tumor detection in compressive sensing MRI, the result of the average contrast-to-noise ratio (CNR) was plotted as a function of sparsity in Figure 4. Since early-stage tumors are often too small to be detected, in the conventional T2 weighted image, the CNR values represented by the solid blue line remain flat and hover around zero. With an increased amount of undersampled data, the CNR values fell below zero, indicating that increased noise interfered with the major MR features and resulted in low quality reconstruction

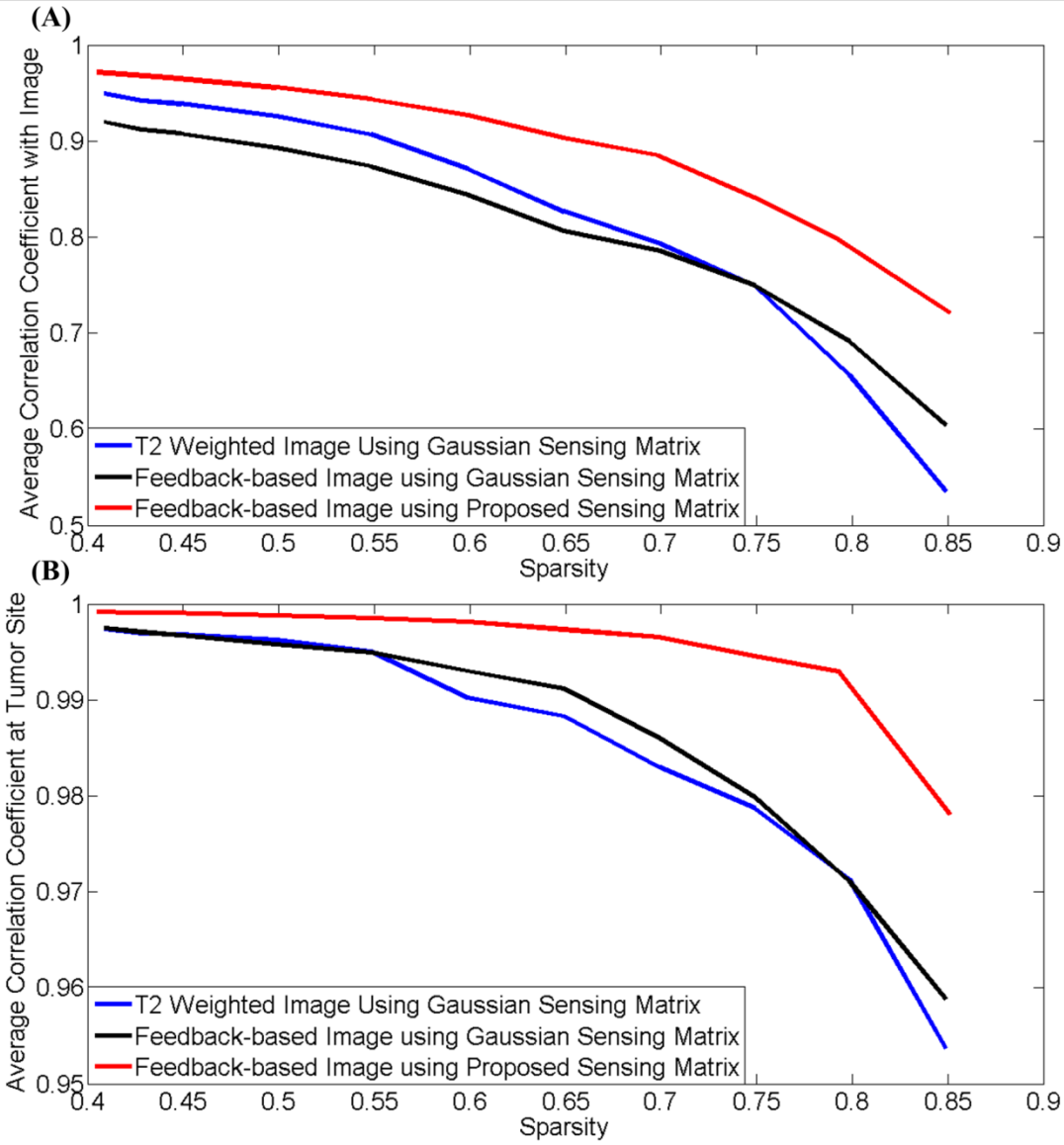


Figure 3. Plot of the average correlation coefficient with the image (A) and the average correlation coefficient at the tumor site (B) as a function of sparsity. Values of correlation coefficients were computed from three reconstructions: the T2-weighted image that was recovered using the Gaussian sensing matrix (solid blue line), the feedback-based image that was recovered using the Gaussian sensing matrix (solid black line), and the feedback-based image that was recovered using the proposed patch sensing matrix (solid red line). 30 different sets of randomly sampled data were collected to measure the reconstruction performance.

using the completely unstructured Gaussian sensing matrix. When the nonlinear iteration technique was applied to imaging, the CNR values were elevated significantly. It was consistent with the results of the original feedback-based image and the time constant mapping image shown in Figure 1. The feedback field is sensitive to the small resonance offset differences between early-stage tumors and healthy tissues; therefore, the limited contrast can be amplified by generating nonlinear spin dynamics. The application of the proposed patch sensing matrix in image

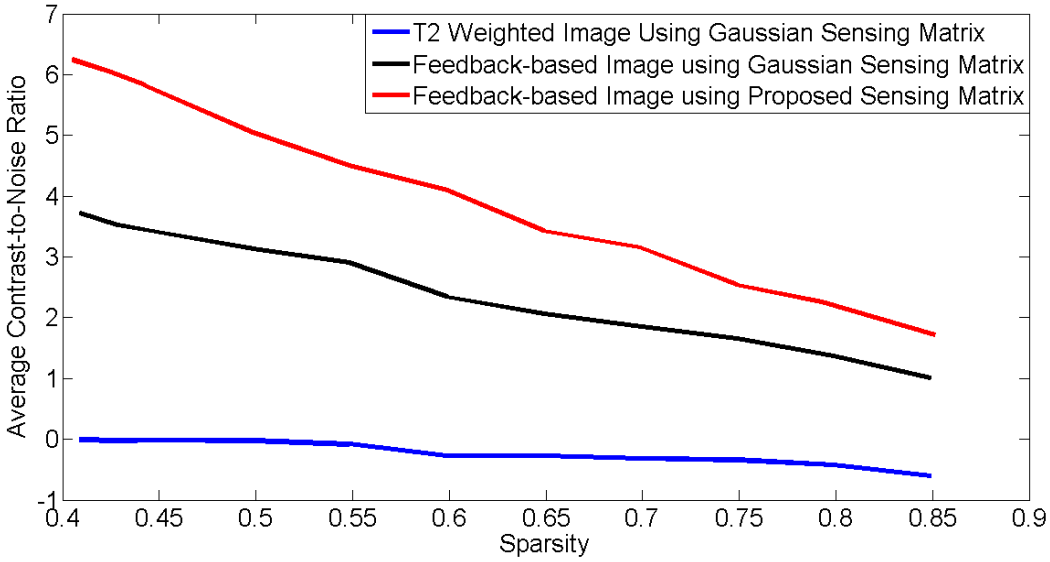


Figure 4. Plot of the average contrast-to-noise ratio as a function of sparsity. Values of CNR were computed from three reconstructions: the T2-weighted image that was recovered using the Gaussian sensing matrix (solid blue line), the feedback-based image that was recovered using the Gaussian sensing matrix (solid black line), and the feedback-based image that was recovered using the proposed patch sensing matrix (solid red line). 30 different sets of random sampled data were collected for to measure the reconstruction performance.

recovery can further improve the contrast-to-noise ratio over 1.5-fold with around only 60% of the data collected. The solid red line plotting the results obtained using the patch sensing matrix is much higher than both the solid black line and the solid blue line plotting the results obtained using the Gaussian sensing matrix. This is consistent with the result shown in Figure 3, as the proposed patch sensing matrix reflects the underlying signal density of the k-space data. Combining the nonlinear iteration imaging technique with the centrally concentrated sampling mechanism not only yielded better reconstruction quality in terms of the average correlation coefficients but also provided a robust and enhanced contrast-to-noise ratio for early tumor detection.

8.3.3 Reconstructed Image Results

Representative results of MRI reconstructed images, illustrated in Figure 5, further validate the advantages of applying the nonlinear iteration imaging technique and the patch sensing matrix to compressive sensing MRI. The tumor location was circled in red in the original feedback-based image reconstructed using the full k-space data (Figure 5A). The T2 weighted image that was recovered using the Gaussian sensing matrix (Figure 5B), the feedback-based image that was recovered using the Gaussian sensing matrix (Figure 5C), and the feedback-based image that was recovered using the patch sensing matrix (Figure 5D) were compared to Figure 5A. Both sensing matrices were 50% sparse and had the same dimensions as the original k-space. As shown in Figure 5, all three recovered images displayed important MR features and details, such as the shape of the brain, white matter and gray matter. However, since T2 weighted imaging is a relaxation-based technique, it was difficult for us to delineate the tumor location in Figure 5B. In addition, as the reconstruction was carried out using a 50% sparse Gaussian sensing matrix, the poor reconstruction quality rendered the recovered image noisier, which

further blurred the tumor area and resulted in a negative contrast-to-noise ratio, which was consistent with the results discussed in Figure 3 and Figure 4. In contrast, the tumor location was

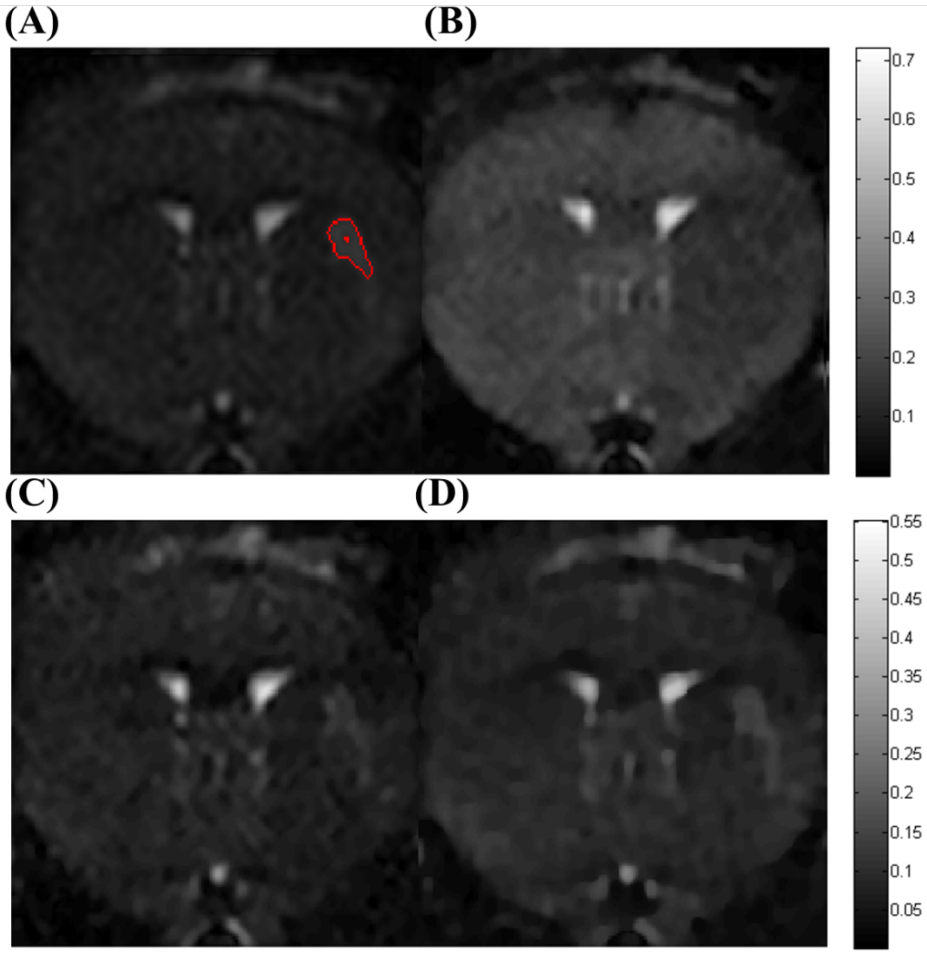


Figure 5. Representative results of MRI reconstruction: (A) feedback-based image reconstructed using the full k-space data, (B) T2 weighted image reconstructed using the Gaussian matrix, (C) feedback-based image reconstructed using the Gaussian matrix, (D) feedback-based image reconstructed using the proposed patch sensing matrix. Both the Gaussian sensing matrix and the patch sensing matrix have the same dimensions as the original image, but the sparsity is only 50% with respect to the full k-space data.

highlighted in the feedback-based image recovered using the Gaussian matrix. And the proposed patch sensing matrix performed even better in the image recovery. Besides the higher average correlation coefficients and contrast-to-noise ratio, it can be seen that Figure 5C is smoother than the other recovered images. Since we filter out most periphery data, the features of the tumor are readily apparent. When more data points are retained, the image will have higher resolution and less noise. This is to be expected, since the central region of k-space controls the contrast of image, with the surrounding region encoding much of the resolution.

The use of the nonlinear iteration technique enhanced the contrast five times better than the conventional imaging methods, but the introduction of the feedback field required us to determine the specific set of parameters for yielding the optimal contrast, which were typically unknown at the onset of measurement. The use of the patch sensing matrix not only accelerated the image acquisition but also extracted all important features and information regarding the early-stage tumor. Future investigation will need to be carried out in order to determine the optimal set of MR experimental conditions for optimizing the contrast through trial and error, and updating the sensing matrix structure and sampling mechanism to obtain a higher quality reconstruction while collecting less data.

Table 1. Performance of the nonlinear iteration technique with patch sensing matrix in compressive sensing MRI evaluated using reconstructed correlation coefficients and contrast-to-noise

Indicators	Sparsity	40%		50%		60%		70%	
		Avg[*1]	Std[*2]	Avg	Std	Avg	Std	Avg	Std
Correlation Coefficient with The Image	Feedback Patch	0.9736	0.001	0.9561	0.007	0.9272	0.026	0.8853	0.027
	Feedback Gaussian	0.9216	0.031	0.8853	0.031	0.8444	0.043	0.7860	0.053
	T2 Gaussian	0.9513	0.035	0.9264	0.042	0.8714	0.072	0.7934	0.110
Correlation Coefficient at Tumor Site	Feedback Patch	0.9993	8.2e-4	0.9988	3.7e-4	0.9982	6.2e-4	0.9966	0.002
	Feedback Gaussian	0.9977	0.001	0.9959	0.003	0.9930	0.004	0.9860	0.014
	T2 Gaussian	0.9974	0.001	0.9963	0.002	0.9903	0.009	0.9830	0.026
Contrast-to-Noise Ration	Feedback Patch	12.000	0.517	9.8960	0.997	8.0271	1.815	5.7573	2.167
	Feedback Gaussian	8.7106	2.340	6.8666	2.357	4.2178	3.351	2.1012	3.026
	T2 Gaussian	5.3e-4	0.434	-0.014	0.563	-0.263	0.689	-0.313	0.697

*1: Avg stands for average values

*2: Std stands for standard deviation

8.4 Conclusion

A computational thinking method for contrast enhancement and imaging acceleration in compressive sensing MRI was proposed in this current paper. The new method used a patch sensing matrix to reconstruct the feedback-based image. The performance was validated by our experimental and simulation results, as the correlation coefficients and contrast-to-noise ratios were significantly improved in comparison to the conventional imaging and reconstruction methods. The success of applying this combined nonlinear iteration technique in advanced clinical biomedical diagnostics can benefit the detection of early stage tumors, where it is becoming increasingly necessary for clinical purposes to generate high-contrast images in a short period of time.

8.5 References

[1] Brown, R. W.; Cheng, Y. N.; Haacke, E. M.; Thompson, M. R.; Venkatesan, R. Magnetic Resonance Imaging: Physical Principles and Sequence Design. Wiley, **1999**.

[2] Hameeduddin, A.; Sahdey, A. Diffusion-Weighted Imaging and Dynamic Contrast-Enhanced MRI in Assessing Response and Recurrent Disease in Gynaecological Malignancies. *Cancer Imaging*. **2015**, *15*, 3.

[3] Kuhl, C. K.; Schrading, S. H.; Bieling, B.; Wardelmann, E.; Leutner, C. C.; Koenig, R.; Kuhn, W.; Schild, H. H. MRI for Diagnosis of Pure Ductal Carcinoma in Situ: a Prospective Observational Study. *The Lancet.* **2007**, *370*, 485-492.

[4] Haider, M. A.; van der Kwast, T. H.; Tanguay, J.; Evans, A. J.; Hashmi, A.; Lockwood, G.; Trachtenberg, J. Combined T2-Weighted and Diffusion-Weighted MRI for Localization of Prostate Cancer. *AJR.* **2007**, *189*, 323-328.

[5] Shannon, C. E. Communication in the Presence of Noise. *Proc. IRS.* **1949**, *37*, 10-21.

[6] Nyquist, H. Certain Topics in Telegraph Transmission Theory. *Trans. Am. IEE.* **1928**, *47*, 617-644.

[7] Feinberg, D. A.; Hale, J. D.; Watts, J. C.; Kaufman, L.; Mark, A. Halving MR Imaging Time by Conjugation: Demonstration at 3.5 kG. *Radiology.* **1986**, *161*, 527–31.

[8] Pruessmann, K. P.; Weiger, M.; Bornert, P.; Boesiger, P. Advances in Sensitivity Encoding with Arbitrary k-space Trajectories. *Magn. Reson. Med.* **2001**, *46*, 638–51.

[9] Seiberlich, N.; Breuer, F. A.; Blaimer, M.; Barkauskas, K.; Jakob, P. M.; Griswold, M. A. Non-Cartesian Data Reconstruction using GRAPPA Operator Gridding (GROG). *Magn. Reson. Med*. **2007**, *58*, 1257–65.

[10] Lustig, M.; Pauly, J. M. SPIRiT: Iterative Self-Consistent Parallel Imaging Reconstruction from Arbitrary K-Space. *Magn. Reson. Med.* **2010**, *64*, 457–71.

[11] Candes, E. J.; Romberg, J.; Tao, T. Robust Uncertainty Principles: Exact Signal Reconstruction from Highly Incomplete Frequency Information. *IEEE Trans. Inf. Theory.* **2006**, *52*, 489-509.

[12] Lustig, M.; Donoho, D. L.; Pauly, J. M. Sparse MRI: The Application of Compressed Sensing for Rapid MR Imaging. *Magn. Reson. Med.* **2007**, *58*, 1182-95.

[13] Donoho, D. L. Compressed Sensing. *IEEE Trans. Inf. Theory*. **2006**, *52*, 1289-1306.

[14] Wang, C.; Lin, Y. Y. Designing Sparse Sensing Matrix for Compressive Sensing to Reconstruct High Contrast MR Images in Early Tumor Detection. (*In Preparation for Submission*)

[15] Abragam, A. Principles of Nuclear Magnetism. Oxford Science, **1961**.

[16] Abergel, D.; Louis-Joseph, A.; Lallemand, J. Y. Amplification of Radiation Damping in a 600-MHz NMR Spectrometer: Application to the Study of Water-Protein Interaction. *J. Biomol. NMR.* **1996**, *8*, 15-22.

[17] Abergel, D.; Louis-Joseph, A.; Lallemand, J. Y. A New Concept for Selective Excitation in NMR. *Chem. Phys. Lett.* **1996**, *262*, 465-469.

[18] Goldstein, T.; Oscher, S. The Split Bregman Method for L1-Regluarized Problems. *SIAM J. Imaging Sci*. **2009**, *2*, 323-343.

[19] Rudin, L. I.; Osher, S.; Fatemi, E. Nonlinear Total Variation Based Noise Removal Algorithms. *Physica D.* **1992**, *60*, 259-268.

[20] Osher, S.; Burger, M.; Goldfarb, D.; Xu, J. J.; Yin, W. T. An Iterative Regularization Method for Total Variation-based Image Restoration. *Multiscale Model Simul.* **2005**, *4*, 460-489.

[21] Osher, S.; Mao, Y.; Dong, B.; Yin, W. Fast Linearized Bregman Iteration for Compressive Sensing and Sparse Denoising. *Commun. Math. Sci.* **2010**, *8*, 93-111.

[22] Wright, S. J.; Nowak, R. D.; Figueiredo, M. A. T. Sparse Reconstruction by Separable Approximation. *IEEE Trans. Signal Process.* **2009**, *57*, 2479-2493.

Chapter 9

MRI Contrast Enhancement in Early Tumor Detection by Using Nonlinear Spin Dynamics in a Radiation Damping Field: Insight from Simulation

9.0 Abstract

Use of MRI to detect early stage tumors, has been severely limited by the imaging contrast. Conventionally, contrast is generated by the varying magnetic resonance properties of different tissues. However, when these differences are minimal, the desired contrast may not be achievable even after a long evolution time. In this paper, we presented a novel approach that utilizes the chaotic spin dynamics induced by the nonlinear evolution of spin system in the presence of a radiation damping feedback field. This approach yielded a more stable and robust contrast that is sensitive to small magnetic susceptibility variations than can be achieved using traditional MRI methods. We first confirmed theoretically the effectiveness of manipulating the spin dynamics by performing Monte Carlo simulations. Experimental results further demonstrate the promise that this approach has for improving the biomedical diagnosis of early stage tumors.

9.1 Introduction

Immensely versatile and useful techniques using Magnetic Resonance Imaging (MIR) have been developed, serving a diverse array of applications ranging from physics to all branches of chemistry, molecular biology, and medicine. However, fundamental challenges limit the

further utility of MRI, including how to enhance the imaging contrast arising from small variations in MR parameters so as to discern the structurally and functionally important features that currently remain hidden using traditional MR imaging methodologies. This is especially important to biomedical diagnoses, where limited contrast makes it difficult to detect the subtle physiological differences that delineate the boundaries of early stage tumors and other lesions.

Image contrast in MRI is typically generated by relaxation properties that vary among different types of tissue. However, relaxation-based contrast mechanisms find their own constraints in the detection of early tumor, where relaxation parameters such as molecular dynamics barely differ between healthy tissues and early-stage tumors. It has been shown that the advent of new tumors can be distinguished macroscopically by their microvascular angiogenesis.[1-7] In the presence of an external magnetic field, the tumor's characteristic physiological microvascular and metabolic changes induce corresponding change in its magnetic susceptibility. However, the linear evolution of conventional imaging modalities, such as longitudinal T_1 and transverse T_2 relaxation-based contrast mechanisms, is relatively insensitive to these small differences, making it difficult to generate sufficient contrast between healthy tissues and early-stage tumors.[8-9] Consequently, we became interested in pursuing a nonlinear approach, and one particular source of such nonlinear perturbation is radiation damping, which is a reactionary field that is dependent upon the coupling between the total sample magnetization and the receiver coil.

We demonstrated in this paper that, in the presence of a radiation damping feedback field, the manipulation of spin dynamics can induce an appreciable MRI contrast enhancement by amplifying the small magnetic susceptibility differences that distinguish healthy tissues from early stage tumors. We firstly explained the basic theory of the nonlinear evolution spin

dynamics and the effects of a radiation damping feedback field on the bulk spin system. Then, based upon a revised physiological model of the tumor microvascular system, we used Monte Carlo simulation[10] to analyze the nonlinear behavior of spins under the influence of radiation damping. Furthermore, we discussed our prospective outcome by changing the simulation parameters and confirming our simulation results by comparing them to the experimental results. We hope our work can provide a novel method to simulate the spin dynamics under the microvascular magnetic agents, and thus improve the image contrast in early state tumor detection.

9.2 Methods

9.2.1 Nonlinear Evolution of Spin Dynamics

The nonlinear evolution of a normalized magnetization vector, $\vec{m}(\vec{r}) = \vec{M}(\vec{r})/M_0$ (M_0 is the equilibrium magnetization for pure water), can be denoted using a classical Bloch equation[11-12]

$$\frac{\partial \vec{m}(\vec{r},t)}{\partial t} = \gamma \vec{m}(\vec{r},t) \times \vec{B}(\vec{r},t) - \frac{m_z(\vec{r},t)-1}{T_1(\vec{r})}\hat{\boldsymbol{z}} - \frac{m_x(\vec{r},t)\hat{\boldsymbol{x}} + m_y(\vec{r},t)\hat{\boldsymbol{y}}}{T_2(\vec{r})} \quad (1)$$

where γ is the gyromagnetic ratio, $T_1(\vec{r})$ and $T_2(\vec{r})$ are the longitudinal and transverse relaxation time constants, respectively. $\vec{B}(\vec{r},t)$ is the effective local field perturbation experienced by $\vec{m}(\vec{r},t)$ in the rotating frame, which is expressed as

$$\vec{B}(\vec{r},t) = \Delta\overrightarrow{B_z}(\vec{r},t) + \overrightarrow{B_{rd}}(\vec{r},t) \quad (2)$$

As shown in equation 2, information concerning magnetic field inhomogeneities $\Delta\overrightarrow{B_z}(\vec{r},t)$ and radiation damping $\overrightarrow{B_{rd}}(\vec{r},t)$ is contained in $\vec{B}(\vec{r},t)$. Note that the calculation of field perturbation $\vec{B}(\vec{r},t)$ that gives rise to the change to the spin magnetization is pivotal to any Monte Carlo

model of the magnetic resonance signal, especially for the nonlinear evolution of the spin dynamics under the influence of the joint effects of magnetic field inhomogeneities and radiation damping. Thus, in our simulation, those two fields' perturbations were modeled separately.

Magnetic field inhomogeneities[13-15] emanate from intravascular/extravascular magnetic susceptibility differences. Based on the infinite cylinder model (ICM) used to describe the blood oxygenation level dependent (BOLD) contrast mechanism,[16-17] blood vessels within the microvasculature system can be approximated by randomly orientated infinite cylinders. Therefore, the magnetic field inhomogeneities "felt" by a proton due to the magnetic susceptibility differences induced by a specific infinite cylinder exposed to an external magnetic field B_0 can be denoted as

$$\Delta B_{z,in}(\vec{r},t) = \frac{1}{2}B_0\Delta\chi(cos^2\,\theta - \frac{1}{3}), \text{ intravascular} \tag{3a}$$

$$\Delta B_{z,ex}(\vec{r},t) = \frac{1}{2}B_0\Delta\chi\left(\frac{R}{r}\right)^2 sin^2\,\theta\, cos(2\phi), \text{ extravascular} \tag{3b}$$

where the external magnetic field B_0 is along $\hat{\boldsymbol{z}}$ direction. R is the cylinder radius and r is the distance from proton position to the cylinder axis. The angle θ is the angle between cylinder axis and the external magnetic field B_0, while ϕ is the angle between vector r and the projection of B_0 onto the plane orthogonal to the cylinder axis. Moreover, $\Delta\chi$ is the susceptibility difference between the intravascular and extravascular spaces, given by $\Delta\chi = HCT(1-Y)\chi_{dHb}$, where HCT is the hematocrit, Y is the fractional oxygenation, and χ_{dHb} is the susceptibility of deoxyhemoglobin. As shown in equation 3, the effect of both intravascular and extravascular magnetic field perturbations is to shift the water resonance frequencies, leading to the contrast enhancement. However, such magnetic field inhomogeneities are independent of the instantaneous magnetization, thus limiting the amount of contrast through the linear evolution of

spins. Therefore, we need to introduce the radiation damping feedback field, which can amplify the magnetic susceptibility differences by using nonlinear spin dynamics.

Radiation damping, according to Lenz's Law, originates from the coupling between the receiver coil and the total transverse magnetization. Thus, this reactionary field can act back onto the sample, accelerating the magnetization back towards the equilibrium position. As a result, radiation damping can be succinctly described as a time-dependent field

$$\gamma B_{RD,+}(t) = \frac{ie^{-i\varphi}}{V\tau_r}\int_V \vec{m}_+(\vec{r},t)\, d^3\vec{r} \tag{4}$$

where $m_+ = m_x + im_y$, φ is the radiation damping field phase, and τ_r is the radiation damping field strength

$$\tau_r = \frac{1}{2\pi\eta M_0 Q\gamma} \tag{5}$$

where Q is the quality factor of the probe and η[18] is the filling factor of the receiver coil. In light of equation 1, it can be seen from equation 4 that the explicit dependence of radiation damping on the sample magnetization renders the evolution of Equation 1 to be nonlinear.

9.2.2 Healthy Tissue and Early Tumor Physiological Models

Since infinite cylinders were used to represent blood vessels within the microvasculature network, both healthy tissues and early stage tumors can be modeled as an ensemble of randomly oriented cylinders surrounded by protons within a cubic voxel. Those homogeneous spatial cylinders, with size following the lognormal distribution (mean radius $R = 10\mu m$ and standard deviation $\sigma = 0.2$), were generated by randomly selecting points within the cube. 3000 protons were also placed randomly within the same cubic voxel, and each proton performed a $3D$ random walk inside this region with step $\lambda = \sqrt{6D\Delta t}$, where $D = 1\times10^{-9}m^2s^{-1}$ is the water diffusion coefficient and $\Delta t = 5\times10^{-4}s$ is the time interval between each step. Since the cylinders used in our simulations were assumed to be impermeable, protons beginning a random

walk inside (outside) a cylinder therefore stayed inside (outside) that cylinder for the duration of its walk, and proton steps resulting in the penetration of cylinders were repeated until a collision-free-step was generated.

The differences between healthy tissue and early stage tumor models are difficult to establish because both tissues share a common morphology. According to tumor angiogenesis, when tumor is relatively small, it remains constrained within the organ it originated in and has not spread into surrounding tissues.[19-22] Thus, it differs little from the surrounding healthy tissue in its microvasculature formation and structure. But cancer cells, like healthy cells, cannot live without oxygen and nutrients. Thus, it is to be expected that as the tumor cells grow faster than the healthy cells, their increasing oxygen consumption will raise the level of deoxyhemoglobin in the blood, resulting in a faster T_2 relaxation time. However, counteracting the increase in oxygen extraction from the blood is a much larger increase in cerebral blood flow from the existing vascular network to the tumor site, bringing it with more oxyhemoglobin. In addition, as the tumor gets bigger, it induces angiogenesis to support its continued growth. With more surrounding capillaries providing oxygen to the tumor area, the net effect is a regional decrease in the level of paramagnetic deoxyhemoglobin as well as a smaller T_2 relaxation rate than that of healthy tissue.

So in our simulation, for healthy tissue, the susceptibility of deoxyhemoglobin χ_{dHb}, as reported, has a value of $2.28ppm$ in SI units. The blood oxygenation level was set up as 0.5 with a hematocrit HCT of 40%. 40 cylinders were assigned within the cubic voxel so that the volume fraction was around 2%. While for early-stage tumors both the susceptibility of deoxyhemoglobin χ_{dHb} and the hematocrit HCT maintain the same values, the blood oxygenation level and the volume fractions of blood vessels around the tumor will vary as a

manifestation of the abnormal metabolism of the early stage tumor. Since there is a decrease in the concentration of deoxyhemoglobin, the blood oxygenation levels for the early tumor were set up as 0.52, 0.55, 0.60, and 0.70 separately, and 10 capillaries with radius $R = 3\mu m$ were added into the original microvascular network to simulate the volume fraction changes.

9.3 Results and Discussion

9.3.1 Physiological Model

To confirm that our nonlinear imaging approach yields a better contrast, the validity of the physiological model was assessed at first by evaluation of the results of the $3D$ Monte Carlo simulations. The physics underlying a Monte Carlo simulation is simple: as protons diffuse through a magnetically inhomogeneous medium, their magnetic spins acquire phase differences with respect to one other, causing destructive interference and thus a characteristic macroscopic decay. We collected the MR signal attenuation as a function of time and calculated the transverse relaxation rate due to the magnetic field inhomogeneities and diffusion. By comparing the observed decay rate with published real world data, we are able to assess the validity of our physiological model for healthy tissues and early stage tumors.

With the assumption that blood vessels are treated as infinite cylinders with homogeneous susceptibility, we generated a microvascular network for healthy tissue (Figure 1a) and an early stage tumor (Figure 1b). The basic configurations for both systems were identical: the total number of magnetized, randomly oriented cylinders was 40, with each size following the lognormal distribution (mean radius $R = 10\mu m$ and standard deviation $\sigma = 0.2$), so that the volume fraction of all cylinders within the cubic voxel was 2%. However, we added 10 more randomly distributed cylinders with size $R = 3\mu m$ into the tumor's microvascular network to

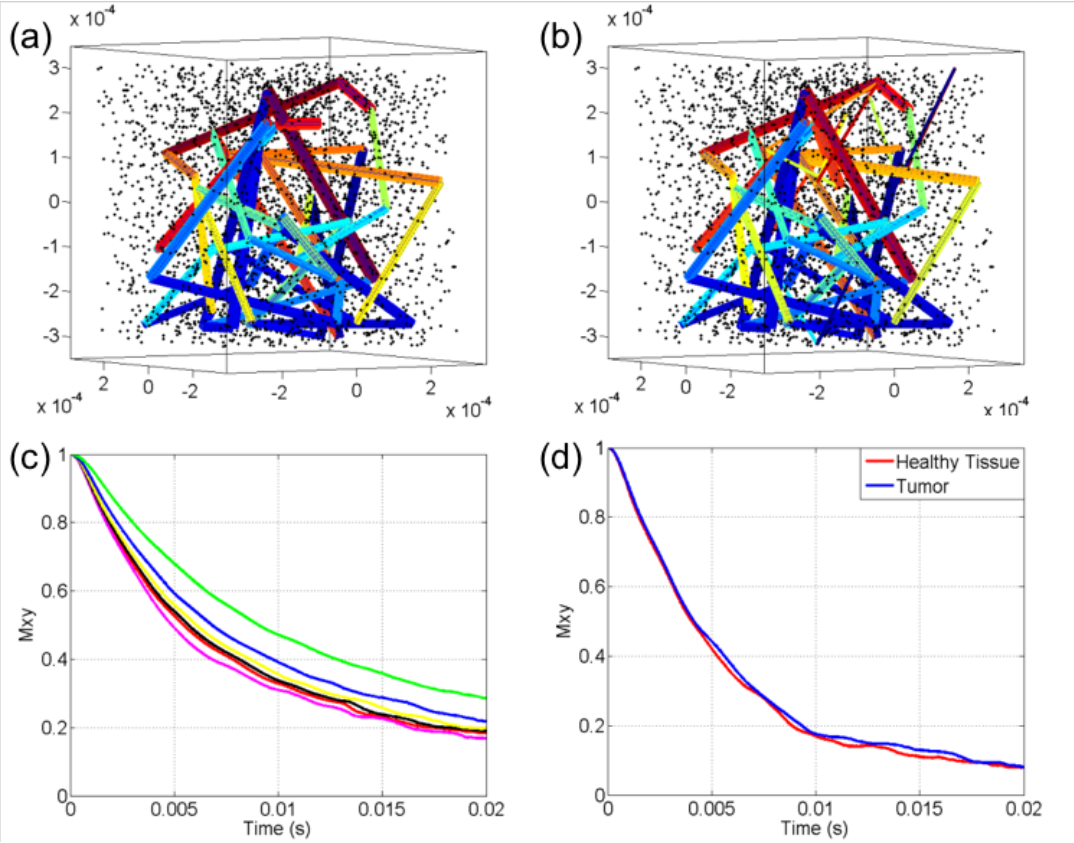


Figure 1. Physiological model of microvasculature structure for both (a) healthy tissue and (b) an early stage tumor represented by randomly oriented cylinders. (c) MR transverse signal attenuation as a function of time under different blood oxygenation levels and (d) MR transverse signal attenuation as a function of time for early stage tumors and healthy tissue.

show a higher vessel intensity, as shown in Figure 1b. Such changes, as described, functionally support the tumor's need for extra blood flow. In addition to the induced angiogenesis, the tumor's blood oxygenation level differences also contributed to its abnormal metabolism.

Figure 1c illustrates the transverse MR signal attenuation as a function of time under different blood oxygenation levels, where the red line represents the healthy tissue with a blood oxygenation of level $Y = 0.5$, and the other colored lines represent tumors with blood oxygenation level ranging from $Y = 0.52$ (black) to $Y = 0.70$ (green). When the blood flow is

sufficiently high, the oxygen transported by the induced vessels increases the blood oxygenation level and therefore decreases the concentration of deoxyhemoglobin around the tumor. The absence of paramagnetic deoxyhemoglobin in the blood vessels causes a susceptibility difference between the vessels and their surrounding tissues. Such susceptibility differences cause dephasing of the MR proton signal, leading to a change in the value of T_2^*. That is why the lines that represent the oxygenation levels of the early stage tumor, as shown in Figure 1c, are higher than the line for the healthy tissue. As reported in the previous literature, the transverse relaxation rate of healthy tissue is 20% faster than the rate of the early stage tumor 13 days after inoculation; however, a difference that significant can already be distinguished through traditional clinical MR imaging protocol. For practical consideration, we choose $Y = 0.55$ with ten more vessels added to model early tumor at stage I, and the difference of transverse relaxation between healthy tissue and early tumor, as shown in Figure 1d, is as small as 0.05, where the blue line stands for the model of the early stage tumor, which gives a relaxation time of $T_2^* = 6ms$ compare to $T_2^* = 5.8ms$ for healthy tissue.

Our validated physiological model suggests that the early stage tumor's relaxivity depends upon the abnormal characteristics of its metabolism, which include the induced angiogenesis and blood oxygenation level. We now consider the implications of the model for the tumor at (a) stage II and III and (b) stage IV. For scenario (a), there will be more vessels around tumor area and an increased blood supply, and therefore the greater magnetic susceptibility differential will make it relatively easy to distinguish the tumor from healthy tissue using traditional MRI. For scenario (b), the tumor is at a late stage, and the vessels around the tumor do not functionally supply blood flow. With the insufficient oxygen, the level of

deoxyhemoglobin increases, and the tumor will suffer from hypoxia, leading to a faster MR transverse signal decay.

9.3.2 Linear Spin Dynamics

If the local effective field only contains the information from magnetic field inhomogeneities, the spin dynamics, as described by Bloch equation 1, are linear. Followed the spin echo pulse sequence, which gives rise to the T_2 weighted image, we performed the Monte Carlo simulation within the physiological model established above. Both the evolution of transverse magnetization and its corresponding accumulated contrast are shown in Figure 2. As we can see, with the presence of magnetic field inhomogeneities, the MR signal from both tissues showed exponential decay, which is the traditional T_2 relaxation. The signal from healthy tissue decays faster than the signal from the early stage tumor due to its abnormal metabolism, which is consistent with the experimental result. However, the conventional T_2-weighted imaging method is relaxation-based and insensitive to such small susceptibility differences. Consequently, as the bulk spin systems evolve with time, the net transverse magnetization of early stage tumor (blue line) deviates little from that of healthy tissue (red line). The accumulated contrast, as shown in Figure 2b, was fairly limited, with the maximum contrast of 0.02. Such a minimal contrast can be indistinguishable from noise, which renders it useless in differentiating an early stage tumor from healthy tissue. As a matter of fact, the evolution of the T_2 spin dynamics is constrained within two-dimensions by the presence of magnetic field inhomogeneities, which reflects the linear property of such dynamics. Therefore, we looked for a nonlinear magnetic field perturbation, which can use the spin chaos to amplify the subtle magnetic susceptibility differences.

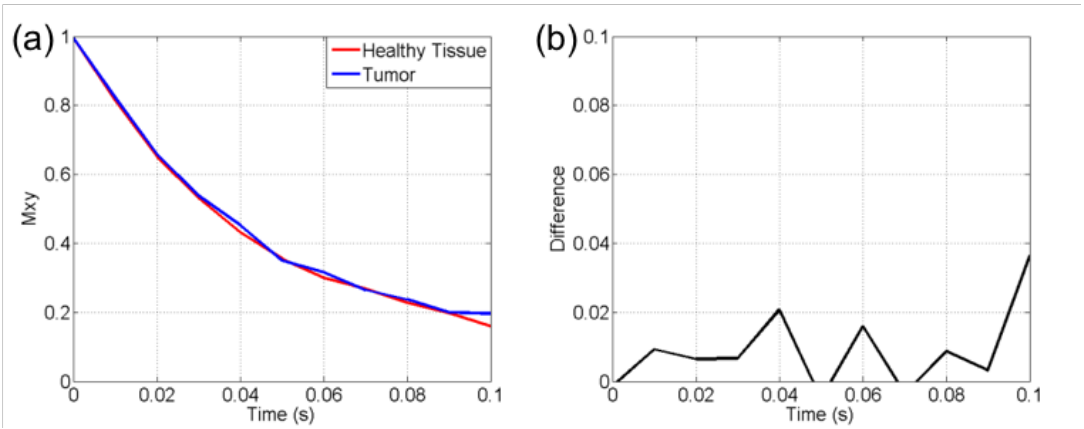


Figure 2. (a) MR transverse signal attenuation as a function of time for both healthy tissue and an early stage tumor with (b) the corresponding accumulated contrast under linear spin dynamics

9.3.3 Nonlinear Spin Dynamics

The inherent dependence of the radiation damping field on the magnetization, as described in equation 4, renders original Bloch equation nonlinear, thus causing the dynamics to become chaotic and unpredictable. The Monte Carlo simulation was performed within the same physiological model in the presence of radiation damping field. It can be seen that the net magnetization of the healthy tissue (red line) and early stage tumor (blue line) effectively repel each other as they spiral towards separated regions of the Bloch sphere, which is illustrated as 3D spin dynamics configuration in Figure 3a. The accumulation of the contrast can be tracked by the measurement of the average transverse magnetization shown in Figure 3b and the average longitudinal magnetization shown in Figure 3d. As seen in Figure 3c and Figure 3d, the maximum contrast accumulated through the nonlinear evolution in the presence of the radiation damping field was about five times higher than that of conventional T_2-weighted imaging, as shown in Figure 2b. More impressively, the contrast between the two components grew as the systems converged. This chaotic dynamic was unexpected, as the evolution of spins in the

absence of radiation damping simply follows the exponential decay and gives rise to limited contrast. The mechanism of this novel approach is a direct consequence of the radiation damping field's tendency to minimize itself. The effect of the radiation damping field, by its description in equation 4, is to naturally bring the total magnetization back towards a more stable equilibrium orientation. Since the radiation damping field is dependent on the instantaneous magnetization, tissues with more contribution tends to be affected more significantly. As a result, the signal from the healthy tissue decayed even faster than that of the early stage tumor tissue, as shown in Figure 3b and Figure 3d, with the highlighted region of tumor should be on the actual clinical image. Moreover, relaxation must be taken into account when considering the development of the contrast between different tissues, as it was previously ignored in the simulation. Relaxation will surely impede the long-term stability of the convergence and contrast, as the signal *in vivo* cannot last more than a few hundred milliseconds and will completely saturate long before the magnetization is able to converge. Despite the signal's proclivity to eventually saturate, we still expect that the initial evolution of the magnetization will advance toward fixed-points. As can be seen in the simulation results Figure 3c and Figure 3e, the developed contrast resulting from the radiation damping is significant at early times, requiring additional evolution time to allow the magnetization to stabilize.

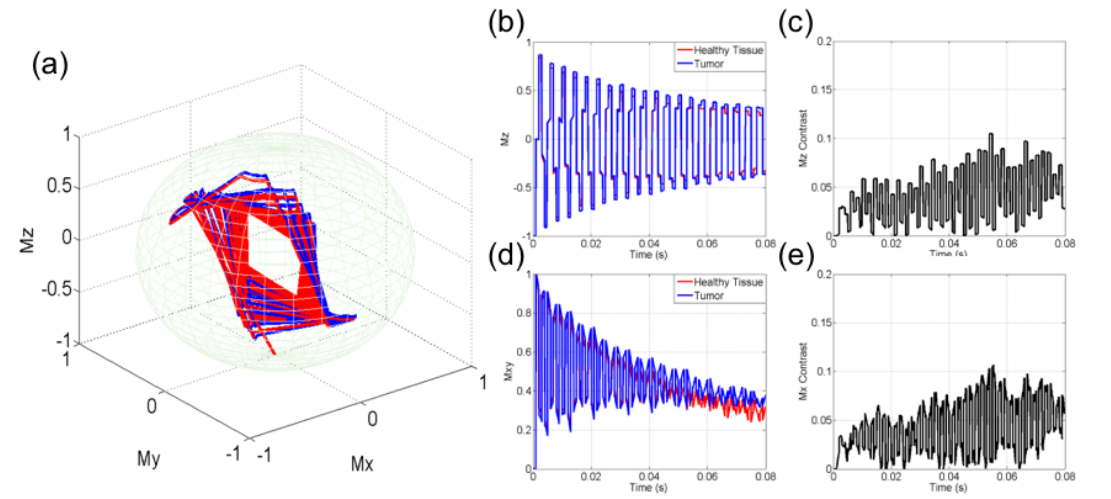


Figure 3. (a) 3D nonlinear spin dynamics configuration of normalized magnetization. (b) MR transverse signal attenuation as a function of time for both healthy tissue and the early stage tumor with (c) the corresponding accumulated contrast. (d) MR longitudinal signal attenuation as a function of time for both healthy tissue and the early stage tumor with (e) the corresponding accumulated contrast.

9.3.4 *In Vivo* Experiments

Simulation results indicated that the application of the radiation damping field requires only a slight resonance offset to generate an effectively robust contrast to differentiate the early stage tumor from healthy tissue. An *in vivo* experiment was performed to verify the effectiveness of this new imaging technique. Stage-I orthotopic GBM mouse models infected with the human U87MG cell line were imaged after 8.4 days' implantation, as shown in Figure 4. By using an active feedback circuit at 300MHz with a micro-imaging probe, the appearance of the early stage tumor in the image (Figure 4a) was much clearer than in the conventional T_2-weighted imaging (Figure 4c). By calculating the average intensity of the tumor pixels and the average intensity of normal brain tissue pixels over time, the maximum contrast-to-noise ratio (CNR) of this active

feedback method was found to be 4.775, which is almost five times higher than the 1.129 maximum CNR of the T_2-weighted image. By fitting the time constant for each pixel, we were able to obtain the mapping for both the active feedback method (Figure 4b) and the T_2-weighted method (Figure 4d), clearly demonstrating that the feedback mapping is able to highlight the early stage tumor location.

9.4 Conclusion

In order to determine how best to enhance the MRI contrast in early tumor detection, we developed a general nonlinear spin dynamics manipulation scheme in the presence of a radiation damping field, leading to the accumulation of a more robust contrast than can be obtained using the conventional imaging method. We confirmed this novel approach theoretically, by carrying out a Monte Carlo simulation within a physiological model of healthy tissue and an early stage tumor, which was based on the magnetic field inhomogeneities that arose from differences in the intravascular/extravascular magnetic susceptibility. As shown by the simulation results, the nonlinear evolution of the spin chaos induced by the radiation damping field is sensitive to small variations in the magnetic susceptibility of healthy tissue and early stage tumors, resulting in an extraordinary fivefold contrast enhancement for imaging purposes. The experimental data further verified the feasibility and outcome of such a nonlinear feedback mechanism. By designing novel pulse sequences in the presence of an enhanced radiation damping feedback field, we were able to fully manipulate the nonlinear spin dynamics and amplify the small magnetic susceptibility differences to expand the potential applications of MRI in the clinical biomedical diagnosis of early stage tumors.

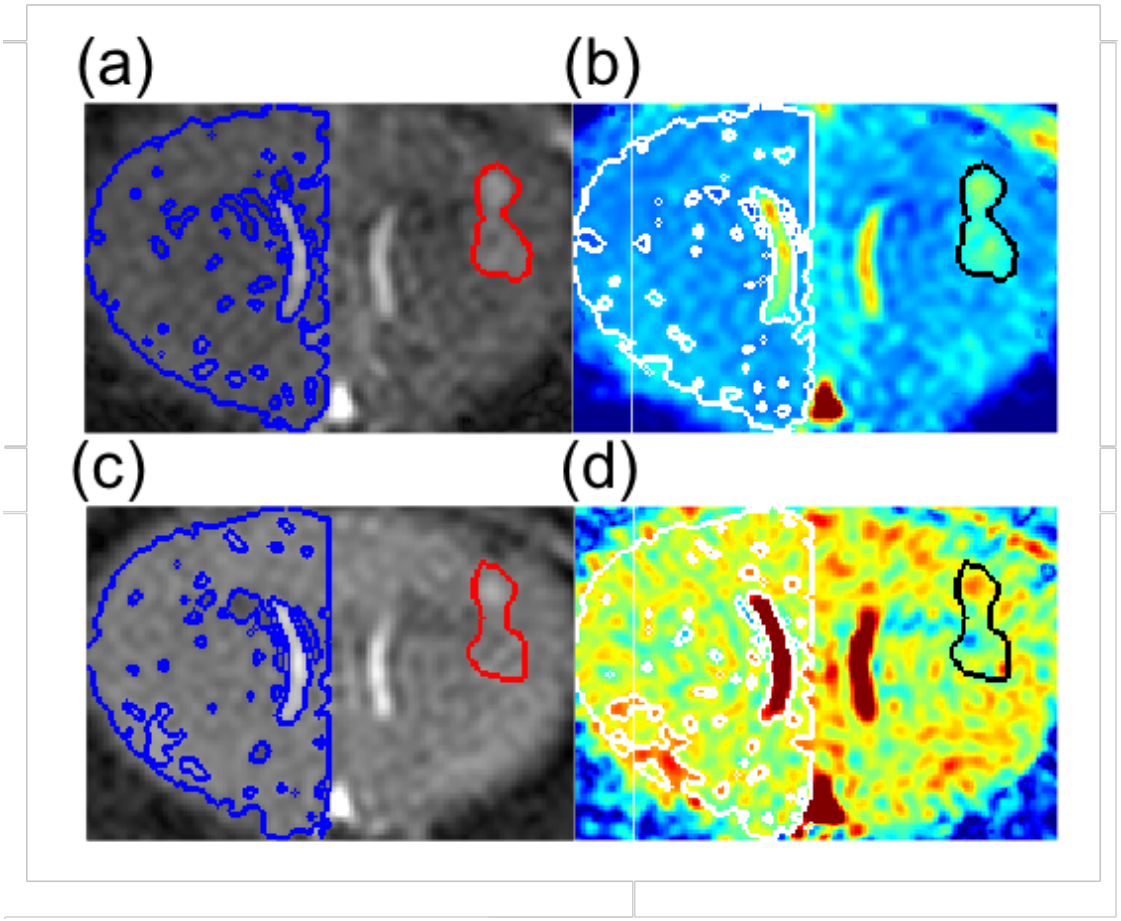


Figure 4. Representative results of *in vivo* images and parameter mapping for Stage-I orthotopic GBM mouse models infected with the human U87MG cell line. (a) Active-feedback image and (b) the corresponding parameter mapping, (c) T_2-weighted image TE=50ms and (d) the corresponding parameter mapping.

9.5 References

[1] Fu, Y.; Nagy, J. A.; Dvorak, A. M.; Dvorak, H. F. *Antiangiogenic Agents in Cancer Therapy*; Cambridge University Press: Totowa, NJ, **2007**; p. 205-224.

[2] Boxerman, J. L.; Hamberg, L. M.; Rosen, B. R.; Weisskoff, R. M. MR Contrast due to Intravascular Magnetic Susceptibility Perturbations. *Magn. Reson Med.* **1995**, *34*, 555-566.

[3] Ogawa, S.; Tank, D.; Menon, R.; Ellermann, J.; Kim, S.; Merkel, H.; Ugurbil, K. Intrinsic Signal Changes Accompanying Sensory Stimulation: Functional Brain Mapping with Magnetic Resonance Imaging. *Proc. Natl. Acad. Sci.* **1992**, *89*, 5951-5955.

[4] Turner, R.; Jessard, P.; Wen, H.; Kwong, K.; Le Bihan, D.; Zeffiro, T.; Balaban, R. Mapping of the Human Visual Cortex at 4 and 1.5 T using Deoxygenation Contrast EPI. *Magn. Reson. Med.* **1993**, *29*, 277-279.

[5] Pathak, A. P.; Schmainda, K. M.; Ward, B. D.; Linderman, J. R.; Rebro, K. J.; Greene, A. S. MR-Derived Cerebral Blood Volume Maps: Issues Regarding Histological Validation and Assessment of Tumor Angiogenesis. *Magn. Reson. Med.* **2001**, *46*, 735–747.

[6] Rhodes, C. G.; Wise, R. J. S.; Gibbs, J. M.; Frackowiak, R. S. J.; Hatazawa, J.; Palmer, A. J.; Thomas, D. G. T.; Jones, T. In Vivo Disturbance of the oxidative Metabolism of Glucose in Human Cerebral Gliomas. *Ann. Neurol.* **1983**, *14*, 614-626.

[7] Hoehn-Berlage, M.; Eis, M.; Schmitz, B. Regional and Directional Anisotropy of Apparent Diffusion Coefficient in Rat Brain. *NMR Biomed.* **1999**, *12*, 45–50.

[8] Muller, R.; Gillis, P.; Moiny, F.; Roch, A. Transverse Relaxivity of Particulate MRI Contrast Media: from Theories to Experiments. *Magn. Reson. Med.* **1991**, *22*, 178-182.

[9] Weisskoff, R.; Zuo, C.; Boxerman, J.; Rosen, B. Microscopic Susceptibility Variation and Transverse Relaxation: Theory and Experiment. *Magn. Reson. Med.* **1994**, *31*, 601-610.

[10] Kalos, M.; Whitlock, P. *Monte Carlo Methods*; John Wiley & Sons, Inc.: New York, **1986.**

[11] Haacke, E. M.; Brown, R. W.; Thompson, M. R.; Venkatesan, R. *Magnetic Resonance Imaging: Physical Principles and Sequence Design*; Wiley: **1999**.

[12] Abragam, A. *Principles of Nuclear Magnetism.* Clarendon Press: **1961**.

[13] Fisel, C.; Ackerman, J.; Buxton, R.; Garrido, L.; Belliveau, J.; Rosen, B.; Brady, T. MR

Contrast due to Microscopically Heterogeneous Magnetic Susceptibility: Numerical Simulations and Applications to Cerebral Physiology. *Magn. Reson. Med.* **1991**, *17*, 336-347.

[14] Hardy, P.; Henkelman, R. M. On the Transverse Rate Enhancement Induced by Diffusion of Spins through Inhomogeneous Fields. *Mag. Reson. Med.* **1991**, *17*, 348-356.

[15] Kennan, R.; Zhong, J.; Gore, J. Intravascular Susceptibility Contrast Mechanisms in Tissues. *Magn. Reson. Med.* **1994**, *31*, 9-21.

[16] Ogawa, S.; Menon, R.; Tank, D.; Kim, S.; Merkle, H.; Ellermann, J.; Ugurbil, K. Functional Brain Mapping by Blood Oxygenation Level-Dependent Contrast Magnetic Resonance Imaging: A Comparison of Signal Characteristics with a Biophysical Model. *Biophys. J.* **1993**, *64*, 803-812.

[17] Marques, J. P.; Bowtell, R. W. Using Forward Calculations of the Magnetic Field Perturbation due to a Realistic Vascular Model to Explore the BOLD Effect. *NMR Biomed.* **2008**, *21*, 553-565.

[18] Huang, S. Y.; Yang, S. S.; Lin, Y. Y. Sensitivity of Feedback-Enhanced MRI Contrast to Macroscopic and Microscopic Field Variations. *Magn. Reson. Med.* **2009**, *61*, 925-936.

[19] Chu, S. C.; Xu, Y.; Balschi, J. A.; Springer, C. S. Jr. Bulk Magnetic Susceptibility Shifts in NMR Studies of Compartmentalized Samples: Use of Paramagnetic Reagents. *Magn. Reson. Med*. **1990**, *13*, 239–262.

[20] Weisskoff, R. M.; Kiihne, S. MRI Susceptometry: Image-Based Measurement of Absolute Susceptibility of MR Contrast Agents and Human Blood. *Magn. Reson. Med.* **1992**, *24*, 375–383.

[21] Ogawa, S.; Lee, T. M. Magnetic Resonance Imaging of Blood Vessels at High Fields: *In Vivo* and *In Vitro* Measurements and Images Simulation. *Magn. Reson. Med.* **1990**, *16,* 9-18.

[22] Ogawa, S.; Lee, T. M.; Nayak, A. S.; Glynn, P. Oxygenation-Sensitive Contrast in Magnetic Resonance Image of Rodent Brain at High Magnetic Fields. *Magn. Reson. Med.* **1990**, *14*, 68-78.

Chapter 10

Conclusion and Outlook

Cancer has taken a devastating toll on our society. Its staggering economic impacts dramatically escalate insurance costs and drive families into bankruptcy. Millions live in fear, suffer, and all too often die. When President Richard Nixon declared a war on cancer in 1971, many believed the cure was right around the corner. But there is no magic bullet or miracle cure to this complex, multi-faceted set of illnesses. That said, very real progress can be made through incremental steps that find new ways to attack the disease and improve on existing methods.

In this dissertation, I have proposed an *in vivo* nano-theranostic system of combined hyperthermia/MRI to simultaneously diagnose and treat cancers. Through active (e.g., antibody-antigen) and passive (e.g., enhanced permeability and retention effect) targeting mechanisms, supramolecular magnetic nanoparticles can serve both as powerful "molecular beacons" to enhance the MR image contrast for early lesion detection and as "molecular bullets" to kill cancer cells and, through hyperthermia, control the release of cancer drugs directly to the tumor site.

Both theoretical calculations and experimental results have validated the applicability and efficacy of my proposed technique: a novel model to evaluate and optimize the heating efficiency of magnetic nanoparticles for *in vivo* MR nano-theranostic hyperthermia, a computational thinking method was established for imaging acceleration, a home-built active feedback electronic device to control the non-linear chaos in spin systems, and general spin amplification dynamics designed for the contrast enhancement in MRI.

More work needs to be done in order to realize the clinical application of this *in vivo* nano-theranostic system of combined hyperthermia/MRI. I plan to continue my research on designing experiments to examine the performance of the high-field MRI hyperthermia using the proposed possibilities, organizing data regarding the contrast enhancement in tumor detection through active feedback MRI, and using artificial intelligence to train MR images to improve the efficiency of data acquisition. I look forward to carrying out transformational work on fundamental physical chemistry theories and advancing nano-theranostic techniques into life-saving applications. The molecular diagnostics and targeted therapeutics described in my dissertation represent an important front in our war on cancer. Working in an interdependent and collaborative manner, I hope to complete this clinical paradigm for solving real-life cancer problems.